The Influence of Biomass Burning on the Arctic Atmosphere

by

Erik M. Lutsch

A thesis submitted in conformity with the requirements
for the degree of Doctor of Philosophy
Graduate Department of Physics
University of Toronto

Abstract

The Influence of Biomass Burning on the Arctic Atmosphere

Erik M. Lutsch

Doctor of Philosophy

Graduate Department of Physics

University of Toronto

2019

Evaluating the influence of biomass burning on the Arctic requires continuous and long-term measurements of the transported emissions. In this thesis, ground-based Fourier transform infrared (FTIR) solar-absorption spectroscopic measurements at the Polar Environment Atmospheric Research Laboratory (PEARL) in Eureka, Nunavut, Canada from 2006-2018 are used to retrieve the atmospheric abundance of the biomass burning species CO, HCN, C_2H_6, C_2H_2, CH_3OH, H_2CO, HCOOH and NH_3. The retrievals of NH_3 from Eureka FTIR measurements are the first long-term ground-based measurements of NH_3 in the high Arctic.

Measurements of NH_3, CO, HCN and C_2H_6 were simultaneously enhanced in July-August 2014 and attributed to the 2014 Northwest Territories wildfires. Enhancements were observed in FTIR measurements at Toronto, and due to the differences in travel times between the sites, an approximate 2-day lifetime of NH_3 in a smoke plume was determined, allowing for NH_3 to undergo long-range transport and therefore suggesting that boreal wildfires may be a considerable episodic NH_3 source to the Arctic.

The greatest enhancements of NH_3, CO, HCN, and C_2H_6 were observed from FTIR measurements at Eureka (2006-2017) and Thule, Greenland (2006-2017) from 17-22 August 2017 and attributed to the 2017 British Columbia and Northwest Territories wildfires. A GEOS-Chem simulation illustrated that these wildfires contributed to surface-layer NH_3 enhancements in the Canadian Archipelago of 0.01-0.11 ppbv from 15-23 August 2017, 0.14-5.50 times the background due to local seabird-colony sources, further indicating that boreal wildfire NH_3 is an important episodic source of NH_3 in the summertime high Arctic in addition to the persistent seabird-colony source.

Detection of wildfire pollution events was performed for Eureka FTIR measurements and nine other Northern high- and mid-latitude Network for the Detection of Atmospheric Composition Change (NDACC) FTIR sites from 2003-2018. Enhancements of CO were detected and correlated with simultaneous enhancements of the biomass burning tracers HCN and C_2H_6, providing a means of wildfire pollution detection. Source attribution of the detected events was performed using a GEOS-Chem tagged CO simulation. Boreal North America and boreal Asia were the largest contributors to anomalous enhancements at all sites, with a recent increase in the boreal North American contribution from 2013-2018.

Acknowledgements

I would like to express gratitude to my advisor, Kim Strong, for her continued support and guidance, providing me with the opportunity to carry out the research presented in this thesis. I would also like to thank my advisory committee: Dylan Jones and Kaley Walker. I am grateful for the helpful discussions with Dylan, his insight, and his patient assistance in running the GEOS-Chem model. I am also grateful for the many helpful discussions I have had with Kaley. Without her organization of the Canadian Arctic ACE/OSIRIS Validation campaigns my research would not have been possible. My doctoral experience has been greatly aided by my advisory committee who have made my experience both rewarding and enjoyable.

I would also like to thank Joseph Mendonca and Dan Weaver for their contribution to Eureka FTIR measurements and operations and for their continued assistance and helpful discussions. I would particularly like to acknowledge Sebastien Roche who has been operating the Eureka FTIR with me during my doctoral studies. Finally, I would also like to thank Stephanie Conway and Camille Viatte for their guidance when I was first learning to use SFIT4.

This research has been greatly aided by a number of scientists whom I would like to acknowledge here: the members of the NDACC IRWG and TCCON groups who all have contributed and from whom I have learned so much through many discussions. I would particularly like to thank my co-authors of my papers and presentations who were all an essential part of this research. I would like to thank PEARL operators Mike Maurice, Peter McGovern and John Gallagher, and PEARL Site Manager Pierre Fogal for maintaining operations of the Eureka FTIR. The Canadian Arctic ACE/OSIRIS Validation campaigns were an important contribution to my doctoral experience. For that, I would like to acknowledge and thank the ECCC Weather Station staff and the members of the campaign team who made my trips to the Arctic such an enjoyable and memorable experience.

Contents

List of Tables

List of Figures

List of Abbreviations

ACE Atmospheric Chemistry Experiment

AIE aerosol indirect effect

AERONET Aerosol Robotic Network

AOD aerosol optical depth

AIRS Atmospheric Infrared Sounder

AUST Australia and New Zealand

BB biomass burning

BC British Columbia

BOAS boreal Asia

BONA boreal North America

CAMS Copernicus Atmospheric Monitoring System

CANDAC Canadian Network for the Detection of Atmospheric Change

CEAM Central America

CEAS Central East Asia

CDNC cloud-droplet number concentration

CM composition measurements

CTM chemical transport model

CrIS Cross-track Infrared Sounder

CST Community Solar Tracker

DOFS degrees of freedom for signal

ECCC Environment and Climate Change Canada

EDGAR Emission Database for Global Atmospheric Research

EQAS Equatorial Asia

ER emission ratio

EnhR enhancement ratio

ESA European Space Agency

EURO Europe

EU European Union

FINN Fire Inventory from NCAR

FLEXPART Flexible Particle

FTIR Fourier transform infrared

FTS Fourier transform spectrometer

FP forward processing

FWHM full width half maximum

GEOS Goddard Earth Observing System

GEM-MAC Global Environmental Multi-scale Modelling Air Quality and Chemistry

GFAS Global Fire Assimilation System

GFED Global Fire Emission Database

GMAO Global Modeling and Assimilation Office

GUI graphical user interface

HITRAN High-resolution Transmission Molecular Absorption Database

HWHM half width half maximum

HYSPLIT Hybrid Single Particle Lagrangian Integrated Trajectory

IAGOS In-service Aircraft for a Global Observing System

IASI Infrared Atmospheric Sounding Interferometer

ILS instrument line shape

MCE modified combustion efficiency

MEGAN Model of Emissions of Gases and Aerosols from Nature

MERRA Modern-Era Retrospective analysis for Research and Applications

ME modulation efficiency

MIDE Middle East

MIR mid-infrared

MODIS Moderate Resolution Imaging Spectroradiometer

NASA National Aeronautics and Space Administration

NCAR National Center for Atmospheric Research

NCEP National Centers for Environmental Prediction

NDACC Network for the Detection of Atmospheric Change

NDSC Network for Detection of Stratospheric Change

NETCARE Network on Climate and Aerosols

NHAF Northern Hemisphere Africa

NHSA Northern Hemisphere South America

NIDFORVal Nitrogen Dioxide and Formaldehyde for Validation

NIES National Institute for Environmental Studies

NIR near-infrared

NIWA National Institute of Water and Atmospheric Research

NMVOC non-methane volatile organic compound

NWT Northwest Territories

OEM optimal estimation method

OPAL Zero Altitude Auxiliary Laboratory

OPD optical path difference

PAHA Probing the Atmosphere of the High Arctic

PEARL Polar Environment Atmospheric Research Laboratory

PES potential emission sensitivity

PE phase error

QA4ECV Quality Assurance for Essential Climate Variables

QFED Quick Fire Emission Database

RD rapid delivery

RMS root mean square

SAFIRE Surface and Atmospheric Flux, Irradiance and Radiation Extension

SEAS Southeast Asia

SHAF Southern Hemisphere Africa

SHSA Southern Hemisphere South America

SSH secure shell

SNR signal-to-noise ratio

TCCON Total Carbon Column Observing Network

TES Tropospheric Emission Spectrometer

TENA temperate North America

TOMAS Two-Moment Aerosol Sectional

TROPOMI Tropospheric Monitoring Instrument

UTC coordinated universal time

VOC volatile organic compound

VMR volume mixing ratio

VNC virtual network connection

ZPD zero path difference

Chapter 1

Introduction and Motivation

1.1 Introduction

Biomass burning is a process that involves the geochemical cycling of gases and particulates from the biosphere to the atmosphere (Levine, 2003). It is a process of global change and refers to the burning of living or dead vegetation. Examples of biomass burning globally, illustrated in Figure 1.1, include forest fires or wildfires of temperate and boreal forests, bushfires of Australia, and agricultural fires of Africa and Asia. The onset of these fires is often due to natural causes, driven by hot and dry conditions and an ignition source, most commonly lightning. Man-made fires are also a common occurrence in tropical developing countries where they are used as a means of cropland clearing referred to as slash-and-burn and make an appreciable contribution to global biomass burning emissions. In the Northern hemisphere, boreal wildfires are a dominant source of biomass burning, brought on by persistent warm and dry conditions resulting in increased fire risk and ignition from lightning. Both periods of greater fire risk and lighting activity are expected to occur with increasing frequency at Northern high-latitudes as a result of anthropogenic-induced climate change (Krause et al., 2014; Veraverbeke et al., 2017). The magnitude and intensity of boreal wildfire activity are also projected to increase with future climate change (Amiro et al., 2009; Westerling et al., 2006; Flannigan et al., 2009; Wotton et al., 2010; Boulanger et al., 2014).

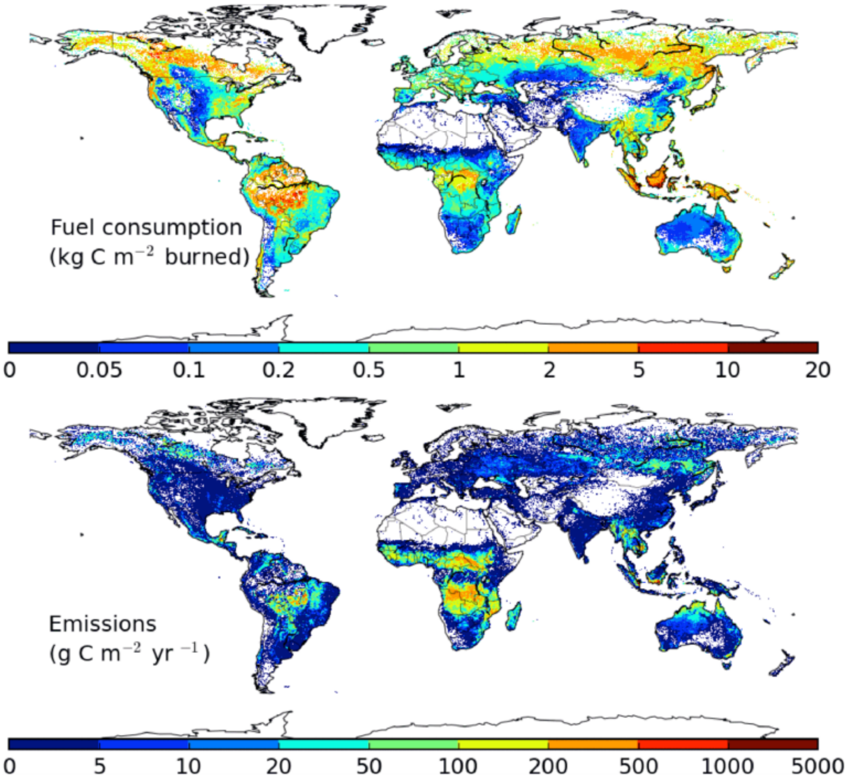

Figure 1.1: Global Fire Emission Database (GFED4) fuel consumption (top), and carbon emissions (bottom) averaged over 1997-2016. Figure from van der Werf et al. (2017).

The Arctic is a major receptor for pollution from mid-latitude regions (Stohl et al., 2006; Law and Stohl, 2007; Shindell et al., 2008). Boreal wildfires are well known to have considerable impacts on the Arctic atmosphere and climate (Amiro et al., 2009; Warneke et al., 2009). Black carbon, also known as soot, is a strong contributor to global warming (Bond and Sun, 2005 and references therein). Black carbon in the Arctic has been studied extensively and it has been found that a substantial fraction of Arctic black carbon is transported from boreal wildfires (Stohl et al., 2006; Sharma et al., 2004, 2006; Wang et al., 2011; Sharma et al., 2013; Evangeliou et al., 2016; Winiger et al., 2019). Black carbon is well known to contribute to episodes of poor air quality and warm the atmosphere by absorbing radiation and covering snow- and ice-covered surfaces, indirectly exerting snow-albedo effects (McConnell et al., 2007; Ramanathan and Carmichael, 2008; Flanner, 2013). Boreal wildfires may also influence the carbon cycle (Conard and Ivanova, 1997; Schimel and Baker, 2002; Mack et al., 2011; Santín et al., 2015). In boreal wildfire events, considerable quantities of carbon monoxide (CO), carbon dioxide (CO_2) and methane (CH_4) are emitted (van der Werf et al., 2017). Boreal wildfire emissions of CO, CO_2 and CH_4 are dependent on burning phase, with greater emissions of CO_2 and CH_4 from flaming combustion, with CO emissions dominated by smoldering and residual phase combustion (Andreae and Merlet, 2001 and the references therein). Emissions of CO, CH_4, nitrogen oxides (NO_X) and volatile organic compounds (VOCs) from wildfires may then be oxidized to form CO_2 and ozone (O_3) (Levine, 2003).

Wildfires also contribute to the emission of a large number of reactive trace gas species, including VOCs, which promote the production of tropospheric O_3 and the formation of aerosols (Jaffe et al., 1999, 2004; Parrington et al., 2013; Wentworth et al., 2018) and therefore negatively impact air quality. Emissions of these species remain highly uncertain as a result of the dependence of emissions on fuel types (Andreae and Merlet, 2001; Akagi et al., 2011; Andreae, 2019); emissions from a particular event are strongly influenced by local meteorology, which has a direct influence on the burning phase and the emission of each species (Yokelson et al., 1996, 1999, 2003; Goode et al., 1999, 2000). Additionally, these reactive species are short-lived and are not easily measured downwind of the fire source. Wildfire plumes may be subject to long-range transport, and therefore it is necessary to measure the concentrations of these reactive trace gas species downwind in order to predict their influence on a global scale.

Global chemical transport models (CTMs) are used to simulate the impact of emissions, transport and chemistry on the atmospheric abundance of a large number of gas phase and particulate species. Global CTMs, in all cases, rely on a number of parameterizations of the emissions, chemistry and transport within the model, in order to simulate atmospheric processes at finite resolution, both in space and time. All CTMs suffer errors as a result of the finite chemical and transport operators (Philip et al., 2016), while transport errors are inherent in the meteorological fields reanalyses that are used to drive the models (Yu et al., 2018). Simulations of biomass burning emissions and their transport are also highly uncertain. Most biomass burning emissions inventories, including the commonly used Fire Inventory from NCAR (FINN; Wiedinmyer et al., 2011), the Quick Fire Emission Database (QFED; Koster et al., 2015), the Global Fire Emission Database (GFED; van der Werf et al., 2017) and the Global Fire Assimilation System (GFAS; Kaiser et al., 2012), are all bottom-up inventories, in which satellite observations of burned areas, burned fraction, fire-radiative power (FRP), and vegetation type are used to estimate the total dry matter burned. The mass of dry matter burned is scaled by the emission factor (EF) for a particular species to yield the total mass of the species emitted. Each quantity used in the estimation of these emissions is subject to its own uncertainty, therefore leading to errors in the calculated total emissions of biomass burning.

In the case of an episodic wildfire plume, these inventories generally do not take into account injection of emissions into the free troposphere which may often occur (Val Martin et al., 2010, 2018). Injection of emissions into the free troposphere would likely result in different transport pathways of the plume compared to those from near-surface emissions. Accounting for this may be particularly important for more accurately capturing the long-range transport of a plume. Global CTMs also suffer from numerical diffusion as a result of their coarse horizontal and vertical resolution and therefore may not accurately simulate the transport of episodic wildfire plumes (Rastigejev et al., 2010; Eastham and Jacob, 2017). It is necessary to evaluate model performance through comparison to observational data in order to better understand model errors and improve model projections of the impacts of biomass burning on the atmosphere. This is particularly important in the Arctic, a difficult region to accurately model as result of the inherent model errors and lack of model validation where observations of transported wildfire emissions remain scarce.

1.2 Quantifying Biomass Burning Emissions

Precise knowledge of biomass burning emissions is required for accurate modelling of their impacts in global CTMs. Biomass burning emissions are often quantified as:

$$M_X = \mathrm{EF}_X \times \gamma \times \rho_f \times A, \tag{1.1}$$

where M_{X} is the total mass (g) of the species X emitted, EF_{X} is the emission factor (g per kg of dry matter) of the species X, γ and ρ_f are the combustion completeness (%) and fuel load (kg/m^2), respectively, while A is the total area burned (m^2). The quantities γ, ρ_f and A are obtained from satellite observations, usually the Moderate Resolution Imaging Spectroradiometer (MODIS; Giglio et al., 2006, 2013). The quantity EF_X specifically describes the emissions of X (mass of X per mass of dry matter burned), and is dependent on the type of vegetation burned (or fuel type) in addition to its combustion phase. The emission factor is related to the emission ratio (ER; Lefer et al., 1994) with respect to the species Y:

$$\mathrm{EF}_X = \mathrm{ER}_{X/Y} \cdot \frac{MW_X}{MW_Y} \cdot \mathrm{EF}_Y \tag{1.2}$$

where MW is the molecular weight of the species and $\mathrm{ER}_{X/Y}$ is the emission ratio of X with respect to Y:

$$\mathrm{ER}_{X/Y} = \frac{[X] - [X]_{bkgd}}{[Y] - [Y]_{bkgd}}, \tag{1.3}$$

where $[X]$ is the fire-affected concentration of the species and $[X]_{bkgd}$ is the background concentration. The emission ratio is calculated with respect to the species Y, usually

CO or CO_2. The emission ratio quantifies the emissions of the species X relative to Y, and is therefore independent of fuel type. Downwind of the fire source, the emission ratio may be considered as the enhancement ratio (EnhR) of an aged plume. For the measurement of the emission ratio or enhancement ratio, the only requirement is simultaneous measurements of X and Y. For this reason, the emission ratio is widely used to quantify emissions from a specific fuel type. If an enhancement ratio is measured, the emission ratio may be obtained by accounting for the loss of each species assuming the plume travel time and species lifetimes are known. The emission factor of X, however, is dependent on the assumed knowledge of the emission factor of Y and is commonly determined from reported values derived from laboratory studies of prescribed burns.

Measurements of emission factors and emission ratios have been reported for various greenhouse gases, trace gas and particulate species since the late 1980s (Andreae and Merlet, 2001; Akagi et al., 2011; Andreae, 2019) and are essential for global biomass burning emission estimates. However, the reported values of the emission ratios and emission factors for a number of species have led to a large range of values, which may be due to the variability of emissions as result of combustion phase and heterogeneous fuel types. Therefore, the variability of these emission estimates leads to greater uncertainty in global estimates of biomass burning emissions.

1.3 Ammonia in the Arctic

1.3.1 Sources and Implications

Ammonia (NH_3) has long been recognized as an important form of reactive nitrogen. The major sources of NH_3 globally are from agricultural practices, including raising livestock and the manufacturing and application of fertilizers (Bouwman et al., 1997; Asman et al., 1998; Bouwman et al., 2002; Erisman et al., 2011). Natural sources of NH_3 include soils, vegetation, oceans and animal excreta (Sutton et al., 2007). Transport and deposition of NH_3 can have negative impacts on nitrogen-sensitive ecosystems, which may lead to eutrophication and acidification of soil and water bodies and a potential loss of biodiversity (Krupa, 2003). The Arctic tends to be nitrogen limited and therefore is sensitive to nitrogen loading (Shaver and Chapin, 1980). It has been noted that the Arctic tundra has a high capacity for nitrogen pollution retention, resulting in a major source of eutrophication (Choudhary et al., 2016), which could have a negative impact on biodiversity. It was thought that the Arctic was free of NH_3 sources and transport of NH_3 from lower-latitudes was unlikely due to its short lifetime ranging from a few hours to a day (Lefer et al., 1999). However, Arctic sources of NH_3 include the hydrolysis of guano from migratory seabirds (Blackall et al., 2007; Riddick et al., 2012) and seal excreta (Theobald et al., 2006). Recently, emissions of NH_3 from snow-free tundra have been identified and are thought to be a considerable source of NH_3 in the Arctic (Croft et al., 2019), although the magnitude of this source is not well known.

1.3.2 Biomass Burning Emissions

Biomass burning has been identified as a major source of atmospheric NH_3 globally (Bouwman et al., 1997). NH_3 emissions from biomass burning were first quantified by Hegg et al. (1988) in which aircraft-based measurements of NH_3 and CO concentrations were performed for several prescribed burns in Canada and the United States and emission ratios of NH_3 with respect to CO were found to vary from 0.002-0.038 (in units of ppbv/ppbv of CO) on average. Based on an average emission ratio of 0.012, Hegg et al. (1988) estimated a total Northern hemisphere biomass burning contribution to NH_3 of 380 Tg yr^{-1}. The authors also acknowledged the large variability of NH_3 emissions in a smoke plume. For example, measurements of the emission ratios of NH_3 from the smoke plume of the prescribed burn in Lodi, California was found to vary by a factor of 19, which the authors attributed to the influence of rainfall between measurement days, resulting in combustion differences.

Since the early 1990s, NH_3 emissions from boreal wildfires have been measured in field experiments, mainly with aircraft-based observation of wildfire plumes in Canada and the United States. Nance et al. (1993) reported an NH_3 emission ratio of 0.13 (ppbv/ppbv of CO) from aircraft-based observations of an Alaskan wildfire in 1990. This value is over an order of magnitude greater than the value reported by Hegg et al. (1988). Subsequent studies of Yokelson et al. (1999) and Goode et al. (2000) reported NH_3 emission ratios of 0.011 (ppbv/ppbv of CO) and 0.147 (ppbv/ppbv of CO) from North Carolinian and Alaskan wildfires, respectively. The studies of Hegg et al. (1988), Nance et al. (1993), Yokelson et al. (1999) and Goode et al. (2000) illustrate the variability of NH_3 emission ratios as a result of fuel type and burning phases. Burling et al. (2011) reported NH_3 emission factors that ranged from 0.12-4.24 g kg^{-1} obtained using aircraft and ground-based measurements for prescribed burns from temperate fuel types of the United States. The emission factors were well correlated with the combustion efficiency of the fire, with greater NH_3 emissions corresponding to lower combustion efficiencies. However, boreal vegetation types were not considered in that study. Given the variability of NH_3 emission ratios and emission factors and the dependence on burning phase, it would therefore be expected that estimating emissions of NH_3 from wildfires would be highly uncertain as a result of assuming a particular emission factor based on a single fire event.

1.3.3 Satellite Measurements

Satellite-based thermal remote-sensing platforms have provided global measurements of NH_3 as shown in Figure 1.2. Such measurements are advantageous as they allow for global and continuous coverage of NH_3. Global satellite observations of NH_3 have been routinely made by several thermal infrared instruments since 2002: the Atmospheric Infrared Sounder (AIRS; Warner et al. (2016); starting in 2002), the Tropospheric Emission Spectrometer (TES; Shephard et al. (2011, 2015); starting in 2004), the Infrared Atmospheric Sounding Interferometer (IASI; Van Damme et al. (2015b); starting in 2006) and the Cross-track Infrared Sounder (CrIS; Shephard and Cady-Pereira (2015); starting in 2011). Measurements of NH_3 within a wildfire plume have been made by these instruments in several studies. Emission ratios of NH_3 have been derived from IASI measurements of NH_3 with simultaneous measurements of CO for tropical biomass burning in South America (Whitburn et al., 2015), Indonesia (Whitburn et al., 2016) and globally (Whitburn et al., 2017). Global biomass burning emissions of NH_3 have also been identified using IASI (Coheur et al., 2009; Clarisse et al., 2010; Van Damme et al., 2014, 2015b), AIRS (Warner et al., 2016) and TES (Shephard et al., 2011). Although biomass burning sources of NH_3 were identified globally by these studies, there have only been a few studies that explicitly examined high-latitude boreal wildfire emissions. Emission ratios of NH_3 were derived from TES observations for the 2007 Alaskan wildfires (Alvarado et al., 2011) and the 2010 Russian wildfires (R'Honi et al., 2013). CrIS has been utilized for studies of wildfires in Northern Canada (Kharol et al., 2018; Whaley et al., 2018; Adams et al., 2019) and the IASI instrument has been used to investigate emissions from the 2008 Siberian wildfires (Coheur et al., 2009), the 2016 Fort McMurray wildfires in Alberta, Canada (Adams et al., 2019) and Alaskan wildfires from 2009-2013 (Paulot et al., 2017). These satellite instruments have provided global observations of NH_3 over the past two decades; however, studies of boreal wildfire NH_3 and its transport to the Arctic remain limited.

The main limitations of NH_3 retrievals from AIRS, TES, IASI and CrIS are the dependence of the measurement on the true NH_3 concentrations and the thermal contrast, defined as the temperature difference between the surface and the boundary layer (Whitburn et al., 2016). The lower surface temperatures of the Arctic region, and the shallower depth of the Arctic boundary layer result in a greater detection limit for NH_3 in comparison to lower-latitude regions. Due to the few sources of NH_3 in the Arctic and minimal long-range transport of NH_3 from lower latitudes, NH_3 concentrations in the Arctic are generally below the detection limit of these instruments. Additionally, thermal infrared retrievals of NH_3 are most sensitive to boundary layer concentrations of NH_3 and less sensitive to NH_3 in the free troposphere, where transported NH_3 in a wildfire plume is likely to be most abundant. As a result of these factors, measurements of NH_3 in the Arctic by thermal sounding instruments remain difficult, resulting in scarce observations in high-latitude regions.

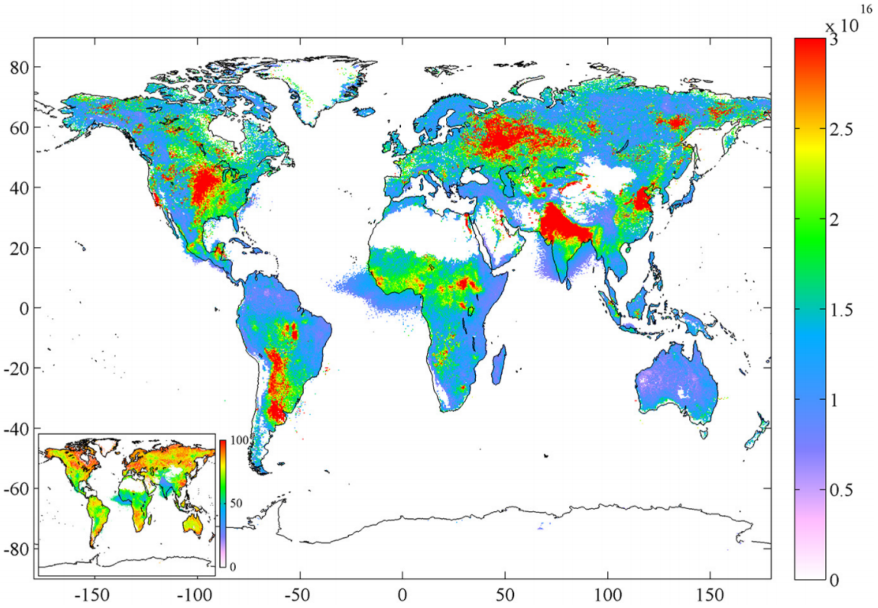

Figure 1.2: NH_3 total columns (molec cm^{-2}) and relative error (bottom-left inset, %) distributions for five years of IASI measurements (1 November 2007 to 31 October 2012), in 0.25°×0.5° cells for the morning overpasses. Figure and caption adapted from Van Damme et al. (2014).

1.3.4 Arctic Measurements and Model Results

In the Canadian high Arctic, in situ shipborne measurements of NH_3 were first performed by Wentworth et al. (2016) as part of the 2014 NETCARE (Network on Climate and Aerosols; Abbatt et al., 2019) Campaign in the Canadian Archipelago during July and August 2014. Measurements of NH_3 on board the Canadian Coast Guard Ship Amundsen were made from 13 July to 7 August 2014 throughout Baffin Bay and the eastern Canadian Archipelago. Surface-layer NH_3 concentrations (shown in Figure 1.3) were found to range from 40-870 pptv, with greatest values measured near Lancaster Sound, which were partly attributed to the 2014 Northwest Territories wildfires that occurred during the period of measurements. The measured NH_3 concentrations were mainly attributed to seabird-colony NH_3 emissions through GEOS-Chem simulations with the inclusion of a seabird-colony NH_3 emission inventory based on Riddick et al. (2012). The simulation also showed an increase in the neutralization of acidic aerosols with seabird-colony NH_3 emission included, indicative of the presence of gas-phase NH_3.

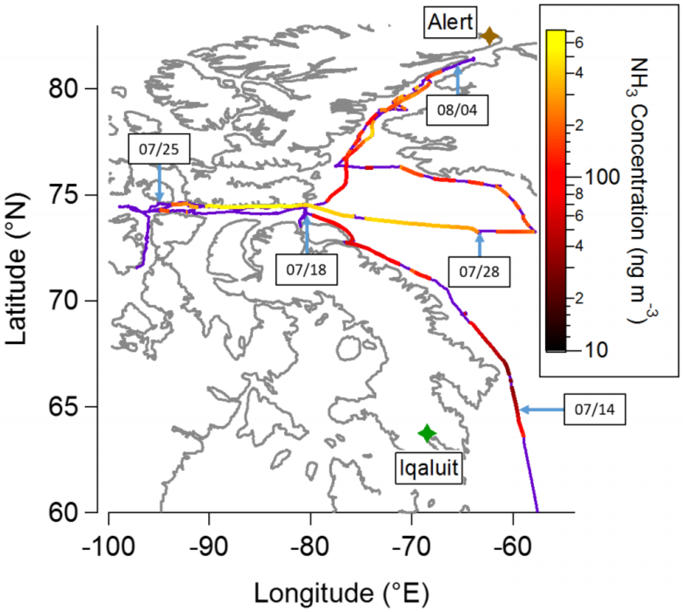

Figure 1.3: Amundsen ship track coloured by gas-phase NH_3 concentrations. Invalid measurements (e.g. instrument troubleshooting, influenced by ship) are shown in purple along the ship track. Relevant landmarks are also labelled. Dates and arrows indicate the position of the ship at 00:00 UTC on that day. Figure and caption adapted from Wentworth et al. (2016).

A later study by Croft et al. (2016b) examined the impact of seabird-colony NH_3 emissions in the Canadian Archipelago using the GEOS-Chem CTM. The seabird-colony NH_3 emissions of Wentworth et al. (2016) were used and a substantial increase of reduced nitrogen (gas-phase NH_3 and particulate NH_4^+) was observed in the model with the inclusion of seabird-colony NH_3 emissions, accounting for 40% of the reduced nitrogen in the Canadian Archipelago. The inclusion of seabird-colony NH_3 was found to increase new particle formation, contributing to cloud condensation nuclei and particle growth.

Croft et al. (2016b) concluded that the seabird contribution to particle formation could lead to radiative cooling of the Arctic atmosphere on the order of 1-2 W m^{-2}, as seen in Figure 1.4, with greater values near large seabird-colony sources. Similarly, a recent study by Croft et al. (2019) concluded that the inclusion of tundra emission of NH_3 improved the model to measurement comparisons and suggested that tundra NH_3 emissions could increase NH_3 by a factor of 1.5 relative to seabird-colony sources. This suggests that tundra emissions could be a significant source of NH_3 in the Canadian Archipelago; however, the magnitude of this source is highly uncertain due to the lack of measurements of the bidirectional NH_3 flux.

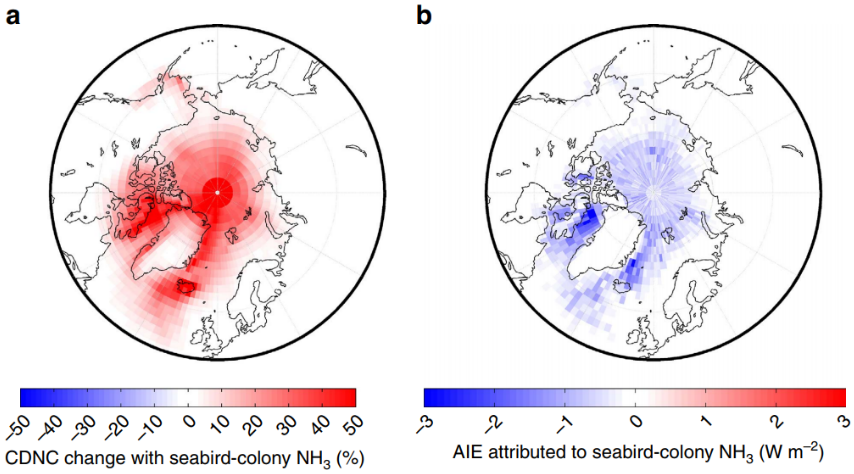

Figure 1.4: (a) Percent difference in pan-Arctic summertime mean cloud-droplet number concentration (CDNC) in the atmospheric boundary layer due to inclusion of seabird NH_3 emissions in the GEOS-Chem-TOMAS model under the assumption of fixed cloud liquid-water content. (b) Pan-Arctic summertime-mean aerosol indirect (cloud-albedo) radiative effect (AIE) attributed to the seabird-colony emissions. Figure and caption from Croft et al. (2016b)

.

The transport of wildfire emissions of NH_3 to the Arctic has not been thoroughly investigated in global chemical transport models. The studies by Wentworth et al. (2016) and Croft et al. (2016b, 2019) used the GEOS-Chem CTM to investigate the influence of seabird-colony NH_3 in the Canadian Arctic. Wildfire emissions of NH_3 were included in these studies but were not explicitly examined, although Wentworth et al. (2016) noted that in the GEOS-Chem model, NH_3 from the 2014 Northwest Territories wildfires contributed significantly to surface-layer NH_3 in the low Arctic. Kharol et al. (2018) examined the deposition of NH_3 at Northern latitudes with CrIS observations and the GEM-MACH (Global Environmental Multi-scale Modelling Air Quality and Chemistry) model and found NH_3 deposition fluxes 2 to 3 times greater in the presence of wildfires as shown in Figure 1.5. Deposition of NH_3 in the Arctic was not examined in this study. Due to the scarcity of NH_3 measurements in high-latitude regions and the episodic nature of wildfire events, more effort is needed to evaluate model performance in order to infer the influence of wildfire NH_3 in the Arctic from model results.

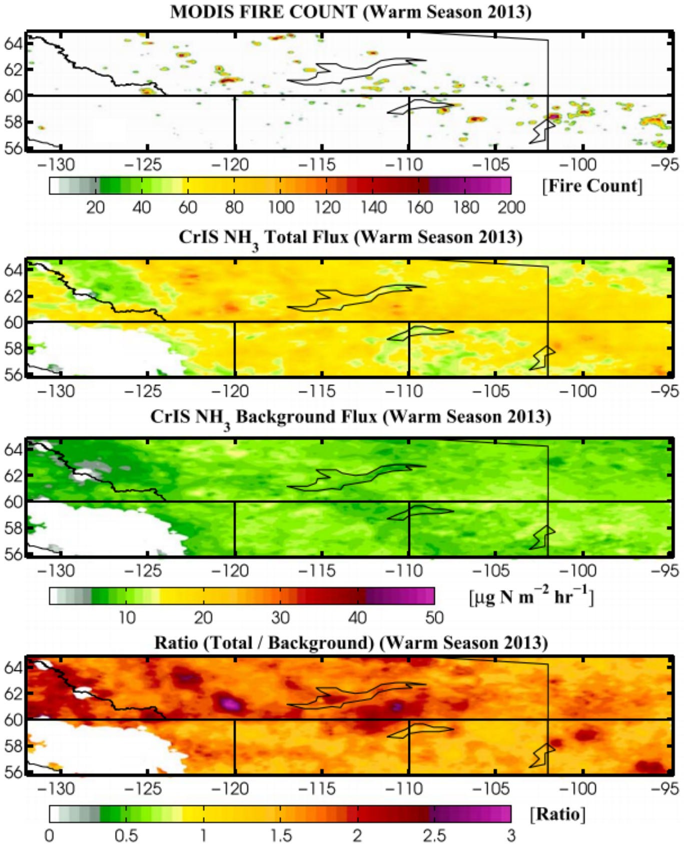

Figure 1.5: Warm season (April-September, 2013) MODIS fire count, CrIS NH_3 total dry deposition flux, CrIS NH_3 background dry deposition flux and flux ratio over the Great Slave Lake region of the Northwest Territories, Canada. Figure and caption adapted from Kharol et al. (2018).

1.4 Polar Environment Atmospheric Research Laboratory

Quantifying the influence of biomass burning on the Arctic atmosphere requires long-term, dedicated measurements of the transported emissions in the Arctic as a result of the interannual variability and episodic nature of wildfire events. The Arctic is a difficult region to study as a result of the lack of dedicated measurement stations. The Canadian Network for the Detection of Atmospheric Change (CANDAC) has established Polar Environment Atmospheric Research Laboratory (PEARL) to perform long-term atmospheric measurements in the Canadian high Arctic. PEARL, located on Ellesmere Island at Eureka, Nunavut (80.05°N, 86.42°W) consists of three facilities: the PEARL Ridge Lab at 610 m above sea level, the Zero-Altitude Auxiliary Laboratory (ØPAL) at sea level and the Surface and Atmospheric Flux, Irradiance and Radiation Extension (SAFIRE). PEARL was established to study ozone, air quality and climate change in the high Arctic using a variety of instruments.

One of the key instruments contributing to the Probing the Atmosphere of the High Arctic (PAHA) Composition Measurements theme, biomass burning (CM-BB) project is the Eureka PEARL Ridge Lab Bruker IFS 125HR Fourier transform infrared (FTIR) spectrometer, which contributes measurements to the Network for the Detection of Atmospheric Composition Change (NDACC). Details of the Eureka FTIR are provided in Chapter 2. The use of ground-based solar-absorption FTIR instruments in the Arctic is advantageous as these instruments provide sufficient sensitivity to the free troposphere where transported wildfire emissions are most abundant, in addition to having a lower detection limit for NH_3 than that of satellite observations (Dammers et al., 2016). The use of FTIR measurements also allows for simultaneous detection of the long-lived biomass burning tracers CO, hydrogen cyanide (HCN) and ethane (C_2H_6), along with a multitude of other biomass burning species (Zhao et al., 2002; Paton-Walsh et al., 2005, 2010;

Vigouroux et al., 2012; Viatte et al., 2013, 2014, 2015). Measurements of CO, HCN and C_2H_6 provide insight into the origin, transport and aging of smoke plumes. The utilization of ground-based FTIR measurement sites in the Arctic provides a long-term time series of NH_3 and other trace gases where measurements from other platforms are lacking sensitivity or are non-existent.

1.5 Thesis Overview

1.5.1 Scientific Objectives

The main scientific objectives of this thesis are summarized as follows:

1. To acquire a long-term time series of biomass burning trace gas species in the Arctic.
2. To quantify the emissions of boreal wildfire NH_3 and its transport to the Arctic.
3. To investigate the frequency of episodic wildfire sources and their contribution to trace gas measurements in the Arctic.

To address these objectives, long-term time series are retrieved from ground-based FTIR measurements at Eureka, Nunavut from 2006-2018. The first objective of this thesis was to improve and continue the long-term measurements of the tropospheric biomass burning species CO, HCN, C_2H_6, C_2H_2, CH_3OH, H_2CO and HCOOH retrieved from mid-infrared solar-absorption spectra. In addition, the first long-term high-Arctic NH_3 measurements were developed as part of this thesis. The results of the first objective are presented in Chapter 3. For the second objective, boreal wildfire emissions of NH_3 were detected in the high Arctic and emissions were quantified. The relative influence of transported wildfire NH_3 emissions in comparison to local seabird-colony sources was also examined with the GEOS-Chem CTM. These results are presented in

Chapters 4 and 5. Lastly, the long-term (2003-2018) detection of episodic wildfire pollution events was examined using FTIR measurements at Eureka and nine other mid- and high-latitude FTIR sites. A tagged CO simulation with the GEOS-Chem model was used for source attribution and to quantify the relative contribution of wildfire emissions to FTIR measurements. This study is presented in Chapter 6.

1.5.2 Outline

The remaining chapters of this thesis are outlined as follows:

> **Chapter 2** provides an overview of FTIR spectroscopy, retrieval theory, and the Eureka FTIR spectrometer that are the foundation for the scientific results of this work.
>
> **Chapter 3** presents the optimized retrievals of the tropospheric trace gas species obtained from Eureka FTIR solar-absorption spectra.
>
> **Chapter 4** investigates NH_3 emissions from the 2014 Northwest Territories wildfires. Measurements of NH_3 and the wildfire pollution tracers CO, HCN, C_2H_6 were made using FTIR measurements at Eureka and Toronto. FLEXPART and HYSPLIT back-trajectories were used to examine the source sensitivity and travel times of the measured smoke plume, in conjunction with the MODIS fire hot-spots. Finally, enhancement ratios and emission ratios of NH_3, HCN and C_2H_6 were determined and compared to literature values, providing insight to the lifetime of NH_3 in a smoke plume.
>
> **Chapter 5** investigates NH_3 emissions from the 2017 Northwest Territories and British Columbia wildfires. Measurements of NH_3, CO, HCN and C_2H_6 from the two high-Arctic sites: Eureka, Nunavut and Thule, Greenland were used to detect wildfire plumes in August 2017. FLEXPART back-trajectories were used to

examine the influence of the wildfire sources on measurements at each FTIR site. The GEOS-Chem chemical transport model was used to quantify the contribution of the 2017 Canadian wildfires on NH_3 and NH_X^+ concentrations in the Arctic in comparison to the local seabird-colony source.

Chapter 6 examines the long-term (2003-2018) contribution of wildfire CO to FTIR measurements at Northern mid- and high-latitude NDACC sites. For each site, enhancements of CO are detected in the time series and correlated with coincident measurements of HCN and C_2H_6 to provide confirmation for the presence of wildfire pollution. The GEOS-Chem tagged CO simulation provides source attribution for the detected events in the FTIR time series, in addition to quantifying the wildfire influence to measured CO concentrations.

Chapter 7 presents the conclusions of this thesis and suggestions for future work.

1.5.3 Contributions

The work in Chapter 3 was carried out by the author, Stephanie Conway, Joseph Mendonca, Dan Weaver, Sebastien Roche and Kim Strong. Operation of the Eureka FTIR was performed by the author, Joseph Mendonca, Dan Weaver and Sebastien Roche. Stephanie Conway implemented the SFIT4 retrieval algorithm at the University of Toronto and contributed to the retrievals.

The work in Chapter 4 was carried out by the author, Enrico Dammers, Stephanie Conway and Kim Strong. The study was designed by the author and Kim Strong. Stephanie Conway performed the retrievals of CO, HCN and C_2H_6 for Eureka and Toronto measurements. The NH_3 retrievals and analysis were performed by the author. All co-authors provided feedback on the analysis.

The work in Chapter 5 was carried out by the author, Kim Strong, Dylan Jones, Ivan Ortega, Jim Hannigan, Enrico Dammers, Mark Shephard, Eleanor Morris, Killian Murphy, Mat Evans, Mark Parrington, Simon Whitburn, Martin Van Damme, Lieven Clarisse, Pierre-Francois Coheur, Cathy Clerbaux, Betty Croft, Randall Martin, Jeff Pierce and Jenny Fisher. The study was designed by the author, Kim Strong and Dylan Jones. Ivan Ortega and Jim Hannigan provided the Thule FTIR measurements. Enrico Dammers performed the GEOS-Chem and IASI comparisons. Eleanor Morris, Killian Murphy and Mat Evans provided the GFAS emissions. Simon Whitburn, Martin Van Damme, Lieven Clarisse, Pierre-Francois Coheur and Cathy Clerbaux provided the IASI measurements. Betty Croft, Randall Martin and Jeff Pierce provided the seabird-colony NH_3 emissions. The analysis was performed by the author and all co-authors provided feedback.

The study in Chapter 6 was designed by the author, Kim Strong and Dylan Jones. Thomas Blumenstock, Stephanie Conway, Jim Hannigan, Frank Hase, Yasko Kasai, Emmanuel Mahieu, Maria Makarova, Isamu Morino, Tomoo Nagahama, Justus Notholt, Ivan Ortega, Mathias Palm, Anatoliy Poberovsky, Ralf Sussmann and Thorsten Warneke provided the FTIR measurements used. Jenny Fisher contributed to the updated GEOS-Chem tagged CO simulation that was used. The analysis was performed by the author and all co-authors provided feedback.

Chapter 2

Fourier Transform Infrared Spectroscopy

2.1 Molecular Spectroscopy

All molecules absorb and emit radiation at discreet energy levels as dictated by quantum theory. Photons of a specific wavelength are absorbed or emitted as a result of changes to the molecule's internal energy due to the transitions between the rotational or vibrational energy. Rotational transitions occur in the microwave region of the spectrum and vibrational transitions occur in the infrared. The spectral lines that result from these energy transitions provide unique spectroscopic signatures of the gases in the atmosphere. The line strength, S, is related to the absorption coefficient $k_{\tilde{\nu}}$:

$$S = \int_{-\infty}^{\infty} k_{\tilde{\nu}} \mathrm{d}\tilde{\nu}, \tag{2.1}$$

where $\tilde{\nu}$ is the monochromatic wavenumber. In reality, the spectral lines are never monochromatic and have a certain width, depth and shape due to the perturbations in the energy levels as a result external influences on the molecule, which are determined by the temperature and pressure of the gas.

2.1.1 Lineshapes

Collisional Broadening

Collisional broadening occurs as a result of collisions between molecules in a gas. The lineshape function f_L of the spectral line is given by a Lorentzian profile (Liou, 2002):

$$f_L(\tilde{\nu} - \tilde{\nu}_\circ) = \frac{1}{\pi} \frac{\alpha_L}{\alpha_L^2 + (\tilde{\nu} - \tilde{\nu}_\circ)^2}, \tag{2.2}$$

where $\tilde{\nu}_\circ$ is the center wavenumber and α_L is the half width at half maximum (HWHM) of the collision-broadened line given by:

$$\alpha_L = \alpha_\circ \frac{P}{P_\circ} \sqrt{\frac{T_\circ}{T}}, \tag{2.3}$$

where $\alpha_\circ$ is the HWHM at the standard pressure $\mathrm{P}_\circ$ and temperature $\mathrm{T}_\circ$. Collisional broadening is greatest in the troposphere below ~20 km due to the pressure dependence of the Lorentz lineshape.

Doppler Broadening

Doppler broadening is the result of the relative motion of the molecule along the line of sight. The lineshape function f_D for a Doppler-broadened line is given by (Liou, 2002):

$$f_D(\tilde{\nu} - \tilde{\nu}_\circ) = \frac{1}{\alpha_D \sqrt{\pi}} \exp\left[-\frac{(\tilde{\nu} - \tilde{\nu}_\circ)^2}{\alpha_D^2} \right], \tag{2.4}$$

where α_D is a measure of the Doppler-broadened line width and is given by:

$$\alpha_D = \tilde{\nu}_\circ \sqrt{\frac{2kT}{mc^2}}, \tag{2.5}$$

where m is the mass of the molecule, c is the speed of light, T is the temperature, and k is the Bolztmann constant. Doppler broadening dominates in the stratosphere above ~50 km as a result of its temperature dependence.

Voigt Lineshape

In the atmosphere, where both collisional and Doppler broadening occur, the lineshape can be modelled by the convolution of the Lorentz and Doppler lineshapes (Liou, 2002) known as the Voigt lineshape:

$$
\begin{aligned}
f_V(\tilde{\nu} - \tilde{\nu}_\circ) &= f_L(\tilde{\nu}' - \tilde{\nu}_\circ) * f_D(\tilde{\nu}' - \tilde{\nu}_\circ) && (2.6) \\
&= \int_{-\infty}^{\infty} \frac{\alpha_L}{\alpha_L^2 + (\tilde{\nu}' - \tilde{\nu}_\circ)^2} \frac{1}{\alpha_D \sqrt{\pi}} \exp\left[-\frac{(\tilde{\nu} - \tilde{\nu}_\circ)^2}{\alpha_D^2}\right] \mathrm{d}\tilde{\nu}', && (2.7)
\end{aligned}
$$

which is commonly used in spectroscopy to represent the lineshape of an absorbing gas in the atmosphere.

2.2 FTIR Spectroscopy

The FTIR spectrometer at the Eureka PEARL Ridge Lab is a Bruker IFS 125HR from Bruker Optics GmbH. It is a high-resolution spectrometer and currently the most robust and stable commercially available FTIR spectrometer (Wunch et al., 2011). The principal component of the Bruker IFS 125HR is the Michelson interferometer. In this section, the fundamentals of the operation of an FTIR spectrometer with respect to the Bruker IFS 125HR will be presented. Further details of the Eureka Bruker IFS 125HR will be given in the following sections.

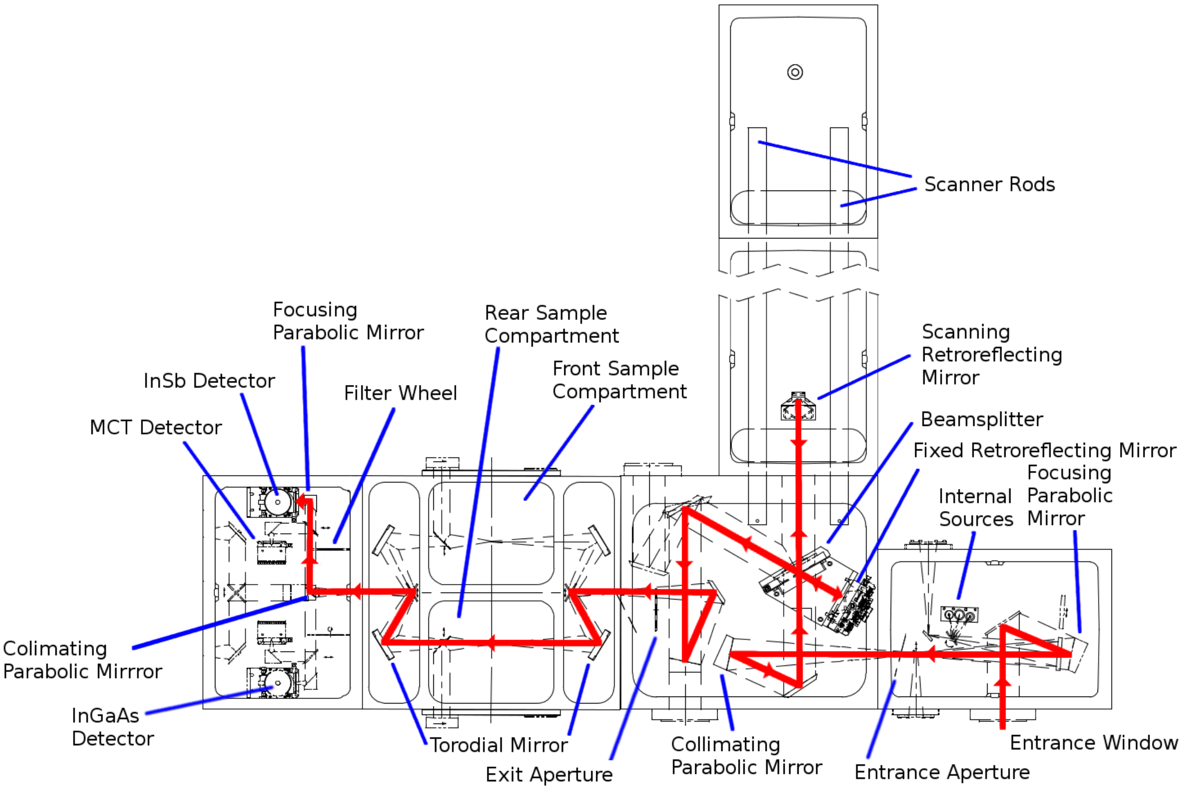

Figure 2.1: Schematic diagram of the Eureka Bruker IFS 125HR. The red line indicates the path of the solar beam. The main components are labelled and indicated by the blue lines. Image was taken from Bruker Optik GmbH (2006).

The input beam, from either the solar or lamp source, is focused onto the entrance aperture in the source compartment as illustrated in Figure 2.1. The light passes through the input aperture into the interferometer compartment of the instrument, where the beam is collimated by a parabolic collimating mirror. The collimated beam is directed onto the beamsplitter where it is split into two beams of equal intensity. One beam is directed onto the fixed mirror and the other to the scanning mirror in the interferometer arm. The two beams are directed back to the beamsplitter and due to their optical path difference (OPD), there is a phase difference between the two. The beams are recombined at the beamsplitter and focused onto the exit aperture through a series of flat mirrors and a parabolic focusing mirror. For the Bruker IFS 125HR, the sizes of both the entrance and exit aperture are variable and controlled by the rotation of an aperture wheel, with the size of the exit aperture always one stop greater than the entrance aperture to account for the possible misalignment of the interferometer and divergence of the beam. Additionally, the exit aperture also reduces the influence of the secondary infrared source from the warm annulus of the entrance aperture (Johnson et al., 2002).

Figure 2.1 also shows two possible paths of the beam to the detector compartment, either through the front or rear sample compartments. The path of the beam is controlled by a series of flat folding mirrors. For all mid-infrared (MIR) measurements, the rear sample compartment is used. In the detector compartment, the beam is collimated by a parabolic collimating mirror and directed to the filter wheel. The rotating filter wheel contains several spectral bandpass filters to limit the sampled spectral range of the beam. The filtered MIR beam is directed to one of two detectors by a series of flat folding mirrors. Details of the bandpass filters and detectors of the Eureka Bruker IFS 125HR are discussed in Section 2.3.

The detector measures the intensity of the beam, where the beam intensity is given by:

$$I(x) = \frac{1}{2}\int_0^{\infty} B(\tilde{\nu})\cos(2\pi\tilde{\nu}x)\mathrm{d}\tilde{\nu}, \tag{2.8}$$

where $I(x)$ is the intensity as a function of OPD x and $B(\tilde{\nu})$ is the intensity of the input beam as a function of wavenumber $\tilde{\nu}$. Applying a Fourier transform to Equation 2.8, we obtain $B(\tilde{\nu})$:

$$B(\tilde{\nu}) = 2\int_0^{\infty} I(x)\cos(2\pi\tilde{\nu}x)\mathrm{d}x. \tag{2.9}$$

The measured intensity $I(x)$ is the interferogram, which is the interference pattern as a result of varying phase difference as the scanning mirror is moved along the path of the interferometer arm. The quantity $B(\tilde{\nu})$ is the measured spectrum, which is the solar absorption spectrum or lamp spectrum of the input beam.

The integrals of Equations 2.8 and 2.9 are an idealization of the real-world case as these expressions assume an OPD ranging from 0, defined as the zero path difference (ZPD), to infinity. In reality, the interferometer has a finite maximum OPD resulting in a finite resolution of the sampled spectrum. Therefore, an apodization is applied to Equation 2.8. A boxcar apodization is generally used in the form:

$$D(x) = \begin{cases} 0 & \text{if } |x| > x_{max} \\ 1 & \text{if } |x| \leq x_{max} \end{cases}, \tag{2.10}$$

where x is the OPD and x_{max} is the maximum OPD. Applying the convolution of Equation 2.10 with Equation 2.8 results in a sinc function after the Fourier transform. The applied apodization therefore influences the resolution of the sampled spectrum. For a boxcar apodization, the resolution is defined using the full width at half maximum (FWHM), corresponding to a resolution of $0.6/x_{max}$ (Bell, 1972). For the Bruker IFS 125HR, the manufacturer defines the resolution as $0.9/x_{max}$.

2.2.1 The Fourier Transform Spectrometer Advantage

There are three main advantages of an FTIR spectrometer over a scanning dispersive spectrometer:

The Jacquinot Advantage

The Jacquinot advantage (Jacquinot and Dufour, 1948) refers to the high optical throughput of the Fourier transform instrument. An aperture is used to control the amount of light entering the instrument, which allows for a high SNR and minimal loss through the instrument compared to an entrance slit.

The Fellgett Advantage

The Fellgett or multiplex advantage (Fellgett, 1951) allows all wavelengths to be sampled simultaneously, therefore resulting in shorter sampling times over a large spectral range in comparison to a dispersive spectrometer.

The Connes Advantage

The Connes advantage (Connes and Connes, 1966) refers to the high wavenumber precision of FTIR instruments. The wavenumber axis is calibrated by a laser beam of known wavelength that passes through the interferometer. The position of the moving mirror and sampling of the inteferogram are defined by the ZPD of the laser beam. The wavenumber axis for dispersive spectrometers is defined by the position of the grating.

2.3 The Eureka Bruker IFS 125HR FTIR

The Eureka Bruker IFS 125HR (shown in Figure 2.2) was installed in July 2006 to replace the existing Bomem DA8 FTIR, which was deployed at Eureka by Environment and Climate Change Canada (ECCC) from 1993 to 2009 (Fast et al., 2011). The Eureka FTIR, as it will be referred to in this work, measures high-resolution solar-absorption spectra under clear-sky conditions during the sunlit season from approximately February 21 to October 20 of each year. The maximum OPD of the instrument is 374 cm, allowing for a maximum resolution of 0.0024 cm^{-1}. Measurements are performed with either a potassium bromide (KBr) or calcium fluoride (CaF_2) beamsplitter with a spectral range of 50-4800 cm^{-1} and 1200-15000 cm^{-1} respectively. MIR measurements for NDACC are generally performed with a KBr beamsplitter, while the CaF_2 beamsplitter is used for Total Carbon Column Observing Network (TCCON) near-infrared (NIR) measurements. Occasionally, MIR measurements are made using the CaF_2 beamsplitter if intermittent MIR and NIR measurements are required. However, the spectral range of the CaF_2

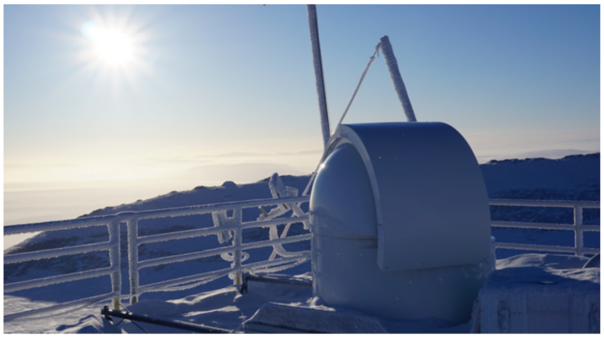

a) Solar Tracker Dome

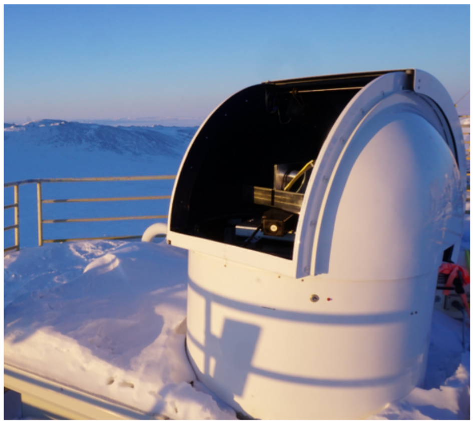

b) Solar Tracker Housed in Dome

c) The Bruker 125HR

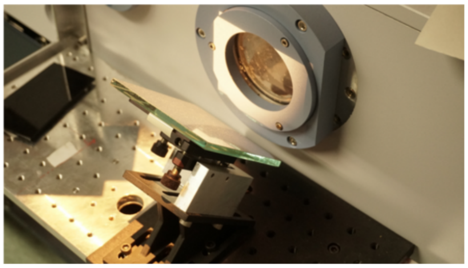

d) Entrance Window to Bruker 125HR

Figure 2.2: The setup of the Eureka Bruker IFS 125HR at the PEARL Ridge Lab.

beamsplitter does not cover NDACC filters 6 or 7 and hence these filters are omitted when measuring in this manner.

A series of narrow bandpass optical filters are used to limit the spectral range of each measurement, resulting in a greater SNR for the measured spectrum. Seven optical filters are used as prescribed by the NDACC Infrared Working Group (IRWG). The spectral ranges of these filters are summarized in Table 2.1. Measurements are made by cycling through the bandpass filters. All solar measurements are made at a maximum OPD of 257 cm, corresponding to a resolution of 0.004 cm^{-1}. From August 2006 to March 2012, each measurement consisted of four co-added scans. Since March 2012, the number of scans has been reduced to two resulting in shorter measurement times and therefore an increase in the number of observations while maintaining a sufficiently high SNR.

For each measurement, the input aperture size is filter dependent (listed in Table 2.1), while the aperture size remains constant for a given filter. Three detectors are currently

Table 2.1: NDACC narrow bandpass filters used with the Eureka FTIR, wavenumber range for the SNR calculation, aperture diameter and the retrieved trace gas species.

NDACC Filter	Wavenumber Range [cm^{-1}]	SNR Wavenumber Rangea] [cm^{-1}]	Aperture Diameter [mm]	Species Retrieved
1	3950 - 4300	4038.727 - 4038.871	1	HF
2	2700 - 3500	3381.275 - 3381.536	1.15	HCN, C_2H_2, H_2CO
3	2420 - 3080	2924.866 - 2925.100	1	CH_4, C_2H_6, N_2O, HCl, O_3, H_2CO
4	1950 - 2700	2526.228 - 2526.618	1.15	CO
5	1800 - 2200	1985.260 - 1985.510	1.3	CO, NO
6	700 - 1350	1139.075 - 1139.168	1.5	O_3, $ClONO_2$, CH_3OH, HCOOH, NH_3
7	700 - 1000	907.854 - 907.977	1.5	$ClONO_2$,NH_3

installed in the instrument: a photovoltaic indium antimonide (InSb) detector sensitive from 1850-10000 cm^{-1}, a photoconductive mercury-cadmium-telluride (HgCdTe or MCT) detector sensitive from 600-6000 cm^{-1}, and an indium-gallium-arsenide (InGaAs) detector which is sensitive from 4000-15000 cm^{-1}. Both the InSb and MCT detectors are liquid-nitrogen cooled and are used for MIR measurements for NDACC with the KBr beamsplitter. The InGaAs detector is used with the CaF_2 beamsplitter for NIR TCCON measurements. Full details of the TCCON measurements are given by Mendonca (2017).

2.3.1 The Community Solar Tracker

The solar tracker is an essential component of the instrumental setup of the Eureka FTIR system. The current Eureka solar tracker is a custom-built Community Solar Tracker (CST) designed at the University of Toronto and Dalhousie University (Franklin, 2015). The CST was installed in July 2013, replacing the ECCC photodiode solar tracker. Details of the ECCC solar tracker are described in Lindenmaier (2012) and Weaver (2018). The CST is housed in a Robodome on the roof of the PEARL Ridge Lab. Both the Robodome and CST are controlled by software written in Python which allows for remote control of both of these components through a graphical user interface (GUI).

With the Robodome open, the CST tracks the position of the Sun via two modes of tracking: passive or active. Passive tracking relies on ephemeris calculations to determine the position of the Sun. However, passive tracking may be prone to systematic errors due to drift of the solar tracker components. Active tracking provides continuous corrections to the tracking by visually locating the centre position of the Sun. The CST does this via a camera located beneath the 45° mirror at the FTIR entrance window (shown in Figure 2.2). This camera continually monitors the visual image of the Sun while the Sun tracker software applies an ellipse-fitting algorithm to the Sun's image to determine the precise centre location. Slight azimuthal and altitude corrections are then applied to the solar tracker mirrors to centre the image of the Sun on the camera sensor. The CST uses a combination of active and passing tracking when taking solar measurements which prevents the tracker from losing the position of the Sun if the image of the Sun were to be obscured by clouds. The CST can be remotely controlled via a virtual network connection (VNC) or command line on a secure shell (SSH) connection. The CST is highly automated as a result of its active and passive tracking features, while additional features such as automated corrections to the camera iris to maintain adequate signal and prevent saturation allow for minimal user interference once tracking is started.

2.3.2 Data Acquisition

Due to the remoteness of the Eureka FTIR and limited operator support, automation of the FTIR instrument and the CST are essential to maximize the number of observations. Currently, operator support is only required at the start of measurements on each day. For MIR measurements, the InSb and MCT detectors must be cooled by manually filling the detectors with liquid nitrogen. The CST and the FTIR measurement sequence must be started manually, either by the on-site operator or via a remote connection. Sky conditions may also be remotely monitored using a webcam installed at the PEARL Ridge Lab. The measurement sequence is controlled from the Bruker OPUS software and a macro is used to automate the acquisition of measurements. The macro is a sequence of measurements for each filter, and the sequence is repeated throughout the day and is terminated when there is insufficient signal in all filters. However, the presence of clouds may result in the termination of the macro before the Sun sets, requiring a manual restart. Further automation of the Eureka FTIR could be performed; however, operator support is required for the mid-day beamsplitter swap to switch from MIR to NIR measurements. Nevertheless, some improvements could be made as suggested in Chapter 7.

2.3.3 Monitoring FTIR Performance

The Bruker IFS 125HR is aligned during installation; however, drift of the instrument optical components is likely over time during routine operation of the instrument. When kept under vacuum, pressure and temperature changes should be minimal, reducing the potential for the instrument to become misaligned. The Eureka FTIR is used for both MIR and NIR measurements and therefore requires routine changes of the beamsplitter for which the instrument must be vented and evacuated each time. Venting and evacuating the instrument regularly (usually once a day) subjects the instrument to additional stress as a result of the pressure changes. Repeated removal and insertion of the KBr and CaF_2 beamsplitters may also result in additional wear and tear. It is therefore important to monitor the alignment of the instrument on a routine basis.

Instrument alignment is monitored by the measurement of the absorption spectrum of a gas-filled cell using an internal lamp source. Three separate cells are used with the Eureka FTIR, each filled with a known amount of gas: hydrogen chloride (HCl), hydrogen bromide (HBr) or nitrous oxide (N_2O). The HCl cell is permanently installed in the front sample compartment (see Figure 2.1) and is reserved for NIR cell tests. Full details of these cell tests are given by Mendonca (2017). Both the HBr and N_2O cells are used for MIR cell tests with the KBr beamsplitter and an MIR globar source.

The HBr cell (HBr cell #30) was obtained from NIES (National Institute for Environmental Studies) in Japan from cells produced for the NDACC IRWG. It is approximately 2.5 cm long and 2 cm in diameter, made of glass with fused sapphire windows and filled with a known amount of HBr gas (Coffey et al., 1998). A cell test consists of a background measurement (no cell in sample compartment) and a cell measurement with the cell placed in the rear sample compartment of Figure 2.1. For both the background and cell measurement, 50 co-added scans are performed at 0.004 cm^{-1} resolution (maximum OPD of 257 cm) using the instrument's internal global source. The cell spectrum is divided by the background spectrum to obtain a transmission spectrum which contains the HBr absorption lines to be fitted. A summary of the fitted microwindows is given in Table 2.2. The cell test is made with NDACC filter 4 and a 1.15 mm diameter input aperture, to be consistent with filter 4 solar measurements.

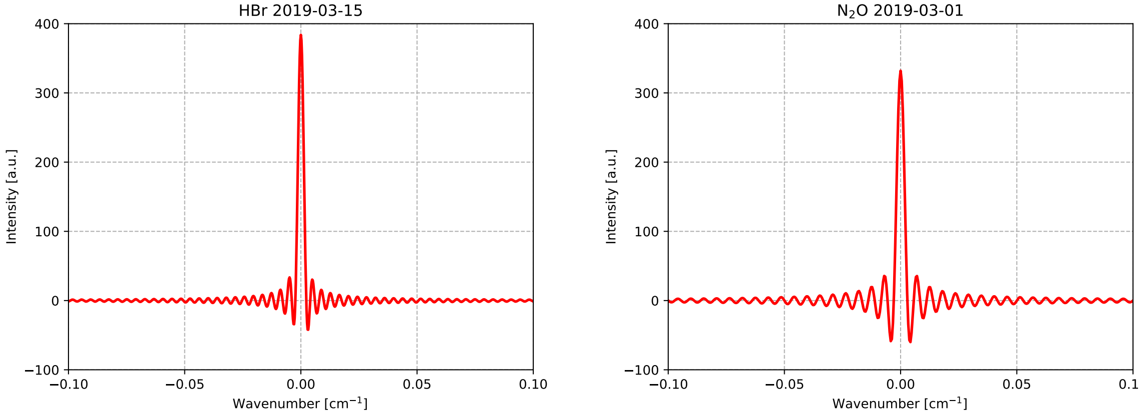

Figure 2.3: Typical ILS retrieved from an HBr #30 cell test on 15 March 2019 and N_2O #11 cell test on 1 March 2019 using
LINEFIT v14.5.

The transmission spectrum is analyzed with LINEFIT v14.5. It should be noted that Lindenmaier (2012) and Weaver (2018) presented the results of past HBr cell tests using LINEFIT v9, but here the entire time series has been reanalyzed with LINEFIT v14.5. The LINEFIT algorithm is described by Hase et al. (1999) and Hase (2012). LINEFIT creates a theoretical ILS, modulation efficiency (ME), and phase error (PE) based on the instrument field of view (FOV) and OPD. The FOV is defined as the ratio of the input aperture radius to the focal length of the input focusing parabolic mirror (41.8 cm). The ILS, ME, and PE are then iteratively varied to match a simulated spectrum to the measured HBr absorption lines. The HBr concentration is also retrieved during the fitting procedure. However, HBr cells are known to slowly leak, resulting in a decrease in concentration and pressure with time. Therefore, LINEFIT is run in an iterative manner. An initial assumption of the cell pressure and concentration of 1.55 mbar and 7.6×10^{20} molec cm^{-2}, respectively, is assumed and LINEFIT is run iteratively, updating the cell pressure based on the retrieved concentration until the pressure converges with a convergence threshold of 0.001 mbar. Generally, only one or two iterations are required. The results of the retrieved ME, PE and column scale factors are shown in Figure 2.4 and an example of a fitted microwindow is shown in Figure 2.5.

Table 2.2: Fitted microwindows for the Eureka FTIR HBr cell test processed with LINEFIT v14.5.

Microwindow	Wavenumber Range [cm^{-1}]
1	2590.32 - 2590.72
2	2590.71 - 2591.11
3	2605.60 - 2606.00
4	2606.00 - 2606.40
5	2620.39 - 2620.79
6	2620.80 - 2621.20
7	2634.70 - 2635.10
8	2635.10 - 2635.50
9	2648.50 - 2648.90
10	2648.90 - 2649.30
11	2661.76 - 2662.16
12	2662.18 - 2662.58
13	2674.52 - 2674.92
14	2674.94 - 2675.34

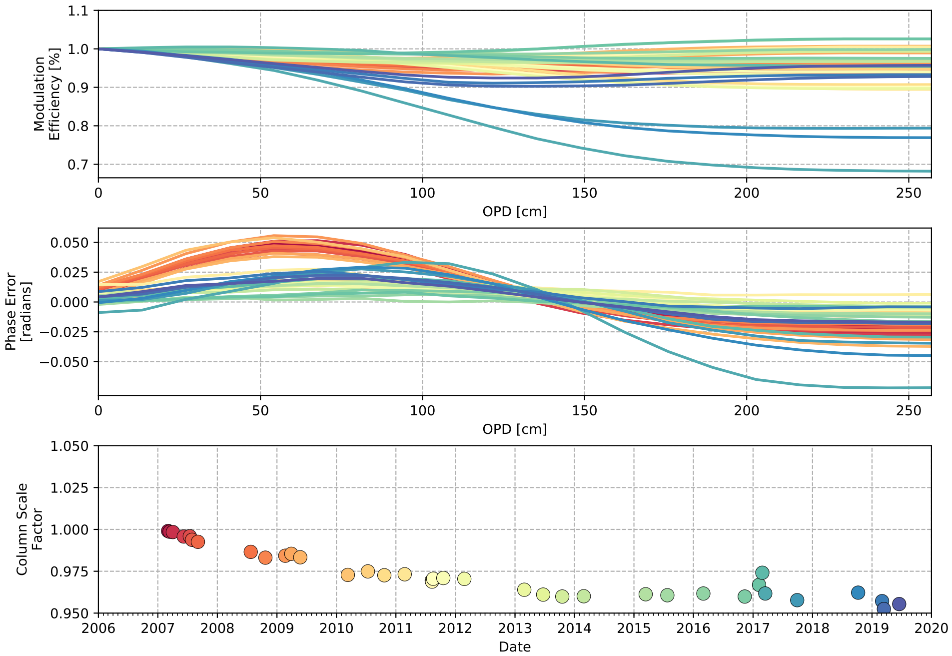

Figure 2.4: Modulation efficiency (ME), phase error (PE) and retrieved column scale factor for Eureka FTIR HBr #30 cell tests analyzed with LINEFIT v14.5.

The ME is normalized to unity at ZPD and generally decreases slightly to maximum OPD of 257 cm. In general, the ME ranges from 0.94 - 1.02 at maximum OPD. An ME greater than unity is the result of a shear misalignment of the interferometer. Shear misalignment is a common issue for Bruker 125HR instruments and is caused by the wearing of the Teflon pads that support the scanning corner cube mirror (Wunch et al., 2011). Shear misalignment results in a decrease in ME near ZPD, therefore contributing to an apparent over-modulation at longer OPD due to the normalization of the ME to unity at ZPD. Decreasing ME as a function of OPD is due to angular misalignment as a result of the misalignment of the fixed corner cube mirror (Wunch et al., 2011).

The PE remains relatively constant over the time series, with values of less than 0.05 radians at all OPDs. An increase in ME at maximum OPD and a decrease in PE is observed in 2010 after the instrument was realigned. Variations in both the ME and PE are mainly attributed to the placement of the beamsplitter, which may vary slightly each time it is removed and re-inserted. The cell column amounts, shown as a scale factor relative to the original value, are found to be decreasing with time as expected due to the cell slowly leaking HBr. Scatter around the decreasing trend is likely due the uncertainty in the input temperature, which is retrieved from the OPUS measurement report and is the temperature of the source compartment and not the sample compartment where the cell is placed. The ILS shown in Figure 2.3 is approximately a sinc function as expected and fairly symmetric about ZPD. The HBr cell test shows a slightly less symmetrical ILS than the N_2O cell test and is likely the result of the poorer fits of the HBr lines, which could be a result of the HBr cell leakage.

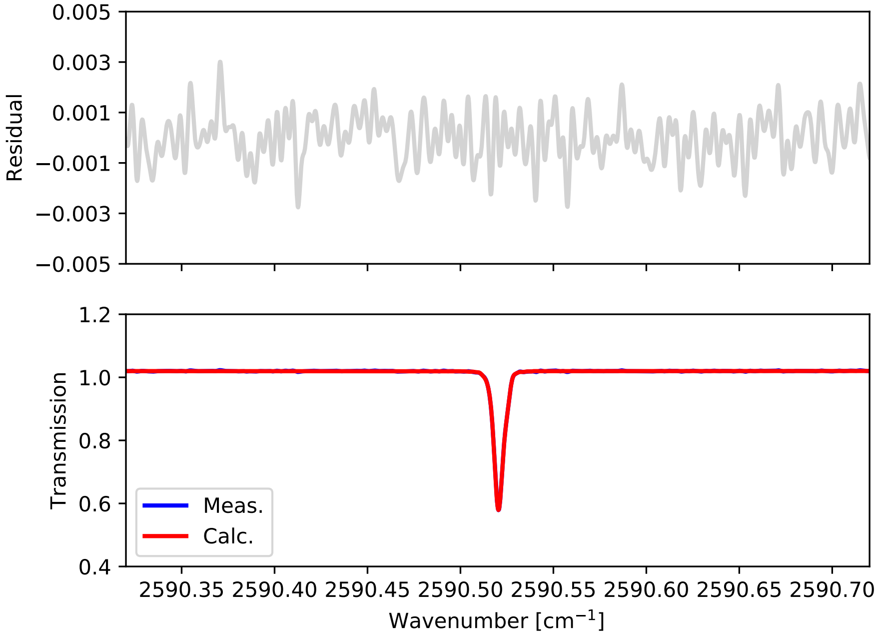

Figure 2.5: Example of the residual (top) and fit (bottom) of microwindow 2 for the Eureka FTIR HBr #30 cell test on 15 March 2019 using LINEFIT v14.5.

In 2016, an N_2O cell was obtained from the NDACC IRWG (N_2O cell #11) and N_2O cells were produced for IRWG sites to provide more precise monitoring of the ILS as N_2O is inert and therefore less prone to leakage from the cell. This cell has been in use since March 2016 and N_2O has been prioritized over HBr cell tests. N_2O cell tests are performed at lower resolution than for the HBr cell as recommended by Frank

Hase (Hase, 2012). The background and cell spectra are recorded at 0.05 cm^{-1} (18 cm maximum OPD) and 0.005 cm^{-1} (180 cm maximum OPD) resolution respectively, with 60 co-added scans each. This results in shorter measurement times for the N_2O cell in comparison to the HBr cell. The N_2O microwindows fitted are listed in Table 2.3. The results of the N_2O cell tests (shown in Figure 2.7) are similar to the those from the HBr cell tests in terms of ILS, ME, and PE. An example of a fitted microwindow is shown in Figure 2.6.

Table 2.3: Fitted microwindows for the Eureka FTIR N_2O cell test processed with LINEFIT v14.5.

Microwindow	Wavenumber Range [cm^{-1}]
1	2167.03-2185.25
2	2222.825-2223.019
3	2224.457-2224.715

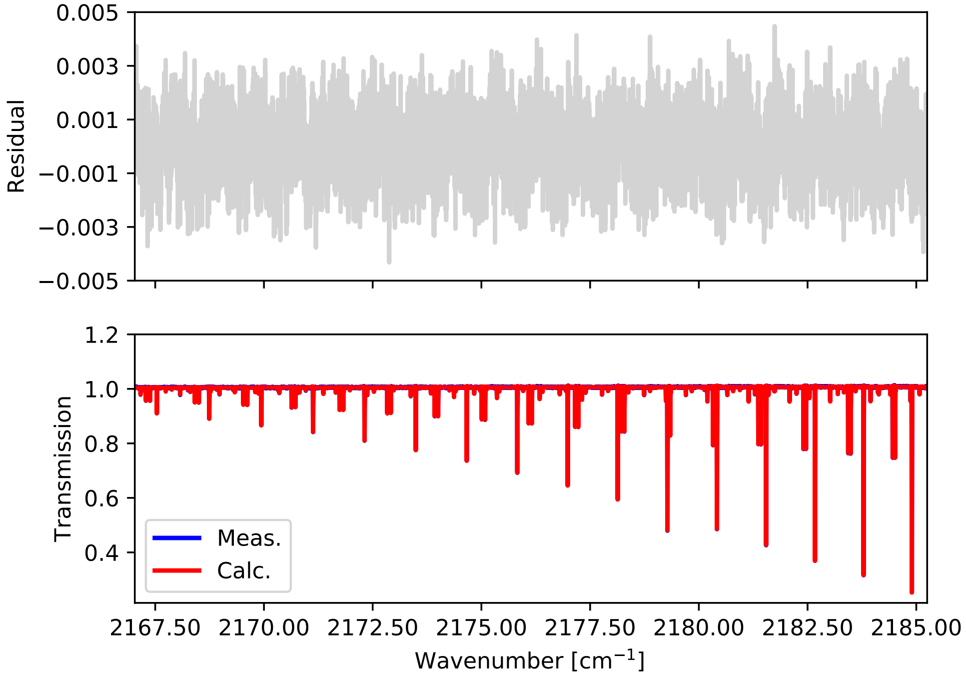

Figure 2.6: Example of a residual (top) and fit (bottom) for microwindow 3 for the N_2O #11 cell test on 1 March 2019 using LINEFIT v14.5.

The results of the N_2O cell tests (Figure 2.7) show a slight over-modulation of 1.02 at maximum OPD of 180 cm prior to March 2017, which is consistent with the HBr cell tests for that period. A considerable drop in the ME to below 0.9 was observed in March 2017 after realignment of the interferometer. The alignment was performed during the 2017 Canadian Arctic ACE/OSIRIS Validation Campaign because the NIR HCl cell tests had been showing a continued decrease in ME and fallen below the TCCON requirement of 0.95-1.05 ME at 45 cm (maximum OPD for TCCON). This decrease was attributed to misalignment due to the wearing of the pads of the moving mirror. The realignment was performed with a home-built alignment kit following the procedure of John Robinson from the National Institute of Water and Atmospheric Research (NIWA) of Lauder, New Zealand. The alignment was performed with a 1 mm aperture (as used by TCCON) and the CaF_2 beamsplitter, allowing the input helium neon (HeNe) laser beam to be visible. After alignment, a near-perfect NIR ILS was observed for the HCl cell tests, but a significant decrease was found for MIR ILS for both the N_2O and HBr cell tests. Small improvements were made as a result of peaking the detector signals, but the MIR ME at maximum OPD remained low, generally around 0.9 or lower.

During the 2018 Canadian Arctic ACE/OSIRIS Validation Campaign, the instrument alignment was verified with the alignment kit and was found to be consistent with the previous year. During the procedure, it was found that rotating between various aperture sizes resulted in changes in the positions of the aperture centre as viewed from the interferometer arm. Repeating the N_2O cell test with the 1 mm entrance aperture (used for TCCON NIR HCl cell tests) instead of the usual 1.15 mm aperture resulted, in a near-perfect ILS and ME near unity at all OPDs, consistent with the HCl cell tests.

It was discovered that this issue with the aperture wheels had been observed with other older Bruker instruments. New and improved aperture wheels were therefore installed on 27 February 2019 during the 2019 Canadian Arctic ACE/OSIRIS Validation Campaign by Sebastien Roche, Tyler Wizenberg and Pierre Fogal. The full alignment procedure was then repeated. Since the installation of the new aperture wheels, the HCl, N_2O and HBr cell tests show much more consistent alignment. It should be noted that the N_2O cell test on 27 February 2019 shows a low ME of 0.85 at maximum OPD after the interferometer alignment. The N_2O cell test on March 1, 2019 shows a considerable increase in the ME to near unity for all OPDs with a decrease in phase error as a result of realignment of the lamp source on the entrance aperture on 28 February 2019.

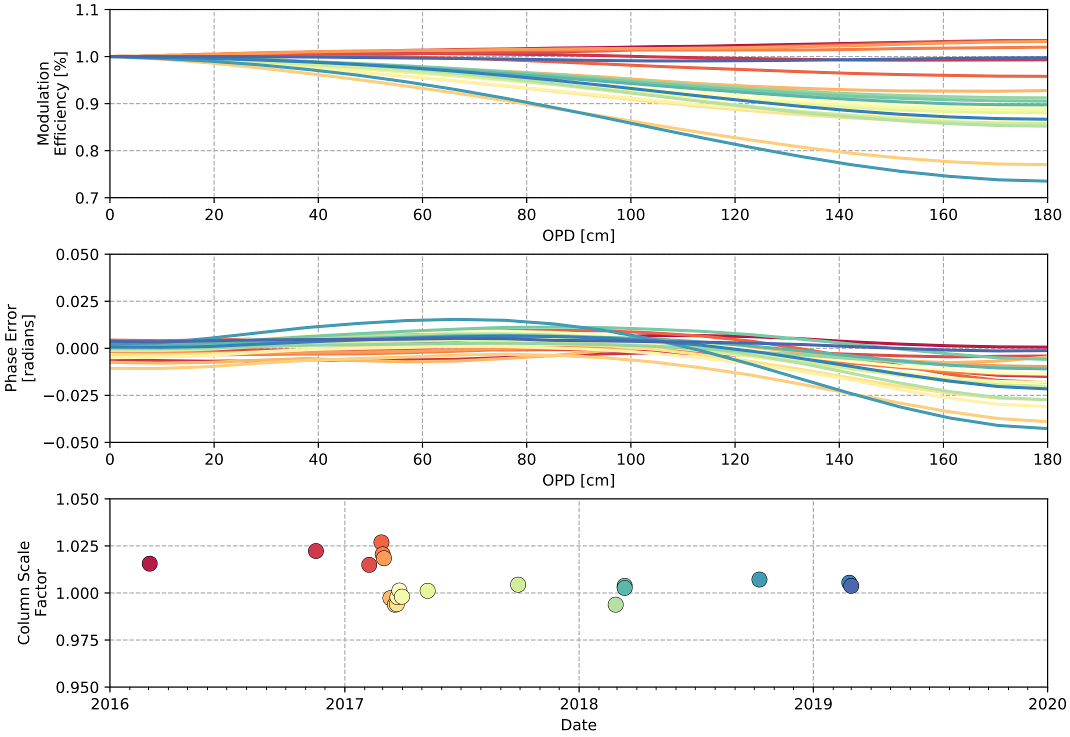

Figure 2.7: Modulation efficiency (ME), phase error (PE) and retrieved column scale factor for Eureka FTIR N_2O #11 cell tests analyzed with LINEFIT v14.5.

2.4 Trace Gas Retrievals

2.4.1 Retrieval Theory

The Inverse Problem

Vertical volume mixing ratio (VMR) profiles and integrated columns are retrieved from FTIR solar-absorption spectra using the optimal estimation method (OEM; Rodgers, 1976, 1990, 2000). The measured atmospheric state, $\mathbf{y}$, may be related to the true atmospheric state, $\mathbf{x}$ as:

$$\mathbf{y} = \mathbf{F}(\mathbf{x}, \mathbf{b}) + \boldsymbol{\epsilon}, \tag{2.11}$$

where $\mathbf{F}$ is the forward model, $\mathbf{b}$ is all other model parameters and $\boldsymbol{\epsilon}$ is the measurement error. The inverse function of $\mathbf{F}$ is denoted by $\mathbf{I}$. The retrieved, or estimated, atmospheric state ($\hat{\mathbf{x}}$) is then related to the measured and true atmospheric state as:

$$\hat{\mathbf{x}} = \mathbf{I}\left(\mathbf{y}, \mathbf{b}, \mathbf{x}, \mathbf{c}\right), \tag{2.12}$$

where $\mathbf{c}$ denotes other parameters the inverse model is dependent on. In order to relate the retrieved state $\hat{\mathbf{x}}$ to the true state $\mathbf{x}$, the a priori state $\mathbf{x}_a$ is defined, which is an initial guess of the true state. Assuming that both $\mathbf{I}$ and $\mathbf{F}$ are linear over the range of the state spaces of $\mathbf{x}$ and $\mathbf{x}_a$, then a Taylor series expansion of Equation 2.12 yields:

$$\hat{\mathbf{x}} = \mathbf{I}\left(\mathbf{F}(\mathbf{x}_a, \hat{\mathbf{b}}) + \mathbf{K}\left(\mathbf{x} - \mathbf{x}_a\right) + \mathbf{K}_b\left(\mathbf{b} - \hat{\mathbf{b}}\right) + \boldsymbol{\epsilon}, \hat{\mathbf{b}}, \hat{\mathbf{x}}, \mathbf{c}\right), \tag{2.13}$$

where $\hat{\mathbf{b}}$ is the best estimate of the model parameters. $\mathbf{K}$ is the weighting function matrix, and $\mathbf{K}_b$ is the parameter space weighting function matrix defined as:

$$\begin{aligned} \mathbf{K} &= \frac{\partial \mathbf{F}}{\partial \mathbf{x}}, && (2.14) \\ \mathbf{K}_b &= \frac{\partial \mathbf{F}}{\partial \mathbf{b}}, && (2.15) \end{aligned}$$

which represent the sensitivity of the forward model to the state vector and ancillary parameters respectively. A second Taylor series expansion of Equation 2.13 is then performed, which yields:

$$
\begin{aligned}
\hat{\mathbf{x}} &= \mathbf{x}_a + \mathbf{GK}\left(\mathbf{x} - \mathbf{x}_a\right) + \mathbf{GK}\left(\mathbf{b} - \hat{\mathbf{b}}\right) + \mathbf{G}\boldsymbol{\epsilon} && (2.16)\\
&= \mathbf{x}_a + \mathbf{A}\left(\mathbf{x} - \mathbf{x}_a\right) + \boldsymbol{\epsilon}_{\mathbf{x}}, && (2.17)
\end{aligned}
$$

where the last two terms have been combined into a single error term $\boldsymbol{\epsilon}_{\mathbf{x}}$, $\mathbf{G}$ is the gain matrix and $\mathbf{A}$ is the averaging kernel. The gain matrix $\mathbf{G}$ represents the sensitivity of the inverse model to the measurement and is defined as:

$$
\mathbf{G} = \frac{\partial \mathbf{I}}{\partial \mathbf{y}}. \qquad (2.18)
$$

The sensitivity of the retrieved state to the true state is given by the averaging kernel:

$$
\begin{aligned}
\mathbf{A} &= \mathbf{GK} && (2.19)\\
&= \frac{\partial \mathbf{I}}{\partial \mathbf{y}} \cdot \frac{\partial \mathbf{F}}{\partial \mathbf{x}} && (2.20)\\
&= \frac{\partial \hat{\mathbf{x}}}{\partial \mathbf{x}}. && (2.21)
\end{aligned}
$$

The averaging kernel characterizes the relationship between the retrieved state and the true atmospheric state (Rodgers, 2000). The sensitivity of the retrieval may be defined as the sum of the rows of the averaging kernel and represents the fraction of the retrieved information content from the measurement as opposed to the a priori (e.g. Vigouroux et al., 2009). The averaging kernel also quantifies the vertical information content of the retrieval, defined as the Degrees of Freedom for Signal (DOFS) which is the trace of the averaging kernel. The DOFS represents the number of independent quantities that can be retrieved from the measurement.

2.4.2 The Maximum a Posteriori Solution

It remains now to find the form of $\mathbf{G}$ and the best estimate of the state $\hat{\mathbf{x}}$. Performing a measurement $\mathbf{y}$ maps the true state $\mathbf{x}$ to the measurement state space through the forward model $\mathbf{F}$. However, since $\boldsymbol{\epsilon}_{\mathbf{x}}$ is only known statistically, a point in state space maps into a region in measurement space that is determined by the Probability Distribution Function (PDF) of $\boldsymbol{\epsilon}_{\mathbf{x}}$. As a result, a statistical approach must be employed in order to relate the true state to the a priori. To do so, we introduce Baye's Theorem:

$$P(\mathbf{x}|\mathbf{y}) = \frac{P(\mathbf{y}|\mathbf{x})}{P(\mathbf{x})}, \tag{2.22}$$

which is the posterior PDF, the probability of $\mathbf{x}$ given $\mathbf{y}$. $P(\mathbf{y}|\mathbf{x})$ is the observation PDF, the probability of $\mathbf{y}$ given $\mathbf{x}$ and is dependent on the forward model and measurement errors. The maximum a posteriori solution is the solution for which $P(\mathbf{x}|\mathbf{y})$ is maximum. To find the a posteriori solution, we assume that the relationship between $\mathbf{x}$ and $\mathbf{y}$ is linear and a Gaussian distribution for the PDF. Under these assumptions:

$$\begin{aligned} P(\mathbf{y}) &= \frac{1}{(2\pi)^{n/2}|\mathbf{S}_y|^{1/2}} \exp\left[-\frac{1}{2}(\mathbf{y}-\bar{\mathbf{y}})^T\mathbf{S}_y^{-1}(\mathbf{y}-\bar{\mathbf{y}})\right], && (2.23) \\ -2\ln\left[P(\mathbf{y})\right] &= (\mathbf{y}-\bar{\mathbf{y}})^T\mathbf{S}_y^{-1}(\mathbf{y}-\bar{\mathbf{y}}) + 2\ln\left[(2\pi)^{n/2}|\mathbf{S}_y|^{1/2}\right] && (2.24) \\ &= (\mathbf{y}-\bar{\mathbf{y}})^T\mathbf{S}_y^{-1}(\mathbf{y}-\bar{\mathbf{y}}), + C_{\mathbf{y}} && (2.25) \end{aligned}$$

where $\bar{\mathbf{y}}$ is the mean of the observation, $\mathbf{S}_y$ is the measurement error covariance matrix, n is the number of vector elements, and C_y is a constant term. A similar expression is also obtained for $P(\mathbf{x})$ and $P(\mathbf{y}|\mathbf{x})$:

$$-2\ln\left[P(\mathbf{x})\right] = (\mathbf{x}-\mathbf{x}_a)^T\mathbf{S}_a^{-1}(\mathbf{x}-\mathbf{x}_a)+C_{\mathbf{x}}, \tag{2.26}$$

$$-2\ln\left[P(\mathbf{y}|\mathbf{x})\right] = \left[\mathbf{y}-\mathbf{F}(\mathbf{x},\mathbf{b})\right]^T\mathbf{S}_\epsilon^{-1}\left[\mathbf{y}-\mathbf{F}(\mathbf{x},\mathbf{b})\right]+C_{\mathbf{yx}}, \tag{2.27}$$

where $\mathbf{S}_a$ and $\mathbf{S}_\epsilon$ are the a priori and error covariance matrices respectively. We then substitute Equations 2.25, 2.26 and 2.27 into Equation 2.22 to obtain:

$$-2\ln\left[P(\mathbf{y}|\mathbf{x})\right] = \left[\mathbf{y}-\mathbf{F}(\mathbf{x},\mathbf{b})\right]^T\mathbf{S}_\epsilon^{-1}\left[\mathbf{y}-\mathbf{F}(\mathbf{x},\mathbf{b})\right]+(\mathbf{x}-\mathbf{x}_a)^T\mathbf{S}_a^{-1}(\mathbf{x}-\mathbf{x}_a)+C, \tag{2.28}$$

where the constants have been combined into a single term C. We now define the cost function $\mathbf{J}(\mathbf{x})$:

$$\mathbf{J}(\mathbf{x}) = \left[\mathbf{y}-\mathbf{F}(\mathbf{x},\mathbf{b})\right]^T\mathbf{S}_\epsilon^{-1}\left[\mathbf{y}-\mathbf{F}(\mathbf{x},\mathbf{b})\right]+(\mathbf{x}-\mathbf{x}_a)^T\mathbf{S}_a^{-1}(\mathbf{x}-\mathbf{x}_a). \tag{2.29}$$

We then substitute Equation 2.29 into Equation 2.28. Taking the derivative of Equation 2.28 and setting it equal to zero:

$$-2\nabla_{\mathbf{x}}\ln\left[P(\mathbf{y}|\mathbf{x})\right] = \nabla_{\mathbf{x}}\mathbf{J}(\mathbf{x}) = 0, \tag{2.30}$$

where $\nabla_{\mathbf{x}}\mathbf{J}(\mathbf{x})$ is given by:

$$\nabla_{\mathbf{x}}\mathbf{J}(\mathbf{x}) = -\nabla_{\mathbf{x}}\left[\mathbf{F}(\mathbf{x},\mathbf{b})\right]^T\mathbf{S}_\epsilon^{-1}\left[\mathbf{y}-\mathbf{F}(\mathbf{x},\mathbf{b})\right]+\mathbf{S}_a^{-1}(\mathbf{x}-\mathbf{x}_a). \tag{2.31}$$

It is evident that $P(\mathbf{y}|\mathbf{x})$ is a maximum when the cost function $\mathbf{J}(\mathbf{x})$ is a minimum. For a moderately linear system as we have assumed here, the optimal solution may be obtained by Gauss-Newton iteration:

$$\mathbf{x}_{i+1} = \mathbf{x}_i - \left[\nabla_{\mathbf{x}}\nabla_{\mathbf{x}}\mathbf{J}(\mathbf{x_i})\right]^{-1}\nabla_{\mathbf{x}_i}\mathbf{J}(\mathbf{x_i}). \tag{2.32}$$

The initial step at $i = 0$ corresponds to the a priori $\mathbf{x}_a$. Substituting this and Equation 2.29 into Equation 2.32, we obtain the optimal solution or the a posteriori estimate $\hat{\mathbf{x}}$:

$$\mathbf{x}_{i+1} = \mathbf{x}_a + (\mathbf{S}_a^{-1} + \mathbf{K}_i^T\mathbf{S}_{\boldsymbol{\epsilon}}^{-1}\mathbf{K}_i)^{-1}\mathbf{K}_i^T\mathbf{S}_{\boldsymbol{\epsilon}}^{-1}\left[(\mathbf{y} - \mathbf{F}(\mathbf{x},\mathbf{b})) - \mathbf{K}_i(\mathbf{x}_a - \mathbf{x}_i)\right], \tag{2.33}$$

where we have used the fact that $\mathbf{K} = \nabla_{\mathbf{x}}\mathbf{F}$. Assuming that the optimal solution is given by $\hat{\mathbf{x}}$ then:

$$\begin{aligned} \hat{\mathbf{x}} &= \mathbf{x}_a + (\mathbf{S}_a^{-1} + \mathbf{K}^T\mathbf{S}_{\boldsymbol{\epsilon}}^{-1}\mathbf{K})^{-1}\mathbf{K}^T\mathbf{S}_{\boldsymbol{\epsilon}}^{-1}(\mathbf{y} - \mathbf{K}\mathbf{x}_a) && (2.34)\\ &= \mathbf{x}_a + \mathbf{G}(\mathbf{y} - \mathbf{K}\mathbf{x}_a), && (2.35) \end{aligned}$$

where $\mathbf{G}$ is defined as:

$$\begin{aligned} \mathbf{G} &= (\mathbf{S}_a^{-1} + \mathbf{K}^T\mathbf{S}_{\boldsymbol{\epsilon}}^{-1}\mathbf{K})^{-1}\mathbf{K}^T\mathbf{S}_{\boldsymbol{\epsilon}}^{-1} && (2.36)\\ &= \mathbf{S}_a\mathbf{K}^T(\mathbf{K}\mathbf{S}_a\mathbf{K}^T + \mathbf{S}_{\boldsymbol{\epsilon}})^{-1}. && (2.37) \end{aligned}$$

It then follows from Equations 2.21 and 2.36 that the averaging kernel $\mathbf{A}$ can be expressed:

$$\mathbf{A} = (\mathbf{S}_a^{-1} + \mathbf{K}^T\mathbf{S}_{\boldsymbol{\epsilon}}^{-1}\mathbf{K})^{-1}\mathbf{K}^T\mathbf{S}_{\boldsymbol{\epsilon}}^{-1}\mathbf{K}, \tag{2.38}$$

and therefore, by this definition, Equation 2.34 becomes:

$$\hat{\mathbf{x}} = \mathbf{x}_a + \mathbf{A}(\mathbf{x} - \mathbf{x}_a). \tag{2.39}$$

Equation 2.39 is interpreted as follows. For a perfect system, the best estimate $\hat{\mathbf{x}}$ would be equal to the true state $\mathbf{x}$ and therefore $\mathbf{A}$ would be the identity matrix and there would be no dependence of the retrieved state on the a priori. In reality, the diagonal elements are not equal to unity and off-diagonal elements of $\mathbf{A}$ are non-zero as the measurement does not have perfect sensitivity to the true state at all levels and is therefore unable to independently resolve the true state at all levels. Therefore, the retrieved state has some dependence on the a priori, as quantified by the values of $\mathbf{A}$.

2.4.3 The SFIT4 Retrieval Algorithm

The OEM method of Rodgers (1976, 1990, 2000) outlined in Sections 2.4.1 and 2.4.2 forms the basis of the SFIT4 retrieval algorithm. SFIT4, released in 2014, is used by most member sites of the NDACC IRWG, with the exception of a few sites who have not yet transitioned from SFIT2 or use the PROFFIT retrieval algorithm (Hase et al., 2004). SFIT4 is based on the SFIT2 retrieval algorithm, which iteratively adjusts trace gas profiles to minimize the difference between the measured and calculated spectra (Pougatchev et al., 1995; Rinsland et al., 2007).

The calculated spectrum is obtained through a forward model calculation. The forward model of SFIT4 is a line-by-line radiative transfer model that assumes a Voigt line shape for the absorbing gases. Local thermodynamic equilibrium and homogeneity are assumed for each vertical layer on the FTIR retrieval grid. The forward model requires prior knowledge of the atmosphere, with temperature and pressure profiles obtained from the US National Centers for Environmental Prediction (NCEP). Spectroscopic parameters are currently taken from HITRAN 2008 (Rothman et al., 2009) as recommended by the NDACC IRWG. However, spectral line parameters from HITRAN 2012 and the atmospheric (atm) line list (Toon, 2015) are also used in particular cases as will be discussed in Section 3. The spectroscopic line parameters are used in the line-by-line calculation of the atmospheric spectrum. A model atmosphere is also created using refractive ray-tracing and airmass paths through the atmosphere from a code called FASTCODE (Meier et al., 2004).

SFIT4 requires instrument parameters including the instrument FOV, maximum OPD, and ILS. The FOV and maximum OPD are acquired from the OPUS spectral measurement file. The aperture varies with the spectral filter for the measurement while a maximum OPD of 257 cm is used as prescribed by the NDACC IRWG. Ideally, the input ILS should be routinely updated based on the routine cell test results. However, an ideal ILS is assumed for all measurements based on the fact that the ILS had been found to not vary significantly over the measurement time series. The solar zenith angle of the measurement is also required for the forward model calculation, and is calculated based on the instrument altitude, latitude and longitude (which are constant) in the SFIT4 module CKOPUS and the measurement time stamp and scan duration. The time for the SZA calculation is defined to be at the middle of the set of the two or four scans that comprise a spectrum.

For the retrieval, the OEM requires the use of a priori VMR profiles of the trace gas to be retrieved and the associated measurement error covariance ($\mathbf{S}_e$) and a priori error covariance ($\mathbf{S}_a$) matrices. The SFIT4 error covariance matrices are defined as:

$$\mathbf{S}_e = \frac{\mathbf{I}}{\mathrm{SNR}^2}, \tag{2.40}$$

where $\mathbf{I}$ is the identity matrix and SNR is the signal-to-noise ratio of each spectrum calculated in a predefined spectral region (listed in Table 2.1) for the respective spectral filter for each measurement. The SNR is defined as the ratio of the maximum signal and the root-mean-square (RMS) residual about zero for the spectral region of interest. In SFIT2, an ad-hoc SNR was chosen based on trade-off curves of the RMS fitting residual as a function of SNR. Using the real SNR of the measured spectra ensures the information content of the retrieval is derived from the measurement rather than ad-hoc information.

The choice of a valid a priori covariance matrix is an essential part of the retrieval process in SFIT4. The a priori covariance matrix should represent the natural variability of the species; however, it may be treated as a tuning parameter in the retrieval. This is particularly true for trace gas species whose profiles are highly variable or unknown. The choice and construction of the a priori covariance matrices will be discussed Chapter 3.

Likewise, as was illustrated in Section 2.4.1, the retrieved profile is dependent on the choice of the a priori profile. As per NDACC IRWG guidelines, the a priori profiles for the standard NDACC species are derived from a 40-year mean (1980-2020) from the Whole Atmosphere Community Climate Model (WACCM v4; Eyring et al., 2007; Marsh et al., 2013). For all species retrieved and presented in this thesis, the WACCM-derived a priori profiles are used, with the exception of NH_3, as will be discussed in Chapter 3.

Retrievals in SFIT4 are performed as follows. A model atmosphere is created from the forward model to generate the a priori calculated spectra for the selected microwindows of interest to be fitted. These microwindows are dependent on the trace gas species to be retrieved and will be discussed in Chapter 3. The initial calculated spectrum is based on the a priori profiles of the target and interfering species being fitted in each microwindow in addition to the NCEP pressure and temperature profiles. The iterative procedure is then begun, and for each iteration, the profiles to be fitted are adjusted and the resulting calculated spectrum is compared to the measured spectrum. This process is repeated until convergence is found. Convergence is determined by the χ^2 value of the RMS residual between the measured and calculated spectrum. For successive iterations, if the difference in χ^2 is less than a convergence threshold, the retrieval is said to converge. If the retrieval does not reach the threshold within the maximum number of iterations, the retrieval does not converge. The iterative process is repeated until convergence is found or the maximum number of iterations is reached. Usually, a maximum of 17 iterations with a χ^2 convergence threshold of 0.1 is used. Retrievals may not converge for a number of reasons. The most common reason is due to poor quality spectra as a result of low signal and hence low SNR. A poor choice of the a priori profile and its corresponding covariance matrix may also cause instability in the retrievals; however, a large part of designing the retrieval strategy for each trace gas involves choosing the a priori profile and its covariance matrix to avoid this issue.

2.5 Inter-layer Correlation

The a priori covariance matrix $\mathbf{S}_a$ is used as a constraint in the retrieval procedure and ideally should reflect the true variability of the species. However, the $\mathbf{S}_a$ may be thought of as a tuning parameter in the retrieval to reduce nonphysical oscillations in the retrieved VMR profiles (Palm, 2014). Oscillations in the retrieved profiles may be the result of large differences between the a priori and true state causing an instability in the retrieval. Generally, the diagonals of $\mathbf{S}_a$ are defined as:

$$\mathbf{S}_a = \mathbf{I} \cdot \sigma^2, \tag{2.41}$$

where σ is the expected deviation of the target species from the a priori profile and is usually reported as a percentage value. In this work, the diagonals of the $\mathbf{S}_a$ are specified as the σ values. For the minor species C_2H_2, CH_3OH and NH_3, which are primarily tropospheric, the diagonals of the $\mathbf{S}_a$ matrix were chosen to allow more variability in the troposphere while restricting changes in the profile at greater altitudes. This was done by scaling the diagonal elements of the $\mathbf{S}_a$ matrix by the layer thickness. Therefore the diagonal elements of $\mathbf{S}_a$ are given by:

$$\mathbf{S}_{a,ii} = \frac{\mathbf{S}_{a,ii}}{\Delta z_i}, \tag{2.42}$$

where Δz is the thickness of the layer in units of km. As the FTIR retrieval grid is more finely spaced at the lower altitudes, the diagonals of the $\mathbf{S}_a$ are greater near the surface allowing for more variability of the retrieved profiles at the lower levels. This was found to improve the DOFS, maintaining at least a minimum of approximately 1.

The diagonal elements of the $\mathbf{S}_a$ matrix are often chosen with respect to the standard deviation (σ) of the mean WACCM profiles, reflecting the natural variability of the species. The diagonals are defined as σ^2 values. However, in SFIT4, the $\mathbf{S}_a$ values are treated as a tuning parameter to account for the expected variability of the target species that may not be well captured in WACCM.

To reduce oscillations in the retrieved profiles, an inter-layer correlation (ILC) may be used. The ILC assumes that VMR profiles are correlated between adjacent retrieval layers and therefore the ILC defines the off-diagonal elements of the $\mathbf{S}_a$ matrix. For all retrievals presented here, an exponential ILC is used, with the elements of $\mathbf{S}_a$ given by:

$$\mathbf{S}_{a,ij} = \mathbf{S}_{a,ii} e^{-\frac{|z_i - z_j|}{W}} \tag{2.43}$$

where z_i is the altitude at the respective level and W is the correlation width. The choice of correlation width is species dependent but in most cases 4 km is used as is standard practice of the NDACC IRWG.

2.6 Tikhonov Regularization

Tikhonov regularization (Tikhonov, 1963) is used as an alternative to the OEM method if the a priori profile of the target species is not well known. The measurement $\mathbf{y}$ is related to the true state $\mathbf{x}$ through the forward model $\mathbf{F}$ by:

$$\mathbf{y} = \mathbf{F}\mathbf{x}, \tag{2.44}$$

which represents a linear model. The solution to the problem is therefore found by the minimization of the Euclidean norm as in the least-squares approach. For the Tikhonov method, the Euclidean norm is also minimized but with a regularization term:

$$\|\mathbf{F}\mathbf{x}-\mathbf{y}\|^2+\|\mathbf{\Gamma}\mathbf{x}\|^2, \tag{2.45}$$

where $\mathbf{\Gamma}$ is the Tikhonov regularization matrix. The best estimate is then:

$$\hat{\mathbf{x}}=(\mathbf{K}^T\mathbf{K}+\mathbf{\Gamma}^T\mathbf{\Gamma})^{-1}\mathbf{\Gamma}^T\mathbf{y}. \tag{2.46}$$

The Tikhonov regularization matrix is defined by Tikhonov (1963); Sussmann et al. (2011):

$$\mathbf{\Gamma}=\alpha\mathbf{L}_1^T\mathbf{T}\mathbf{L}_1, \tag{2.47}$$

where T denotes the transpose, α is the regularization strength, $\mathbf{L}_1$ is the discrete first derivative operator, and $\mathbf{T}$ is a diagonal matrix that accounts for the non-linear grid spacing. The diagonals of $\mathbf{T}$ are defined by (Sussmann et al., 2011):

$$\mathbf{T}_{ii}=\Delta z_i^{-2}, \tag{2.48}$$

where Δz_i is the thickness of the ith layer. The influence of Tikhonov regularization on the retrievals can be interpreted as follows. The discrete first derivative operator $\mathbf{L}_1$ preferentially constrains the retrievals such that $\mathbf{x}-\mathbf{x}_a$ is a linear profile. The α parameter may then be thought of as a tuning parameter which is adjusted to obtain a particular DOFS. For these reasons, Tikhononov regularization is often implemented when the a priori profile of the trace gas to be retrieved is uncertain, in which case the retrieval is tuned with the regularization strength to account for the lack of a priori knowledge of the profile.

Chapter 3

Eureka FTIR Retrievals

This chapter describes the method used to retrieve VMR profiles and integrated columns of tropospheric biomass burning species from Eureka FTIR MIR solar-absorption spectra. All retrievals are performed using the SFIT4 (`https://wiki.ucar.edu/display/sfit4/`) v9.4.4 retrieval algorithm. The species CO, HCN and C_2H_6 are standard NDACC IRWG gases and therefore the retrieval strategy follows the NDACC IRWG guidelines. Retrievals of CO, HCN and C_2H_6 for the Eureka FTIR spectra were first performed by Batchelor et al. (2009), and later by Lindenmaier (2012) and Viatte et al. (2014) using the SFIT2 retrieval algorithm. With the release of SFIT4 in 2014, these retrievals were adapted for SFIT4 by Stephanie Conway and since then, the methods have remained unchanged with the exception of CO. CO has been retrieved as part of two NDACC harmonization projects: the ESA-funded Quality Assurance for Essential Climate Variable (QA4ECV) project in 2016 and the EU-funded Copernicus Atmospheric Monitoring Service (CAMS27) Rapid Delivery (RD) project beginning in March 2018. As part of these projects, I modified the standard Eureka CO retrieval strategy to conform to the requirements of these projects, as will be discussed below.

Non-standard NDACC species were also retrieved, including acetylene (C_2H_2), formic acid (HCOOH), methanol (CH_3OH), formaldehyde (H_2CO) and NH_3. Retrievals of C_2H_2, HCOOH and CH_3OH were adapted from the SFIT2 retrieval method of Viatte et al. (2014). The H_2CO retrieval strategy was developed by Vigouroux et al. (2018) for validation of the Tropospheric Monitoring Instrument (TROPOMI) on the Sentinel 5 Precursor satellite. Retrievals of NH_3 from the Eureka FTIR were developed as part of this thesis. A description of the retrieval method for each species is discussed in this section and the optimized time series are presented. Retrieval parameters are summarized in Tables 3.1 and 3.2. Examples of the fitted microwindows are shown in Appendix A.

3.1 Carbon Monoxide

Eureka CO retrievals were performed following the NDACC IRWG guidelines. The three standard microwindows were used for CO: a strong line at 2157.51-2159.14 cm^{-1} and two weak lines at 2057.68-2058.00 and 2069.56-2069.76 cm^{-1} (Notholt et al., 1997b; Zhao et al., 2002). The combination of the strong and weak lines results in greater vertical sensitivity of the retrieval in comparison to a single line (Barret et al., 2003). The choice of the $\mathbf{S}_a$ for CO was influenced by the requirements for the QA4ECV and CAMS27 RD projects. The main requirements were:

1. Retrieved DOFS between 1.5 and 3.5 from the surface to 35 km.
2. Total column averaging kernel values between 0 and 1.5 from the surface to 35 km.
3. Harmonized error analysis amongst all sites.

To satisfy these requirements, the diagonals of the $\mathbf{S}_a$ were reduced from a standard deviation of 20% used by Viatte et al. (2014) to 2%. The lower $\mathbf{S}_a$ is largely due to the greater SNR in SFIT4 (mean of ∼1150 over all years for measurements from 2006-2018) as opposed to the ad-hoc value (85) used in SFIT2 retrievals, therefore resulting in an increase in the information content of the retrieval from the measurement rather than the a priori (Palm, 2014). Off-diagonal elements of the $\mathbf{S}_a$ matrix were created using the exponential inter-layer correlation of Equation 2.43 with a correlation width of 2 km. A 2-km correlation width was selected to minimize large averaging kernel values (Langerock, 2016). The interfering species O_3 and N_2O were simultaneously retrieved as profiles, while all other interfering species were retrieved by scaling of the a priori values. The strong constraints placed on $\mathbf{S}_a$ also resulted in a reduction of the strato-mesopheric CO variability of the retrieved profiles as a result of constraining the retrieved profiles to the a priori. The contribution of strato-mesopheric CO is greatest in the early spring (Kasai et al., 2005a), and may not be well captured in the a priori profile due to averaging of the WACCM model profile over a 40-year period. As a result, averaging kernel values in the upper atmosphere are reduced, while those in the stratosphere (<50 km) are >1, resulting in greater sensitivity in this region as shown in Figure 3.1a. All a priori profiles are from WACCM v4. Spectroscopic linelist parameters for CO are from atm16 (Toon, 2015), while all other species use HITRAN 2008 (Rothman et al., 2009).

The mean retrieved VMR profiles are shown in Figure 3.2a. The mean retrieved CO profiles are greater than the a priori values, with surface values of approximately 130 ppbv and 90 ppbv respectively. The retrieved profiles increase slightly from the surface before decreasing to the tropopause. An increase in the retrieved CO is then observed in the stratosphere due to the CO source from the oxidation of CH_4 and photolysis of CO_2. The CO time series is shown in Figure 3.3a. The seasonal cycle of CO at Eureka is characterized by the greatest total columns in the early spring and decreasing total columns through the summer.

3.2 Hydrogen Cyanide

HCN is retrieved using the two required microwindows of the NDACC IRWG: 3268.00-3268.38 and 3287.00-3287.48 cm^{-1} as used in Viatte et al. (2014), and a third optional mircrowindow from 3299.40-3299.60 cm^{-1} used by Lindenmaier (2012). The use of the third microwindow provided an increase in the vertical sensitivity while improving the fitting of H_2O. Profiles of HCN are retrieved with diagonal values of $\mathbf{S}_a$ with a standard deviation of 20% and off-diagonals corresponding to an exponential inter-layer correlation with a 4 km correlation width. H_2O is retrieved as a profile while all other interfering species are retrieved by scaling of a priori profiles. All a priori profiles are from WACCM v4 and the linelist parameters from HITRAN 2008 are used.

A mean DOFS of 2.8 with a standard deviation of 0.6 is retrieved over all years from 2007-2018. It should be noted that measurements of HCN at Eureka began in 2007 when NDACC filter 2 was installed. The main sensitivity (>0.5) is observed from approximately 1-34 km as shown in Figure 3.1b. The HCN retrievals are primarily sensitive to the lower atmosphere below 34 km, with little contribution from the upper atmosphere (>50 km). The vertical sensitivity coincides with the vertical distribution of HCN and shows greatest abundances in the troposphere and lower stratosphere as illustrated in Figure 3.2b for both the a priori profiles and retrieved profiles.

The retrieved time series of HCN is shown in Figure 3.3b. The seasonal cycle of HCN is predominantly due to the influence of boreal wildfire emissions. Due to the long lifetime of HCN, ranging from weeks to months in the troposphere, HCN will accumulate in the atmosphere during the boreal wildfire season. Episodic enhancements are observed regularly in the time series, particularly in July and August. Notable cases include the 2010 Russian wildfires (Viatte et al., 2013, 2015), the 2014 Northwest Territories wildfires, and the 2017 Northwest Territories and British Columbia wildfires. The 2014 and 2017 events will be discussed in further detail in Chapters 4 and 5 respectively.

3.3 Ethane

Retrievals of C_2H_6 are performed using the standard NDACC IRWG microwindows: 2976.66-2976.95 (Mahieu et al., 1997; Rinsland et al., 2007; Paton-Walsh et al., 2010), 2983.20-2983.55 (Meier et al., 2004) and 2986.50-2986.95 cm^{-1} (Notholt et al., 1997b). Diagonal elements of $\mathbf{S}_a$ correspond to a 50% standard deviation with off-diagonal values from the exponential inter-layer correlation with a correlation width of 4 km. All interfering species are retrieved as scaled profiles. A priori profiles are from WACCM v4 and all linelist parameters are from HITRAN 2008.

The mean retrieved DOFS is 1.9 with a standard deviation of 0.3. The sensitivity peaks from the surface to approximately 15 km as shown in Figure 3.1c. The retrieved profiles of C_2H_6 are shown in Figure 3.2c. The retrieved profiles are generally greater than a priori values with mean concentrations of approximately 1.2 ppbv and 0.03 ppbv at the surface respectively. The a priori profile remains relatively constant throughout the troposphere and decreases in the upper troposphere to lower stratosphere to values near zero. The retrieved profiles increase slightly from the surface to approximately 4 km before decreasing with altitude to zero in the lower troposphere.

The time series of C_2H_6 (Figure 3.3c) shows a similar seasonal cycle to CO as result of their common sources and the influence of seasonally variable transport and loss to OH (Rudolph, 1995). In recent years, an increasing trend in Northern Hemispheric C_2H_6 since 2009 has been identified and attributed to increased North American oil and gas production (Franco et al., 2016; Helmig et al., 2016). C_2H_6 enhancements are observed regularly in the Eureka FTIR time series in July and August due to the transport of boreal wildfire emissions to the Arctic. However, these enhancement of C_2H_6 are not as pronounced as CO or HCN as a result of the lower emissions of C_2H_6 from boreal wildfires (Andreae and Merlet, 2001; Akagi et al., 2011; Andreae, 2019).

3.4 Acetylene

C_2H_2 retrievals for Eureka FTIR spectra are performed following Viatte et al. (2014). Two microwindows are used: 3250.43-3250.7700 cm^{-1} (Petersen et al., 2008), 3255.18-

3255.73 cm^{-1} and 3304.83-3305.35 cm^{-1} (Paton-Walsh et al., 2010). Diagonals of $\mathbf{S}_a$ correspond to a standard deviation of 50% and were scaled by the square root of the inter-layer thickness to increase the DOFS and allow for more variability of the retrieved profiles in the troposphere. Off-diagonal elements from an exponential inter-layer correlation with a correlation width of 4 km were used to minimize nonphysical oscillations in the retrieved profiles. The interfering species H_2O and HDO are scaled from a priori values in the retrieval. All a priori profiles are from WACCM v4 and linelist parameters are from HITRAN 2008.

The mean retrieved DOFS (2007-2018) is 1.4 with a standard deviation of 0.3 and vertical sensitivity primarily from the surface to approximately 21 km. The sensitivity (Figure 3.1d) and VMR profiles (Figure 3.2d) of C_2H_2 show a similar vertical structure to C_2H_6. Surface concentrations of C_2H_2 are 0.12 and 0.24 ppbv for the a priori profile and mean retrieved profiles, respectively. The retrieved profiles remain relatively constant to approximately 6 km and decrease rapidly to near zero at approximately 15 km.

The time series of C_2H_2 (Figure 3.3d) is similar to that for CO as a result of their common sources from combustion, and therefore C_2H_2 is often highly correlated with CO (Xiao et al., 2007 and the references therein). Biomass burning is a considerable source of C_2H_2, and its long lifetime in the troposphere of approximately 2 months allows for long-range transport of wildfire emissions to the Arctic. Enhancements of C_2H_2 are observed in the time series (Figure 3.3d) as a result of the influence of boreal wildfires, along with simultaneous enhancements of the biomass burning tracers CO, HCN, and C_2H_6.

3.5 Methanol

CH_3OH is one of the most abundant non-methane volatile organic gases in the atmosphere (Jacob et al., 2005) and is an important precursor for the formation of CO (Duncan et al., 2007) and H_2CO (Millet et al., 2008). Methanol is relatively short-lived with a lifetime ranging from several days in the boundary-layer to several weeks on a global scale (Jacob et al., 2005; Stavrakou et al., 2011).

The CH_3OH retrieval strategy followed the method of Rinsland et al. (2007) and Viatte et al. (2014). Two wide microwindows were used from 992.00-998.70 cm^{-1} and 1029.00-1037.00 cm^{-1}. O_3 is the dominant absorption feature in these bands and therefore O_3 is simultaneously retrieved as a profile while all other interfering species are retrieved as scaled profiles. All a priori profiles are from WACCM v4 and linelist parameters are from HITRAN 2008.

Due to the large seasonal variability of CH_3OH, diagonal values of the $\mathbf{S}_a$ correspond to a standard deviation of 100% that are scaled by Equation 2.42, allowing for greater variability of the retrieved profiles at the lower levels. Off-diagonal elements of the $\mathbf{S}_a$ matrix were constructed following Equation 2.43, with a correlation width of 4 km to reduce oscillations in the retrieved profiles. Mean DOFS of $\sim$1 was obtained with standard deviation of less than 1%.

As a result of the strong absorption features of O_3 and the seasonal dependence of CH_3OH sources, the CH_3OH absorption features are not resolved at the beginning and end of the measurement season. Retrievals of CH_3OH generally do not converge during these periods, resulting in a shorter measurement season for CH_3OH, ranging from April to September, with the majority of measurements occurring between May and August as seen in Figure 3.3e. The retrieved profiles of CH_3OH generally increase slightly from the surface to a peak near 4 km of approximately 1.2 ppbv, before decreasing with altitude to the troposphere and lower-stratosphere as shown in Figure 3.2e. The averaging kernel values and sensitivity (Figure 3.1e) illustrate as similar structure, with a slight increase above 30 km due to the non-zero a priori and retrieved values in this region.

3.6 Formaldehyde

Retrievals of H_2CO for Eureka were performed as part of the ESA Nitrogen Dioxide and Formaldehyde for Validation (NIDFORVal) harmonization project for the validation of TROPOMI. The FTIR retrieval method for H_2CO is described in detail by Vigouroux et al. (2018) and summarized here for the Eureka FTIR retrievals. Two narrow microwindows containing strong lines from 2778.15-2779.10 cm^{-1} and 2780.65-2782.00 cm^{-1} were selected as used in previous studies (Notholt et al., 1997b; Jones et al., 2009; Vigouroux et al., 2009; Paton-Walsh et al., 2010; Viatte et al., 2014). Two additional microwindows were included to improve the information content of the retrievals: 2763.42-2764.17 cm^{-1} and 2765.65-2766.01 cm^{-1}. Tikhonov regularization was used to constrain the retrieved profiles of H_2CO with a regularization strength α of 25. The interfering species N_2O was retrieved as a scaled profile, while all other interfering species profiles were simultaneously retrieved. All a priori profiles are from WACCM v4 and spectral line parameters are from atm2016, with H_2CO lines from HITRAN 2012 (Rothman et al., 2013), which improved the spectral fits as found by Vigouroux et al. (2018).

Retrieved H_2CO VMR profiles (Figure 3.2f) show a maximum of 0.12 ppbv, which decreases upwards through the troposphere. An increase in VMR is observed in the stratosphere, which follows the shape of the a priori profile. The vertical sensitivity of the retrieved profiles is greatest from the surface to approximately 31 km, with the majority of the information content from below 20 km as shown in Figure 3.1f. The time series of H_2CO (Figure 3.3f) illustrates a summer maximum, similar to HCN (Figure 3.3b), HCOOH (Figure 3.3g) and CH_3OH (Figure 3.3e) as a result of their common biogenic and biomass burning sources.

3.7 Formic Acid

Retrievals of HCOOH were performed following the method of Vigouroux et al. (2012) and Viatte et al. (2014). The primary microwindow is from 1102.00-1109.000 cm^{-1}, which is a widened version of the single microwindow used by Vigouroux et al. (2012) and Viatte et al. (2014). A second microwindow was also used for the Eureka FTIR retrievals from 1178.40-1178.80 cm^{-1}. The second microwindow does not contain any HCOOH absorption lines but is used to improve the fitting of HDO in the first microwindow. A common method of improving the fitting of H_2O and its isotopes for retrievals at humid sites is to pre-fit these features in the measured spectra and to run a second retrieval to retrieve the target trace gas with the vapour features accounted for. For Eureka, a generally dry site, water vapour may be difficult to retrieve as a result of its weak absorption at low concentrations and large seasonal variability. To overcome this difficulty, HDO is not fitted in the main microwindow 1178.40-1178.80 cm^{-1}. In the second microwindow, the strong HDO line is fitted to constrain the HDO retrieval. The HDO VMR profile retrieved in this microwindow is incorporated into the forward model spectrum and therefore is indirectly fitted in the main microwindow. In other words, all measurement information for HDO is derived from the second microwindow and included in the calculated spectrum for the first microwindow through the forward model calculation. The use of these two microwindows was found to reduce the RMS residual of the fits in comparison to the single microwindow of Vigouroux et al. (2012) and Viatte et al. (2014). Furthermore, the use of the two microwindows was also found to improve the stability of the retrieval in SFIT4, reducing the number of nonphysical oscillations in the retrieved VMR profiles and increasing the number of converged retrievals.

As shown in Figure 3.2g, the retrieved HCOOH VMR profiles are much greater than the WACCM v4 a priori values. As such, the choice of $\mathbf{S}_a$ was particularly important. As stated previously, one method to compensate for a small a priori VMR profile is to increase the values of $\mathbf{S}_a$. However, for HCOOH, it was found that the mean DOFS remained relatively constant and low (<0.8) even for large values of the $\mathbf{S}_a$ diagonals (>200%). A second approach would be to increase the a priori VMR profile by a constant scaling, which would result in increased DOFS as the a priori profile tends to true values. To maintain consistency with other NDACC sites retrieving HCOOH including Thule, Boulder and Jungfraujoch, this approach was not selected. Instead, Tikhonov regularization was implemented which tends to scale retrieved profiles from a priori values, thereby eliminating the need to scale the initial a priori VMR profile. The regularization strength α was then chosen to maintain a minimum DOFS of ∼1 throughout the measurement season, which corresponded to an optimal α value of 5. The interfering species O_3 is retrieved as a profile with diagonal values of 5% and exponential inter-layer correlation with a correlation width of 4 km. All other interfering species are scaled from a priori values.

The mean retrieved DOFS of HCOOH is 1.0 with a standard deviation of 0.2 and therefore, the profile retrievals of HCOOH are essentially that of a scaled profile retrieval. The sensitivity (Figure 3.1g) of the retrieval peaks from the surface to approximately 21 km. HCOOH is primarily a tropospheric species, but appreciable amounts are observed in the lower stratosphere as shown in Figure 3.2g and the top panel of Figure 3.3g. Local sources of HCOOH near Eureka are minimal and the seasonal variability of HCOOH at Eureka is driven by the transport of HCOOH from natural sources including secondary production from biogenic sources (Stavrakou et al., 2011) and boreal wildfire emissions (Goode et al., 2000; Yokelson et al., 1999; R'Honi et al., 2013; Urbanski, 2013). As a result, the HCOOH time series at Eureka shows summer maximum in July and August due to the boreal wildfire influence in addition to the contribution from biogenic sources as seen in Figure 3.3g.

3.8 Ammonia

The retrieval strategy for NH_3 was based on the method of Dammers et al. (2015). The two main microwindows of Dammers et al. (2015) were used: 929.40-931.4 cm^{-1} and 962.10-970.00 cm^{-1}. Due to the low concentrations of NH_3 at Eureka, a third microwindow from 950.20-952.2 cm^{-1} was used to improve the retrieved DOFS. H_2O is the main interfering species in this microwindow; however, due to the dry conditions of Eureka, H_2O interference was minimal.

The standard NDACC IRWG WACCM v4 a priori profile was not used. Instead, a modified NH_3 a priori profile was developed based on those used by Dammers et al. (2015) which were derived from balloon-based measurements taken near Fairbanks, Alaska (Toon et al., 1999). This profile was interpolated onto the Eureka FTIR vertical retrieval grid and scaled to a surface concentration of 1 ppbv. The a priori profile was then scaled down further and adjusted based on the shape of the retrieved profiles. Iteratively scaling the a priori profile in this way would result in an increase in DOFS to approximately 1 as the a priori approached the expected true state. The final a priori profile is shown in Figure 3.2h, with a corresponding surface concentration of 140 pptv.

At the time of the development of this retrieval, the only reported measurements of surface-layer NH_3 in the high Arctic were from in-situ measurements in the Canadian Archipelago by Wentworth et al. (2016) with NH_3 concentrations ranging from 40 - 870 pptv, with the upper limit being attributed to nearby seabird colonies. The Eureka NH_3 a priori surface concentration falls within this range but is likely greater than the true concentration due to the isolation from seabird colony NH_3 sources. However, a slightly high a priori profile is preferred as background concentrations of NH_3 at Eureka are very low, but the influence of wildfire NH_3 plumes could increase NH_3 concentrations by several orders of magnitude.

Since a priori NH_3 concentrations at Eureka were unknown, the choice of the $\mathbf{S}_a$ was particularly important. For Eureka NH_3, the $\mathbf{S_a}$ was chosen largely as a tuning parameter for the retrieval to improve the DOFS and minimize the RMS residuals of the fitted spectra. Due to the unknown variability of NH_3 at Eureka, the diagonals of the $\mathbf{S}_a$ matrix were selected corresponding to a standard deviation of 100% and scaled using Equation 2.42. Off-diagonal elements correspond to the exponential inter-layer correlation of Equation 2.43, with a correlation width of 100 km. This large correlation width more strongly constrains the upper layers, while allowing for more variability near the surface due to the finer spacing of the layers. The interfering species HNO_3, H_2O and O_3 were retrieved as profiles, while all other interfering species were retrieved as scaled profiles as was done by Dammers et al. (2015). Aside from NH_3, all other a priori profiles are from WACCM v4 with linelist parameters from HITRAN 2008 for all species.

The mean retrieved VMR profile of NH_3 is shown in Figure 3.2h. The retrieved VMR profiles are generally smaller than those of the a priori profile due to the low ambient concentrations of NH_3 at Eureka, as shown in Figure 3.3h. The sensitivity (Figure 3.1h) shows a peak near 5 km with the greatest sensitivity from the surface to approximately 18 km. Background concentrations are likely due to the contribution of seabird-colony Wentworth et al. (2016) and tundra (Croft et al., 2019) NH_3 emissions. Summertime enhancements of NH_3 are the result of boreal wildfires as will be discussed further in Chapters 4 and 5.

Table 3.1: Summary of parameters for Eureka FTIR retrievals.

Species	Microwindows [cm^{-1}]	Interfering Species[a]	ILC[b][km]	S$_a$ [%]	A Priori	Linelist
CO	2057.70 - 2058.00	O_3, CO_2, OCS	2	2[c]	WACCM v4	atm16
	2069.56 - 2069.76	O_3, CO_2, OCS				
	2157.50 - 2159.15	O_3, CO_2, OCS, N_2O, H_2O				
HCN	3268.05 - 3268.40	H_2O, C_2H_2	4	15	WACCM v4	HITRAN 2008
	3287.10 - 3287.35	CO_2, C_2H_2				
	3299.40 - 3299.60	H_2O, $H_2^{18}O$				
	3331.40 - 3331.80	H_2O, $H_2^{17}O$, CO_2, N_2O				
C_2H_6	2976.66 - 2976.95	H_2O, O_3, CH_4	4	50	WACCM v4	HITRAN 2008
	2983.20 - 2983.55	H_2O, O_3, CH_4				
	2986.50 - 2986.95	H_2O, O_3, CH_4				
C_2H_2	3250.43 - 3250.77	H_2O	4	50[c]	WACCM v4	HITRAN 2008
	3255.18 - 3255.725	H_2O				
	3304.825 - 3305.35	H_2O, HDO				
H_2CO	2763.42 - 2764.17	CH_4, CO_2, O_3, N_2O	Tikhonov	25[d]	WACCM v4	atm16
	2765.65 - 2766.01	CH_4, CO_2, O_3, N_2O				
	2778.15 - 2779.10	CH_4, CO_2, O_3, N_2O				
	2780.65 - 2782.00	CH_4, CO_2, O_3, N_2O				
CH_3OH	992.00 - 998.70	O_3, O_3^{686},O_3^{668},O_3^{676}, O_3^{667},H_2O, CO_2	4	100[c]	WACCM v4	HITRAN 2008
	1029.00 - 1037.00	O_3, O_3^{686},O_3^{668},O_3^{676}, O_3^{667},H_2O, CO_2				
HCOOH	1102.00 - 1109.00	O_3, H_2O, CCl_2F_2, CHF_2Cl, NH_3	Tikhonov	5[d]	WACCM v4	atm16
	1178.40 - 1178.80	HDO, N_2O, CH_4				
NH_3	930.32 - 931.32	H_2O, O_3, CO_2^1, CO_2^2, N_2O, CO_2^3, HNO_3	100	100[c]	WACCM v4	HITRAN 2008
	966.97 - 967.675	H_2O, O_3, CO_2^1, CO_2^2, N_2O, CO_2^3, HNO_3				

[a] Superscript refers to the isotopologue of the species as defined by Rothman et al. (2009).

[b] Exponential inter-layer correlation (ILC) width [km] unless Tikhonov regularization was used as stated.

[c] Diagonals of $\mathbf{S}_a$ were scaled by the square-root of the inter-layer thickness.

[d] α value for Tikhonov regularization.

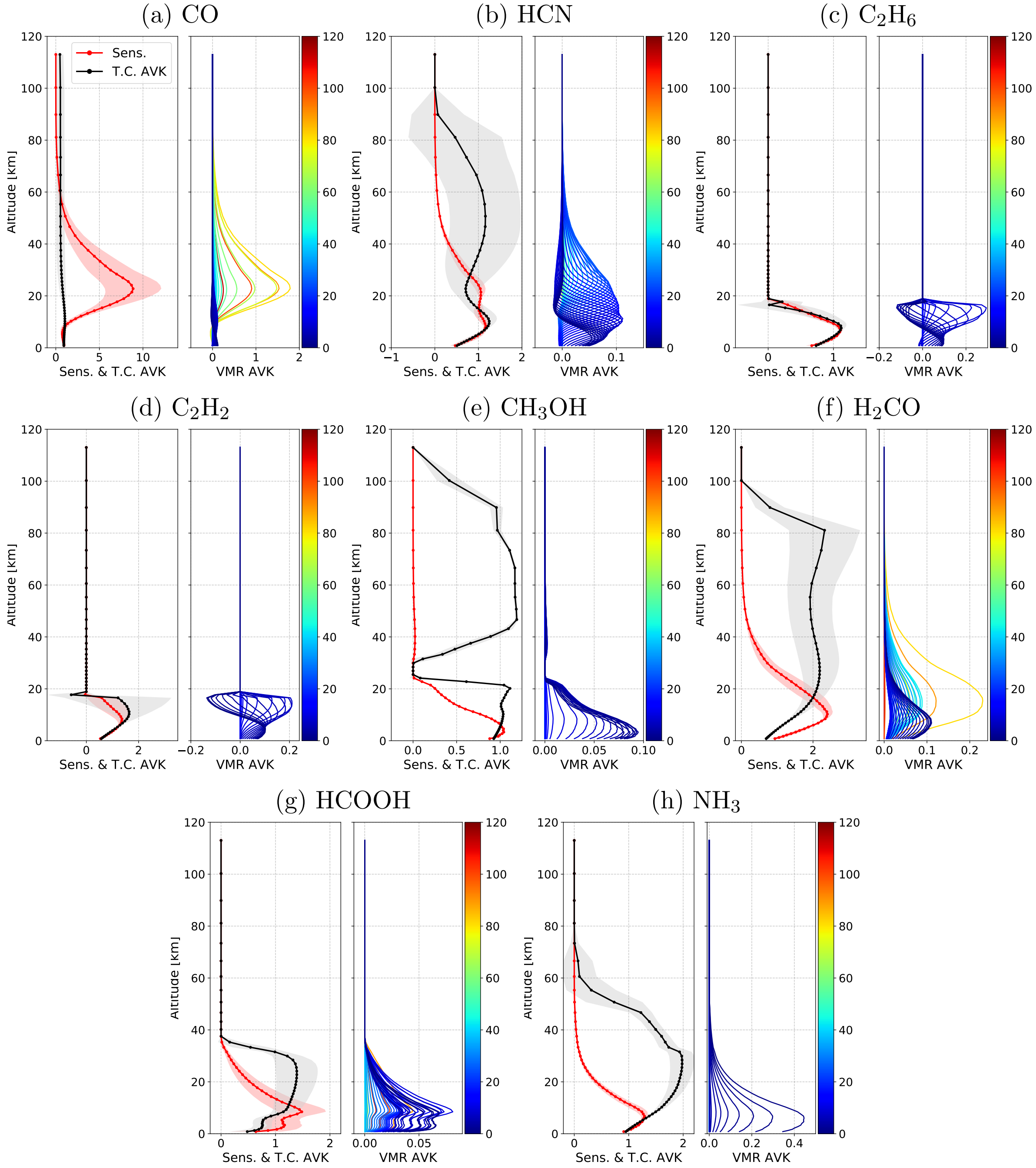
(a) CO (b) HCN (c) C_2H_6

(d) C_2H_2 (e) CH_3OH (f) H_2CO

(g) HCOOH (h) NH_3

Figure 3.1: Mean sensitivity, total column averaging kernels and VMR averaging kernel values for CO, HCN, C_2H_6, C_2H_2, CH_3OH, H_2CO, HCOOH and NH_3. The left panel of each subplot shows the mean sensitivity (red) and total column averaging kernels (black) taken over all years of measurements (2006-2018). The shaded region indicates the standard deviation from the mean. The circle markers indicate the layer centers of the FT-IR vertical retrieval grid. The right panel shows the mean VMR averaging kernels in VMR/VMR units, where the colour bar indicates the altitude.

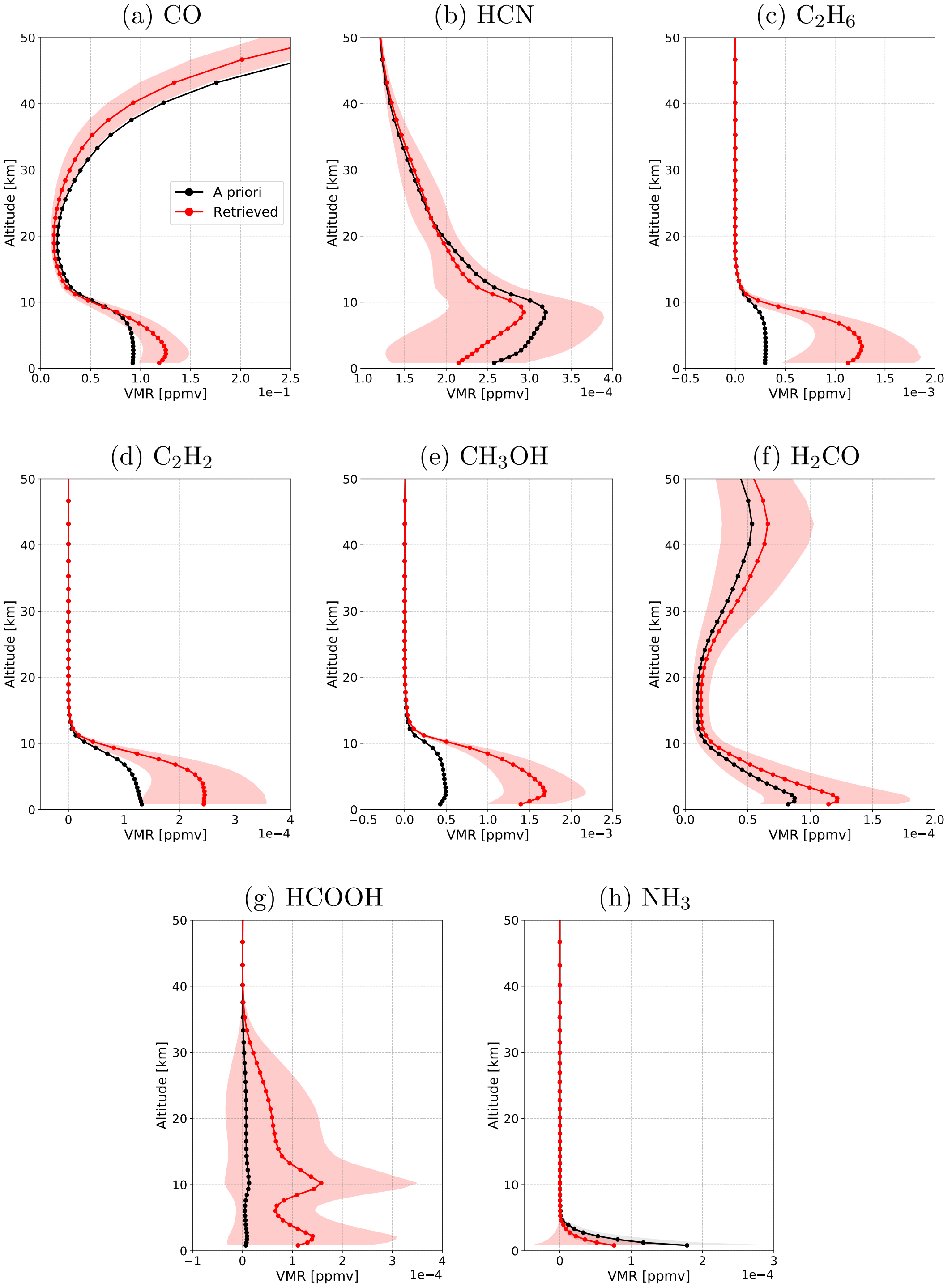

Figure 3.2: Mean retrieved VMR profiles for CO, HCN, C_2H_6, C_2H_2, CH_3OH, H_2CO, HCOOH and NH_3. The a priori profile (black) and the mean retrieved profile (red) taken over all years of measurements (2006-2018) are shown. The circle markers indicate the layer centers of the FTIR vertical retrieval grid. The shaded region indicates the standard deviation from the mean.

(a) CO

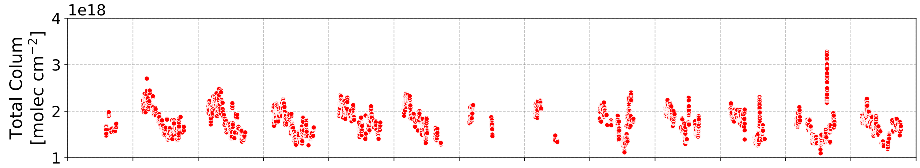

(b) HCN

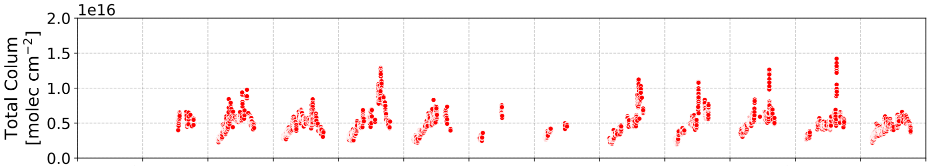

(c) C_2H_6

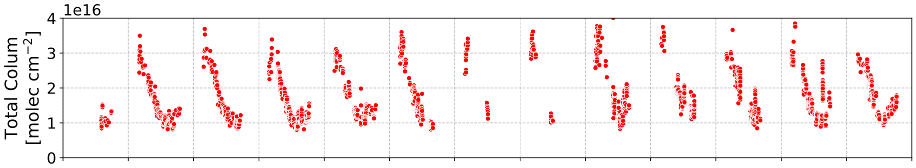

(d) C_2H_2

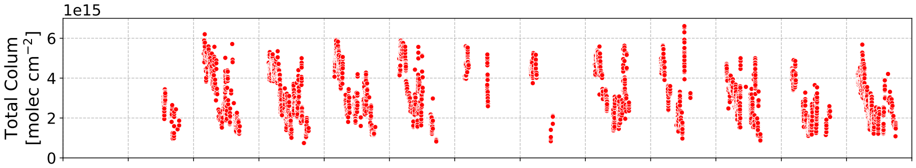

(e) CH_3OH

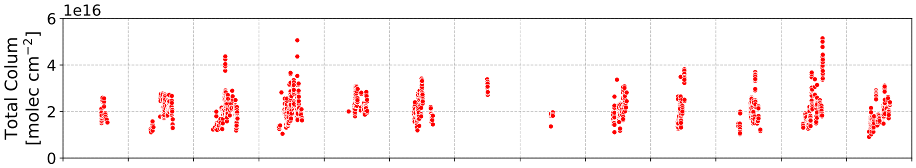

(f) H_2CO

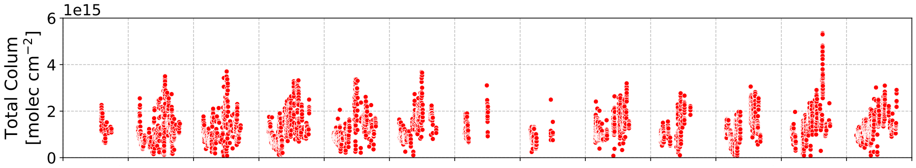

(g) HCOOH

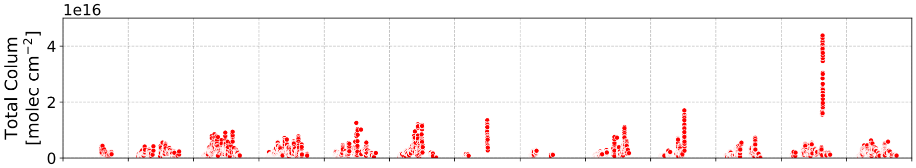

(h) NH_3

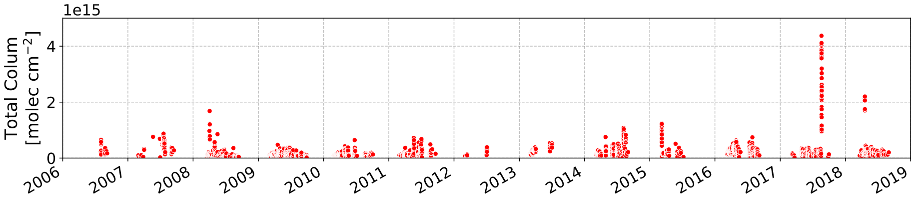

Figure 3.3: Total column time series for CO, HCN, C_2H_6, C_2H_2, CH_3OH, H_2CO, HCOOH and NH_3 from 2006-2018.

Table 3.2: Summary of mean parameters for Eureka FTIR tropospheric trace gas retrievals taken over all years of measurements from 2006-2018. The values in parentheses are the standard deviation from the mean.

Species	Total Column [molec cm^{-2}]	Trop. Column[a] [molec cm^{-2}]	Uncertainty[b] [%]	Random Unc.[b] [%]	Systematic Unc.[b] [%]	DOFS	Sensitivity Range[c] [km]
CO	1.77×10^{18} (2.86×10^{17})	1.68×10^{18} (2.82×10^{17})	5.0 (4.9)	3.5 (4.2)	3.7 (3.4)	2.2 (0.4)	0.61 - 57.78
HCN	4.86×10^{15} (1.59×10^{15})	4.16×10^{15} (1.53×10^{15})	4.9 (0.5)	2.9 (0.8)	3.9 (0.1)	2.8 (0.6)	1.01 - 34.23
C_2H_6	1.63×10^{16} (6.09×10^{15})	1.62×10^{16} (6.10×10^{15})	4.2 (0.4)	1.0 (0.4)	4.1 (0.3)	1.9 (0.3)	0.61 - 14.84
HCOOH	2.02×10^{15} (2.49×10^{15})	1.79×10^{15} (2.15×10^{15})	10.6 (6.7)	6.3 (7.6)	7.4 (2.8)	1.0 (0.2)	0.61 - 20.80
C_2H_2	3.19×10^{15} (1.20×10^{15})	3.18×10^{15} (1.20×10^{15})	5.7 (3.2)	5.7 (3.2)	0.3 (0.1)	1.4 (0.3)	0.61 - 17.12
CH_3OH	2.12×10^{16} (5.81×10^{15})	2.12×10^{16} (5.80×10^{15})	9.6 (1.6)	2.9 (1.7)	9.1 (1.3)	1.0 (0.0)	0.61 - 13.76
H_2CO	1.21×10^{15} (6.42×10^{14})	1.17×10^{15} (6.16×10^{14})	17.7 (6.7)	12.4 (9.2)	9.4 (5.6)	1.1 (0.3)	0.61 - 30.69
NH_3	2.30×10^{14} (3.33×10^{14})	2.30×10^{14} (3.33×10^{14})	30.2 (7.3)	21.0 (11.4)	22.1 (2.8)	1.0 (0.0)	0.61 - 18.31

[a] Tropospheric column from the surface (0.61 km) to 12.71 km in altitude.

[b] Uncertainty reported as percentage of total column.

[c] Vertical range of where sensitivity is 0.5 or greater.

3.9 Error Analysis

Error analysis is performed for all retrievals following Rodgers (2000) as described in Wiacek (2006) and Lindenmaier (2012). The forward model errors considered for the Eureka FTIR retrievals are the solar zenith angle error ($\mathbf{S}_a$), spectroscopic line parameter errors ($\mathbf{S}_{line}$), and errors in the temperature profiles ($\mathbf{S}_{temp}$). Interference error ($\mathbf{S}_{int}$) as described by Rodgers and Connor (2003) is included and accounts for the uncertainties due the simultaneous retrieval of the interfering species. Retrieval parameter errors ($\mathbf{S}_{ret}$) are also taken into account and include the uncertainties due to solar line shifts, wavenumber shifts, phase error, zero line shifts, background slopes or curvature of the measured spectra. The finite vertical retrieval grid introduces a smoothing error ($\mathbf{S}_{sm}$) which is calculated but not reported as recommended by the NDACC IRWG since smoothing errors are inherent to remote sensing measurements of this kind, and do not represent the expected deviation of the retrieved state from the true state (von Clarmann, 2014). Errors are divided into two types: systematic ($\mathbf{S}_{sys}$) and random ($\mathbf{S}_{ran}$). The spectroscopic line parameter errors are considered to be systematic. The temperature uncertainty has both a systematic and random component, while all other errors are considered to be random. The total systematic and random errors are determined by adding all components in quadrature.

Table 3.3: Line parameter errors from HITRAN 2008 and atm16 for all species except CO used in the uncertainty budget for the error analysis of each species retrieval.

Species	Intensity [%]	Pressure-broadening [%]	Temperature-broadening [%]
HCN	3.5	3.5	7.5
C_2H_6	4.0	4.0	4.0
C_2H_2	15	15	15
CH_3OH	15	20[a]	20[a]
H_2CO	15	20[a]	20[a]
HCOOH	7.5	20[a]	20[a]
NH_3	20[a]	7.5	15

[a] Assumed value.

The errors are specified as follows. The solar zenith angle error accounts for the uncertainty of the line-of-sight of the instrument. The solar tracker is assumed to point directly at the centre of the Sun throughout the measurement. However, for each measurement, two co-added scans are used each with an approximate 6-minute scan duration. The solar zenith angle used in the forward model calculation is taken at the time of the midpoint of the co-added scans. Therefore the solar zenith angle will vary slightly during the duration of each measurement. The variation of the solar zenith angle between the start and end of each measurement is approximately 0.06° and therefore this value is used for the uncertainty. Solar tracking errors are not considered in this calculation as they are expected to be of much lower magnitude than the variation of the solar zenith angle over the measurement duration. Spectroscopic line parameters include the line intensity, temperature-broadened half-width and pressure-broadened half-width errors. These values are obtained directly from the reported uncertainties of the linelists used in the retrieval and when no uncertainty is specified, a value of 20% is assumed. Line parameter errors are summarized in Table 3.3. The temperature uncertainties are determined by comparison of the daily NCEP temperature profiles to Eureka radiosonde measurements. The average difference is taken as the systematic error and the standard deviation is the random uncertainty. For altitudes above the maximum altitude of the radiosondes (∼30 km), the reported NCEP temperature uncertainties are used. The temperature uncertainties are summarized in Table 3.4. The retrieval harmonization for CO also included the harmonization of the error budget, and the error budget of CO is common amongst all sites. The uncertainty values used for CO are summarized in Table 3.5.

Table 3.4: Temperature uncertainties used for Eureka FTIR retrievals. For layer centres at 50.70 km or above, the uncertainties are constant at the values indicated.

Layer Centre [km]	Systematic Uncertainty [K]	Random Uncertainty [K]
113.00 - 50.70	1.00	9.00
46.68	1.00	7.00
43.19	1.00	7.00
40.17	1.00	7.00
37.56	1.00	6.00
35.29	1.00	6.00
33.30	1.00	5.00
31.53	1.00	5.00
29.92	1.04	1.30
28.40	1.08	1.37
26.94	1.04	1.36
25.52	0.84	1.11
24.13	0.74	0.90
22.77	0.65	0.81
21.45	0.61	0.76
20.17	0.60	0.68
18.93	0.60	0.71
17.72	0.58	0.69
16.54	0.50	0.62
15.40	0.52	0.64
14.30	0.50	0.63
13.24	0.49	0.65
12.21	0.61	0.79
11.21	0.75	1.21
10.25	0.81	1.44
9.33	1.07	1.45
8.45	1.10	1.10
7.61	0.80	1.08
6.80	0.79	0.96
6.03	0.78	0.96
5.30	0.74	0.95
4.61	0.76	0.98
3.95	0.85	1.10
3.33	0.88	1.16
2.75	0.92	1.22
2.21	1.04	1.38
1.70	1.04	1.33
1.24	1.25	1.54
0.81	1.60	1.95

Table 3.5: Specified error budgets for the harmonized CO error analysis.

Solar zenith angle[a]	Random	0.06°
	Systematic	0.001°
Temperature	Inter-layer correlation	2 km
	Grid	-0.02 4 6 10 13 25 40 120 km
	Random	2 2 4 4 2 3 6 1 K
	Systematic	1 1 1 2 2 2 4 5 K
Apodization function	Random	5.0 %
	Systematic	5.0 %
Field of View	Random	0.1 %
	Systematic	0.1 %
SZA	Random	0.5 %
	Systematic	0.1 %
Phase Function	Random	0.1 %
	Systematic	0.1 %
Curvature	Random	0.1 %
	Systematic	0.1 %
Zero level shift	Random	1.0 %
	Systematic	1.0 %
CO line intensity	Systematic	2.0 %
H_2O line intensity	Systematic	15 %
CO line pressure-broadening	Systematic	5.0 %
H_2O line pressure-broadening	Systematic	5.0 %
CO line temperature-broadening	Systematic	5.0 %
H_2O line temperature-broadening	Systematic	5.0 %

[a] SZA uncertainty was modified from the harmonized relative uncertainty to an absolute uncertainty due to the high SZA of measurements at Eureka.

3.10 Quality Assurance

Quality assurance is a trade-off between maintaining data quality and omitting data, and is a necessary final step in the data processing to remove erroneous outliers in the dataset. Filtering data based on column or profile amounts may seem reasonable; however, outliers in these quantities may occur as a result of natural processes such as episodic emissions from biomass burning events. Instead, it is preferable to use diagnostic quantities that are indicative of the validity of the spectral fit. The RMS residual of the fit is indicative of the goodness-of-fit for the fitted microwindows. Larger RMS values are often associated with poor quality spectra with low SNR. Additionally, greater RMS residual values may also indicate problematic fits such as the interfering species not being adequately accounted for in the retrieval. Another diagnostic quantity is the retrieved DOFS of the target species. Typically, DOFS are inversely related to the RMS residual, with greater DOFS obtained for low RMS residuals. Additionally, DOFS and RMS have opposing seasonal cycles, with greatest DOFS occurring at the beginning and end of the year due to the longer slant paths through the atmosphere. In contrast, RMS residuals have lower values as a result of the lower SNR and greater contribution of the interfering species during these periods.

The quality assurance is performed based on the method of Sussmann et al. (2011) in which the RMS/DOFS ratio is used as the filtering criteria. For the reasons stated above, the RMS/DOFS ratio should remain constant throughout the year. Poor quality spectra would result in larger RMS values and smaller DOFS, therefore resulting in larger RMS/DOFS values. The value of the RMS/DOFS threshold is determined by a trade-off curve of the number of measurements filtered as described by Sussmann et al. (2011). The values selected for these species are summarized in Table 3.6.

Table 3.6: RMS/DOFS thresholds for quality assurance of Eureka FTIR retrievals.

Species	RMS/DOFS Threshold
CO	2.5
HCN	0.22
C_2H_6	1.5
C_2H_2	2.0
CH_3OH	5.0
HCOOH	4.0
NH_3	3.5

Chapter 4

The 2014 Northwest Territories Wildfires

4.1 Introduction

This chapter summarizes the results of a case study of the 2014 Northwest Territories wildfires with a focus on the first long-term measurements (2006-2014) of NH_3 in the high Arctic using the ground-based Eureka FTIR. The results of this study have been published as: Long-range transport of NH_3, CO, HCN and C_2H_6 from the 2014 Canadian Wildfires, *Geophys. Res. Lett.*, 2016 (Lutsch et al., 2016).

Two FTIR instruments at Eureka, Nunavut and Toronto, Ontario were used to detect transported NH_3 emissions from the 2014 Northwest Territories fires. The location of the fire source near Great Slave Lake (61.67°N, 114.00°W) is approximately 2300 km and 3100 km from Eureka and Toronto, respectively. NH_3 was measured at both sites, with detection of total column enhancements 2-5 times the background during the burning period. Simultaneous enhancements of CO, HCN and C_2H_6 on the order of 1.5-2 times the background were also observed, providing further indication of long-range transport of fire emissions. The spatial separation between sites and differences in travel times of the smoke plume also allowed for an NH_3 lifetime of approximately 48 hours to be estimated. The enhancements at Eureka confirm the possibility of long-range transport of NH_3 and suggest that boreal fires may be a significant episodic source of NH_3 in the summertime Arctic.

The FTIR retrievals of CO, HCN, C_2H_6 and NH_3 from Eureka FTIR measurements were described in detail in Chapter 3. An analogous method was adapted for retrievals of NH_3 from solar-absorption spectra measured using the University of Toronto Atmospheric Observatory (TAO) ABB Bomem DA8 in Toronto. Toronto NH_3 retrievals are also published in Dammers et al. (2016) and Dammers et al. (2017). Retrievals of CO, HCN and C_2H_6 are standard NDACC FTIR products and therefore the Toronto retrievals were performed following the standard NDACC IRWG guidelines and recommendations as discussed in Chapter 3.

4.2 Results & Discussion

4.2.1 FTIR Time Series

The total column time series for CO, HCN, C_2H_6 and NH_3 at Eureka and Toronto are shown in Figure 4.1. All years (2006-2014 for Eureka and 2002-2014 for Toronto) are shown in grey, while 2014 measurements are highlighted in red for Eureka and blue for Toronto. The maximum monthly-mean CO total columns are observed in March at Eureka (2.07×10^{18} molec cm^{-2}) and April at Toronto (2.41×10^{18} molec cm^{-2}). Minimum monthly-mean total columns are observed in September at Eureka (1.59×10^{18} molec cm^{-2}) and Toronto (1.85×10^{18} molec cm^{-2}). The main sources of CO are fossil-fuel combustion and oxidation of volatile organic compounds (VOCs) and CH_4, as well as biomass burning emissions (Holloway et al., 2000). The primary sink of CO is oxidation by hydroxyl (OH), which contributes to the seasonal cycle of CO at both sites. Larger total columns of CO are observed for Toronto due to nearby anthropogenic sources.

Transport of CO from mid-latitudes also contributes to the seasonal cycle at Eureka, while transported biomass burning emissions are observed in the summer months.

Maximum monthly mean total columns of HCN are observed in August at Eureka (6.80×10^{15} molec cm^{-2}) and July at Toronto (6.79×10^{15} molec cm^{-2}). Since HCN is relatively inactive, it serves as a good tracer of biomass burning (Rinsland et al., 2001). Additional sources are the result of emissions from plants, bacteria and fungi due to increased vegetative activity in the springtime (Cicerone and Zellner, 1983). The lifetime of HCN in the troposphere is approximately 5 months (Li et al., 2003), with main sinks due to OH and O(^{1}D) reaction (Cicerone and Zellner, 1983) and ocean uptake (Li et al., 2003). Large variability of HCN is observed in the summer months at Eureka corresponding to the boreal fire season from May-August (Macias Fauria and Johnson, 2008). Particularly large fire events in Russia during July 2008 and August 2010 are observed in the time series (Viatte et al., 2013, 2015) in addition to the 2014 Northwest Territories fires.

The sources of C_2H_6 are natural gas and fossil fuel emissions (Singh and Zimmerman, 1992) in addition to biomass burning, while its main sink is reaction with OH. The seasonal cycle of C_2H_6 is similar to that of CO due to their common sources and sinks. Maximum monthly-mean total columns are observed in March at Eureka (2.67×10^{16} molec cm^{-2}) and February at Toronto (2.97×10^{16} molec cm^{-2}) with minima in August at Eureka (1.2×10^{16} molec cm^{-2}) and Toronto (1.49×10^{16} molec cm^{-2}). Both CO and C_2H_6 have relatively long atmospheric lifetimes at 52 days (Daniel and Solomon, 1998) and 80 days (Xiao et al., 2008), respectively.

The time series of NH_3 at Eureka and Toronto show maximum monthly-mean total columns in the summer months (2.79×10^{14} molec cm^{-2} in July at Eureka 9.80×10^{15} molec cm^{-2} in May at Toronto) as a result of its biogenic sources, biomass burning and agricultural emissions. The lower abundance of NH_3 at Eureka is due to its isolation from nearby sources. However, as discussed previously in Chapter 1, seabird colonies

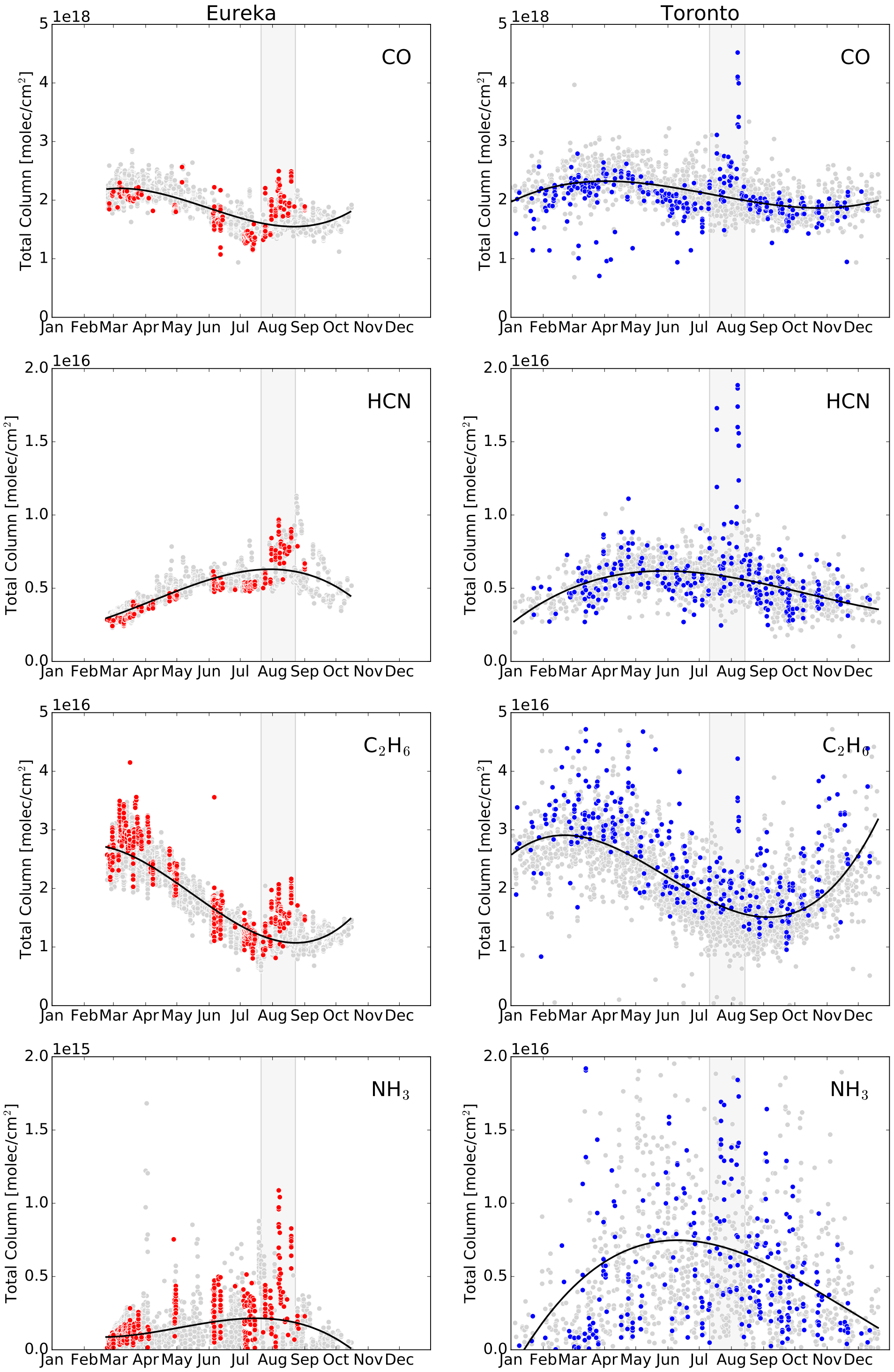

Figure 4.1: Total column time series of CO, HCN, C_2H_6 and NH_3 for Eureka (left, 2006-2014) and Toronto (right, 2002-2014). All years are shown in grey, while 2014 is highlighted. The grey vertical bar indicates periods of fire-affected measurements in 2014 (25 July to 22 August for Eureka and 11 July to 13 August for Toronto). The black line represents a polynomial fit to the data for all years.

are a considerable source of NH_3 in the Arctic (Wentworth et al., 2016). For both sites, NH_3 is highly variable due to its short lifetime and its emissions being rather episodic in nature. For both Eureka and Toronto, large enhancements of NH_3 are observed in July and August 2014 due to boreal wildfires in the Northwest Territories as shown in Section 4.2.2.

4.2.2 Source Attribution

Enhancements in the time series of each species were first identified by measurements with a total column greater than a 3σ standard deviation from the monthly mean from all measurements including enhancements, taken over all years. By this criterion, three main enhancements were found for each site in July and August 2014. The first initial detection for Eureka occurred on 25 July 2014 (14:40 UTC) which corresponds to the maximum CO total column measured on that day. Two later enhancements were also detected at Eureka on 7 August 2014 (17:20 UTC) and 19 August 2014 (19:15 UTC). Similarly, the initial enhancement at Toronto was found to have occurred on 11 July 2014 (14:09 UTC) with two later maxima on 18 July 2014 (19:05 UTC) and 7 August 2014 (17:20 UTC).

To determine the source of the observed enhancements, the FLEXPART (Stohl et al., 2005) Lagrangian dispersion model was used. Backward-dispersion runs were initialized by releasing an ensemble of 60,000 air-tracer particles over a 6 hr period about the observed peak enhancement for CO. The particles were released from the surface to an altitude of 10 km over a $3^\circ \times 3^\circ$ box centered on each site. This box was selected to capture the full spatial extent of the plume which may cover a large area around each site. The model was run backwards in time for 7 days driven by meteorological data from the NCEP Climate Forecast System (CFS V2) 6-hr product (Saha et al., 2011). The FLEXPART model was run for each of the three peak enhancements observed at both sites.

The sensitivity of the measurement to various source regions is proportional to the residence time of the air-tracer particles. The FLEXPART sensitivities are shown in Figure 4.2 for both sites. The Moderate Resolution Imaging Spectroradiometer (MODIS) Active Fire data (Giglio et al., 2006) provide the locations of active fires as shown in Figure 4.2. The FIRMS (Fire Resource Management System, https://earthdata.nasa.gov/earth-observation-data/near-real-time/firms/active-fire-data) fire product was used, where the plotted points correspond to fire detections with a confidence ratio of 0.75 or greater. For all FLEXPART backward runs, sensitivity to the Northwest Territories fires is observed. The initial enhancements on 25 July 2014 for Eureka and 11 July 2014 for Toronto show the least sensitivity to these fires, while the greatest sensitivity is observed in the 7 August 2014 FLEXPART runs for both sites, which is consistent with the largest enhancements observed at that time.

4.2.3 Trace Gas Correlations

The enhancement ratio (EnhR) is used to quantify emissions from biomass burning events for periods of fire-affected measurements. Fire-affected measurements were first classified as those with total column amounts greater than a 1σ standard deviation from the monthly-mean over all years. The 1σ standard deviation was used to capture all fire-affected measurements in addition to the peak enhancements detected with the 3σ standard deviation described in Section 4.2.2. Since each species was retrieved in a different spectral region measured using optical filters, the enhancement ratio was limited to measurements occurring within 1 hr of a CO measurement, where each CO measurement was only used once in the correlation. The correlations of HCN, C_2H_6 and NH_3 with CO for Eureka and Toronto are shown in Figure 4.3. The coloured points represent fire-affected measurements from 25 July to 22 August 2014 for Eureka (red) and 11 July to 13 August 2014 for Toronto (blue). For C_2H_6, there is a linear trend for all measurements

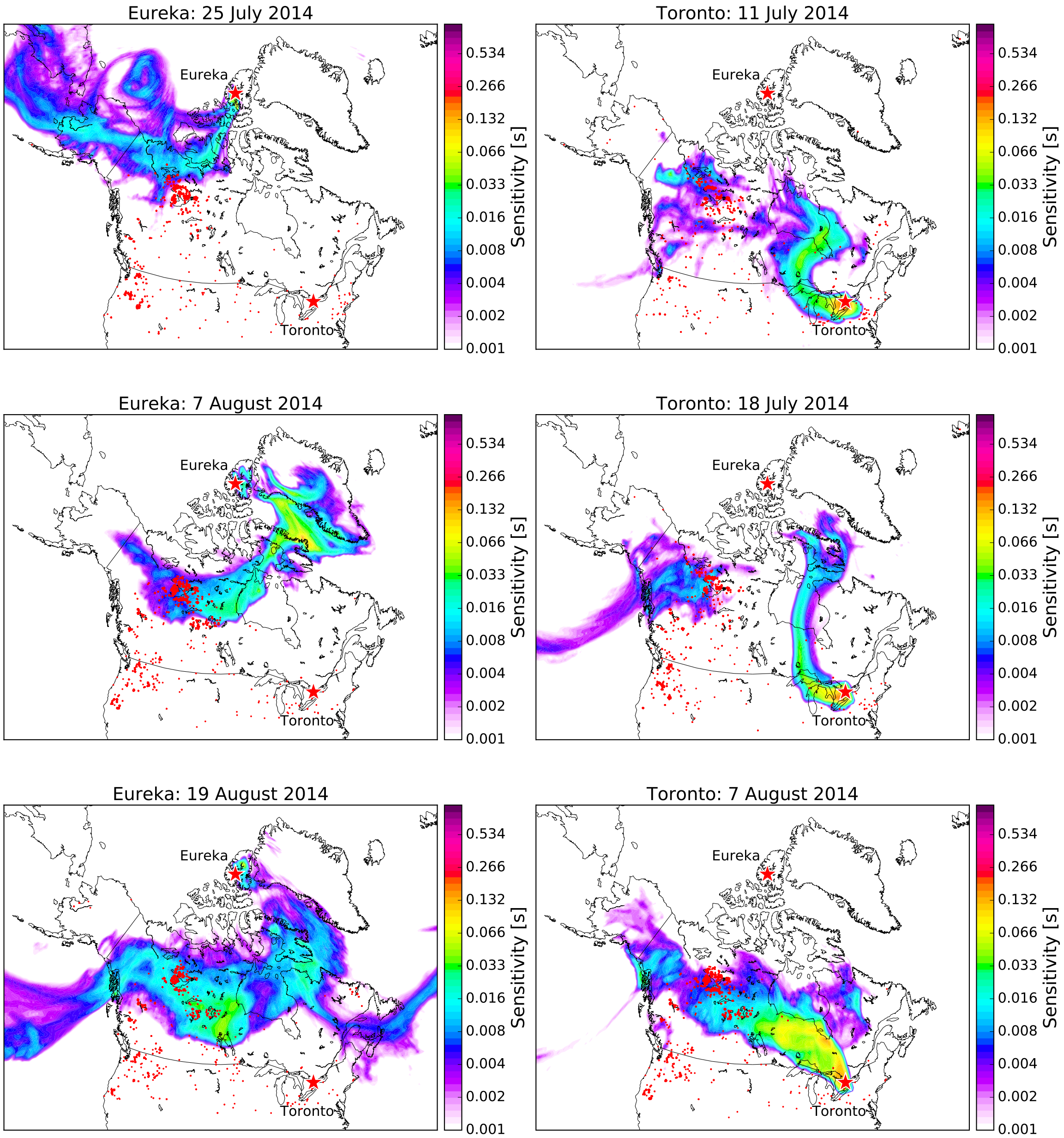

Eureka: 25 July 2014

Toronto: 11 July 2014

Eureka: 7 August 2014

Toronto: 18 July 2014

Eureka: 19 August 2014

Toronto: 7 August 2014

Figure 4.2: FLEXPART backward dispersion runs showing the total column sensitivity. MODIS fire hotspots are shown in red for 7 days prior to the release time. Particle release times for each panel correspond to the main CO enhancements observed at each site. Each panel represents a single FLEXPART model run, run backwards in time for 7 days starting at the initial particle release.

as a result of the similar seasonal cycles of CO and C_2H_6. No trend is observed for HCN and NH_3 with CO due to their differing seasonal cycles.

The unified least-squares procedure of York et al. (2004), which accounts for errors in both the ordinal and abscissa coordinates, was used to determine a linear regression for the fire-affected measurements. The result of the linear regression is shown as the dashed line in Figure 4.3, the slope of which is the enhancement ratio of the target species. The uncertainty of the enhancement ratio is the standard error of the slope given by York et al. (2004). There is generally a good correlation with CO for HCN and C_2H_6 with correlation coefficients ranging from 0.70 to 0.93. For NH_3, the correlation coefficient is 0.70 for Eureka and 0.45 for Toronto. The lower correlation for Toronto NH_3 measurements is likely due to the variability of the total column amounts of NH_3 due to nearby agricultural and anthropogenic sources.

Since measurements are made at a distance from the fire source, the measured smoke plumes have experienced aging, resulting in some loss of each species. Aging of the plume is accounted for by calculation of the emission ratio (ER) at the fire source assuming a first-order loss of each species. The emission ratio is defined by:

$$\mathrm{ER}_X = \mathrm{EnhR}_X \cdot \frac{\exp\left(\frac{t}{\tau_X}\right)}{\exp\left(\frac{t}{\tau_{CO}}\right)}, \tag{4.1}$$

where τ_X is the lifetime of the species and t is the travel-time. Lifetimes for CO, HCN and C_2H_6 were chosen to be 30, 75 and 45 days respectively following Viatte et al. (2015), which were determined by model comparisons to FTIR measurements. The travel times to each site were determined by HYbrid Single-Particle Lagrangian Integrated Trajectory (HYSPLIT, Stein et al., 2015; Rolph, 2016) back-trajectories. For each of the three peak CO enhancements at each site described in Section 4.2.2, the HYSPLIT model was run backwards in time for 10 days. For each HYSPLIT model run, three trajectory altitudes between 3-10 km were used. The start time of each model run was adjusted to

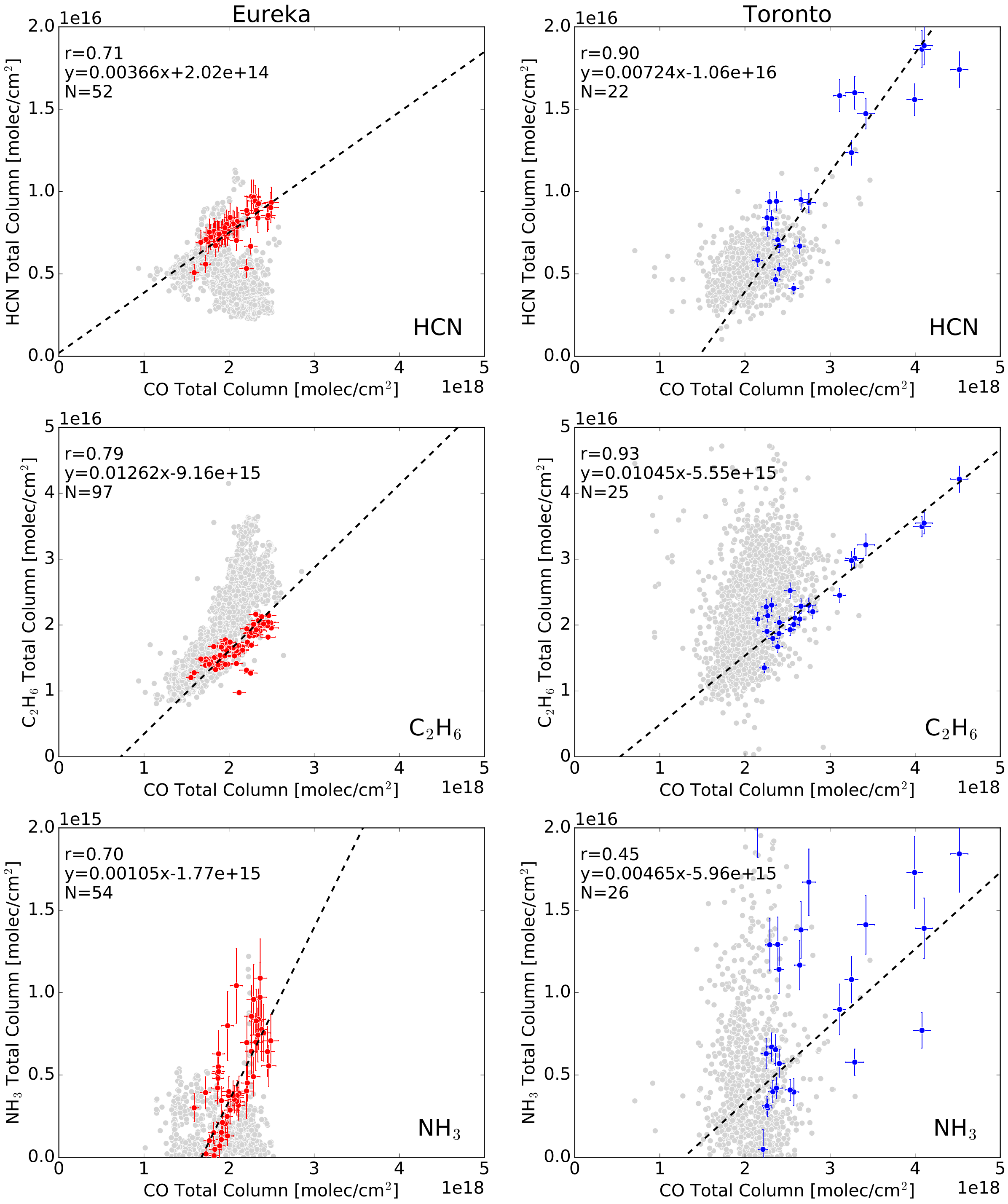

Figure 4.3: Enhancement ratios for HCN, C_2H_6 and NH_3 for fire-affected measurements (25 July - 22 August 2014 for Eureka in red and 11 July - 13 August for Toronto in blue). The grey points represent all other measurements from 2006-2014 for Eureka and 2002-2014 for Toronto. The correlation coefficient r, linear equation of the fit, and number of fire-affected measurements are shown. Error bars correspond to the retrieval uncertainties for the respective species.

within 2 hr of the observed peak CO enhancement while the trajectory altitudes were also adjusted in order to provide back-trajectories that were consistent with the fire source regions identified by the FLEXPART model runs and MODIS fire data. From the three HYSPLIT model runs for each site, an average travel time was found to be 6 days for Eureka and 3 days for Toronto, with a standard deviation of 2 days and 1 day for Eureka and Toronto, respectively. The average travel times and standard deviation were determined from the three HYSPLIT runs over the three trajectory altitudes. The emission ratios were calculated using these travel times and are shown in Table 4.1.

Because the travel time is dependent on the meteorological conditions along the trajectory of the smoke plume, it is difficult to account for variations in the travel time during the period of fire-affected measurements. For the long-lived species CO, HCN and C_2H_6, the variability of the travel times is small compared to the lifetime of each species. It was found that the variability in the emission ratios for HCN and C_2H_6 due to the estimated variability of the travel times was within the uncertainties due to the enhancement ratios. For NH_3, the assumed lifetimes vary from 12-48 hr and are comparable to the estimated travel times. Assuming this range of NH_3 lifetimes, the emission ratios were found to vary over several orders of magnitude for a single travel time. The variability of the emission ratio due to the estimated variability of the travel times for a single NH_3 lifetime was within this range. It was therefore concluded that the lifetime of NH_3 was the dominant source of uncertainty on the emission ratio. For these reasons, we have chosen the enhancement ratio uncertainty as the predominant uncertainty in the calculation of the emission ratio for all species.

For HCN, the emission ratios differ between Eureka (0.0037 ± 0.0005) and Toronto (0.0072 ± 0.0003), with a relative difference of approximately 82%, while a relative difference of 7% is found for the emission ratios of C_2H_6 at Eureka (0.0109 ± 0.0004) and Toronto (0.0101 ± 0.0005). The large difference in the HCN emission ratios suggests additional sources of HCN were present for Toronto. This is evident in the FLEXPART

Table 4.1: Comparison of calculated enhancement ratios, emission ratios and emission factors for HCN, C_2H_6 and NH_3 at Eureka and Toronto. The values in parentheses denote the reported uncertainties.

				Eureka			**Toronto**		
Species	Source	Platform	EF_{CO} [g kg^{-1}]	EnhR	ER	EF [g kg^{-1}]	EnhR	ER	EF [g kg^{-1}]
HCN	This Study	Ground-based	127 (45)[a]	0.0037 (0.0005)	0.0032 (0.0005)	0.40 (0.15)	0.0072 (0.0003)	0.0068 (0.0003)	0.84 (0.30)
	Akagi et al. (2011)	Compilation	127 (45)	–	–	1.52 (0.81)	–	–	1.52 (0.81)
	Andreae and Merlet (2001)[b]	Compilation	107 (37)	–	–	0.81	–	–	0.81
	Viatte et al. (2015)[c]	Ground-based	127 (45)	–	0.0034 (0.0009)	0.36 (0.17)	–	0.0034 (0.0009)	0.36 (0.17)
	Goode et al. (2000)[d]	Aircraft	88.8	–	0.0069	0.61	–	0.0069	61
	Simpson et al. (2011)[e]	Aircraft	112 (72)	–	0.0082 (0.0002)	0.89 (0.29)	–	0.0082 (0.0002)	0.89 (0.29)
	Rinsland et al. (2007)	Satellite	86 (17)	–	0.0024 (0.0003)	0.20 (0.05)	–	0.0024 (0.0003)	0.20 (0.05)
	Tereszchuk et al. (2013)	Satellite	–	–	0.0027 (0.0018)	–	–	0.0027 (0.0018)	–
Species	Source	Platform	EF_{CO} [g kg^{-1}]	EnhR	ER	EF [g kg^{-1}]	EnhR	ER	EF [g kg^{-1}]
C_2H_6	This Study	Ground-based	127 (45)[a]	0.0126 (0.0005)	0.0118 (0.0005)	1.61 (0.57)	0.0104 (0.0005)	0.0101 (0.0005)	1.38 (0.49)
	Akagi et al. (2011)	Compilation	127 (45)	–	–	1.42 (0.43)	–	–	1.42 (0.43)
	Andreae and Merlet (2001)[b]	Compilation	107 (37)	–	–	0.60 (0.15)	–	–	0.60 (0.15)
	Viatte et al. (2015)[c]	Ground-based	127 (45)	–	0.0096 (0.0031)	1.09 (0.74)	–	0.0096 (0.0031)	1.09 (0.74)‘
	Nance et al. (1993)[f]	Aircraft	81 (12)	–	0.0073 (0.0031)	0.66 (0.35)	–	0.0073 (0.0031)	0.66 (0.35)
	Goode et al. (2000)[d]	Aircraft	88.8	–	0.0073	0.66	–	0.0073	0.66
	Simpson et al. (2011)[e]	Aircraft	112 (72)	–	0.0046 (0.0009)	0.56 (0.13)	–	0.0046 (0.0009)	0.56 (0.13)
	Rinsland et al. (2007)[f]	Satellite	86 (17)	–	0.0098 (0.0008)	0.91 (0.19)	–	0.0098 (0.0008)	0.91 (0.19)
	Tereszchuk et al. (2013)[f]	Satellite	–	–	0.0069 (0.0023)	–	–	0.0069 (0.0023)	–
Species	Source	Platform	EF_{CO} [g kg^{-1}]	EnhR	ER	EF [g kg^{-1}]	EnhR	ER	EF [g kg^{-1}]
NH_3	This Study (τ=36 hr)	Ground-based	127 (45)[a]	0.0011 (0.0001)	0.0471 (0.0039)	3.64 (1.32)	0.0047 (0.0004)	0.0311 (0.0029)	2.40 (0.88)
	This Study (τ=48 hrs)	Ground-based	127 (45)[a]	0.0011 (0.0001)	0.0173 (0.0014)	1.34 (0.49)	0.0047 (0.0004)	0.0189 (0.0018)	1.46 (0.53)
	Akagi et al. (2011)	Compilation	127 (45)	–	–	2.72 (2.32)	–	–	2.72 (2.32)
	Andreae and Merlet (2001)[b]	Compilation	107 (37)	–	–	1.40 (0.80)	–	–	1.40 (0.80)
	Nance et al. (1993)[d]	Aircraft	81 (12)	–	0.0130 (0.0050)	0.64 (0.31)	–	0.0130 (0.0050)	0.64 (0.31)
	Goode et al. (2000)[d]	Aircraft	88.8	–	0.0158	0.86	–	0.0158	0.86
	Alvarado et al. (2011)[g]	Satellite	–	–	0.0100 (0.0050)	–	–	0.0100 (0.0050)	–
	R'Honi et al. (2013)[h]	Satellite	–	–	0.0310	–	–	0.0310	–

[a] EF_{CO} for boreal forests from Akagi et al. (2011) used for conversion of ER to EF.

[b] Values reported for extratropical forests.

[c] Ground-based FTIR measurements at Eureka, Nunavut.

[d] Measurements from Alaskan fires.

[e] Measurements from Canadian fires.

[f] ACE-FTS observations from Canadian and Alaskan fires.

[g] TES observations from Canadian and Alaskan fires.

[h] Average value from IASI observations of the 2010 Russian fires.

sensitivities of Figure 4.2. For each FLEXPART run for Toronto, considerable sensitivity to Northern Ontario and the Great Lakes region of Canada and the United States was observed. In addition, the emission ratios of HCN are an order of magnitude lower than those of C_2H_6 and the influence of additional sources is likely amplified.

Since NH_3 is short-lived, plume aging has a significant effect on the measured enhancement ratio. To determine the emission ratios, four lifetimes for NH_3 were chosen: 12, 24, 36 and 48 hrs. The 12, 24 and 36 hr lifetimes were chosen following Whitburn et al. (2015) from Dentener and Crutzen (1994), Aneja et al. (2001), and R'Honi et al. (2013) respectively. The 12 hr and 24 hr NH_3 lifetimes yielded large emission ratios ($\sim$10-100) and differed by an order of magnitude between sites. For this reason, these lifetimes were omitted from further analysis and it was inferred that the NH_3 lifetime must be considerably longer. Agreement was found assuming a 36 hr lifetime with emission ratios of 0.0471 ± 0.0039 and 0.0311 ± 0.0029 for Eureka and Toronto respectively. The best agreement was found assuming a 48 hr lifetime, which yielded emission ratios of 0.0173 ± 0.0014 and 0.0189 ± 0.0018 for Eureka and Toronto respectively.

The assumption of a 48 hr NH_3 lifetime is supported by comparison of the emission ratios to previously published values. Emission ratios for NH_3 of 0.0130 ± 0.0050 and 0.0158 were reported by Nance et al. (1993) and Goode et al. (2000), obtained from aircraft-based measurements of emissions from Canadian and Alaskan fires. The NH_3 emission ratio determined from TES observations of Canadian and Alaskan fires was 0.0100 ± 0.0050 (Alvarado et al., 2011). Using observations of the 2010 Russian fires from IASI, R'Honi et al. (2013) reported average NH_3 emission ratios ranging from 0.010 to 0.052. Our emission ratios are slightly larger than the values from aircraft and TES observations but agree with the lower limit from R'Honi et al. (2013). Since the 2010 Russian fires included peatland burning (Konovalov et al., 2011) in addition to boreal forest, the larger NH_3 emission ratios from R'Honi et al. (2013) are likely due to peatland burning.

The good agreement of the emission ratios of NH_3 between both sites and previous literature values assuming a 48 hr lifetime suggests that the NH_3 lifetime is enhanced within a smoke plume. Bi-directional exchange of NH_3 between the atmosphere and the surface has been noted to increase NH_3 atmospheric concentrations and lifetimes (Zhu et al., 2015). However, the effects of bi-directional exchange are limited to the boundary layer and are of a different order of magnitude compared to the column enhancements due to transported biomass burning plumes. NH_3 may react rapidly with acidic gases to form ammonium particles (Hertel et al., 2012), which could then be transported over large distances with lifetimes of 1-15 days (Karlsson et al., 2013), therefore extending the spatial extent over which ammonia may be deposited. However, the abundance of other reactive trace gases and pre-existing aerosol loads in a fire plume remain poorly known. It is possible that aerosol-gas exchange of NH_3 may extend the lifetime and long-range transport of NH_3 in a fire plume, although the magnitude of these effects are highly uncertain.

4.2.4 Emission Factors

Trace gas emissions from biomass burning are characterized by the emission factor. The emission factor is defined by (Andreae and Merlet, 2001):

$$\mathrm{EF_X} = \mathrm{ER_X} \cdot \left(\frac{\mathrm{MW_X}}{\mathrm{MW_{CO}}}\right) \cdot \mathrm{EF_{CO}}, \tag{4.2}$$

where MW is the molecular weight. To convert our emission ratios to equivalent emission factors, the emission factor of CO from Akagi et al. (2011) was used, which is based on a compilation of studies for boreal forest fuel types. Both Akagi et al. (2011) and Andreae and Merlet (2001) report emission factors for HCN, C_2H_6 and NH_3 that can be compared to our calculated values (see Table 4.1). The values reported in Andreae and Merlet (2001) correspond to an extratropical fuel type that is a combination of boreal and temperate forests. Literature values for emission ratios and emission factors for boreal forests derived from ground-based, aircraft and satellite platforms are also included in Table 4.1.

The emission factor for CO of 127 ± 45 g kg^{-1} from Akagi et al. (2011) was used here to convert our calculated emission ratios to emission factors. As a result, differences in emission factors between sites are due to the same differences in the emission ratios discussed in Section 4.2.3. For HCN, our emission factor for Eureka (0.40 ± 0.13 g kg^{-1}) is smaller than the compilation studies (Akagi et al. (2011) and Andreae and Merlet (2001)) and the aircraft based studies (Goode et al. (2000) and Simpson et al. (2011)) but agrees within the combined uncertainties with the ground-based (Viatte et al., 2015) and satellite (Rinsland et al., 2007) studies. Similarly, our emission factor for C_2H_6 and those determined by ground-based (Viatte et al., 2015) and satellite platforms (Rinsland et al., 2007) are generally larger than those from aircraft studies (Nance et al., 1993 and Goode et al., 2000). For NH_3 with a lifetime of 48 hrs, our emission factors agree within the uncertainties with the compilation studies (Andreae and Merlet (2001) and Akagi et al. (2011)), but are larger than the aircraft-based studies of Nance et al. (1993) and Goode et al. (2000). These differences are likely to be the result of lower emission factors of CO reported by Nance et al. (1993) and Goode et al. (2000) since the emission ratios of NH_3 were found to agree as stated in Section 4.2.3.

4.3 Conclusions

The first long-term measurements of NH_3 in the Canadian Arctic have been presented here. Total columns of CO, HCN, C_2H_6 and NH_3 were measured by ground-based FTIR spectrometers at Eureka, Nunavut and Toronto, Ontario. Emission ratios for HCN, C_2H_6 and NH_3 with respect to CO were determined for both sites. The observed NH_3 enhancements at Eureka indicate that the 2014 Northwest Territories fires were a considerable episodic source of NH_3 to the Canadian Arctic. Simultaneous enhancements of CO, HCN and C_2H_6 at Eureka, along with FLEXPART sensitivity runs, provided confirmation that the detected NH_3 enhancements originated from the Northwest Territories fires. Detection of simultaneous enhancements of all species at Toronto further demonstrated the long-range transport of NH_3 emissions from these fires. The consistency of the emission ratios for HCN, C_2H_6 and NH_3 with respect to CO between the two sites and compared to literature values, particularly for NH_3 with a estimated lifetime of 48 hrs, provides further confidence in these observations.

Chapter 5

The 2017 British Columbia and Northwest Territories Wildfires

5.1 Introduction

This chapter summarizes the results of a case study of the 2017 British Columbia and Northwest Territories wildfires. The work presented is published as: Unprecedented ammonia concentrations detected in the high Arctic from the 2017 Canadian wildfires, *J. Geophys. Res.: Atmos.*, 2019 (Lutsch et al., 2019).

In this chapter, we examine two separate wildfire events in British Columbia (BC) and the Northwest Territories (NWT) of Canada in August 2017. We aim to quantify the influence of transported NH_3 emissions from these events to the Arctic with the use of FTIR measurements at two high-Arctic sites: Eureka, Nunavut, and Thule, Greenland. The simultaneous influence of the BC and NWT wildfires resulted in the greatest observed enhancements of NH_3 in the decade-long time series at both Eureka (2006-2017) and Thule (1999-2017). The exceptional magnitude of these enhancements was due to the intensity of both the BC and NWT wildfires, which resulted in volcano-like injection of smoke throughout the troposphere and lower stratosphere (Khaykin et al., 2018; Peterson et al., 2018). The record-setting magnitude of the 2017 BC wildfires, with over 1.2 million ha burned (BC Wildfire Service, 2017), was the result of persistent warm temperatures and increased wildfire risk made substantially greater by anthropogenic climate change (Kirchmeier-Young et al., 2019). Given the extreme magnitude of this event, these wildfires present an opportunity to investigate the influence of wildfire NH_3 emissions on the Canadian high Arctic. The exceptional magnitude of transported NH_3 emissions from the 2017 BC and NWT wildfires may serve as a harbinger of future events as wildfire frequency and intensity are expected to increase in the future (Flannigan et al., 2009; Wotton et al., 2010; Boulanger et al., 2014; Wotton et al., 2017).

5.2 Methods

5.2.1 FTIR Retrievals

Full details of the Eureka FTIR retrievals are given in Chapter 3 and are summarized here. For Eureka and Thule, retrievals of CO, HCN and C_2H_6 are performed following NDACC IRWG recommendations. For both sites, retrievals of NH_3 were performed following the procedure presented in Chapter 3.

For all retrievals, a full error analysis was performed following Rodgers (2000). The retrieval uncertainties include forward model parameter error and measurement noise error. Adding these in quadrature, average uncertainties for the retrieved total columns of CO, HCN, C_2H_6 and NH_3 are 5.4%, 4.6%, 4.2%, and 30.2%, respectively, for Eureka and 2.6%, 6.9%, 1.6%, and 12.5%, respectively, for Thule. The average DOFS for CO, HCN, C_2H_6 and NH_3 are 2.0, 2.4, 1.7, and 1.0, respectively, for Eureka and 3.0, 3.5, 1.7, and 1.1, respectively, for Thule. For CO, HCN and C_2H_6, the total column averaging kernels show peak values in the upper troposphere at both sites, whereas the total column averaging kernels of NH_3 peak near the surface and decrease upwards to 5 km. The shape of the total column averaging kernel profiles is due to the vertical distribution of the species, which follows a similar structure to the a priori profile. The minimum retrieved total columns of NH_3 are on the order of $\sim 10^{14}$ molec cm^{-2} in clear-sky conditions, which corresponds to NH_3 surface concentrations of ∼0.1-0.3 ppbv. The surface concentration is estimated as the retrieved volume mixing ratio of the lowest level in the FTIR retrieval grid. The ambient concentrations of CO, HCN, and C_2H_6 exceed the detection limits of the FTIR instrument under normal clear-sky conditions.

5.2.2 IASI Observations

We use CO and NH_3 total column abundances retrieved from observations by the IASI instrument on board the Metop-A satellite. The satellite has a polar sun-synchronous orbit providing twice daily global coverage at 9:30 local time and 21:30 local time overpasses. The instrument has a scan swath width of approximately 2200 km and observations have a circular footprint of approximately 12 km in diameter at nadir (Clerbaux et al., 2009). We used the most recent CO and NH_3 data products (`http://iasi.aeris-data.fr/`). For CO, the FORLI-CO product (Hurtmans et al., 2012) was used, which has been validated against ground-based FTIR measurements and found to show good agreement with no significant bias (Kerzenmacher et al., 2012). For NH_3, we use the latest ANNI-NH_3-v2.1 product (Van Damme et al., 2017). The current ANNI-NH_3-v2.1 version has not yet been compared to FTIR measurements, although the previous version, v1 (Whitburn et al., 2016), was validated using ground-based FTIR observations by Dammers et al. (2016, 2017). IASI has been found to underestimate NH_3 total columns by an average of ∼32% in comparison to FTIR observations. Greater underestimation (>50%) was observed for FTIR sites with low NH_3 total columns ($<5\times10^{15}$ molec cm^{-2}), and IASI showed better agreement (∼22%) for FTIR sites with greater local NH_3 total columns. The underestimation of IASI is the result of the dependence of the retrieval on the NH_3 concentration and the thermal contrast at the surface. For instance, Van Damme et al. (2014, 2015a) estimated a detection limit of 9.68×10^{15} molec cm^{-2} for a thermal contrast of 20 K, while a thermal contrast of 10 K corresponds to a detection limit of 1.69×10^{16} molec cm^{-2}. An approximate 3 ppbv surface-layer NH_3 concentration was estimated as an average detection limit of IASI, although in an NH_3 plume with well-mixed concentrations in a thick boundary layer, the detection limit could be as low as 1 ppbv at the surface with sufficient thermal contrast (Clarisse et al., 2010).

5.2.3 GEOS-Chem Chemical Transport Model

The GEOS-Chem CTM (`www.geos-chem.org`), version v11.01, was used at a horizontal resolution of $2° \times 2.5°$ with 47 vertical hybrid levels from the surface to 0.01 hPa in altitude. The model is driven with assimilated meteorological fields from the Goddard Earth Observing System version 5.11.0 (GEOS-FP) from the NASA Global Model and Assimilation Office (GMAO). For each simulation, an eight-month model spin-up was performed from 1 January to 1 August 2017. Transport and chemical operator time steps of 10 min and 20 min, respectively, were chosen to minimize simulation errors (Philip et al., 2016). Global anthropogenic emissions are provided by the Emissions for Database for Global Atmospheric Research (EDGARv4.3.1; Janssens-Maenhout et al. (2013)) emissions inventory. Global anthropogenic and natural NH_3 emissions are provided by Bouwman et al. (1997). Biomass burning emissions from the Global Fire Assimilation System (GFASv1.2; Kaiser et al. (2012)) are used. GFAS provides global emissions for open fires on a $0.1°\times0.1°$ grid at 3-hourly resolution, which are derived from assimilation of fire radiative power (FRP) observations of the Moderate Resolution Imaging Spectroradiometer (MODIS) on the Aqua and Terra satellites. The use of the GFAS emission inventory was chosen based on the availability of emissions for the 2017 period compared to the Global Fire Emission Database (GFEDv4), and the better representation of boreal North American emissions in comparison to the Fire Inventory from NCAR (FINNv1.0) (Shi et al., 2015). Seabird-colony NH_3 emissions based on Riddick et al. (2012) were also included to investigate the contribution of seabird-colony NH_3 emissions in the Arctic.

Emissions were considered for seabird colonies located north of 50°N following Wentworth et al. (2016) and Croft et al. (2016b).

Surface emissions in GEOS-Chem v11.01, including biomass burning emissions, are released within the boundary layer, and boundary layer mixing is implemented using the non-local mixing scheme of Holtslag and Boville (1993). Simulated aerosol species include sulfate-nitrate-ammonium (Park et al., 2004, 2006), with the sulfate-nitrate-ammonium chemistry based on the ISORROPIA II thermodynamic model (Fountoukis and Nenes, 2007), which partitions ammonia and nitric acid between the gas and aerosol phases. Dry deposition in GEOS-Chem is implemented following a standard resistance in series scheme (Wesely, 1989), with surface resistances for sulfate, nitrate and ammonium aerosols as described by Zhang et al. (2001). Wet removal takes place in large-scale clouds and convective updrafts (Liu et al., 2001).

5.3 Results & Discussion

5.3.1 FTIR Time Series

The time series of CO, HCN, C_2H_6 and NH_3 total columns for Eureka and Thule are shown in Figure 5.1. For CO and C_2H_6, similar seasonal cycles, with a maximum in February and March and a minimum in the summer months, July and August, are observed as a result of the common anthropogenic source of these species from fossil fuel combustion and their main sink due to reaction with OH (Stein and Rudolph, 2007; Xiao et al., 2008). During the polar night, OH formation ceases and transport of pollutants from mid-latitude regions (Klonecki, 2003; Stohl et al., 2006; Shindell et al., 2008) allows CO and C_2H_6 to accumulate in the Arctic atmosphere. Decreasing total columns are observed throughout the spring and summer as a result of increased loss due to the production of OH during the sunlit season. Average lifetimes of CO and C_2H_6 are approximately 2 months (Singh and Zimmerman, 1992) and 3 months (Xiao et al., 2008) respectively, making them suitable tracers of long-range transport.

The seasonal cycles of HCN and NH_3 are opposite in phase to those of CO and C_2H_6 as result of their different sources. The primary source of HCN is biomass burning, but plant and fungal emissions also represent considerable sources (Li et al., 2003). Due to its long atmospheric lifetime of ~2-4 months (Li et al., 2000), HCN tends to accumulate in the atmosphere. Its main loss is a result of dry deposition to the ocean (Li et al., 2003) and reaction with OH and $O^1(D)$ (Cicerone and Zellner, 1983). For NH_3, the main source in the Arctic is from the hydrolysis of migratory seabird-colony guano (Blackall et al., 2007; Riddick et al., 2012; Wentworth et al., 2016), while wildfires may present a considerable episodic source as shown in Chapter 4. As a result, the seasonal cycle of NH_3 shows a summer maximum at both sites, due to the presence of migratory seabirds and the influence of tundra and wildfire NH_3 emissions. However, the relative contributions of these sources have not yet been quantified on a multi-year time scale.

For the long-lived species CO, HCN and C_2H_6, the seasonal amplitudes are similar between Eureka and Thule as these species are well mixed in the troposphere. For NH_3, the mean total columns in the peak summer months are over a factor of two greater at Thule than Eureka. Due to the short lifetime of gas-phase NH_3, on the order of a few hours to a day, the transport of NH_3 surface emissions to the free troposphere is limited (Adams et al., 2019). The Eureka FTIR is located at an altitude of 610 m a.s.l., whereas the Thule instrument is at 210 m a.s.l., and consequently the Thule measurements are more sensitive to the influence of surface emissions. Additionally, large seabird colonies have been identified on the western coast of Greenland (Circumpolar Seabird Data Portal, 2018) and would likely contribute to the greater NH_3 total columns at Thule.

For CO, HCN, and C_2H_6, enhanced total columns are periodically observed in May to September at Eureka and Thule, corresponding to the boreal wildfire season (Macias Fauria and Johnson, 2008). While enhancements of CO, HCN, and C_2H_6 due to

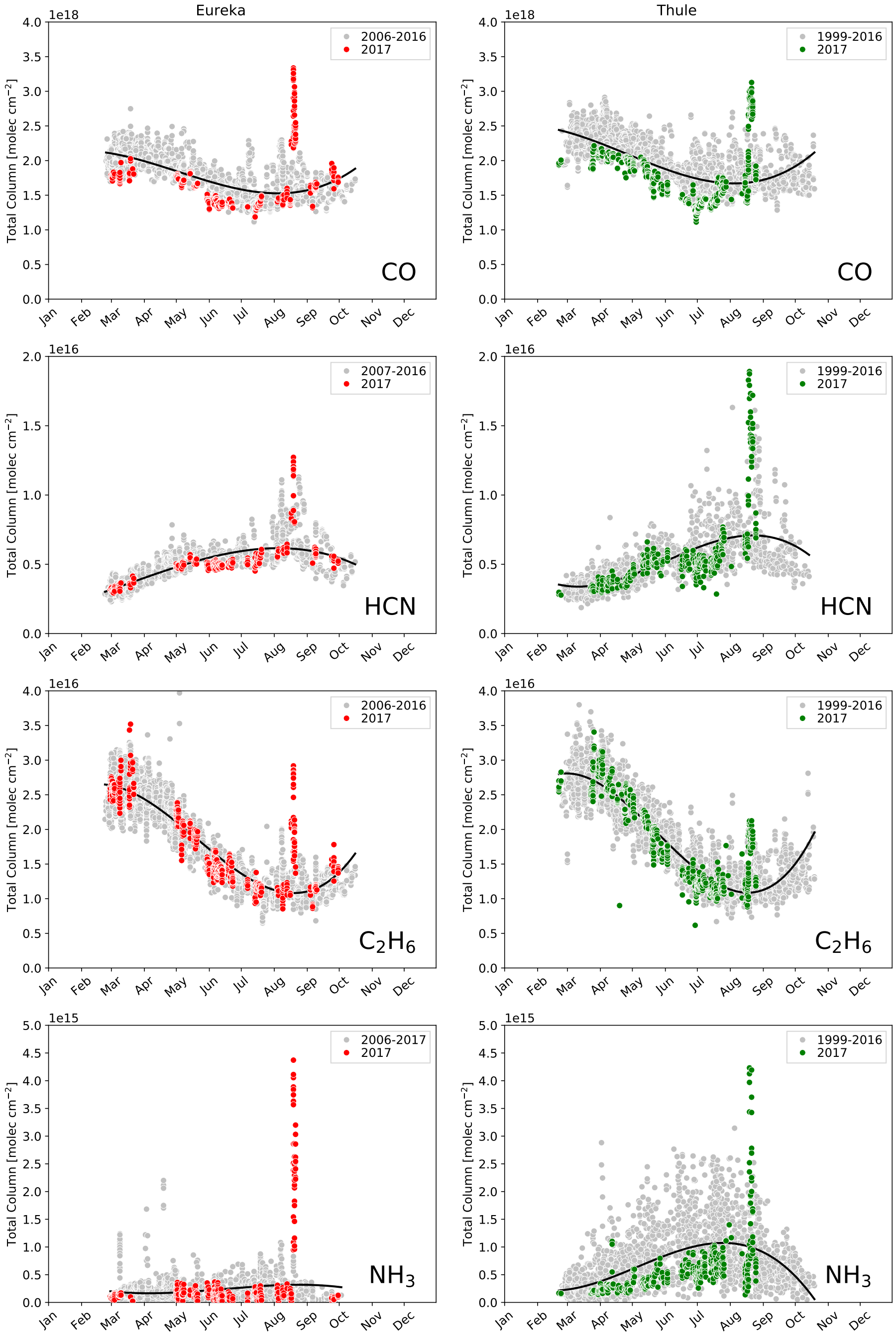

Figure 5.1: Total column time series of CO, HCN, C_2H_6, and NH_3 for Eureka (left, 2006-2017) and Thule (right, 1999-2017). The colored points indicate measurements taken in 2017, while all other years are shown in grey. The black line indicates a third-order polynomial fit to all measurements.

wildfire emissions are observed annually (Viatte et al., 2015), the only clear case of NH_3 wildfire emissions in the past was observed in July to August 2014 from the NWT wildfires as was presented in Chapter 4. However, this does not take into account possible missed events due to instrument downtime or non-clear sky conditions preventing measurements. For all species, the 2017 Canadian wildfires in BC and NWT resulted in the greatest observed enhancements in the entire time series at both sites, which were on the order of 2-5 times their ambient concentrations. The source attributions for the observed enhancements due to wildfire emissions for the 2017 events are discussed in the following section.

5.3.2 Source Attribution

The FLEXPART (Stohl et al., 2005) Lagrangian transport model is used to diagnose the sensitivity of FTIR measurements to source regions. Enhancements in the measured FTIR total columns are first identified by CO total columns that are a standard deviation of 1σ greater than the monthly mean taken over all years of measurements at each site. The identified CO enhancements then define the period of fire-affected measurements. The days of fire-affected measurements are 17, 19, 20, and 21 August 2017 for Eureka and 19, 20, 21, and 22 August 2017 for Thule. It should be noted that non-clear sky conditions prevented measurements on 18 August at Eureka and for several days after 21 and 22 August for Eureka and Thule, respectively. For each day of fire-affected measurements, FLEXPART simulations are initialized for every hour of measurements. The FLEXPART model was run backwards in time for 7 days, driven by meteorological data from the NCEP Climate CFS V2 6-hr product (Saha et al., 2011). For each FLEXPART simulation, an ensemble of 1000 air-tracer particles was released over a 1-hr period from the surface to an altitude of 10 km. This vertical region was chosen in order to capture the likely altitude of the plume and the range where the CO total column measurement sensitivity is the greatest (total column averaging kernels at both sites show values near 1).

The sensitivity of the measurements to various source regions, or the so-called potential emission sensitivity (PES, in units of seconds), is proportional to the residence time of the air-tracer particles. For each FLEXPART simulation, the sensitivity is considered for the following three cases:

(a) Residence time at the surface for all particles released in the tropospheric column (0-10 km);

(b) Residence time at the surface for particles released in the lower-tropospheric column (0-5 km);

(c) Residence time at the 5-km altitude surface for particles released in the upper-tropospheric column (5-10 km).

For (a), all particles released from the 0-10 km altitude range are considered and the residence time at the surface is given, therefore representing the tropospheric column sensitivity to surface emissions. For (b), the residence time at the surface of particles released in the lower troposphere (0-5 km) is considered and represents the lower-tropospheric column sensitivity to near-surface emissions. For (c), only particles released in the upper troposphere are considered (5-10 km) and the residence time at the 5 km altitude surface is therefore indicative of upper-tropospheric sensitivity to emissions injected into the upper troposphere. In all three cases, the residence time is reported at the lowest level of the altitude range considered.

The FLEXPART sensitivities are shown in Figures 5.2 and 5.3 for Eureka and Thule respectively. The MODIS Burned Area Product Collection 6 (Giglio et al., 2018) provides the locations of burned areas during the 7-day period of the FLEXPART simulation. It is seen in Figures 5.2 and 5.3 that sensitivity to fire-affected regions is observed for all days of fire-affected FTIR measurements at both sites; however, the lower and upper tropospheric sensitivity differ between measurement days as discussed below.

For Eureka on 17 August, the first day of fire-affected measurements, the FLEXPART PES for 0-10 km shows greatest sensitivity to the wildfires in the NWT and a number of smaller fires in the northwestern United States, and little sensitivity to the BC wildfires. A similar spatial distribution of the sensitivity is observed for the 0-5 km PES, although with no sensitivity to the NWT wildfires. For the 5-10 km PES, the sensitivity is primarily to the NWT wildfires, with no sensitivity to the other fire source regions. The difference in sensitivity between the 0-5 km and 5-10 km PES implies that enhancements originating from the BC wildfires are due to near-surface emissions, and those from the NWT wildfires are due to upper tropospheric injection of emissions. On 19 August, a similar spatial distribution is seen for the FLEXPART PES with some sensitivity observed to the BC wildfires and an eastward shift of the 0-5 km PES to the NWT fires. The FLEXPART PES on 17 and 19 August suggests that the main contribution to the enhanced total columns of all species measured at Eureka is emissions from the NWT wildfires, with upper tropospheric injection of emissions being predominant on 17 August and near-surface emissions on 19 August. For 20 and 21 August at Eureka, the FLEXPART PES is similar for the 0-10 km range, indicating sensitivity to both the BC and NWT wildfires on those two days. The main sensitivity to the BC wildfires is observed for the 5-10 km PES with some sensitivity observed for the 0-5 km PES. For the NWT wildfires, the sensitivities for the 0-5 km and 5-10 km PES are similar. On 20 and 21 August, the greater sensitivity to BC wildfires for the 5-10 km PES suggests that the enhancements observed at Eureka on these days are the likely result of the upper tropospheric injection of emissions from the BC wildfires.

For Thule, the FLEXPART PES of Figure 5.3 shows similar spatial patterns between the four fire-affected measurement days from 19-22 August. On 19 August, sensitivity to both the BC and NWT wildfires is observed, with the main contribution from the NWT

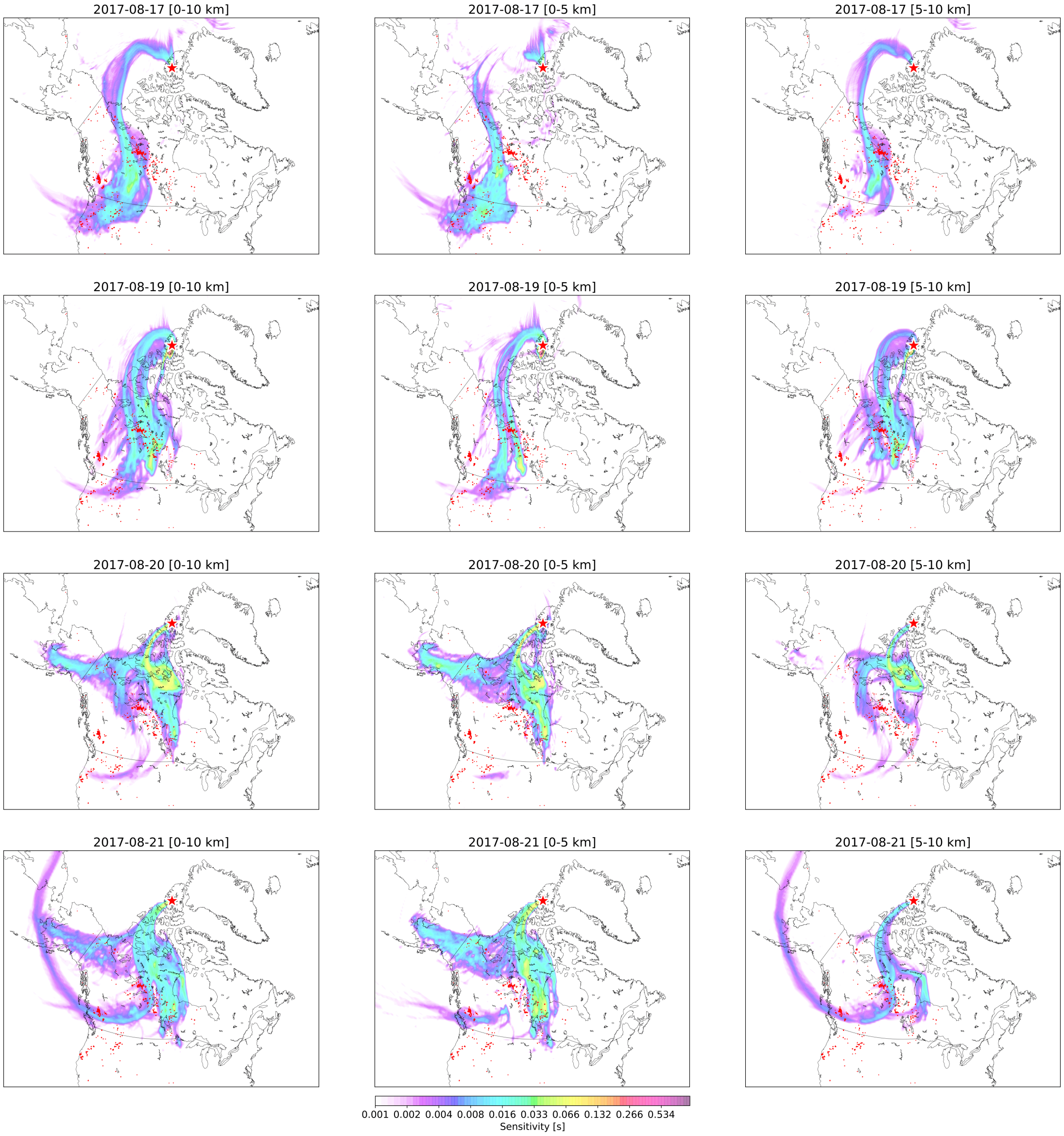

Figure 5.2: Typical FLEXPART sensitivity for Eureka on measurement days 17, 19, 20, and 21 August 2017. The red areas indicate MODIS burned areas for 7 days prior to the time of measurement and the location of the Eureka FTIR site is indicated by the red star. The vertical region (0-10 km, 0-5 km, and 5-10 km) indicates the vertical range of released particles.

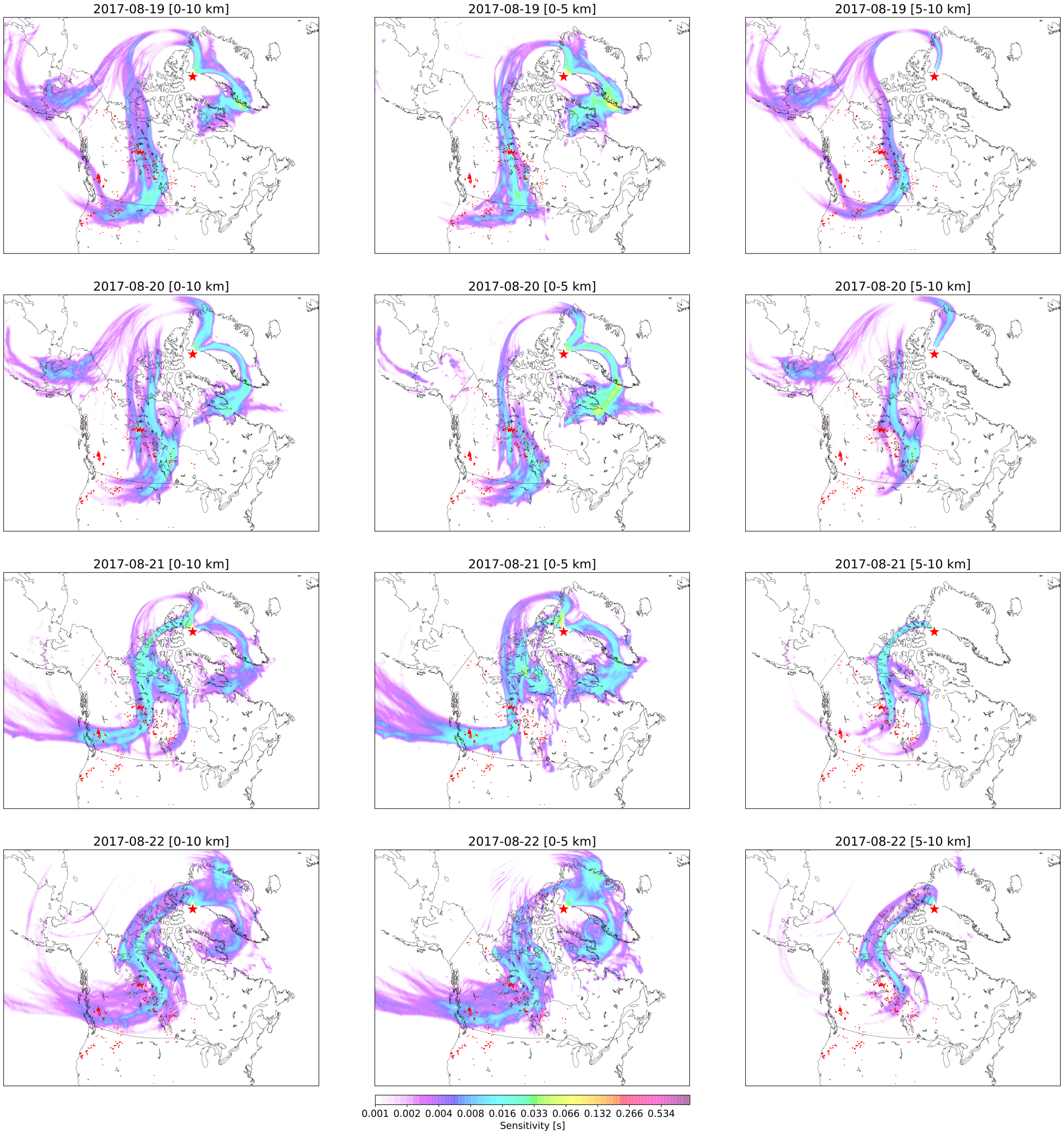

Figure 5.3: Same as Figure 5.2 but for Thule.

fires occurring in the 0-5 km range and the main contribution from the BC wildfires occurring in the 5-10 km range. For 20 August, the NWT wildfires are the primary contributors to the measured total column enhancements for both the 0-5 km and 5-10 km altitude ranges. For 21 and 22 August, the spatial distribution of the FLEXPART PES is dominated by the 0-5 km range, indicating sensitivity to surface emissions from both the BC and NWT wildfires.

5.3.3 Trace Gas Correlations

Since the FTIR measurements are made at distance from the fire source, the composition of the smoke plume is subject to physical and chemical processing. Therefore we present the enhancement ratio of each species with respect to CO (Lefer et al., 1994) rather than the emission ratio (Andreae and Merlet, 2001; Akagi et al., 2011). The enhancement ratio is related to the emission ratio, which quantifies emissions near the source without the influence of plume aging. Since measurements are made downwind of the fire source, we did not account for background concentrations in the calculation of the enhancement ratio, or the so-called excess mixing ratio, since ambient concentrations of all species are likely to vary greatly over large spatial scales. The varying background conditions and influence of mixing may therefore cause uncertainty in interpreting the excess enhancement ratio (Yokelson et al., 2013).

To calculate the enhancement ratio for each species, enhanced CO measurements are identified by a standard deviation of 1σ from the monthly mean of all measurements, including enhancements, taken over all years, as described in Section 5.3.2. The identified CO enhancements are then paired with the nearest measurement of the target species, HCN, C_2H_6, and NH_3 recorded within 1 hr, with each CO measurement only used once for each species. A 1-hr window was chosen in order to maximize the number of pairs for each species while being sufficiently short to minimize the effects of plume aging. In most cases, the differences in measurement times between each species and the paired CO measurement were within 20 min. The enhancement ratio (in units of molec cm^{-2}/molec cm^{-2}) is then defined as the slope of the linear correlation of the target species relative to CO. The unified least-squares procedure of York et al. (2004) was used to determine a linear regression for the fire-affected measurements. The results of the linear regression are shown in Figure 5.4 and tabulated in Table 5.1.

For the case of a smoke plume originating from a single source, it is expected that a strong linear correlation would be found for the enhancement ratio, even over several days of measurements. This is particularly true for the long-lived species HCN and C_2H_6, as the lifetimes of these species are much greater than the plume travel times, which are generally on the order of several days. A strong linear correlation was observed for the enhancement ratios of HCN and C_2H_6 at Eureka for the 2014 NWT fires as seen in Chapter 4 and similarly for the 2010 Russian fires (Viatte et al., 2013), with correlation coefficients (r) generally greater than 0.7 and in many cases greater than 0.85 for the enhancement ratios of HCN and C_2H_6 taken over one week or more of measurements. For the fire-affected measurements detected at Thule in August 2017, the linear correlations are generally weaker with correlation coefficients of 0.66 and 0.64 for HCN and C_2H_6, respectively, taken over four days of fire-affected measurements. For Eureka, stronger correlations are observed, with correlation coefficients of 0.96 and 0.83 for HCN and C_2H_6, respectively. The strong correlations at Eureka are the result of measurements predominately being recorded over one day for HCN and two days for C_2H_6, therefore minimizing the influence of the variability of emissions and transport between days. For the enhancement ratios of NH_3, Eureka show a much weaker linear correlation than Thule with correlation coefficients of 0.08 and 0.68, respectively.

To examine the influence of the variability of the source sensitivities presented in Section 5.3.2 on the measured concentration of each species, the enhancement ratio of each species was calculated for each day of fire-affected measurements. The results are summarized in Table 5.1. The enhancement ratio for each species was calculated only if

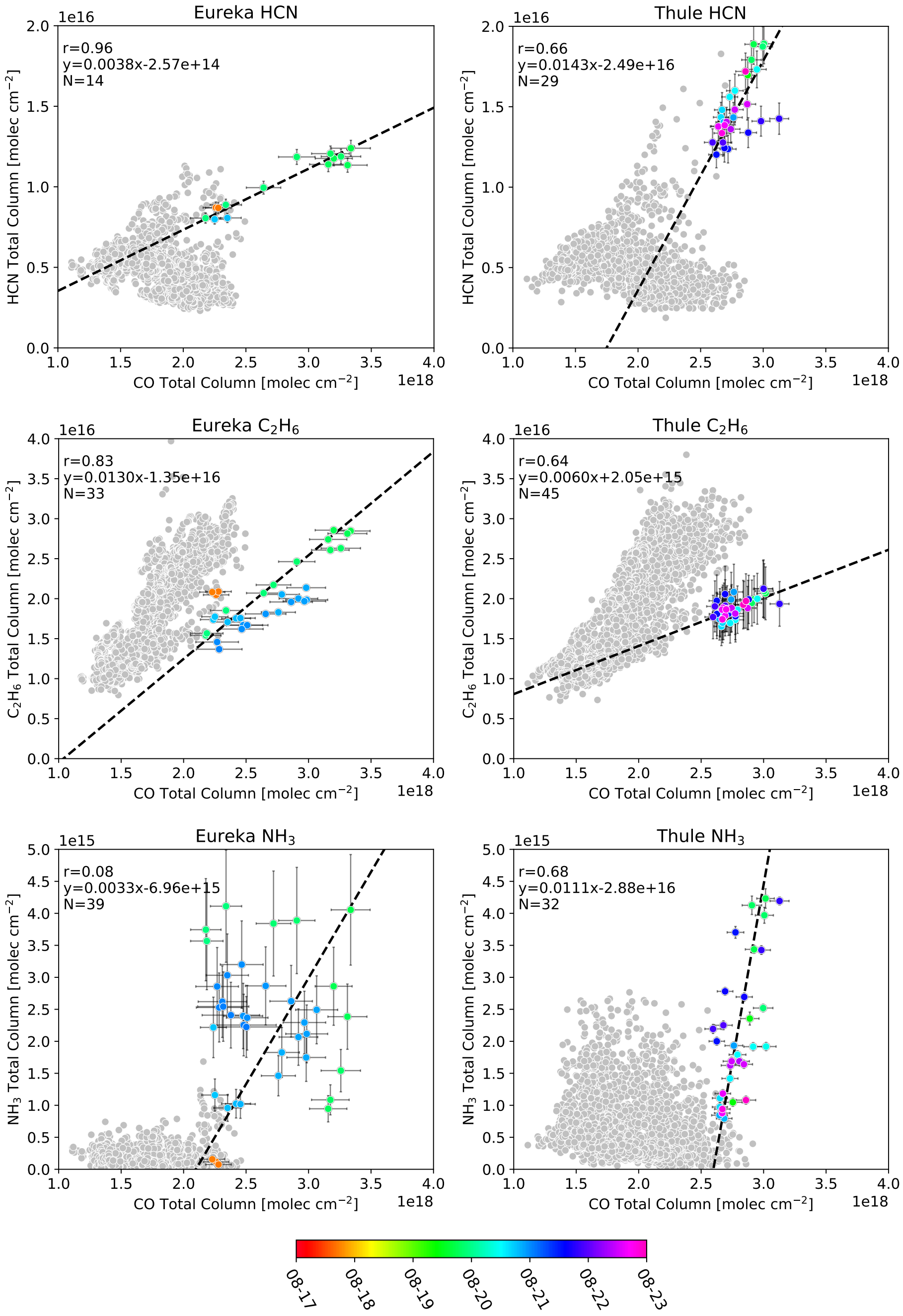

Figure 5.4: The enhancement ratios of HCN, C_2H_6 and NH_3 at Eureka and Thule. The grey points indicate all years of measurements. The colored points are measurements taken during the 2017 wildfire event where the colorbar represents the time of the measurement. The dashed black line is the linear-regression to the colored points. The number of measurements (N), linear equation and correlation coefficient (r) are also shown.

Table 5.1: Enhancement ratios (molec cm^{-2}/molec cm^{-2}) for HCN, C_2H_6, and NH_3 versus CO for each day of fire-affected measurements at Eureka and Thule. Enhancement ratios were only calculated for days with five or more measurements for the species of interest. For each enhancement ratio calculated, the number of measurements (N) and the linear correlation coefficient (r) are also shown. The uncertainty on the calculated enhancement ratios are indicated by the value in parentheses, given by the standard error of the slope of the linear regression.

		HCN			**C_2H_6**			**NH_3**		
Site	Date	N	r	EnhR	N	r	EnhR	N	r	EnhR
Eureka	2017-08-17	2	–	–	3	–	–	3	–	–
	2017-08-19	10	0.95	0.0036 (0.0005)	12	0.99	0.0113 (0.0011)	11	−0.56	−0.0033 (0.0004)
	2017-08-20	2	–	–	15	0.85	0.0059 (0.0009)	16	0.46	0.0018 (0.0004)
	2017-08-21	0	–	–	3	–	–	9	−0.25	−0.0021 (0.0019)
	All	14	0.96	0.0038 (0.0004)	33	0.83	0.0130 (0.0011)	39	0.08	0.0033 (0.0003)
Thule	2017-08-19	5	0.80	0.0147 (0.0147)	6	0.95	0.0133 (0.0253)	7	0.75	0.0164 (0.0069)
	2017-08-20	8	0.89	0.0122 (0.0054)	14	0.54	0.0084 (0.0100)	9	0.81	0.0048 (0.0012)
	2017-08-21	8	0.92	0.0041 (0.0019)	12	0.46	0.0033 (0.0054)	8	0.86	0.0050 (0.0009)
	2017-08-22	8	0.82	0.0137 (0.0063)	13	0.64	0.0051 (0.0109)	8	0.49	0.0080 (0.0047)
	All	29	0.66	0.0143 (0.0022)	45	0.64	0.0060 (0.0035)	32	0.68	0.0111 (0.0014)

the number of measurements paired with CO for that day was greater than or equal to 5. For Eureka, on 17 August, non-clear-sky conditions limited the number of measurements and therefore no enhancement ratios were calculated. On 19 August, the strongest linear correlations are found for HCN and C_2H_6 at Eureka, with correlation coefficients of 0.95 and 0.99, and a negative correlation for the NH_3 enhancement ratio with a correlation coefficient of -0.56. A negative correlation has no physical interpretation but is due to the large variability of NH_3 as a result of transformation to its particulate phase or loss by deposition. Enhancement ratios of 0.0036 ± 0.0005 and 0.0113 ± 0.0011 for HCN and C_2H_6, respectively, were found to be in agreement with the enhancement ratios for the 2014 NWT wildfires of 0.0037 ± 0.0005 for HCN and 0.0126 ± 0.0005 for C_2H_6 reported in Chapter 4. The agreement is consistent with the FLEXPART PES of Figure 5.2 on 19 August, which shows sensitivity to wildfires in a nearby region to those identified in Chapter 4, suggesting that a similar vegetation type was burned. The forest type for both the 2014 and 2017 NWT fires were classified as the Taiga Shield (Natural Resources Canada, 2013), consisting mainly of spruce trees, mosses and lichens (Beaudoin et al., 2014). In contrast, the 2017 BC wildfires corresponded to the Montane Cordillera forest type, which primarily consists of Douglas fir and Ponderosa pine (Ireland and Petropoulos, 2015). On 20 August, measurements of HCN were limited at Eureka and no HCN enhancement ratio could be determined. A strong linear correlation was found for the C_2H_6 enhancement ratio ($r = 0.85$) and a moderate linear correlation was found for NH_3 ($r = 0.46$). For 21 August, no enhancement ratios were found for HCN or C_2H_6, and the absence of a positive correlation was found for NH_3 with a poor correlation ($r = -0.25$).

The HCN enhancement ratios at Thule show strong linear correlations on individual measurement days, with correlation coefficients exceeding 0.80. The enhancement ratios of HCN at Thule are greater than at Eureka, likely due to the greater sensitivities to the BC wildfires (as shown in Figure 5.3) as compared to Eureka (shown in Figure 5.2).

Additionally, for Thule, the sensitivities of both the BC and NWT wildfires correspond to near surface emissions, commonly associated with smoldering combustion, which tends to have greater HCN emissions, while emissions of C_2H_6 tend to have less dependence on burning phase as it is produced in both smoldering and flaming combustion processes (Burling et al., 2010, 2011). For Thule, lower correlation coefficients of C_2H_6 enhancement ratios in comparison to those for HCN could also indicate that smoldering combustion was the dominant source of the smoke plume. However, the plume is likely a combination of both smoldering and flaming components that cannot be distinguished by ground-based measurements of this kind.

For Thule, the enhancement ratios of NH_3 illustrate positive linear correlations on all days; however, the enhancement ratios are quite variable between measurement days, with the greatest values (0.0164 ± 0.0069) measured on 19 August and a minimum (0.0048 ± 0.0012) on 20 August. The variability of NH_3 enhancement ratios at Thule is partly due to the differences in emission sensitivity between days, as shown in Figure 5.3, as is the variability of the enhancement ratios for longer lived HCN and C_2H_6. In addition, it was shown here that the enhancement ratios of HCN and NH_3 at Thule were on average greater than at Eureka. For the days of fire-affected measurements at both sites, Eureka was more predominantly influenced by emissions from the NWT wildfires, whereas for Thule, greater sensitivity was observed to the BC wildfires. It has been found that for wildfires in the northern Rocky Mountains of the United States, a region of similar vegetation type to BC, the modified combustion efficiency (MCE) of these fires was substantially lower than for other coniferous-dominated forest types (Urbanski, 2013). Lower MCE implies incomplete smoldering combustion (Ward and Hardy, 1991), resulting in greater emissions of reduced nitrogen compounds such as HCN and NH_3 (Burling et al., 2011). The MCE of a fire is dependent on the vegetation type, fuel load, moisture and meteorology, and therefore can be highly variable. Pyrolysis temperature has also been found to have a strong influence on the emissions of HCN and

NH_3, with greater emissions of HCN and NH_3 for high-temperature and low-temperature pyrolysis respectively (Sekimoto et al., 2018). It should be noted that Sekimoto et al. (2018) also found that low-temperature and high-temperature pyrolysis may not exactly correspond to smoldering and flaming combustion respectively, while emissions of HCN and NH_3 are similar for different fuel types. The fuel types studied were representative of Western United States ecosystems consisting mainly of pine and fir species. However, the combination of larger HCN and NH_3 enhancements at Thule in comparison to Eureka, and the greater surface sensitivity of Thule measurements to the BC wildfires suggests that smoldering phase emissions from these fires were the dominant contribution to the measured enhancements at Thule. For Eureka, the comparison of the enhancement ratios in Table 5.1 and the FLEXPART sensitivities shown in Figure 5.3 suggest that the NWT wildfires were the main contribution for enhanced total columns of all species at Eureka for 17 and 19 August, and a combination of both the BC and NWT wildfires for 20 and 21 August.

5.3.4 GEOS-Chem Comparison to FTIR Measurements

Due to the scarcity of NH_3 measurements at the low concentrations often observed in the high Arctic, it is difficult to investigate the large-scale influence of wildfire NH_3. The use of a chemical transport model allows for transported emissions of NH_3 to the Arctic to be simulated and therefore provides estimates of both surface and total column NH_3 concentrations in high Arctic regions. The FTIR measurements provide a means of evaluating model performance in the high Arctic. As a result of its long lifetime, atmospheric CO acts a tracer of wildfire emissions and is relatively unaffected by chemical aging during transport over several days. It therefore serves as a diagnostic of model transport and emissions. In contrast, NH_3 is short-lived and is strongly influenced by model chemistry and removal processes.

Comparisons of GEOS-Chem modeled CO and NH_3 total columns were performed as follows. The GEOS-Chem partial column profiles were smoothed by the FTIR total column averaging kernel using the following equation (Rodgers, 2000):

$$\hat{x}_m = x_a + \mathbf{a}^T \left(\mathbf{x}_m - \mathbf{x}_a \right), \tag{5.1}$$

where T denotes the transpose, $\hat{x}_m$ is the smoothed model total column, x_a is the FTIR a priori total column, $\mathbf{x}_m$ is the model partial column profile, $\mathbf{a}$ is the FTIR total column averaging kernel, and $\mathbf{x}_a$ is the FTIR a priori partial column profile. Smoothing removes biases due to the a priori profile and limited vertical sensitivity of the FTIR measurement and therefore allows the model total column to be treated as if it were measured using the ground-based FTIR instrument. For each GEOS-Chem model output timestep, the profile was interpolated onto the FTIR vertical grid and smoothed by the mean FTIR total column averaging kernel taken over all years for the respective species and site. The smoothed GEOS-Chem total columns for CO and NH_3 at Eureka and Thule are shown in Figures 5.5 and 5.6, respectively, for the following three simulation scenarios:

1. Fire emissions only;
2. Seabird-colony NH_3 emissions only;
3. Fire and seabird-colony NH_3 emissions.

Scenario (1) allows for the contributions of wildfire emissions of NH_3 to the Arctic to be examined, whereas scenario (2) is representative of background concentrations of NH_3 in the Arctic due to the persistent influence of local seabird-colony NH_3 emissions during the warm season. The inclusion of both seabird-colony and fire emissions of scenario (3) represents the real-world case. It should be noted that inclusion of seabird-colony NH_3 emissions in the model has little influence on CO, as seen in Figures 5.5 and 5.6. Gas-phase NH_3 concentrations do not necessarily respond linearly to additional NH_3

emissions. This non-linearity is because NH_3 partitioning to particulate NH_4^+ is sensitive to the amount of available sulfuric and nitric acid. The overall increase in CO of scenarios (1) and (3) in comparison to the seabird-only case of scenario (2) illustrates the influence of accumulation of CO in the atmosphere from global biomass burning sources.

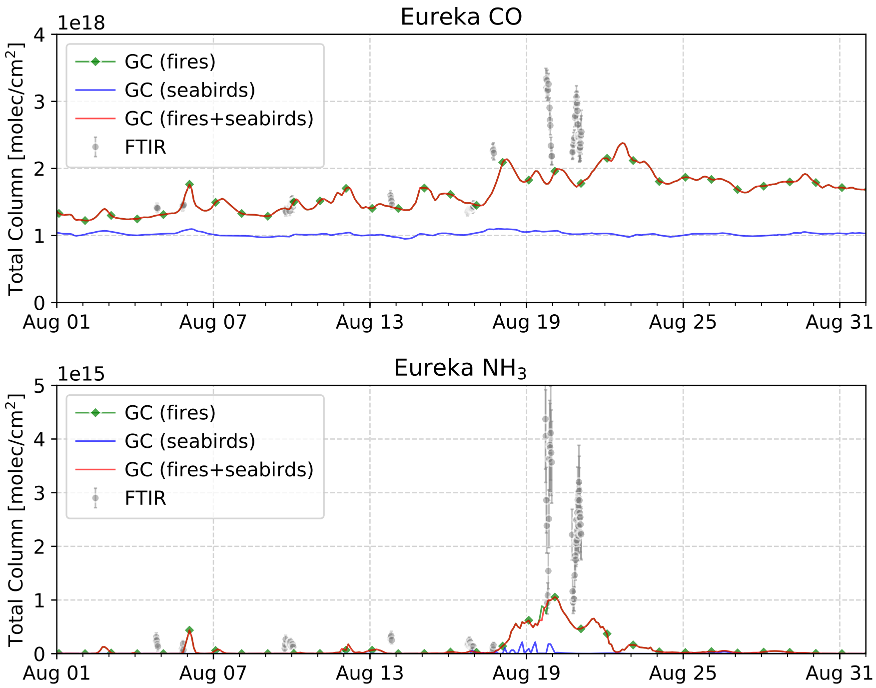

Figure 5.5: Smoothed GEOS-Chem CO (top) and NH_3 (bottom) total column time series for the month of August 2017. The three GEOS-Chem simulation scenarios are shown: fire emission only (green), seabird-colony NH_3 emissions only (blue), and fire and seabird emissions (red). FTIR measurements are shown in grey along with their associated measurement uncertainties represented by the error bars.

In Figure 5.5, there is some indication that GEOS-Chem captures the influence of the wildfire emissions during the period of enhanced FTIR measurements from 17-21 August, although the model is underestimating the magnitude of the enhancements. For Thule, as shown in Figure 5.6, wildfire enhancements of CO observed in the FTIR measurements are well captured by the model. As discussed in Section 5.3.2, Thule was predominantly influenced by the smoke plume originating from the BC wildfires, whereas these wildfires had a lesser influence at Eureka. As will be shown in the following sections, the GFAS emissions appear to underestimate the magnitude of the NWT plume in comparison to IASI measurements, resulting in the underestimation of modeled CO emissions at Eureka. In contrast, the plume originating from the BC wildfires shows better agreement between the model and IASI CO measurements.

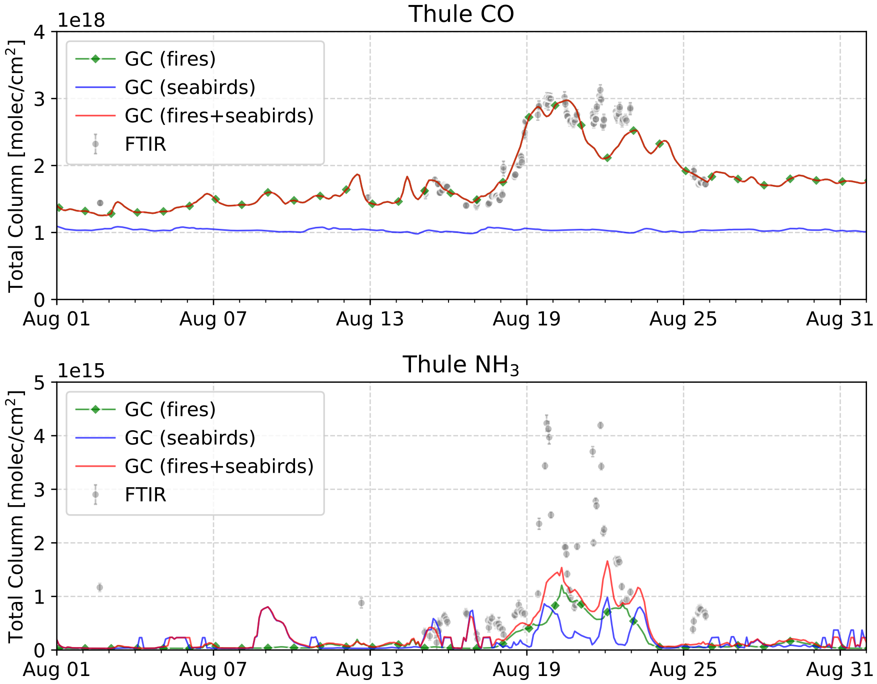

Figure 5.6: Same as Figure 5.5 but for Thule.

The GEOS-Chem NH_3 simulation shows an underestimation in all three cases in comparison to the FTIR measurements at both sites. For Eureka, as shown in Figure 5.5, there is little influence of seabird-colony NH_3 emissions and therefore, GEOS-Chem NH_3 at Eureka is attributed to transported wildfire emissions. For Thule, as shown in Figure 5.6, the inclusion of both seabird-colony NH_3 and fire emissions most accurately represents the FTIR measurements. It is also seen in Figure 5.6 that the influence of seabird-colony and wildfire NH_3 appear to occur simultaneously; this is a result of the wind direction, transporting both seabird-colony and wildfire emissions from north of Thule.

It has been found that the bi-directional exchange of NH_3 may extend the spatial influence of NH_3 emission sources (Zhu et al., 2015; Whaley et al., 2018), but it was not included in the model simulations here. However, the locations of the seabird colonies are primarily in coastal regions, while the Arctic Ocean has been found to be a net sink of NH_3 (Wentworth et al., 2016). Therefore, transport of NH_3 from the larger seabird colonies of the Greenland coast to the Canadian Archipelago by bi-directional exchange processes would be limited. The influence of bi-directional exchange could likely be of greater importance for wildfire NH_3. The deposition of wildfire NH_3 would increase the nitrogen pool at the surface, which may be released at later times, thereby prolonging the influence of wildfire NH_3. Tundra emissions may also be a considerable source of NH_3 in the Arctic that was not considered here. Croft et al. (2019) reported an upper estimate of tundra NH_3 emissions, which was approximately 1.5 times the contribution from seabird-colony sources in the Canadian Archipelago. Tundra NH_3 emissions are highly uncertain but inclusion of these emissions in model simulations would likely increase background NH_3 concentrations as found by Croft et al. (2019).

The general underestimation of both CO and NH_3 at Eureka and Thule, and the inability of the model to capture the magnitude of the enhancements, is possibly a result of underestimation of modelled emissions and the assumption of boundary layer emissions in GEOS-Chem that may not be realistic in many cases as wildfire emissions are often injected into the free troposphere (Turquety et al., 2007; Val Martin et al., 2010). Once injected into the free troposphere, transport patterns are likely to differ from the surface. Additionally, the loss processes may differ in the free troposphere, particularly for the short-lived NH_3, which is subject to loss by wet and dry deposition and chemical loss. Injection of NH_3 into the free troposphere could favour the production of NH_4^+ due to colder temperatures, and with sufficient quantities of nitrate (NO_3^-) and nitric acid (HNO_3), could also promote the production of ammonium nitrate (NH_4HNO_3). Loss of NH_3 by dry and wet deposition may also be limited due to the reduced turbulent diffusion and drier conditions of the free troposphere. Global models also tend to suffer from numerical diffusion errors (Rastigejev et al., 2010; Eastham and Jacob, 2017) as a result of the coarse vertical and horizontal resolution. Underestimation of plume transport due to numerical diffusion is, however, likely to be of minor importance in comparison to the lack of realistic wildfire emission injection heights.

5.3.5 GEOS-Chem Comparison to IASI Measurements

To investigate the influence of possible transport and emissions errors in the GEOS-Chem model, a qualitative comparison of GEOS-Chem CO and NH_3 from the fire-only scenario to measurements from IASI was performed over the entire domain of Canada and Greenland, from 40°N, 180°W to 86°N, 15°E. For comparison of the GEOS-Chem model to IASI observations, the following method was applied. For each day, the GEOS-Chem model output was interpolated to the overpass time of each individual IASI observations and each IASI observation was gridded onto the $2° \times 2.5°$ GEOS-Chem horizontal grid. The interpolated GEOS-Chem total columns and gridded IASI total columns were then daily averaged over the entire spatial domain. The results are shown in Figures 5.7 and 5.8 for CO and NH_3, respectively, for selected days during the simulation period.

The results are shown for four days from 10 August 2017, corresponding to the initial start of the fire plume, until 23 August 2017, when measurements at Eureka and Thule both return to ambient levels. On 10 August, the initial plume is observed to have originated in BC in the lower-left of the domain of Figure 5.7. From the comparison of IASI to GEOS-Chem CO in Figure 5.7, it is seen that the spatial distribution of the fire source is well represented by the model using the GFAS emission inventory, although the model tends to underestimate the CO concentration within the plume. The second main wildfire source, located south of Great Slave Lake in the NWT, is also observed in both IASI and GEOS-Chem where good agreement is found between the two. On subsequent days, transport of both plumes poleward is observed. The general shape of the fire plume from the BC wildfires is well represented in GEOS-Chem, but is lower in magnitude than IASI. The NWT wildfires appear to be underestimated by the model in comparison to IASI on 14 August. Due to the influence of the BC wildfire plume, it is difficult to distinguish the individual contribution of the BC and NWT wildfires on the observed CO plume. Due to the vertical sensitivity of IASI, which tends to peak in the mid- to upper-troposphere (George et al., 2009; Hurtmans et al., 2012; Kerzenmacher et al., 2012), near-surface CO from the NWT wildfires may be underestimated by IASI observations on 14 August, while the transport of the plume from the BC wildfires becomes more visible as the plume is advected vertically. However, it is found that the CO plume originating from the NWT is generally of lower concentration in the model than IASI. This observation is consistent with the FLEXPART sensitivity analysis in Section 5.3.2 and the comparisons of GEOS-Chem to the FTIR measurements in Section 5.3.4. In Section 5.3.2, it was shown that measurements at Eureka were more strongly influenced by the NWT wildfires than Thule, while a low bias in GEOS-Chem CO at Eureka, in comparison to the FTIR measurements, was shown in Figure 5.5, which is consistent with an underestimation of emissions from the NWT wildfires.

From 10 to 14 August in Figure 5.7, in both the IASI observations and model, the smoke plume originating in BC is transported poleward across central Canada and passes over the NWT wildfires. The combined plume is then transported north into the Canadian Arctic. On 17 August, the plume reaches Eureka, which is consistent with the FTIR enhancements. Transport of the plume towards Thule is also observed during this time, arriving at Thule on 19 August. From 20 August onwards, the plume passes both Eureka and Thule before the CO total columns at both sites return to ambient levels on 24 August.

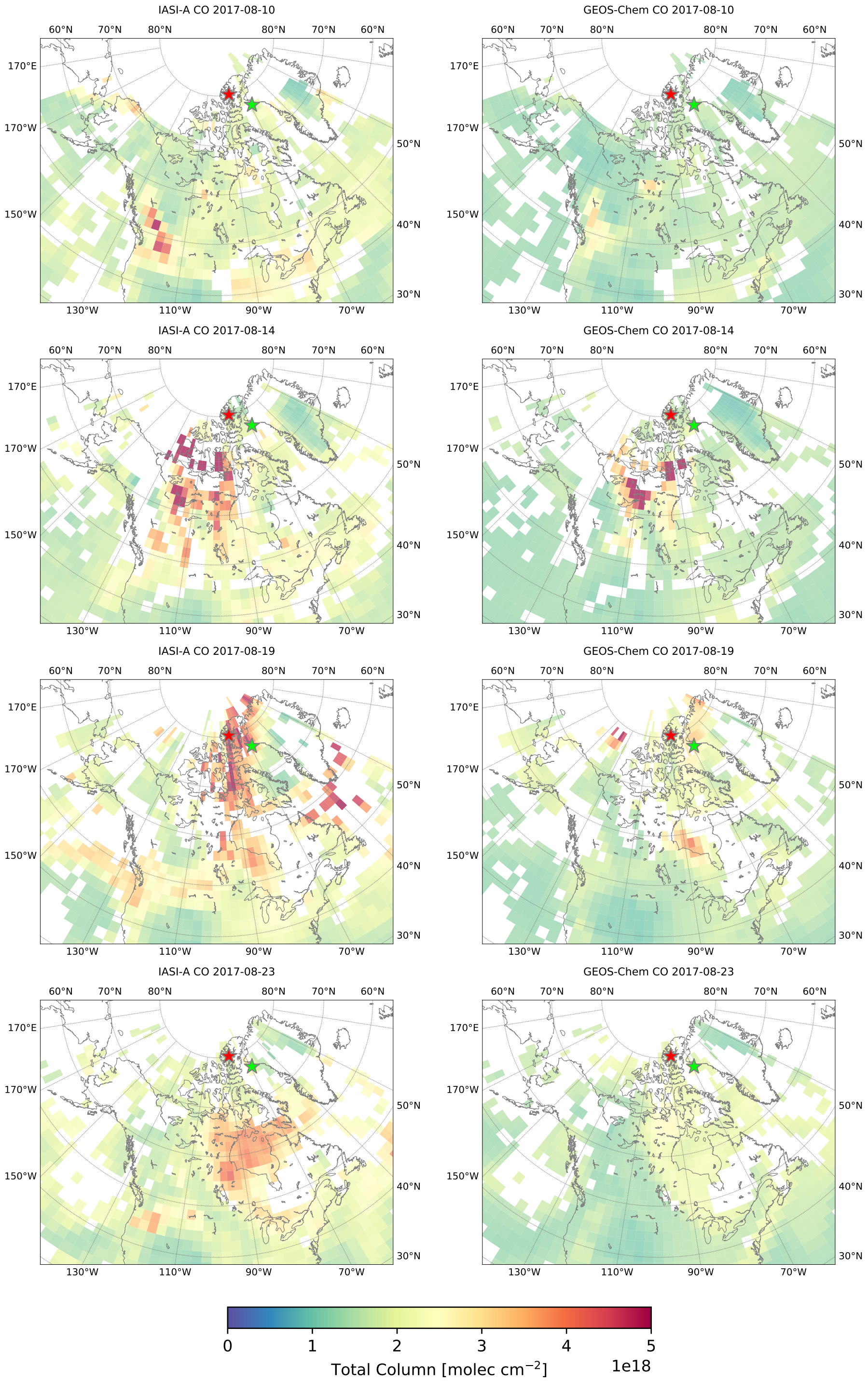

Figure 5.7: Left: IASI CO measurements gridded onto the 2°×2.5° GEOS-Chem grid and daily averaged. Right: GEOS-Chem CO total columns interpolated to match IASI overpass time and daily averaged. Locations of the FTIR sites Eureka and Thule shown by the red and green stars respectively.

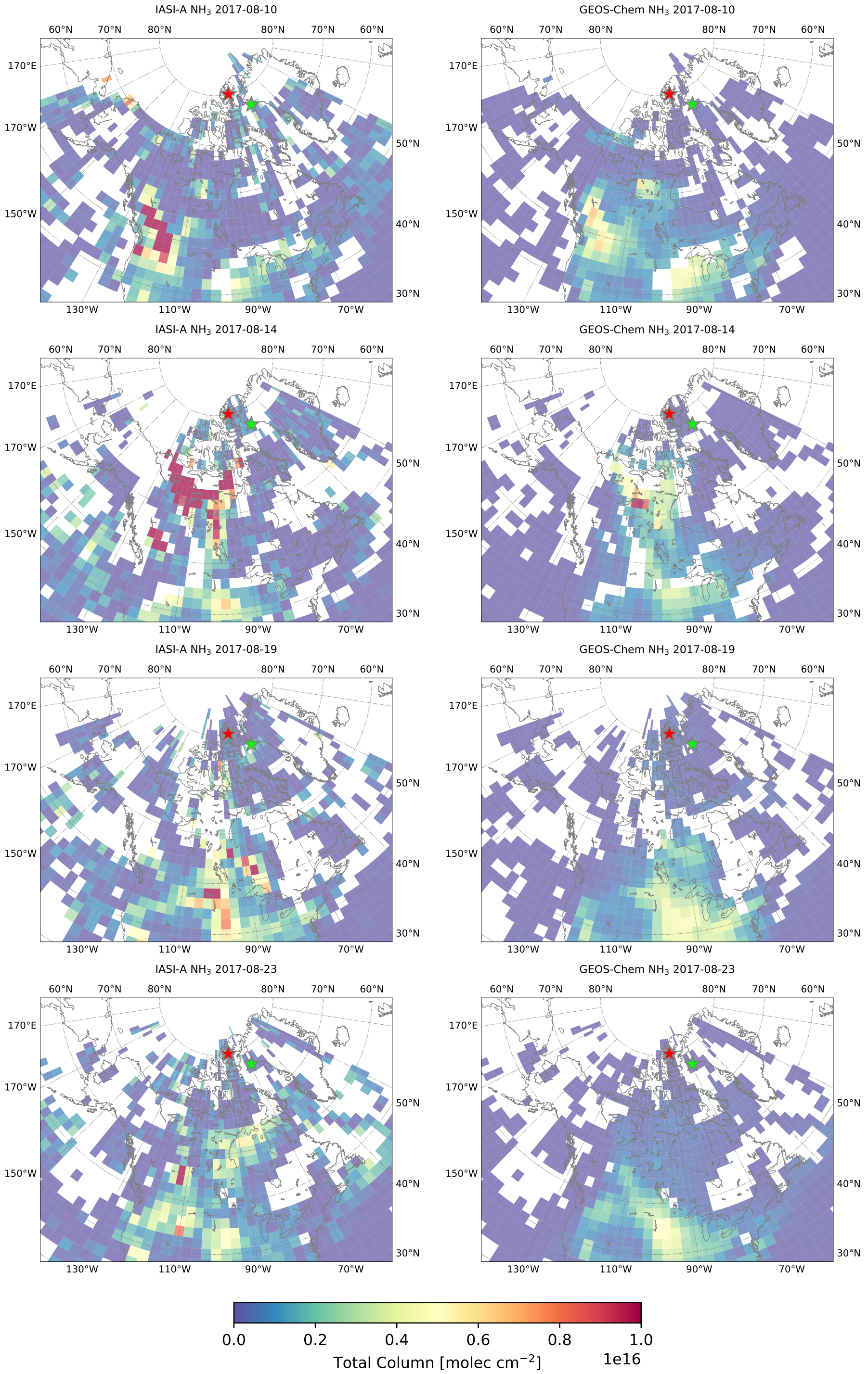

Figure 5.8: Same as Figure 5.7 but for NH$_3$.

The emissions and transport of GEOS-Chem NH$_3$ show similar spatial and temporal variability to that of CO, as illustrated in Figure 5.8. While the transport of the NH$_3$

plume as observed by IASI is well represented in GEOS-Chem, the modeled NH_3 total columns are low in comparison to IASI. Within the plume, the GEOS-Chem NH_3 may be a factor of 2 lower than IASI. On 10 August, GEOS-Chem modeled NH_3 total columns are are substantially less influenced by the BC wildfires. On subsequent days, the NH_3 plume dissipates rapidly, resulting in decreased total columns as the plume is transported poleward. On 14 August, the loss of NH_3 is particularly evident as the plume originating from the BC wildfires has reached the NWT wildfire source. As was observed in the IASI CO observations shown in Figure 5.7, the plume originating in BC is indistinguishable from the NWT wildfire source region. For NH_3, IASI shows similar results with high values in the regions exceeding $5{\times}10^{16}$ molec cm^{-2}. GEOS-Chem NH_3 does not exhibit these high values within the plume although the NWT wildfire source can clearly be distinguished from the plume in the model . On following days, the modeled NH_3 plume dissipates as it is transported poleward, resulting in the underestimation of GEOS-Chem in comparison to the FTIR measurements, as was shown in Section 5.3.4.

5.3.6 GEOS-Chem NH_3 and NH_4^+ in the Arctic

In this section, GEOS-Chem is used to estimate the influence of wildfire NH_3 on surface-layer and total column concentrations in the Canadian Arctic. As was shown in Sections 5.3.4 and 5.3.5, the model underestimates the transport of wildfire NH_3 in comparison to FTIR and IASI measurements. As such, we would expect modeled wildfire NH_3 in the Arctic to also have a low bias. We also consider the influence of NH_4^+. The sum of NH_3 and NH_4^+ is defined as total ammonia ($NH_x \equiv NH_3 + NH_4^+$) and is an important contribution to reactive nitrogen. After emission, NH_3 will partition rapidly to an equilibrium state with NH_4^+. The relative amounts of NH_3 and NH_4^+ are dependent on the availability of reactants and temperature. For wildfire emissions, it has been found that a large fraction (up to 30%) of emitted NH_3 is converted to NH_4^+ within 1.4 hr (Yokelson et al., 2009). Due to the longer lifetime of NH_4^+, from several days to weeks, this would enable long-range transport and therefore NH_4^+ could be an important contributor to reactive nitrogen in the Arctic (Karlsson et al., 2013).

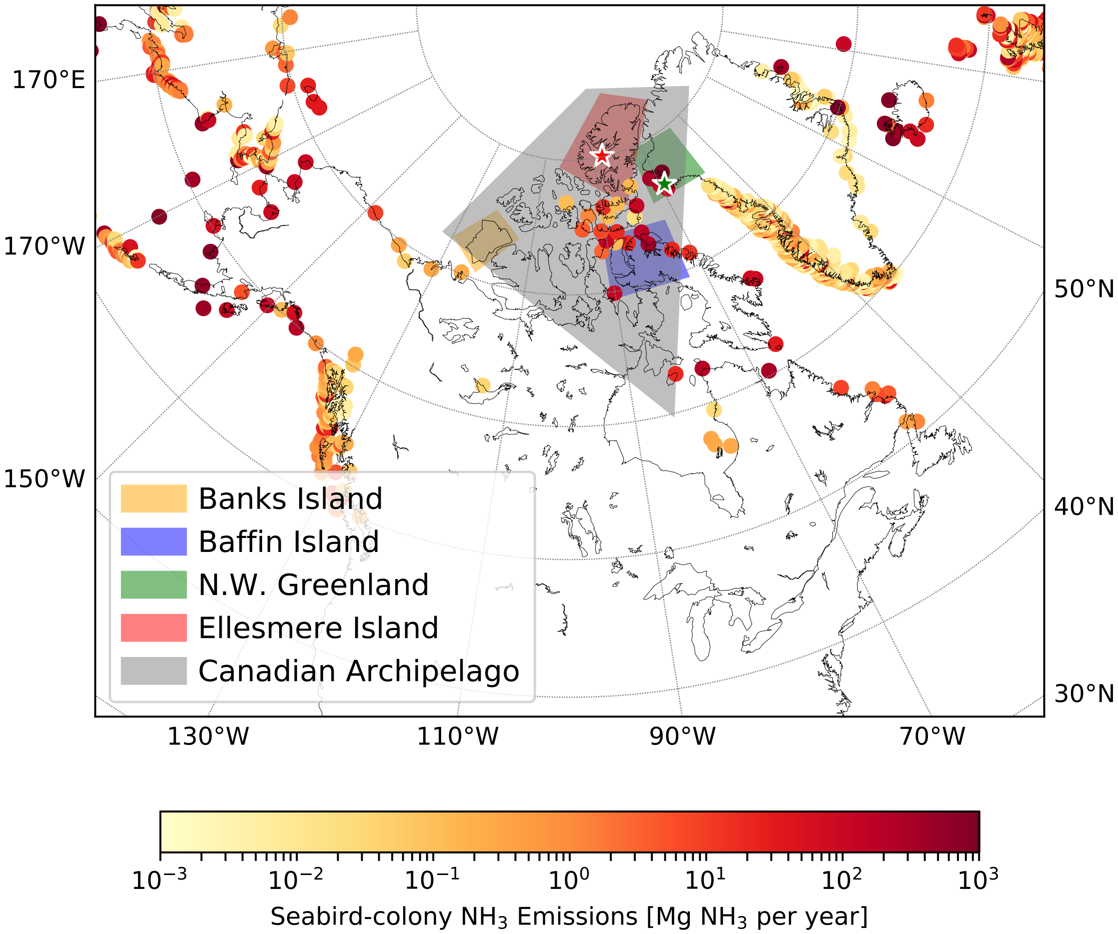

Figure 5.9: Locations chosen to evaluate spatially averaged GEOS-Chem NH_3 and NH_4^+ surface concentrations and total columns for the fire-affected period from 15-23 August 2017. Seabird-colony NH_3 emissions in GEOS-Chem are also shown.

To examine the surface influence of wildfire NH_3 and NH_4^+ in the Arctic, the following five regions of interest were chosen: Banks Island, Baffin Island, Northwestern Greenland, Ellesmere Island, and the Canadian Archipelago (shown in Figure 5.9). These regions represent locations within the high Arctic, both with and without seabird colonies. Banks Island does not contain any considerable seabird colonies and is closest in proximity to the wildfire source regions. Ellesmere Island includes the Eureka FTIR site and is free of any considerable seabird colonies. While some seabird colonies are present in the

Baffin Island region, it is also strongly influenced by seabird-colony NH_3 emissions from Greenland. The Northwestern Greenland region was chosen to include the location of the Thule FTIR site and the seabird colonies of the northwestern coast of Greenland and therefore represents the extreme case of high seabird-colony NH_3 emissions. Lastly, the Canadian Archipelago region is representative of the majority of the Canadian high Arctic, and includes all of the aforementioned regions. For each of these five regions, the GEOS-Chem grid boxes that lie within the defined boundaries illustrated in Figure 5.9 are spatially averaged for each 2-hourly GEOS-Chem output timestep from 15-23 August 2017, which corresponds to the period of fire-affected FTIR measurements at Eureka and Thule. We consider the following three GEOS-Chem simulation scenarios: (1) fire emissions only, (2) seabird-colony NH_3 emissions, (3) fire and seabird-colony NH_3 emissions. The results are shown in Figures 5.10 and 5.11 and are tabulated in Table 5.2.

As shown in Figure 5.10 and Table 5.2, it is found that the greatest NH_3 surface concentrations occur in northwestern Greenland with a mean value of 0.47 ppbv in the GEOS-Chem simulation with fire and seabird-colony NH_3 emissions. From the seabird-only simulation, it is evident that the seabird-colony NH_3 emissions are the dominant contribution in this region, with a mean surface-layer contribution of 0.45 ppbv. Ellesmere Island is also strongly influenced by seabird-colony NH_3 emissions, with a mean surface concentration of 0.07 ppbv with a standard deviation of 0.04 ppbv from the seabird-only simulation and 0.01 ppbv with a standard deviation of 0.01 ppbv from the fire-only simulation. Baffin Island shows nearly equal contributions from the seabird-colony (0.02 ppbv) and wildfires (0.03 ppbv). Banks Island is predominantly influenced by wildfire emissions, with a mean surface concentration from the fire-only simulation of 0.11 ppbv. These results are consistent with the loss of NH_3 in the plume by deposition in the low latitude regions (Banks Island and Baffin Island), with decreasing surface-layer influence in the high latitude regions (Northwestern Greenland and Ellesmere Island). For the period of fire-affected measurements from 15-23 August, wildfire and seabird-colony NH_3

had equal contributions 0.07 ppbv to surface-layer NH_3 over the Canadian Archipelago. However, in all regions, total column concentrations of NH_3 were predominantly due to wildfire NH_3 emissions, with the exception of Northwestern Greenland. In this region, the seabird-colony and wildfire NH_3 emissions had nearly equivalent contributions of 0.35 and 0.32×10^{15} molec cm^{-2} respectively.

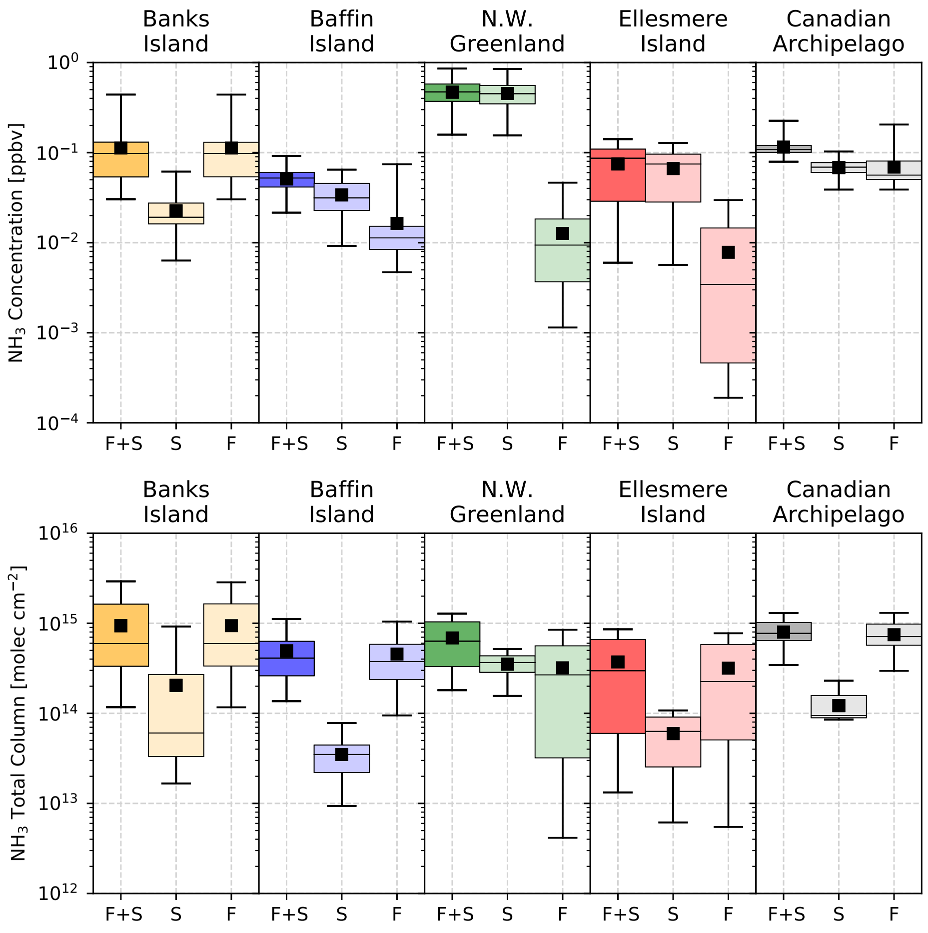

Figure 5.10: Box-and-whiskers plots of GEOS-Chem spatially averaged surface-layer concentrations (top) and total columns (bottom) of NH_3 from 15-23 August 2017 for the fire and seabird emissions (F+S), seabird-only (S) and fire-only (F) simulations. The box indicates the quartile values of the data and the whiskers represent the range of the data. The black horizontal line indicates the median value and the black square is the mean of all data.

The surface-layer concentrations of NH_4^+ show somewhat similar results to those for NH_3, with greater influence of wildfire NH_4^+ for the lower-latitude regions, as seen in Figure 5.11 and Table 5.2. In all regions, wildfire emissions are the dominate source of NH_4^+, with mean surface-layer concentrations ranging from 1.07 ppbv for Banks Island and to 0.05 ppbv at Ellesmere Island. Over the Canadian Archipelago, a mean concentration of 0.42 ppbv was found, with large variation (standard deviation of 0.45 ppbv) due to the spatial and temporal variability of the plume during the fire-affected period. As was the case for NH_3, total column amounts of NH_4^+ are greatly enhanced due to the transport of wildfire emissions, with a mean wildfire contribution of 7.11×10^{15} molec cm^{-2} in the Canadian Archipelago for the fire-only simulation.

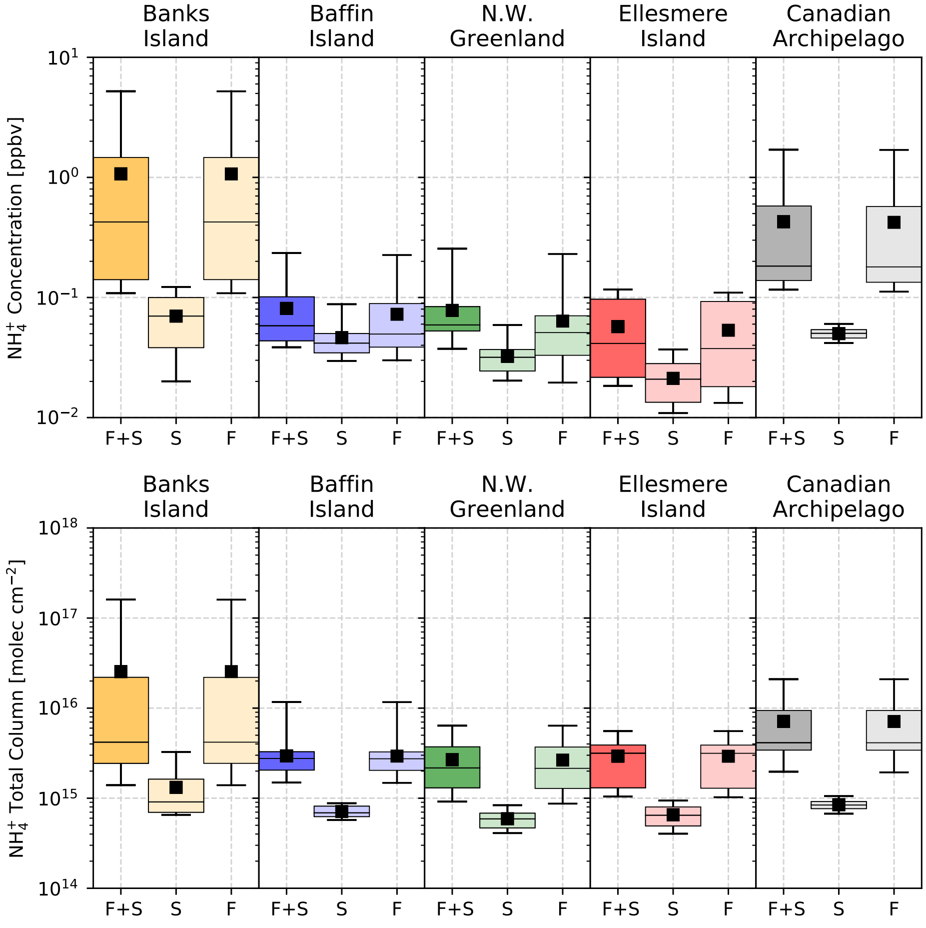

Figure 5.11: Same as Figure 5.10 but for NH_4^+.

Table 5.2: GEOS-Chem NH_3 and NH_4^+ surface concentrations and total columns in the regions defined in Figure 5.9 temporally averaged from 15-23 August, 2017. The values in parentheses indicate the standard deviation of the mean. Results are shown for the three GEOS-Chem simulations: fire and seabird NH_3 emissions, fire-only, and seabird-only emissions.

	NH_3			**NH_4^+**		
Surface Concentration [ppbv]	Fires+Seabirds	Seabirds	Fires	Fires+Seabirds	Seabirds	Fires
Banks Island	0.11 (0.08)	0.02 (0.01)	0.11 (0.08)	1.07 (1.37)	0.07 (0.03)	1.07 (1.37)
Baffin Island	0.05 (0.01)	0.03 (0.01)	0.02 (0.01)	0.08 (0.05)	0.05 (0.02)	0.07 (0.05)
Northwestern Greenland	0.47 (0.16)	0.45 (0.15)	0.01 (0.01)	0.08 (0.05)	0.03 (0.01)	0.06 (0.05)
Ellesmere Island	0.07 (0.04)	0.07 (0.04)	0.01 (0.01)	0.06 (0.04)	0.02 (0.01)	0.05 (0.04)
Canadian Archipelago	0.12 (0.03)	0.07 (0.01)	0.07 (0.03)	0.43 (0.45)	0.05 (0.00)	0.42 (0.45)
Total Column [10^{15} moleccm^{-2}]	Fires+Seabirds	Seabirds	Fires	Fires+Seabirds	Seabirds	Fires
Banks Island	0.94 (0.78)	0.20 (0.28)	0.94 (0.79)	25.44 (43.68)	1.32 (0.86)	25.44 (43.67)
Baffin Island	0.49 (0.28)	0.03 (0.02)	0.45 (0.27)	2.95 (1.48)	0.71 (0.10)	2.93 (1.48)
Northwestern Greenland	0.69 (0.37)	0.35 (0.10)	0.32 (0.29)	2.68 (1.63)	0.59 (0.12)	2.65 (1.64)
Ellesmere Island	0.37 (0.30)	0.06 (0.03)	0.32 (0.28)	2.93 (1.43)	0.65 (0.17)	2.92 (1.43)
Canadian Archipelago	0.80 (0.24)	0.12 (0.05)	0.75 (0.25)	7.12 (6.07)	0.85 (0.11)	7.11 (6.07)

It can therefore be concluded that the 2017 Canadian wildfires events had a significant influence on surface-layer NH_3 and NH_4^+. It should be noted that although these enhancements occurred over a short period of time, from 15-23 August, the enhanced surface-layer concentrations of NH_3 were comparable to the persistent contribution of seabird-colony NH_3. For NH_4^+, the influence of wildfire emissions greatly enhanced both surface-layer and total column concentrations in all regions. As was discussed in Sections 5.3.4 and 5.3.5, GEOS-Chem was shown to underestimate the transport of wildfire NH_3 and CO in comparison to FTIR and IASI observations. It is therefore likely that the modeled influence of transported wildfire emissions on Arctic NH_3 and NH_4^+ presented here is a low estimate.

The influence of wildfires on the reactive nitrogen budget of the high Arctic remains unknown. It has been shown that the Arctic has been undergoing an increase in the areal extent of vegetated land as a result of warming in the Arctic (Myneni et al., 1997; Zhu et al., 2016; Keenan and Riley, 2018) and increased community plant height has also been observed as a result of this warming (Bjorkman et al., 2018). Plant growth in the Arctic is strongly limited by nutrient availability (Schimel and Bennett, 2004), therefore the wildfire contribution to nitrogen deposition in the form of NH_x could potentially facilitate an increase in plant growth, especially if extreme wildfire events such as these become more frequent. The effects on nitrogen deposition in the Canadian high Arctic are still uncertain, although it has been noted that high Arctic tundra has a high capacity for nitrogen pollution retention, resulting in a major source of eutrophication (Choudhary et al., 2016), which could have a negative impact on biodiversity.

5.4 Conclusions

The 2017 BC and NWT wildfires resulted in the greatest observed enhancements of total column NH_3, CO, HCN, and C_2H_6 in the decade-long time series of FTIR measurements at Eureka, Nunavut, and Thule, Greenland. The magnitude of the these enhancements was on the order of 2-5 times the ambient levels of these species at each site. The observed NH_3 enhancements provide evidence for the importance of wildfires as an episodic source of NH_3 in the summertime Arctic, supporting the results of Chapter 4. Enhancement ratios of NH_3, HCN, and C_2H_6 were calculated with respect to CO at both sites. It was found that variations in these enhancement ratios were due to the influence of multiple fire plumes and variations in the burning phases of the fire events. Evidence for this was provided by FLEXPART sensitivities, which showed the influence of the BC and NWT plumes, with the influence of each fire source varying between measurement days at both sites. Eureka FTIR measurements were found to be most sensitive to the NWT wildfires, and Thule FTIR measurements were most sensitive to the BC wildfires, based on the FLEXPART sensitivity analysis.

The GEOS-Chem CTM was used to simulate the transport of wildfire emissions to the Arctic. Through comparisons of GEOS-Chem NH_3 and CO to FTIR measurements at Eureka and Thule, and to observations from IASI, it was shown that the model underestimates the transport of wildfire emissions to the Arctic for the observations examined here. The underestimation of modeled NH_3 and CO in comparison to Eureka FTIR measurements suggests an underestimation of emissions from the NWT fire source. This is consistent with the model comparisons to IASI measurements, which suggested an underestimation of emissions from the NWT wildfires in the model. At Thule, GEOS-Chem showed good agreement to the FTIR measurements for CO, but underestimated the wildfire NH_3 contribution. The reason for the underestimation of GEOS-Chem CO and NH_3 in comparison to FTIR and IASI measurements remains unclear, and is likely the result of several factors including the underestimation of emissions, plume height, chemistry and transport errors in the model. These aspects of the model should be investigated in future studies. Increased temporal and spatial sampling of NH_3 and NH_4^+ by in-situ, ground-based and satellite instruments is recommended to better evaluate model performance and infer wildfire impacts on NH_3 in the Arctic. Tundra NH_3 emissions should be examined in these studies. Furthermore, the use of satellite observations, such as the studies of Kharol et al. (2018) and Adams et al. (2019), should also be the focus of future work in order to quantify boreal wildfire NH_3 emissions and transport to the Arctic.

Simulated transport of wildfire emissions in GEOS-Chem was found to be a significant contributor to reactive nitrogen in the form of NH_3 and NH_4^+ in the high Arctic for the fire-affected period of 15-23 August 2017. GEOS-Chem surface-layer NH_3 and NH_4^+ was shown to be greatly enhanced during the fire-affected period. A mean wildfire contribution of 0.07 ppbv in the Canadian Archipelago from 15-23 August 2017 was equivalent to the local background from seabird-colony NH_3 sources. Surface-layer NH_4^+ was greatly enhanced during this period as well, with a mean concentration of 0.42 ppbv in the Canadian Archipelago in the fire-only simulation, whereas for the seabird-only simulation a mean concentration of 0.05 ppbv was observed. Due to the influence of transported wildfire emissions, total column NH_3 and NH_4^+ were found to be enhanced several times greater than background levels associated with the seabird-colony sources. The strong episodic influence of the BC and NWT wildfires on the reactive nitrogen budget of the high Arctic could have significant impacts on nutrient availability and eutrophication of this sensitive ecosystem.

Chapter 6

Pan-Arctic Detection of Wildfire Pollution

6.1 Introduction

This chapter presents the results of a study on the influence of wildfires on atmospheric composition using measurements by ten FTIR spectrometers in the Northern mid- and high latitudes. This work is currently in a manuscript in preparation as: Lutsch et al., Detection of wildfire pollution in the Arctic using a network of FTIR spectrometers, to be submitted to *Atmospheric Chemistry & Physics*.

The usefulness of FTIR measurements for the detection of wildfire pollution events has been illustrated in Chapters 4 and 5 in addition to the past studies of Zhao et al. (2002), Paton-Walsh et al. (2005, 2010), Vigouroux et al. (2012) and Viatte et al. (2013, 2015). However, each of these studies has only considered individual events or events that occurred in a short time series. Measurements using FTIR spectrometers have been routinely made since the mid-1980s (Zander et al., 2008), with an increasing number of measurement sites since the inception of the Network for Detection of Stratospheric Change (NDSC; Kurylo, 1991) in 1991, which has been formally known as NDACC since 2005 (De Mazière et al., 2018). Several global FTIR sites have been measuring the biomass burning tracers CO, HCN and C_2H_6 over the last two decades. Currently, no study has explicitly examined the long-term and inter-annual influence of biomass burning species observed using FTIR measurements. A recent study by Petetin et al. (2018) investigated the impact of biomass burning on CO as measured by the In-service Aircraft for a Global Observing System (IAGOS), which focused on airport clusters in Europe, North America, Asia, India and Southern Africa over the period 2002-2017. However, no study of this kind has been performed for the Arctic and high-latitude regions.

In this chapter, the influence of wildfires on atmospheric composition from 2003-2018 is examined using FTIR measurements from three high-Arctic NDACC sites: Eureka, Canada; Ny-Ålesund, Norway and Thule, Greenland. Three Arctic sites are also included: Kiruna, Sweden; Poker Flat, Alaska and St. Petersburg, Russia. Additional measurements are obtained at four mid-latitude sites: Zugspitze, Germany; Jungfraujoch, Switzerland; Toronto, Canada and Rikubetsu, Japan. Potential wildfire pollution events are first identified in the CO time series at each site through the detection of anomalous enhancements of CO. For the detected CO enhancements at each site, enhancement ratios of HCN and C_2H_6 with respect to CO are calculated. Since CO, HCN and C_2H_6 are co-emitted from biomass burning sources, a strong linear correlation for the enhancement ratios of HCN and C_2H_6 are indicative of wildfire pollution events. Further confirmation of the detection of wildfire pollution at each site was provided by total aerosol optical depth (AOD) measurements from adjacent AERONET (Aerosol Robotic Network) sites. A GEOS-Chem tagged CO simulation from 2003-2018 was performed and provided a means of source attribution for the detected events at each FTIR site in addition to quantifying the contribution to CO from various biomass burning source regions.

6.2 Methods

6.2.1 FTIR Sites and Retrievals

The NDACC FTIR sites included in this study were selected to provide coverage of high- and mid-latitude regions and are listed in Table 6.1. Due to the broad spectral range measured at high resolution, typically from 700-4400 cm^{-1} at 0.0035 cm^{-1} resolution, a multitude of trace gas species may be retrieved from solar-absorption FTIR measurements. Measurements of CO, HCN, and C_2H_6, all of which are standard products of the NDACC IRWG are the focus of this study. Retrievals of each species were performed by processing of solar-absorption spectra using the SFIT4 (`https://wiki.ucar.edu/display/sfit4/`) or PROFITT9 (Hase et al., 2004, for Kiruna and Zugspitze) retrieval algorithm which use the optimal estimation method (Rodgers, 2000) to obtain volume mixing ratio (VMR) profiles and integrated column abundances by iteratively adjusting VMR profiles to minimize the difference between the measured and calculated spectra (Pougatchev et al., 1995; Rinsland et al., 1998). Further details of the retrievals for each FTIR site are given in the references listed in Table 6.1.

High-Arctic Sites

The highest-latitude FTIR site of NDACC is Eureka, located on Ellesmere Island in the Canadian Archipelago. It has been shown in previous studies that Eureka is regularly influenced by the transport of boreal wildfire emissions from North America and Asia (Viatte et al., 2013, 2014, 2015; Lutsch et al., 2016, 2019). Located approximately 500 km from Eureka is the site Thule on the Northwest coast of Greenland, which provides complementary measurements to Eureka as wildfire pollution events detected at Eureka are generally also observed in measurements at Thule (Viatte et al., 2015; Lutsch et al., 2019). Ny-Ålesund in Spitsbergen, Norway is the second highest-latitude FTIR site of NDACC. Ny-Ålesund is isolated from the direct influence of anthropogenic and wildfire emissions, but is affected by the long-range transport of pollution originating from Northern hemisphere mid-latitudes. For the purposes of this study, Eureka, Ny-Ålesund and Thule will be referred to as the "clean" high-Arctic (>75°N) sites because they are free of local pollution sources.

Arctic Sites

The Arctic sites are defined as those located between 60°N and 75°N, and include Poker Flat, Alaska; Kiruna, Sweden; and St. Petersburg, Russia. Poker Flat is strongly influenced by the transport of anthropogenic pollution from Siberia and Asia (Kasai et al., 2005b). Asian anthropogenic emissions have been found to be a predominant source of pollution in Alaska, with a greater influence in years with strong El Niño conditions (Fisher et al., 2010). Siberian wildfires are a substantial source of summertime pollution in Alaska (Jaffe et al., 2004; Warneke et al., 2009) in addition to local wildfires within the boreal forests of Alaska. It should be noted that for this reason, and the dependence of FTIR measurements on clear-sky conditions, smoke plumes within Alaska may prevent measurements by FTIR. As a result, summertime measurements at Poker Flat can be sparse.

Kiruna is mainly influenced by anthropogenic emissions from mid-latitude Europe; however, aerosol smoke layers from injection of Canadian wildfire emissions into the lower stratosphere have been identified in the past at Kiruna (Fromm et al., 2000). Similarly, the urban site of St. Petersburg would be most sensitive to local sources within Europe. Both Kiruna and St. Petersburg may sample the long-range transport of boreal Asian plumes that could circle the Northern Hemisphere (Damoah et al., 2004), although such plumes would be well aged and diluted. Through injection of wildfire emissions into the upper troposphere and lower stratosphere, North American boreal wildfire plumes may be efficiently transported to Europe (Khaykin et al., 2018; Hu et al., 2019). Although the effects of the long-range transport of wildfire emissions on air quality are likely to be minimal, they can have an influence on tropospheric composition of long-lived species.

Alpine Sites

Both Zugspitze and Jungfraujoch are considered clean Alpine sites, isolated from local pollution sources and therefore provide measurements that are representative of background concentrations of central Europe (Franco et al., 2015). For the purpose of this study, as the result of the close proximity between the two sites (∼200 km), Zugspitze and Jungfraujoch are considered to be complementary to one another. Differences in measured column amounts between the two sites as a result of long-range transport are likely due to their altitude differences, 2964 m a.s.l. and 3580 m a.s.l. for Zugspitze and Jungfraujoch, respectively. It has been previously shown that Zugspitze is weakly influenced by nearby pollution sources, while Jungfraujoch is considered a remote site, mainly influenced by long-range transport (Henne et al., 2010). However, as a result of the high altitudes of these sites, the measured composition is largely driven by long-range transport in the mid to upper troposphere.

Mid-latitude Sites

Toronto, an urban site, is most sensitive to local pollution sources in southeast Canada and the United States (Whaley et al., 2015) and periodically subject to wildfire pollution episodes as demonstrated by Griffin et al. (2013); Whaley et al. (2015). Rikubetsu, located in Hokkaido, Japan, is free of considerable local anthropogenic pollution sources, with contributions of CO mainly due to transported Asian anthropogenic emissions (Zhao et al., 2000). In the summertime, Rikubetsu is influenced by the transport of biomass burning pollution from within Asia (Li et al., 2000), while the region of Hokkaido is often affected by pollution episodes from Siberian wildfires of boreal Asia (Jeong et al., 2008; Tanimoto et al., 2000; Yasunari et al., 2018).

Table 6.1: Summary of NDACC and AERONET sites used in this study.

	Site	Latitude, Longitude	Elevation [m a.s.l.]	Measurement Years	Key References
NDACC	**Eureka**	80.05°N, 86.42°W	610	2006-2018	Batchelor et al., 2009; Lutsch et al., 2016, 2019, Viatte et al., 2013, 2014, 2015
AERONET	PEARL	80.05°N, 86.42°W	610	2007-2018	Saha et al., 2010; O'Neill et al., 2012
	Ny-Ålesund	78.92°N, 11.93°E	15	1992-2018	Notholt et al., 1997a,b, 2000
	Horsund	77.00°N, 86.42°W	12	2004-2018	Rozwadowska et al., 2010
	Thule	76.53°N, 68.74°W	225	1999-2018	Hannigan et al., 2009; Viatte et al., 2015 Lutsch et al., 2019
	Thule	76.52°N, 68.77°W	225	2007-2018	Tomasi et al., 2015
	Kiruna	67.84°N, 20.41°E	419	1996-2018	Blumenstock et al., 1997, 2009
	Andenes	69.28°N, 16.01°E	379	2002-2018	Rodríguez et al., 2012
	Poker Flat	65°N, 142°W	610	1999-2011	Kasai et al., 2005a,b
	Bonanza Creek	65.74°N, 148/32°W	353	1994-2018	Eck et al., 2009
	St. Petersburg	59.88°N, 29.83°E	20	2009-2018	Makarova et al., 2011; Timofeyev et al., 2016
	Toravere	58.27°N, 26.47°E	85	2002-2018	Arola et al., 2007
	Zugspitze	47.42°N, 10.98°E	2964	1995-2018	Sussmann and Schäfer, 1997, Sussmann and Buchwitz, 2005
	Davos	46.81°N, 9.84°E	1589	2001-2018	Gubler et al., 2012
	Jungfraujoch	46.55°N, 7.98°E	3580	1984-2018	Mahieu et al., 1997; Zander et al., 2008, Dils et al., 2011
	Davos	46.81°N, 9.84°E	1589	2001-2018	Gubler et al., 2012
	Toronto	43.66°N, 79.40°W	174	2002-2018	Wiacek et al., 2007; Whaley et al., 2015, Lutsch et al., 2016
	Toronto	43.79°N, 79.47°E	186	1996-2018	Sioris et al., 2017
	Rikubetsu	43.46°N, 143.77°E	380	2002-2018	Zhao et al., 1997, 2000, 2002
	Noto	37.34°N, 137.14°E	200	2001-2018	Makar et al., 2018

6.2.2 GEOS-Chem

To interpret the influence of anthropogenic, chemical, and biomass burning sources on CO columns at each FTIR site, the GEOS-Chem CTM is used (`http://geos-chem.org/`;Bey et al., 2001b) in a tagged simulation of CO at a horizontal resolution of 2°×2.5° with 47 vertical hybrid levels. GEOS-Chem version 12.1.1 (The International GEOS-Chem User Community, 2018) was used and driven by global meteorological inputs from the MERRA-2 (Modern-Era Retrospective Analysis for Research and Applications, Version 2; Gelaro et al., 2017) from the NASA GMAO. MERRA-2 is produced with the GMAO/GEOS-5 Data Assimilation System Version 5.12.4. The GEOS-Chem simulation was initialized with a 1-year spin-up from 1 January 2002 to 1 January 2003. Chemical and transport operator time-steps of 1 hr and 10 min, respectively, were used.

Biomass burning emissions are from GFASv1.2 (Kaiser et al., 2012; Giuseppe et al., 2018) which assimilates MODIS burned area and FRP products to estimate emissions for open fires. GFASv1.2 emissions have a 0.1°×0.1° horizontal resolution with 3-hourly temporal resolution. GFAS was chosen for the availability of emissions over the analysis period from 2003-2018. Global anthropogenic emissions are provided from the EDGARv4.3.1 (Crippa et al., 2016) emissions inventory, overwritten by regional emission inventories in the Northern hemisphere as described in Fisher et al. (2010). Biogenic emissions of precursor VOCs are from the Model of Emissions of Gases and Aerosols from Nature (MEGANv2.1; Guenther et al., 2012) and biofuel emissions are taken from Yevich and Logan (2003).

The main loss mechanism for CO is from photochemical oxidation by OH. The OH fields are prescribed in the tagged CO simulation and were obtained from the TransCom experiment (Patra et al., 2011) which implements semi-empirically calculated tropospheric OH concentrations from Spivakovsky et al. (2000) to reduce the high bias of OH from the GEOS-Chem full-chemistry simulation (Shindell et al., 2006). Surface emissions in GEOS-Chem are released within the boundary layer, and boundary layer mixing is implemented using the non-local mixing scheme of Holtslag and Boville (1993). Biomass emissions are released by uniformly distributing emissions from the surface to the mean altitude of maximum injection based on the injection height information as described in Rémy et al. (2017) which includes an injection height parameterization by Sofiev et al. (2012) and a plume rise model by Freitas et al. (2007).

GEOS-Chem version 12.1.1 tagged CO simulation includes the improved secondary CO production scheme of Fisher et al. (2017), which assumes production rates of CO from CH_4 and NMVOC oxidation from a GEOS-Chem full-chemistry simulation therefore reducing the mismatch between the CO-only simulation and the full-chemistry simulation. The anthropogenic source regions are shown in Figure 6.1, while biomass burning source regions are implemented following the standard GFED (Giglio et al., 2013) regions and are also shown in Figure 6.1.

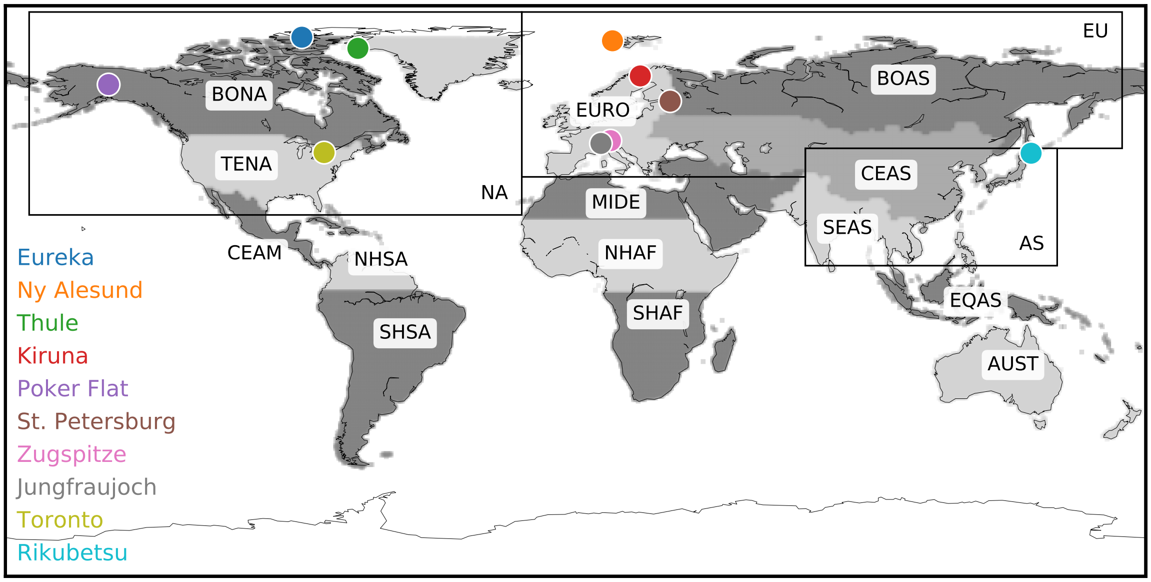

Figure 6.1: Locations of ground-based FTIR sites used in this study. The GFED basis regions (shaded), and anthropogenic source regions (black rectangles) used for the GEOS-Chem tagged CO simulation are also shown and summarized in Table 6.2.

Table 6.2: Summary of the source regions used in the GEOS-Chem tagged CO simulation.

Type	Name	Description
Anthropogenic	NA	North America
	EU	Europe
	AS	Asia
	ROW	Rest of World
Biomass Burning	BONA	Boreal North America
	TENA	Temperate North America
	CEAM	Central America
	NHSA	Northern Hemisphere South America
	SHSA	Southern Hemisphere South America
	EURO	Europe
	MIDE	Middle East
	NHAF	Northern Hemisphere Africa
	SHAF	Southern Hemisphere Africa
	BOAS	Boreal Asia
	CEAS	Central East Asia
	SEAS	Southeast Asia
	EQAS	Equatorial Asia
	AUST	Australia and New Zealand
Other	CH_4	Methane oxidation
	NMVOC	Non-methane volatile organic compound oxidation

6.2.3 AERONET

The Aerosol Robotic Network (AERONET; `https://aeronet.gsfc.nasa.gov`; Holben et al., 1998) is a federation of ground-based remote sensing aerosol networks established by NASA and PHOTONS (PHOtométrie pour le Traitement Opérationnel de Normalisation Satellitaire; Univ. of Lille 1, CNES, and CNRS-INSU). AERONET consists of a network of CIMEL sun photometers which provides globally distributed observations of spectral aerosol optical depth (AOD). At each AERONET site, observations are recorded every 15 minutes and are cloud screened. Inversion of aerosols products and cloud screening for the AERONET Version 3 database are described in (Giles et al., 2019). AERONET sites selected for this study were based on the availability of data during the operational period of the FTIR instruments and proximity to the FTIR site. The selected AERONET sites nearest to the NDACC FTIR sites are listed in Table 6.1.

6.3 Results & Discussion

6.3.1 Retrieved FTIR Products

Time Series

The weekly-mean time series of CO, HCN and C_2H_6 tropospheric partial columns for each site are shown in Figures 6.2, 6.3 and 6.4 respectively. The tropospheric partial columns are the integrated column amounts from the surface to an altitude of 12.71 km at each site. In this study, all presented column amounts correspond to this partial column for CO, HCN and C_2H_6. The weekly mean is taken over all years of measurements for the respective species at each site, while the shaded region indicates a 1σ deviation from the mean. For all sites, the seasonal cycle of CO shows a maximum in winter and early spring (February-March), with decreasing total columns through the spring. The main sources of CO are the combustion of fossil fuels and biomass burning, while oxidation of VOCs and CH_4 are also a considerable source (Holloway et al., 2000). The main sink of CO is due to reaction with OH, leading to a lifetime of approximately 1-2 months (Bey et al., 2001a). In winter and spring months, decreased sunlit hours limits OH production by photolysis of ozone, therefore minimizing the loss of CO. The seasonal cycle of OH largely drives the seasonal variations of CO. Transport of CO from mid-latitude to high-latitude regions also contributes to the seasonal cycle as the isentropic transport is greater in the winter and spring months (Klonecki, 2003; Stohl et al., 2006). Furthermore, the stronger seasonal cycle of OH production also contributes to the greater seasonal amplitudes at high latitudes as observed in Figure 6.2.

Enhanced tropospheric columns of CO are observed in the summertime, mainly in July-September at all sites as illustrated in Figure 6.2 as a result of the hemispheric influence of boreal wildfires (Honrath, 2004). These enhancements are most pronounced at the clean high-Arctic sites of Eureka and Thule, which are strongly influenced by boreal fires in North America and Asia. Similar enhancements are also observed at the other Arctic sites of Ny-Ålesund and Kiruna, but are not as pronounced, which is partly due to the longer transport times to these sites. Ny-Ålesund also exhibits an increase in CO beginning in August as a result of the accumulation of CO from Northern Hemisphere biomass burning sources. Poker Flat, located in the boreal forests of Alaska is greatly influenced by boreal wildfire emissions in these regions; however, in many instances these events result in smokey conditions that prevent FTIR measurements. As a result, detection of enhancements at Poker Flat are likely to be underestimated due to the strong influence of wildfire smoke.

A slight increase in CO concentrations is observed at Zugspitze and Jungfraujoch as a result of the long-range transport of boreal wildfire emissions. Emissions from these events are often lofted into the free troposphere where long-range transport is favoured (Jaffe et al., 2004; Val Martin et al., 2006). However, the transport of emissions over continental scales results in the dilution of the smoke plume and therefore, the enhancements observed at Zugspitze and Jungfraujoch are not as pronounced as for the other sites.

St. Petersburg and Toronto are urban sites that are strongly influenced by local anthropogenic sources, but enhanced columns of CO are observed in July and August as a result of the boreal wildfire influence. Rikubetsu is strongly affected by anthropogenic CO sources from Asia, resulting in the large variability of CO (Zhao et al., 1997, 2002). The greatest enhancements at Rikubetsu are observed in July and August, due to boreal Asian wildfires in Siberia.

HCN has a long atmospheric lifetime ranging from days to months, while its dominant source is due to biomass burning emissions (Li et al., 2000, 2003, 2009). Plant and fungal emissions represent a minor source of HCN, while dry deposition to the ocean and oxidation by OH are the main sinks (Cicerone and Zellner, 1983). As a result, HCN will accumulate in the Northern Hemisphere in the summer months due to the influence of wildfire and biogenic emissions. The seasonal cycle of HCN peaks in the summer months with low total columns in the winter and fall as illustrated in Figure 6.3. A sharp maximum is observed in August at the high-Arctic sites (Eureka, Thule and Ny-Ålesund) due to activation of its biogenic sources and the onset of wildfire emissions. A similar increase in the HCN total columns is observed at the high-latitude sites (Kiruna, Poker Flat and St. Petersburg), although not as pronounced. For Toronto, enhanced total columns are also observed in August due to wildfires, consistent with the CO time series. Rikubetsu shows the greatest concentrations of HCN in the spring in May, with a secondary peak in August. The springtime enhancements of HCN are due to the earlier onset of East and Southeast Asian biomass burning, which occurs annually from March to May (Streets et al., 2003).

The seasonal cycle of C_2H_6 is similar to that of CO, as shown in Figure 6.4. The primary sources of C_2H_6 include natural gas production, biofuel use and biomass burning (Rudolph, 1995; Logan et al., 1981; Xiao et al., 2008). The main loss of C_2H_6 is due to reaction with OH, resulting in an average lifetime of approximately three months (Xiao et al., 2008). The summertime wildfire influence of C_2H_6 is less pronounced than for CO and HCN. Enhancements of C_2H_6 are particularly evident at Eureka and Thule, due to the generally clean background of these sites, while wildfire enhancements of C_2H_6 are not evident at the other sites due to the influence of local sources in addition to dilution of the plume during long-range transport. Therefore, C_2H_6 enhancements due to wildfire pollution are not generally apparent over background concentrations. Additionally, the emissions of C_2H_6 are an order of magnitude lower than those of HCN for boreal forest, temperate forests and peatland burning sources (Andreae and Merlet, 2001; Akagi et al., 2011; Andreae, 2019).

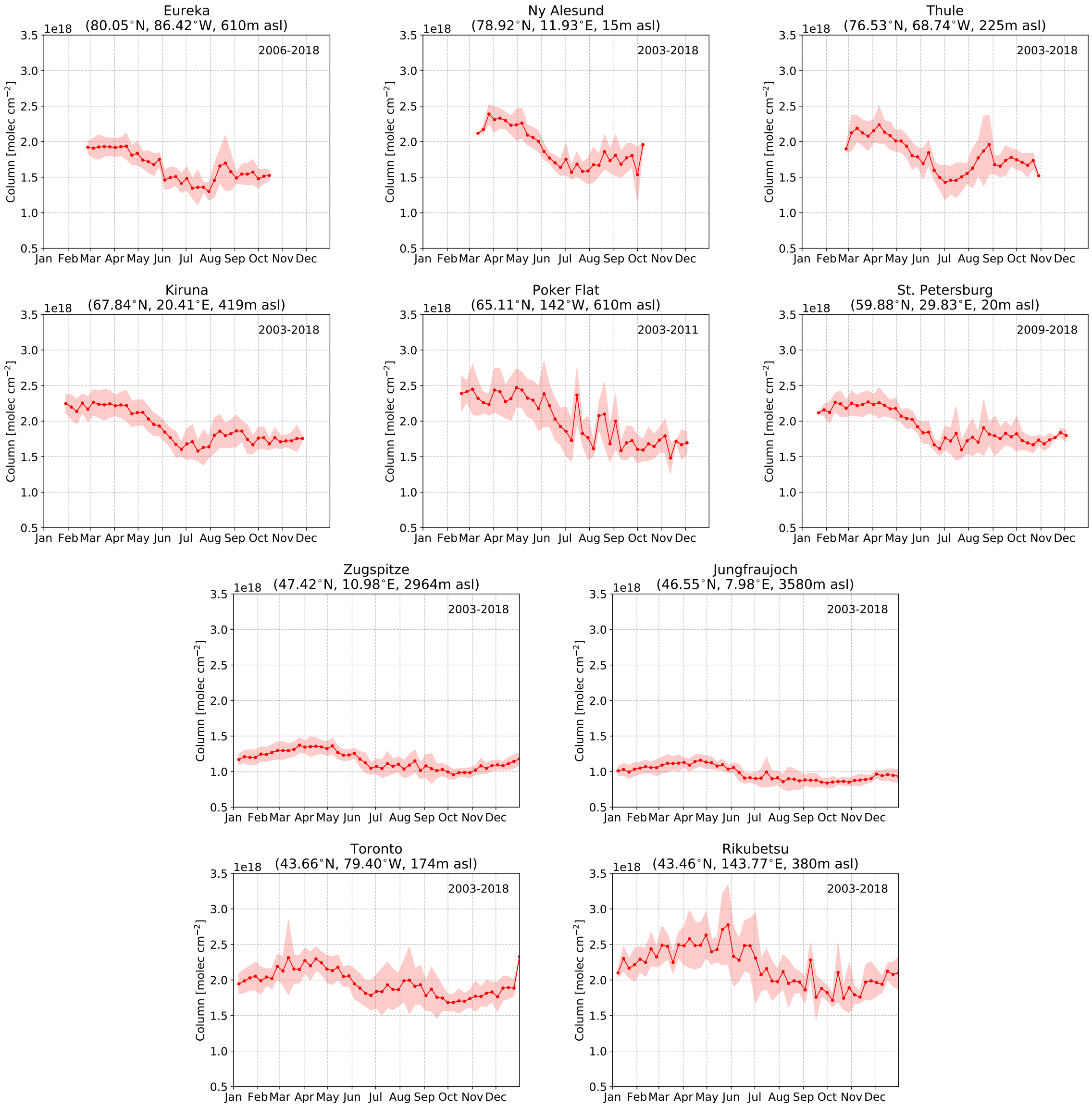

Figure 6.2: Weekly-mean CO tropospheric partial columns taken over all years of measurements at each site. The years included in the mean are listed in the top left corner of each panel. The shaded region represents a 1σ standard deviation from the mean.

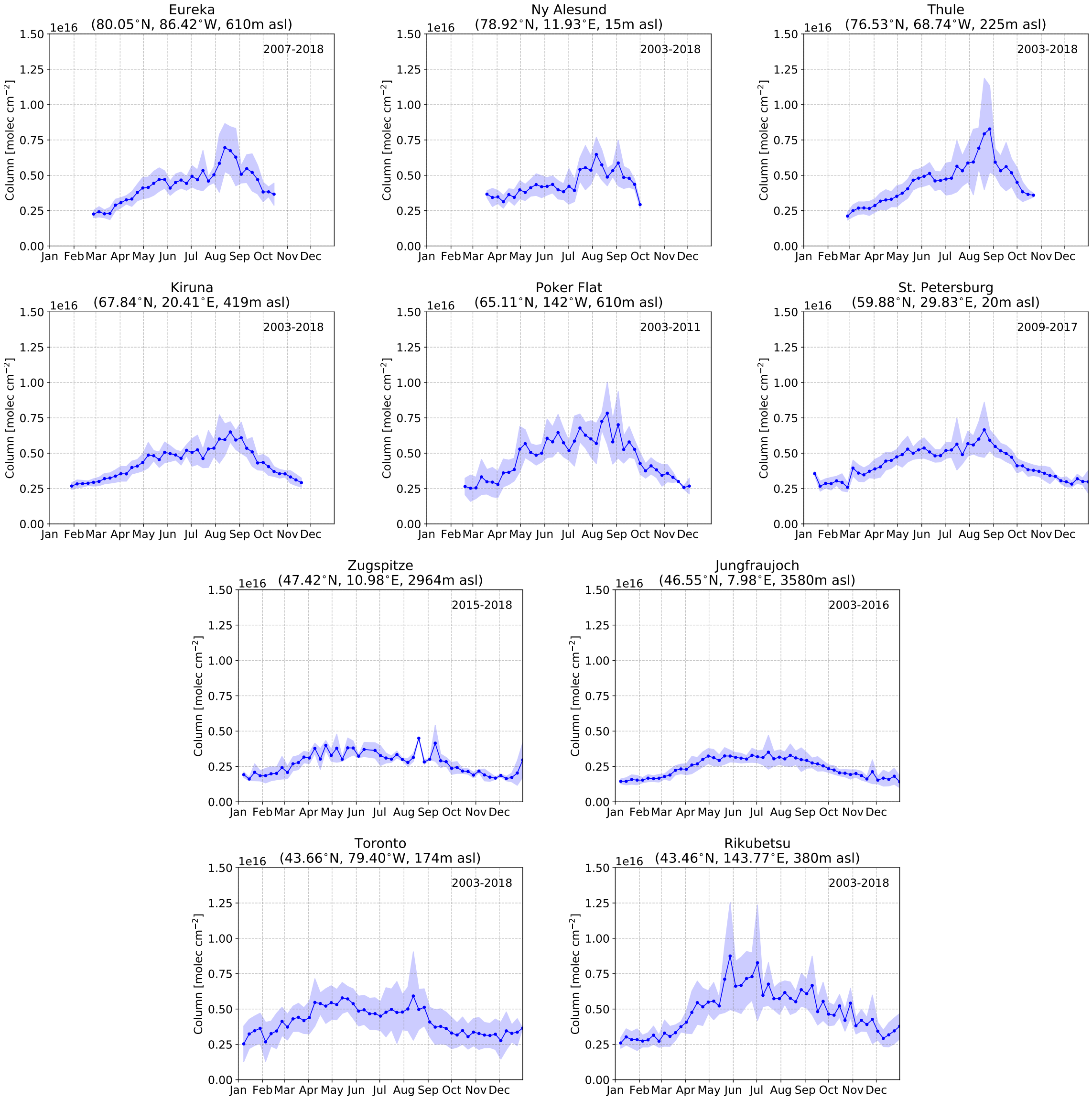

Figure 6.3: Same as Fig. 6.2 but for HCN.

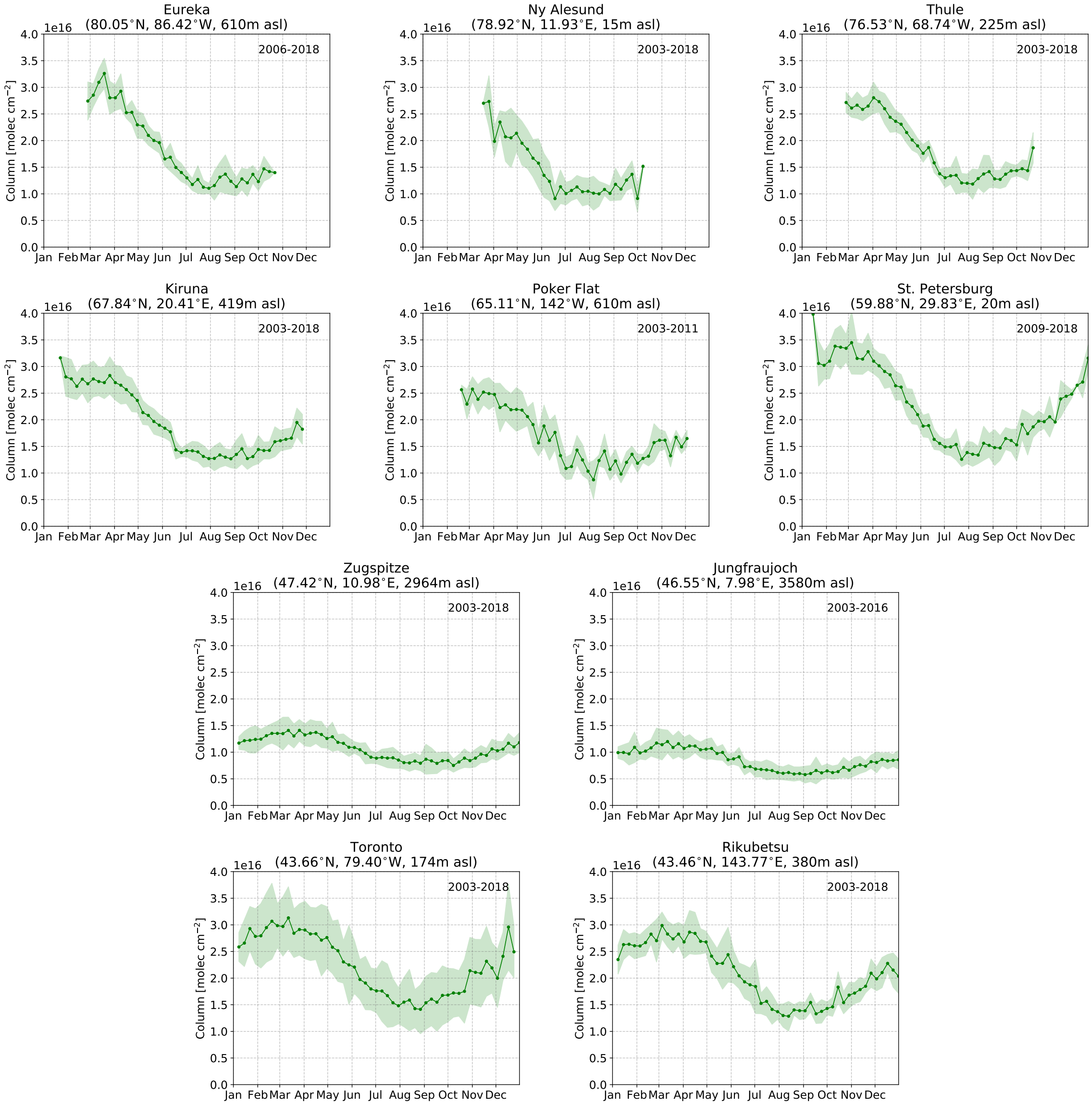

Figure 6.4: Same as Fig. 6.2 but for C_2H_6.

Volume Mixing Ratio Profiles

The VMR profiles of CO, HCN and C_2H_6 for all sites are shown in Figures 6.5, 6.6 and 6.7. In all cases, the profiles of each species are similar between sites and tend not to show drastic differences. It should be noted, that these profiles do not represent the true atmospheric profile of the species due to limited vertical resolution of the measurement, which is inherent in remote sensing measurements of this kind. The retrieved profiles generally follow a similar shape to the a priori profile, where deviations from the a priori are a result of the measurement. The information content of the retrieval will be discussed in the following section. In general, the profiles of all species exhibit greatest variability in the troposphere due to the abundance of these species in this region as these species are considered to be primarily tropospheric. The the tropospheric column of CO, HCN and C_2H_6 comprise, on average, greater than approximately 90% of the total column for CO, 95% for HCN, and 98% for C_2H_6.

The VMR profiles of CO (Figure 6.5) exhibit the greatest values in the lower free troposphere (surface-6 km) at all sites, with values ranging from approximately 120-170 ppbv, with greater concentrations at the polluted sites of Toronto, St. Petersburg and Rikubestu. These sites also illustrate a peak CO concentration at the surface layer due to the influence of local or nearby emissions. For Rikubetsu, a slight increase in concentration from the surface (∼170 ppbv) to 1 km (∼175 ppbv) with concentrations decreasing with altitude as a result of the transport of CO in the free troposphere from nearby Asian sources is observed. Decreasing concentrations and reduced variability of the retrieved profiles with altitude is observed at all sites as transported CO is generally well mixed. Poker Flat shows greatest variability of the CO profiles due to the transport of Asian pollution in the spring and wildfires in Eurasia and Alaska in the summer (Kasai et al., 2005b).

The VMR profiles of HCN (Figure 6.6) are variable amongst sites, with surface-layer concentrations ranging from ∼190-310 pptv. For most sites, a peak in the concentration is observed between 6-10 km, with decreasing concentrations above. The HCN vertical profiles generally show increasing concentrations from the surface to the mid-troposphere and decreasing concentrations above. The urban sites, St. Petersburg and Toronto show decreasing concentrations from the surface due to the influence of local anthropogenic sources, mainly automobile use (Baum et al., 2007; Moussa et al., 2016). Accumulation of HCN in the upper troposphere is the result of its long lifetime and limited dry deposition to the ocean (Singh, 2003). This is most evident at Ny-Ålesund, which is isolated from local sources and illustrates an upper-troposphere peak between 7-9 km, with a concentration of approximately 330 pptv.

The VMR profiles of C_2H_6 (Figure 6.7) follow a similar vertical structure to that of CO as a result of their common sources. For the urban sites, St. Petersburg and Toronto, the concentration is greatest at the surface layer, approximately 2 ppbv and 2.4 ppbv respectively, as a result of local sources. Rikubetsu shows a peak near 1.7 km of 1.6 ppbv, due to the transport of emissions in the free troposphere from nearby Asian sources. For Arctic sites, Eureka, Ny-Ålesund, Kiruna and Poker Flat, C_2H_6 profiles show a broad peak in the free troposphere, generally between 1-7 km, which is indicative of the long-range transport of pollution.

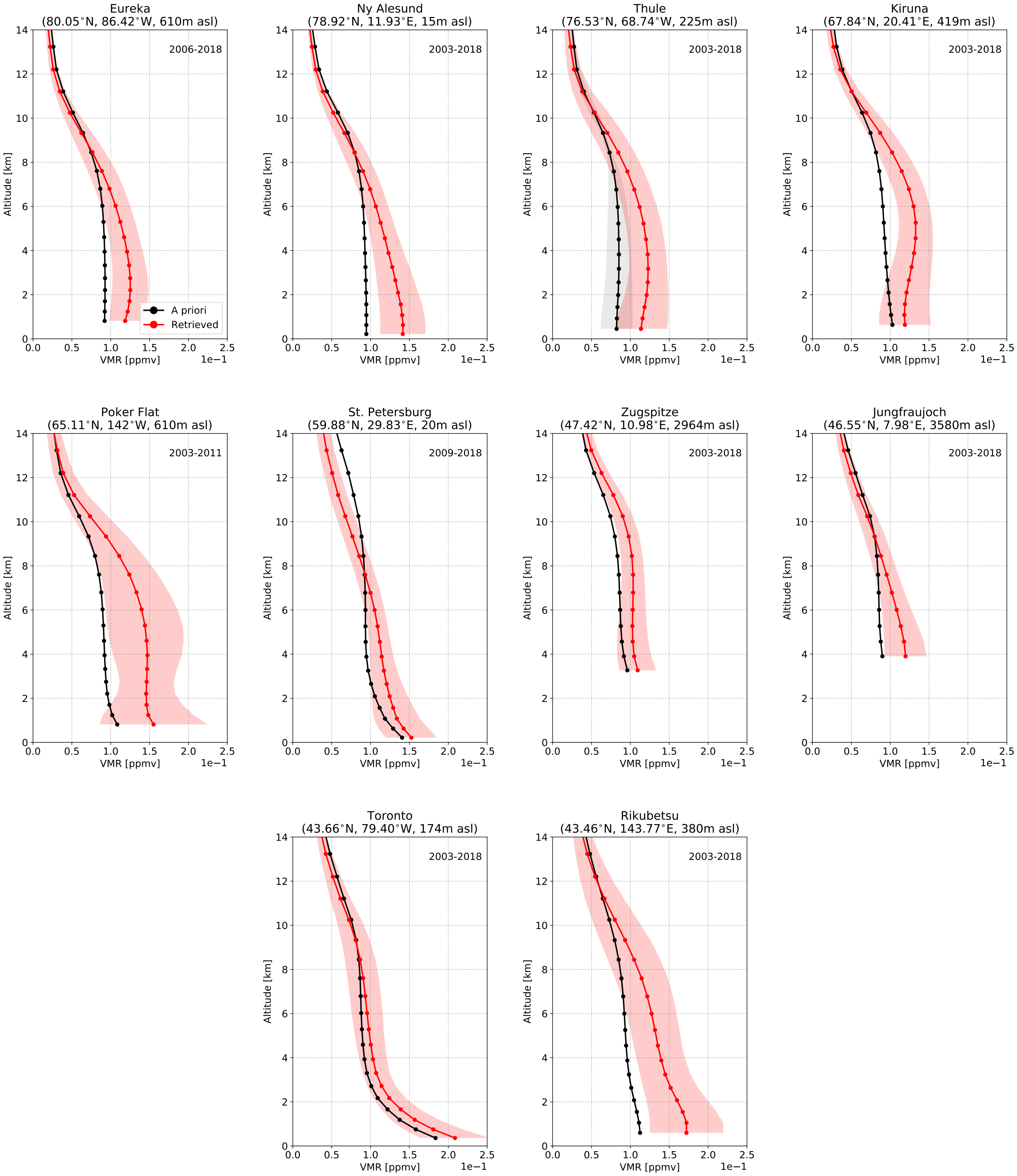

Figure 6.5: Mean retrieved (red) and a priori (black) VMR profiles of CO taken over all years of measurements at each site. The shaded region indicates the 1σ standard deviation from the mean. The circle markers indicate the layer centers of the FTIR vertical retrieval grid.

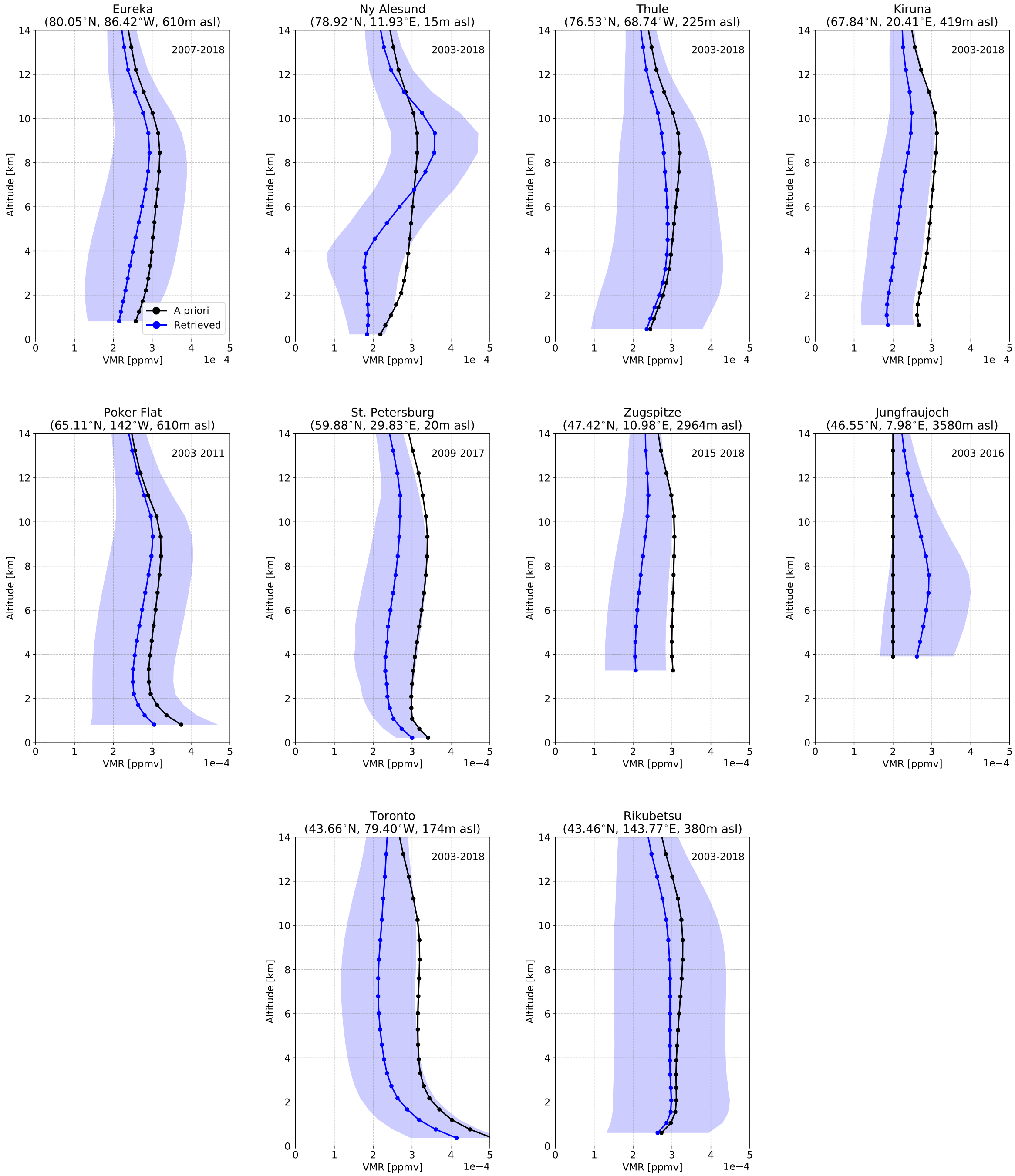

Figure 6.6: Same as Fig. 6.5 but for HCN.

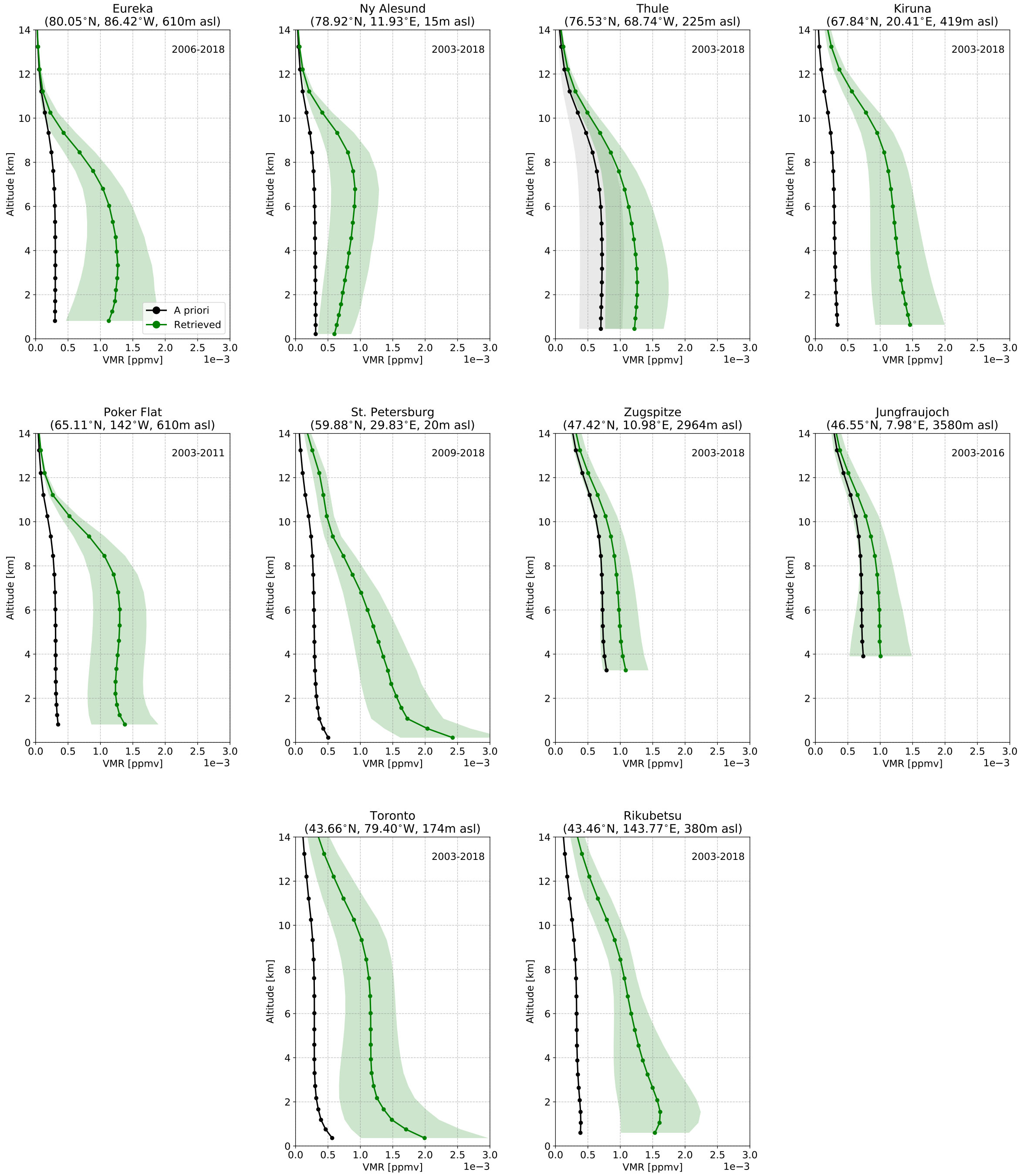

Figure 6.7: Same as Fig. 6.5 but for C_2H_6.

Averaging Kernels

The averaging kernel characterizes the vertical information content of the retrievals as described in Rodgers (2000). We consider the total column averaging kernel (**a**), rather than the averaging kernel matrix (**A**). We define the total column averaging kernel vector:

$$\mathbf{a} = \mathbf{C}^T\mathbf{A}, \tag{6.1}$$

where **C** is the total column operator in units of molecules cm^{-2} and T denotes the transpose. The VMR averaging kernel matrix, **A**, is in VMR/VMR units. The total column averaging kernel may be normalized:

$$\hat{a}_i = a_i/C_i, \tag{6.2}$$

where i is the index of the ith level of the FTIR vertical retrieval grid. The normalized total column averaging kernel ($\hat{\mathbf{a}}$) is unitless and represents the sensitivity to a change in partial column for the vertical level i. The normalized total column averaging kernel may then be applied to the partial column profile to obtain the smoothed column, as will be discussed further in Section 6.3.5. For this purpose, normalized total column averaging kernel values near unity throughout the troposphere are desired, which would minimize biases due to differences in the vertical sensitivities when computing the ratios of columns of different species (as will be done in the following section).

The mean normalized total column averaging kernels, referred to as simply the total column averaging kernel hereinafter, for CO, HCN and C_2H_6 are shown in Figure 6.8. For all sites, the total column averaging kernels of CO show a value near 1 throughout the troposphere, with a slight decrease to values below unity above 5 km. For HCN, the total column averaging kernels increase from the surface, with maximum values in the upper troposphere. The total column averaging kernels of C_2H_6 show similar structure to HCN, with maximum values in the mid to upper troposphere. For all sites, it can be concluded that CO retrievals exhibit minimal sensitivity bias in the troposphere. For HCN and C_2H_6, the total column averaging kernel is greatest in the upper troposphere.

For all species and sites, the total column averaging kernels are not highly variable in time. The variability of the total column averaging kernel is mainly due the changes in the vertical distribution of the species. In particular, total column averaging kernel values generally increase with greater concentration of the species. There is some dependence on the SZA of the measurement which varies seasonally, as the SZA is related to the sampled slant path through the atmosphere. At high SZAs, the longer slant path results in greater DOFS, and hence greater averaging kernel values. The a priori covariance matrix, which is site and species dependent, also influences the total column averaging kernel.

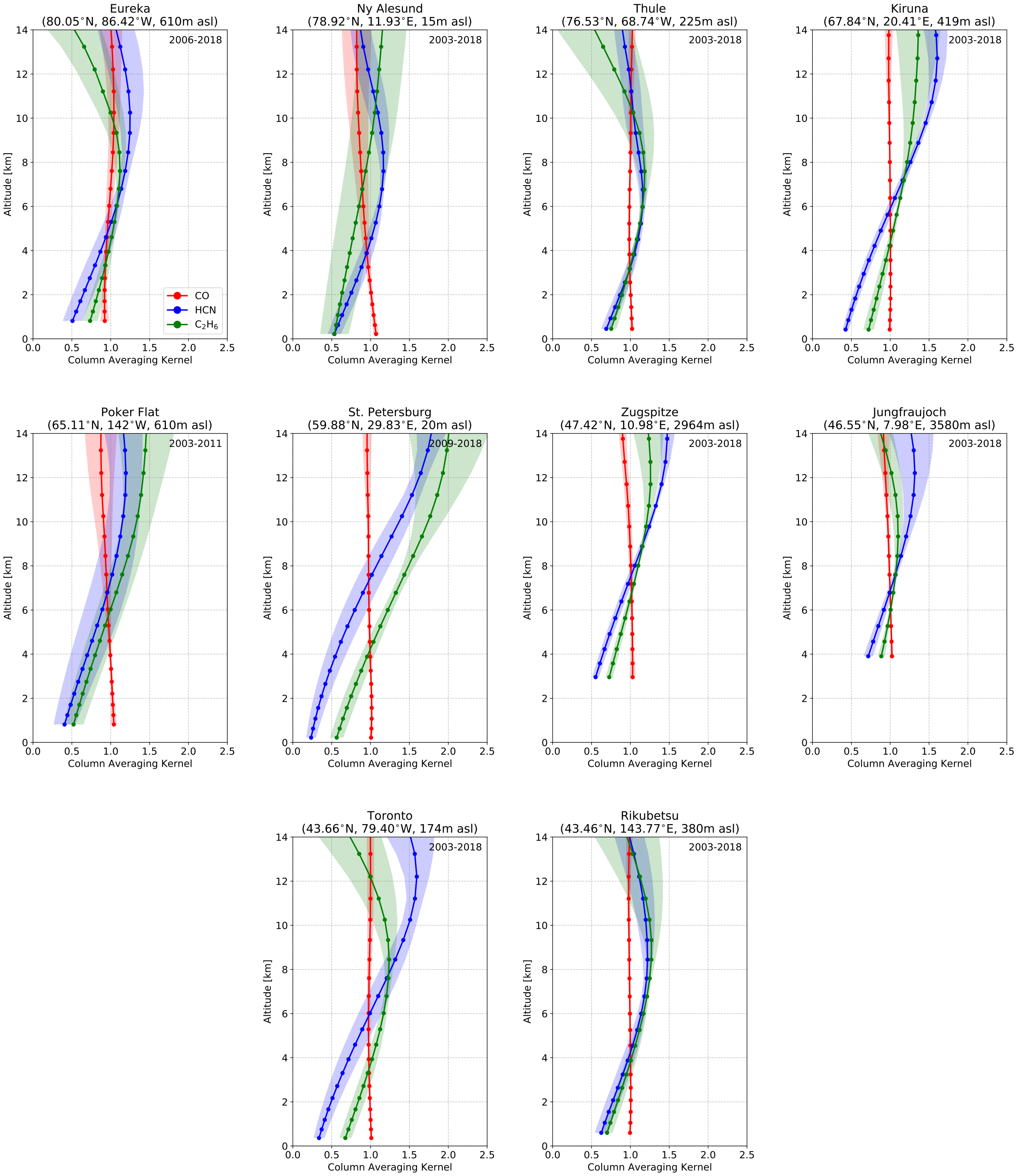

Figure 6.8: Mean CO, HCN and C_2H_6 normalized total column averaging kernels in units of molec cm^{-2}/ molec cm^{-2}, taken over all years of measurements at each site. The shaded region indicates a 1σ standard deviation from the mean. The circle markers indicate the layer centers of the FTIR vertical retrieval grid.

6.3.2 Detection of Wildfire Pollution Events

As was illustrated in Section 6.3.1 and Figure 6.2, a seasonal cycle of CO is observed, with the amplitude varying by site location. Over a long time series, CO may be subject to inter-annual trends as a result of changing emissions of CO and its precursors. Additionally, non-clear sky conditions and instrument downtime result in periodic gaps in measurements and non-uniform time intervals between measurements. As a result of these factors it can be difficult to determine baseline or ambient concentrations of CO and therefore to detect enhancements of CO in the FTIR time series. To mitigate these influences, we account for the seasonal cycle and inter-annual variability of the CO time series measured at each FTIR site following Thoning et al. (1989):

$$C(t) = a_0 + a_1 t + a_2 t^2 + \sum_{n=1}^{4} b_n \cos(2\pi n t) + c_n \sin(2\pi n t), \tag{6.3}$$

where C is the column CO concentration as a function of time t. The coefficients a_n account for the inter-annual trends of CO, while the fourth-order Fourier series with coefficients b_n and c_n captures the seasonal cycle of CO. The choice of order for both the polynomial and Fourier components of the fits were limited to third and fourth order following past studies (Thoning et al., 1989; Zellweger et al., 2009).

In Chapters 4 and 5, fire-affected periods in the FTIR CO total column measurements were identified by CO measurements that exceeded a 1σ standard deviation from the monthly mean over all years of measurements at the respective site. This method was employed as a preliminary means of identifying the fire-affected measurements in the CO time series; however, this method does not take into account the inter-annual variability and trends of CO and therefore may result in an over detection of CO enhancements over a long-term time series. Instead, an alternative method is applied following Zellweger et al. (2009) to detect CO enhancements in the time series at each site.

First, the fitted function is subtracted from the data to yield the residual. Assuming a normal distribution of baseline values around the fitted function, the negative residual is mirrored into the positive direction. Enhanced CO measurements are defined as those greater than a specified threshold of the mirrored residual above the fitted function. The threshold is defined as a multiple of the standard deviation σ of the mirrored negative residual as listed in Table 6.3. The threshold is 1σ for all sites, with the exception of Rikubetsu where a 2σ standard deviation was used as a result of the greater variability CO due to nearby Asian sources. The selected values are listed in Table 6.3.

The detected CO enhancements at each site are then binned by date to define individual events. The time window selected for binning is listed in Table 6.3 for each site and based on the measurement density at the respective site. Enhanced CO measurements separated in time by this duration are binned as separate events, while consecutive measurements within this time window are defined as a single event. Binning events minimizes the influence of varying plume composition, and also separates CO enhancements that may not be of wildfire origin. This is particularly important for the calculation of the enhancement ratio which will be described below. Longer separation times are selected for sites that are likely to be continually influenced by wildfire emissions. These values are summarized in Table 6.3. At this stage, no attribution of the detected CO enhancements to any source has been performed and these enhanced periods simply indicate possible pollution events.

To isolate potential wildfire pollution events, we exploit the fact that trace gas emissions from wildfires are specific to burning phase and vegetation type (Ward and Hardy, 1991; Yokelson et al., 1999; Andreae and Merlet, 2001; Yokelson et al., 2009; Akagi et al., 2011; Urbanski, 2013, 2014) and therefore it would be expected that emissions of CO, HCN and C_2H_6 originating from a wildfire source would be correlated within a plume. Emissions at the fire source are characterized by the emission ratio (ER; Andreae and Merlet, 2001; Akagi et al., 2011) relative to CO, which quantifies the amount of a trace gas species emitted relative to the amount of CO emitted. Since FTIR observations of this kind are measuring the emissions downwind of the source, the enhancement ratio (EnhR; Lefer et al., 1994) is considered:

$$\mathrm{EnhR_X} = \mathrm{slope}\left(\frac{[\mathrm{X}]}{[\mathrm{CO}]}\right)_{\Delta t=1\mathrm{hr}} \tag{6.4}$$

where [X] is the column of the trace gas of interest, and [CO] is the column of CO. The enhancement ratio is related to the emission ratio with the influence of plume aging by chemical loss, deposition and dilution of the plume during transport. Lifetimes of CO, HCN and C_2H_6 are generally longer than plume transport times which range from several days to approximately two weeks (Damoah et al., 2004) and therefore these species do not undergo chemical considerable chemical loss. Furthermore, we do not take into account the background concentrations which can cause uncertainty in interpreting the enhancement ratio as the ambient conditions are likely to vary along the plume trajectory (Yokelson et al., 2013).

To calculate the enhancement ratios from the FTIR measurements, the detected CO enhancements for each event were paired with the nearest HCN and C_2H_6 measurement taken within 1 hr. A 1-hr time interval was chosen to maximize the number of pairs since CO, HCN and C_2H_6 are measured using different spectral filters and hence the measurements do not occur simultaneously. For events with paired measurements of HCN or C_2H_6 with CO that are fewer than 5, the event is omitted. Setting a minimum number of pairs mitigates the potential of false detections as a result of spurious measurements.

The unified least-squares fitting procedure of York et al. (2004) which accounts for errors in both the ordinal and abscissa coordinates was used to determine a linear regression for the paired fire-affected measurements. The slope of the linear regression is the enhancement ratio for the respective species defined in Equation 6.4. To identify enhancements due to wildfire pollution events, we require that the correlation coefficient

(r) be greater than or equal to 0.5 for both the enhancement ratios HCN and C_2H_6, unless otherwise stated, as summarized in Table 6.3.

HCN is retrieved from NDACC Filter 2 measurements, which is generally covered at least once per measurement sequence of all filters. Similarly, C_2H_6 is retrieved through filter NDACC filter 3. All filters have a different response to the input solar beam intensity and therefore, the measurement noise may vary between subsequent measurements of different filters. For this reason, adequate signal may not be obtained through all filters in the case of partially cloudy or non-clear sky conditions. It was found that for all sites, with the exception of Jungfraujoch, there are a greater number of CO measurements than HCN or C_2H_6. Because of this non-uniform distribution of measurements, the number of detected wildfire events is limited by the number of paired measurements for HCN or C_2H_6 with CO. For this reason, for Ny-Ålesund, Poker Flat and Rikubetsu, the enhancement ratio correlation criteria (shown in Table 6.3) were omitted, resulting in a lower confidence for the detected wildfire pollution events. However, for detected events at these sites, the adjacent AERONET sites provide additional evidence for the detection of wildfire emissions if the measured AOD is simultaneously enhanced with CO as shown in Figure 6.9. Furthermore, the GEOS-Chem tagged CO simulation provides further confidence in the detected wildfire pollution events as discussed in the following section.

Table 6.3: Summary of wildfire pollution event detection criteria for all sites.

Site	CO Enhancement[a] Detection Threshold [σ]	Event Separation[b] [days]	$\mathrm{EnhR_{HCN}}$[c] Minimum r	$\mathrm{EnhR_{C_2H_6}}$[d] Minimum r
Eureka	1.0	7	0.5	0.5
Ny-Ålesund[e]	1.0	14	–	–
Thule	1.0	7	0.5	0.5
Kiruna	1.0	7	0.5	0.5
Poker Flat[e]	1.0	7	–	–
St. Petersburg	1.0	10	0.5	0.5
Zugspitze	1.0	7	0.5	0.5
Jungfraujoch	1.0	7	0.5	0.5
Toronto	1.0	8	0.5	0.5
Rikubetsu[e]	2.0	14	–	–

[a] Threshold for detection of enhanced CO measurements.

[b] Time separation between detected CO enhancements to categorize individual events.

[c] Minimum correlation coefficient r for $\mathrm{EnhR_{HCN}}$.

[d] Minimum correlation coefficient r for $\mathrm{EnhR_{C_2H_6}}$.

[e] No criteria applied for enhancements ratios due to a lack of coincident CO, HCN and C_2H_6.

Table 6.4: Number of measurements of CO, HCN and C_2H_6 for all sites from 2003-2018 unless otherwise stated. Number of pairs of HCN and C_2H_6 with CO in the 1-hr window is also shown with the mean time difference between paired measurements (Δt).

Site	CO	HCN	HCN:CO	Δt [min]	C_2H_6	C_2H_6:CO	Δt [min]
Eureka[a]	5411	4674	4352	10	3578	3316	11
Ny-Ålesund	1349	1115	512	28	1129	541	25
Thule	6369	2586	1399	22	3894	1782	11
Kiruna	1999	1866	1597	15	2650	1883	32
Poker Flat[b]	2602	1791	1432	24	1638	1343	28
St. Petersburg[c]	4289	3846	2552	31	4154	3706	0[d]
Jungfraujoch[e]	4844	3244	2409	31	11372	6572	34
Zugspitze[f]	19445	903	895	17	13539	13307	8
Toronto	3779	2978	2104	33	4276	2877	22
Rikubetsu	1199	1105	784	19	1057	633	31

[a] From 2006-2018.

[b] From 2003-2011.

[c] From 2009-2018.

[d] Jungfraujoch uses five non-standard filters resulting in a greater number of C_2H_6 measurements.

[e] St. Petersburg uses two non-standard broadband filters and therefore CO and C_2H_6 measurements occur simultaneously.

[f] Zugspitze HCN measurements began in 2015 while CO and C_2H_6 measurements are reported from 2003-2018.

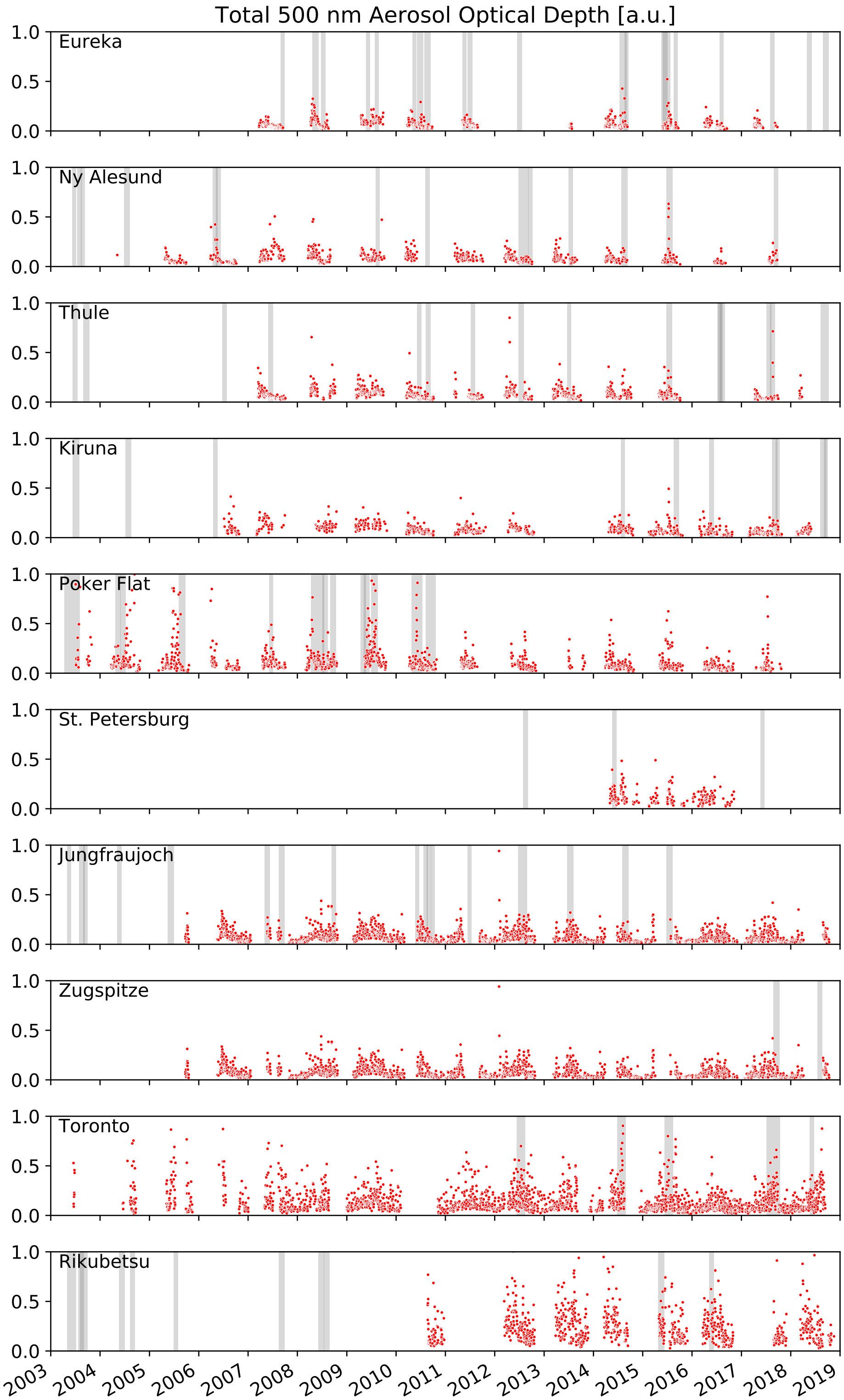

Figure 6.9: Total 500 nm aerosol optical depth from the adjacent AERONET sites listed in Table 6.1. The grey shaded regions indicated the period of fire-affected measurements detected at each FTIR site.

6.3.3 Source Attribution

A GEOS-Chem tagged CO simulation was performed as described in Section 6.2.2 for the time period of 2003-2018, giving 6-hourly instantaneous VMR profiles of the tracers listed in Table 6.2. The GEOS-Chem simulation provides a means of evaluating the source attribution for the detected wildfire pollution events in the FTIR time series. Source attribution is performed as follows. First, the GEOS-Chem CO VMR profiles in the grid box containing the respective FTIR site were converted to partial column profiles and linearly interpolated and regridded onto the FTIR vertical retrieval grid. This was necessary in order to account for the differences in the surface levels of the model and the FTIR sites (Barret et al., 2003). For each of the detected events, the period of fire-affected measurements is considered. For this fire-affected window, we define the first-order rate of change of the CO partial column contribution for each of the GEOS-Chem tagged biomass burning CO tracers:

$$\frac{\mathrm{d}[\mathrm{CO}]_{\mathrm{X}}}{\mathrm{d}t} = \frac{[\mathrm{CO}]_{\mathrm{X}}(t_i) - [\mathrm{CO}]_{\mathrm{X}}(t_{i-1})}{t_i - t_{i-1}}, \tag{6.5}$$

where $[\mathrm{CO}]_{\mathrm{X}}$ is the column (in molec cm^{-2}) of the CO tracer X and t_i is the time of the GEOS-Chem timestep. Within a wildfire pollution event, it is expected that a rapid increase of the CO contribution would be observed, resulting in a positive value $d[\mathrm{CO}]_{\mathrm{X}}/dt$. Similarly, as the plume passes or dissipates, a negative value of $d[\mathrm{CO}]_{\mathrm{X}}/dt$ would be observed. Considering this, the so-called impulse is then defined:

$$I_{\mathrm{X}} = \int_{t_0}^{t_f} \left| \frac{\mathrm{d}[\mathrm{CO}]_{\mathrm{X}}}{\mathrm{d}t'} \right| \mathrm{d}t' \tag{6.6}$$

where t_0 and t_f correspond to the start time and end times of the detected event. The absolute value is used since we do not discriminate against positive of negative rates of change. Since the model output timesteps are discrete and constant, using the definition of Equation 6.5, Equation 6.6 may be approximated as:

$$I_{\mathrm{X}} = \sum_{i=1}^{N} |[\mathrm{CO}]_{\mathrm{X}}(t_i) - [\mathrm{CO}]_{\mathrm{X}}(t_{i-1})| \qquad (6.7)$$

where N is the number of GEOS-Chem output timesteps for the detected FTIR event from t_0 and t_f. The result of Equation 6.7 can be easily interpreted. For a wildfire event, the concentration would rapidly increase as the plume approaches the FTIR site and rapidly decreasing CO concentrations as the plume passes. In contrast, anthropogenic, chemical or biogenic sources of CO are less likely to contribute to episodic enhancements, as these sources tend to vary on seasonal timescales and are more likely to contribute to background concentrations of CO rather than anomalous enhancements. However, the transport of anthropogenic emissions in the winter and spring may result in episodic pollution events. Detection of anthropogenic pollution events was mitigated by the use of the correlation criteria for the enhancement ratios of HCN and C_2H_6 as mentioned previously. For Ny-Ålesund, Poker Flat and Rikubetsu where no correlation criteria was used, winter and spring anthropogenic events were identified and removed based on a qualitative assessment of the GEOS-Chem and AERONET AOD time series.

The value of I_{X} would be greatest for the GEOS-Chem tagged CO tracer contributing to the episodic enhancement detected by the FTIR instrument, and for the reasons stated above, is likely to be of wildfire origin. The source of the detected FTIR enhancement therefore corresponds to the GEOS-Chem tagged CO tracer for which I_{X} from Equation 6.7 is a maximum. The source attribution for the detected wildfire pollution events in the FTIR time series is illustrated in Figure 6.10.

The mean enhancement ratios of HCN and C_2H_6 are summarized in Table 6.5 for the detected wildfire pollution events from BONA and BOAS at all sites. Similar enhancement ratios of HCN and C_2H_6 are observed at Eureka and Thule for both BONA and BOAS. This similarity is expected due to the close proximity of these sites. For Kiruna, slightly lower mean enhancement ratios of HCN were observed of 0.005 for both BONA and BOAS. The enhancement ratio of C_2H_6 at Kiruna is greater than Eureka and Thule, which likely represents the longer travel times of the plume resulting in the dilution of the plume with the background, which can be interpreted as follows. Assuming lifetimes of CO, HCN and C_2H_6 of 30, 75 and 45 days following Viatte et al. (2013, 2015) and Lutsch et al. (2016), the enhancement ratio (EnhR) is given with respect to the emission ratio (ER):

$$\mathrm{EnhR}_X = \mathrm{ER}_X \cdot \frac{\exp\left(-\frac{t}{\tau_X}\right)}{\exp\left(-\frac{t}{\tau_{CO}}\right)}. \tag{6.8}$$

It is easily seen from Equation 6.8 that the enhancement ratios of HCN and C_2H_6 would increase with longer plume travel times t. For example, assuming a 7 day travel time, the enhancement ratios of HCN and C_2H_6 would be a factor of 1.15 and 1.08 greater than their respective emission ratio. For a 14 day travel time, the enhancement ratios of HCN and C_2H_6 would increase by a factor of 1.32 and 1.16, respectively, from their respective emission ratios. However, this is neglecting the influence of plume dilution. With longer travel times, the plume is likely to mix with the background resulting in the enhancement ratios tending to background values. Therefore, the enhancement ratio of C_2H_6 would likely be greater than the enhancement ratio of HCN as a result of the greater mean columns of C_2H_6 in comparison to HCN observed at all sites, as illustrated in Figures 6.3 and 6.4.

With the exception of Toronto, which is likely influenced by local HCN sources, the greatest HCN enhancement ratios are observed at Eureka and Thule, with greater values for the BOAS events, 0.008 and 0.009 for Eureka and Thule, respectively. It is possible that this could reflect the greater HCN emissions of BOAS due to the substantial fraction of peat burning from these events (Yurganov et al., 2011; R'Honi et al., 2013). Lower enhancement ratios of HCN are observed at all other sites (except Toronto) for both BONA and BOAS sources. The lower enhancement ratios of HCN likely reflect the longer travel times to these sites and the dilution of the plume as described above.

Episodic wildfire pollution events at all sites are attributed to either BONA or BOAS sources, with two detected events from SEAS at Jungfraujoch. Temporal correlation of events amongst all sites is observed, with events occurring near in time at different sites is attributed to the same source. Particularly evident are the 2012 Siberian wildfires (Kozlov et al., 2014; Teakles et al., 2017) observed at several sites and attributed to BOAS. Similarly, the 2017 Canadian wildfires (Khaykin et al., 2018; Peterson et al., 2018; Kirchmeier-Young et al., 2019; Lutsch et al., 2019) are also observed at a number of sites. Although, the majority of detected events from 2003-2018 are attributed to BOAS, from 2013-2018 there is an observed increase in the number of events attributed to BONA, with 24 BONA and 14 BOAS events detected during this period amongst all sites. Prior to 2013, 17 BONA and 37 BOAS events were detected. The recent increase in BONA events could be indicative of changes in large-scale climatic patterns (Macias Fauria and Johnson, 2008) resulting in an increase in lighting-induced wildfires (Macias Fauria and Johnson, 2006; Veraverbeke et al., 2017). However, this apparent increase in BONA events does not take into account the possibility of missed detections due to instrument downtime or cloudy sky conditions. Contributions of the biomass burning source regions to CO tropospheric columns at each site will be discussed in the following section.

Table 6.5: Mean enhancement ratios of HCN and C_2H_6 for BONA and BOAS for all detected wildfire events. The value in parenthesis is the 1σ standard deviation of the mean. The number of detected events for each site and source are also given.

	BONA			BOAS		
Site	Nr.	HCN	C_2H_6	Nr.	HCN	C_2H_6
Eureka	9	0.007 (0.003)	0.012 (0.005)	10	0.008 (0.004)	0.013 (0.003)
Ny-Ålesund	9	–	–	6	–	–
Thule	13	0.007 (0.004)	0.010 (0.003)	4	0.009 (0.002)	0.012 (0.003)
Kiruna	4	0.005 (0.002)	0.014 (0.010)	8	0.005 (0.001)	0.016 (0.010)
Poker Flat	8	–	–	5	–	–
St. Petersburg	1	0.004	0.005	3	0.004 (0.001)	0.019 (0.014)
Zugspitze	1	0.003	0.012	1	0.001	0.001
Jungfraujoch	8	0.006 (0.005)	0.015 (0.014)	9	0.004 (0.002)	0.012 (0.004)
Toronto	4	0.010 (0.008)	0.023 (0.008)	1	0.007	0.028
Rikubetsu	0	–	–	11	–	–

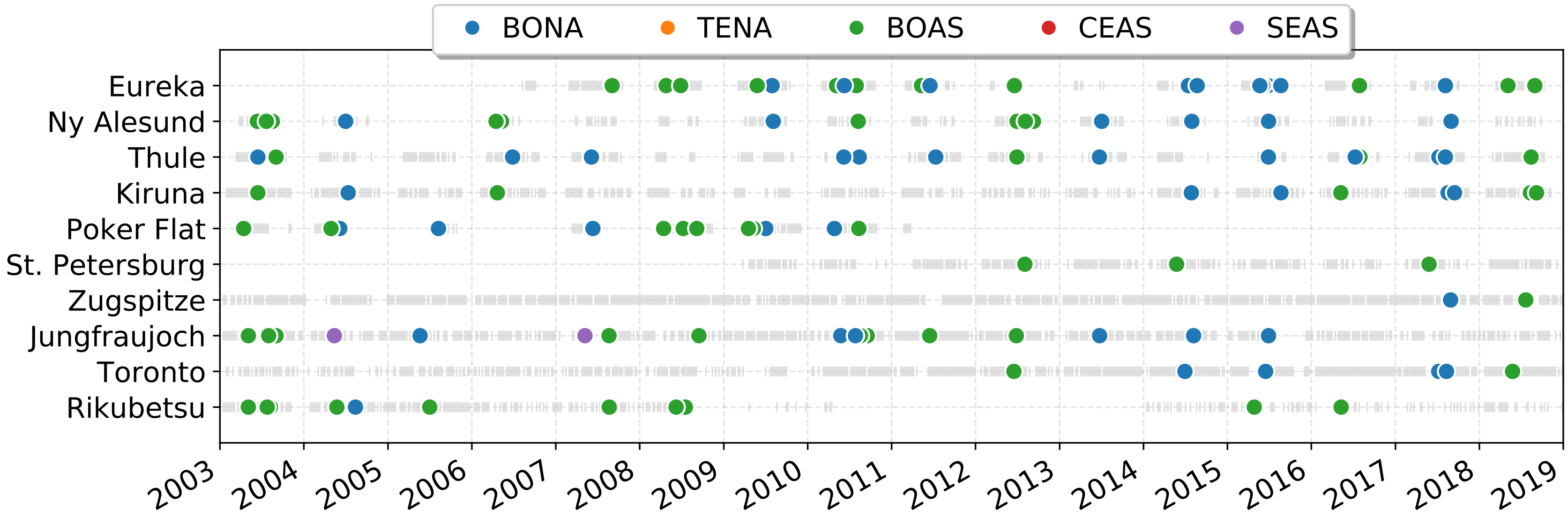

Figure 6.10: Summary of detected wildfire pollution events. The grey bars indicate periods of CO measurements and the coloured points represent the identified wildfire pollution events and their respective source attributed by the GEOS-Chem tagged CO simulation.

6.3.4 Wildfire Contribution to CO

The GEOS-Chem tagged CO simulation provides a means of evaluating the contribution of CO from anthropogenic, chemical and biomass burning sources to the measured CO columns at each FTIR site. Figures 6.12 to 6.15 show the daily-averaged GEOS-Chem and FTIR CO tropospheric columns (surface-12.71 km) for the simulation period from 2003-2018. The relative contribution of biomass burning tracers are also shown. Biomass burning tracers with a mean contribution of less than 3% are not shown. For all GEOS-Chem tagged CO tracers, the partial column profile was linearly interpolated onto the FTIR retrieval grid to account for the differences in surface elevation of the model and FTIR sites.

For all sites, the oxidation of CH_4 is the greatest contribution to the tropospheric CO column as illustrated in Figure 6.11. The magnitude of this source is similar amongst all sites, with the exception of Zugspitze and Jungfraujoch due to their high altitude. Anthropogenic Asian CO sources exhibit the greatest seasonal amplitude at all sites, due to the magnitude of the emissions and the influence of seasonally variable transport (Klonecki, 2003; Stohl et al., 2006; Fisher et al., 2010). European and North American anthropogenic sources show a similar seasonal cycle but smaller in amplitude in comparison to the Asian source. Of note, at Zugspitze and Jungfraujoch, comparable contributions from anthropogenic sources in Asia, North America, Europe and the rest of the world are observed. The oxidation of NMVOCs is a considerable source at all sites, with little seasonal dependence. A slight increase in the NMVOC contribution is observed in the summertime, particularly in July and August, as a result of emissions of NMVOC from biogenic sources and wildfires (Guenther et al., 2000; Wentworth et al., 2018).

Biomass burning sources of CO exhibit the greatest differences amongst sites as seen in Figure 6.11. For most sites, the onset of the biomass burning contribution begins in May with a maximum in August. Similar to the anthropogenic influence, Zugspitze and Jungfraujoch are generally isolated from the direct influence of biomass burning emissions and only show a minor enhancement in the summer. For Rikubetsu, the onset of the biomass burning contributions is observed earlier than for the other sites beginning in March as a result of the influence of Asian biomass burning sources (CEAS, SEAS and EQAS), with slight influence in the summer for boreal emissions from BOAS. The contributions of the biomass burning sources to each site with respect to the results of Section 6.3.3 are discussed below.

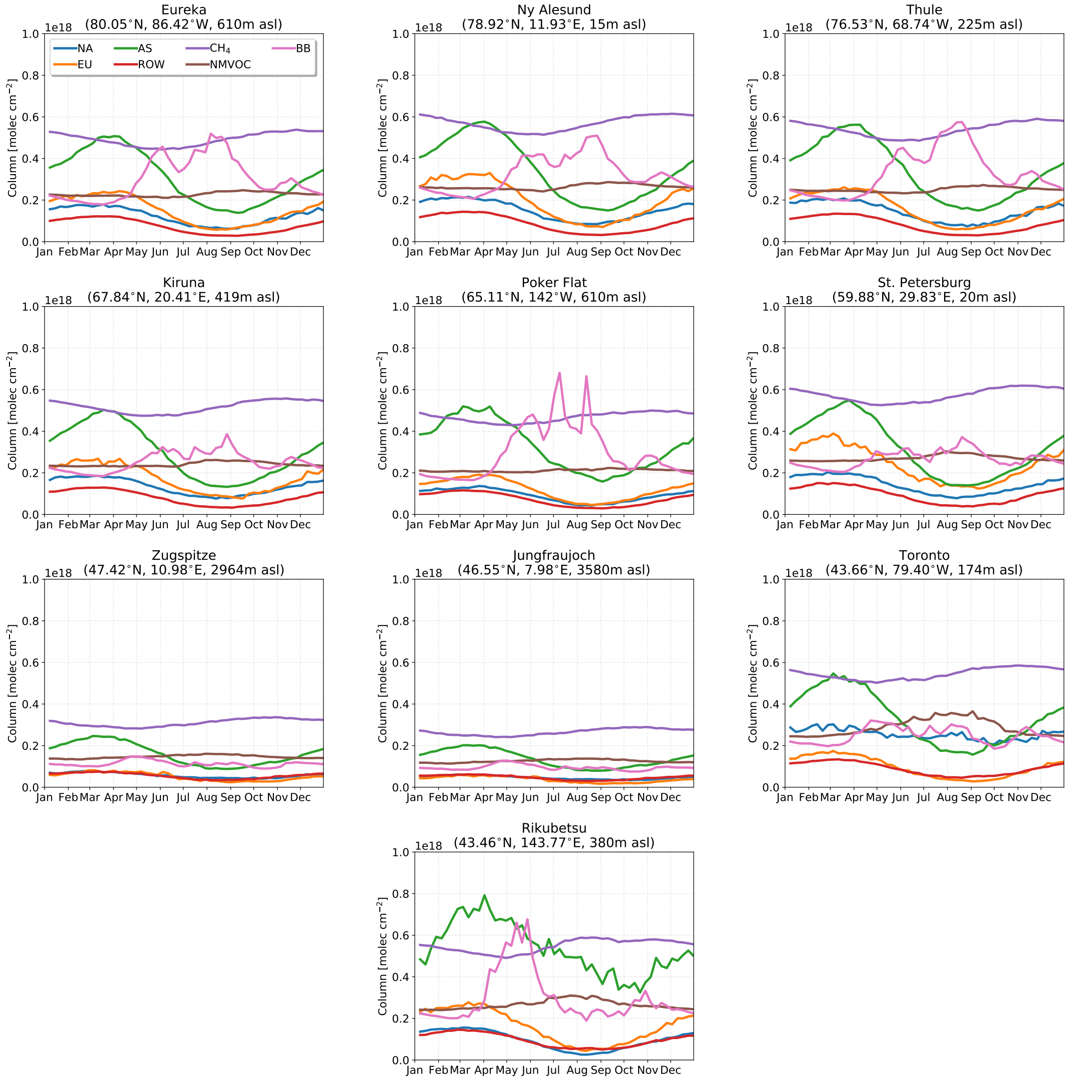

Figure 6.11: Weekly-mean GEOS-Chem tagged CO tracer tropospheric columns. The tagged CO tracer correspond to those listed in Table 6.2. The total biomass burning (BB) contribution is shown and is the sum of all biomass burning tracers from Table 6.2.

High-Arctic Sites

The high-Arctic sites of Eureka, Ny-Ålesund and Thule illustrate strong summertime enhancements of CO and HCN as seen in Figures 6.2 and 6.3, with a moderate enhancement of C_2H_6 shown in Figure 6.4. These enhancements have a maximum in July and August and from Figure 6.12, it is observed that the enhancements are largely due to the influence of BONA and BOAS wildfires. Wildfires in temperate regions (TENA and CEAS) are a small contribution to the CO tropospheric column (<5%) but do not contribute to the detected episodic enhancements. A moderate contribution to CO from CEAS and SEAS is observed, but these are not a source of anomalous enhancements.

Similar contributions are observed for BONA and BOAS among the high-Arctic sites, with a stronger influence from BONA to Eureka and Thule resulting in episodic enhancements of CO contributing greater than 40% to the CO tropospheric column. The strong influence of these sources is the result of the proximity of the high-Arctic sites to these source regions, as well as the efficient summertime isentropic transport (Stohl, 2006). As a result, the direct influence of wildfire plumes at the high-Arctic sites is observed in the FTIR time series, where the effects of plume dilution are minimal.

Furthermore, an early onset in April of the BOAS contribution is observed and is likely the result of the contribution from Siberian wildfires. Siberian wildfires are associated with low-level injected emissions, mainly within the planetary boundary layer and lower free troposphere (Val Martin et al., 2018). The low-level injection of these emissions and the high latitudes of the sources favour efficient transport to the Arctic (Stohl, 2006). In contrast, the Asian sources, CEAS and SEAS, show minor contributions to the CO tropospheric columns at the high-Arctic sites. Transport of these emissions to the Arctic are limited due to the higher potential temperature of these regions in the summertime, preventing isentropic transport to the Arctic (Klonecki, 2003; Stohl, 2006).

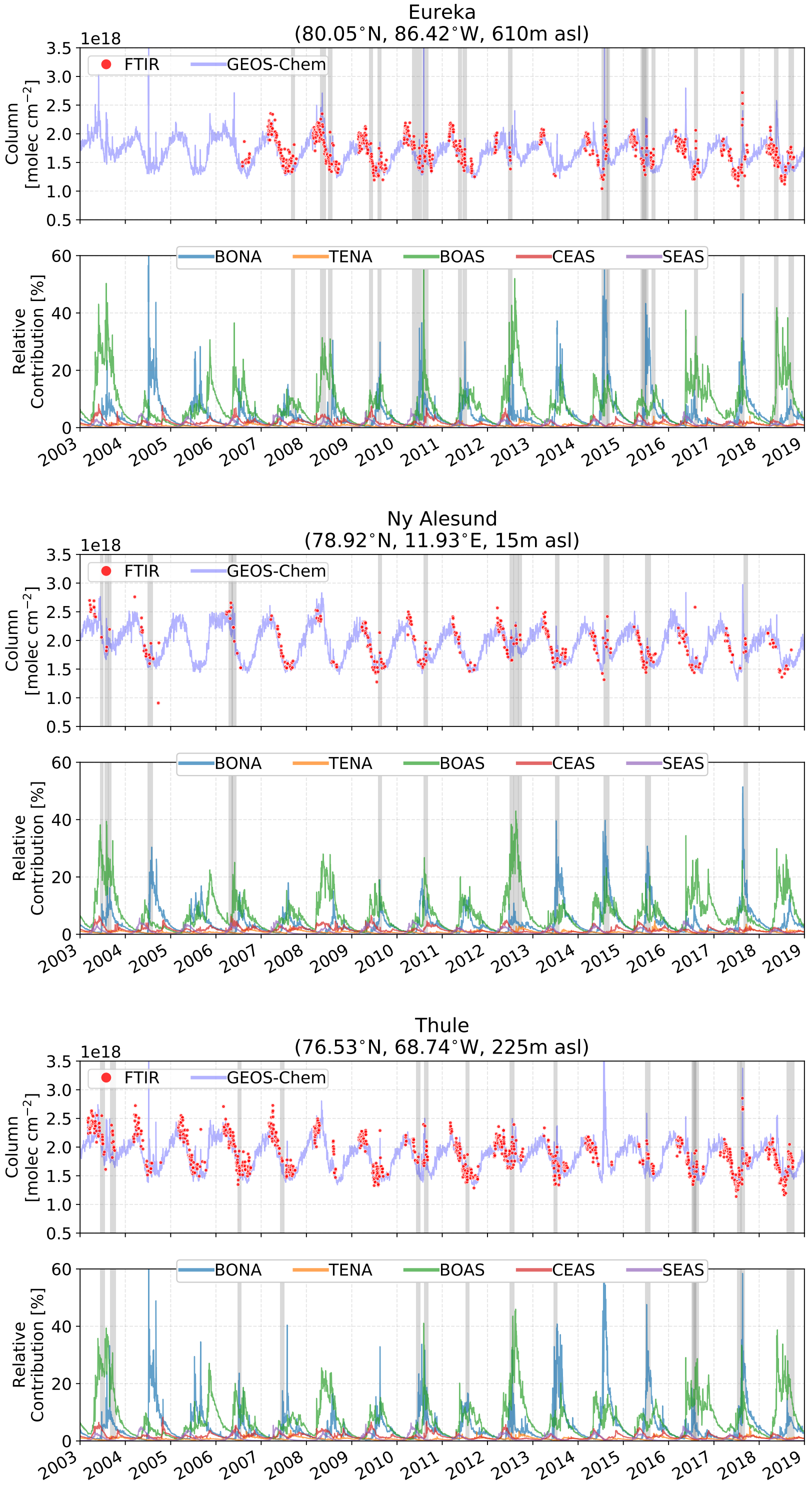

Figure 6.12: Daily-mean CO tropospheric column time series for FTIR and GEOS-Chem (top panel) from 2003-2018 for the high-Arctic sites: Eureka, Ny-Ålesund and Thule. The bottom panel shows the relative contribution (%) of the BONA, TENA, BOAS, CEAS and SEAS CO tracers in the GEOS-Chem simulation to the total CO tropospheric column. The grey shaded regions indicate periods of fire-affected measurements identified in the FTIR time series and summarized in Figure 6.10

.

Arctic Sites

For the high-latitude European sites Kiruna and St. Petersburg, smaller contributions to CO from BONA and BOAS sources are observed, with peak contributions ranging from approximately 5 to 44% for BONA and 12 to 37% for BOAS, with slightly smaller contributions at Kiruna. The smaller contributions from these sites in comparison to the high-Arctic sites is partly due to the greater distances from the wildfire sources. The transport of emissions to these sites is a result of long-range westerly transport that generally exceeds 10 days (Damoah et al., 2004). Because of the long travel times, the plume is often diluted, and therefore, does not generally lead to the episodic enhancements observed at the high-Arctic sites. In contrast, Poker Flat is predominantly influenced by Alaskan wildfires, with contributions to the CO tropospheric column exceeding 50% in many cases. Similarly, the proximity of Poker Flat to BOAS sources makes BOAS a significant contributor to episodic CO enhancements, comparable to the local BONA source.

Similar to the high-Arctic sites, contributions from TENA, CEAS and SEAS to the Arctic sites are minimal and do not contribute to the episodic enhancements of CO, HCN and C_2H_6 detected in the FTIR time series. However, Poker Flat and St. Petersburg generally exhibit greater contributions from CEAS. For Poker Flat, this is the result of Asian outflow transporting emissions from Asian over the Atlantic to Alaska. For St. Petersburg, the proximity to the CEAS sources makes it susceptible to this source. Particularly evident is the large enhancement in July and August of 2010 due to wildfires in the Moscow region (Konovalov et al., 2011; Witte et al., 2011; Yurganov et al., 2011) although not detected in the FTIR time series as there were no measurements during that period.

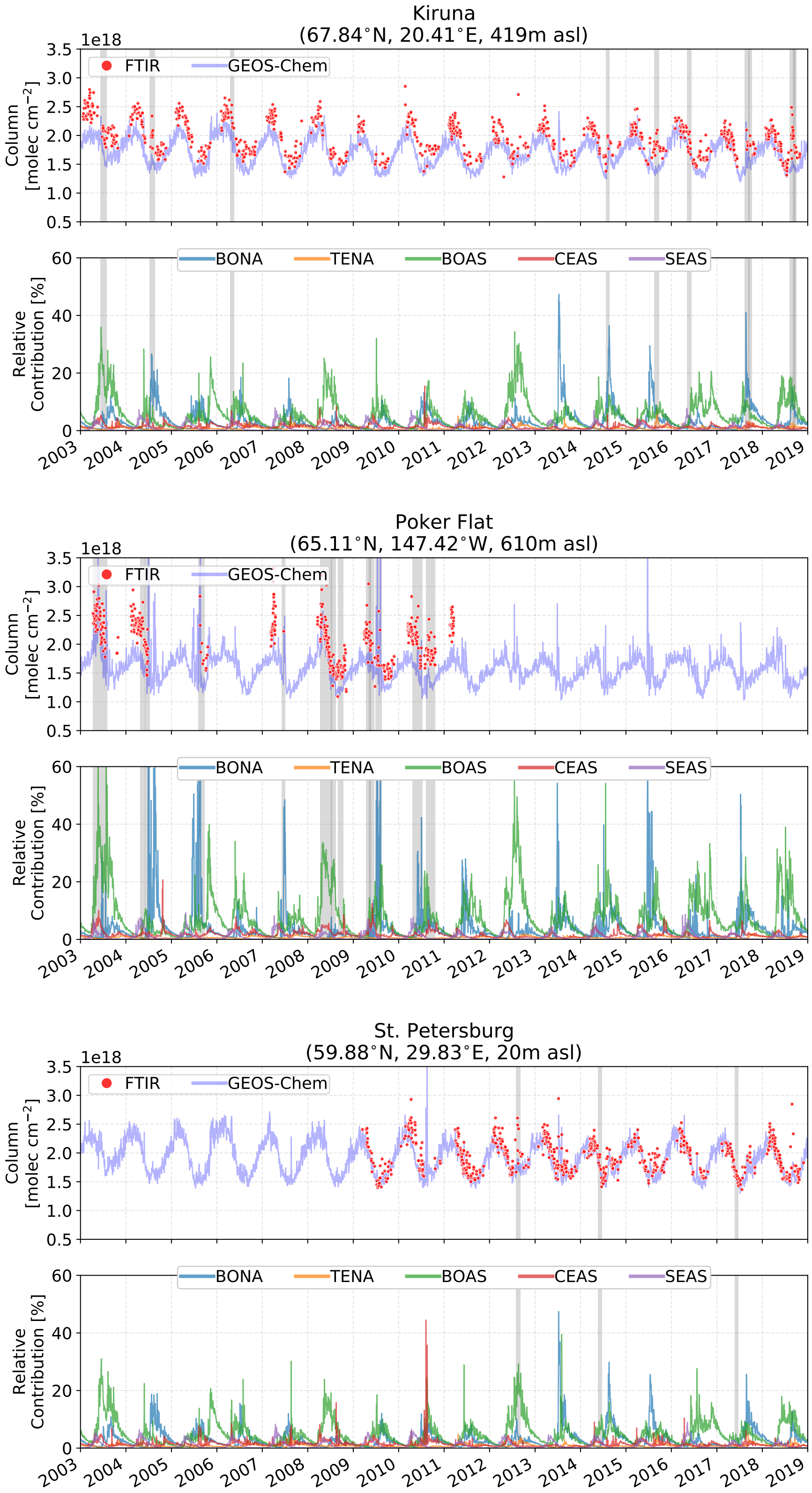
Kiruna
(67.84°N, 20.41°E, 419m asl)

Poker Flat
(65.11°N, 147.42°W, 610m asl)

St. Petersburg
(59.88°N, 29.83°E, 20m asl)

Figure 6.13: Same as Figure 6.12 but for the Arctic sites: Kiruna, Poker Flat and St. Petersburg.

Alpine Sites

The alpine sites, Zugspitze and Jungfraujoch shown in Figure 6.14, differ the most from the other sites considered in this study as a result of their high altitude. It is seen that Zugspitze and Jungfraujoch are most strongly influenced by BOAS, with a mean seasonal maximum contribution of approximately 14% at both sites. The contribution of BOAS emissions to the enhanced columns at Zugspitze and Jungfraujoch are due to hemispheric-scale transport (Damoah et al., 2004), leading to a perturbation to background concentrations of each species. As a result, the enhancements detected in the FTIR time series or GEOS-Chem do not result in the large, episodic enhancements observed at the high-Arctic sites. The contributions from trans-Atlantic transport of BONA emissions, however, exhibit these anomalous enhancements on occasion. Particularly evident are the BONA wildfires of 2013-2015 and 2018. Emissions from boreal Canadian wildfires may be injected into the free troposphere (Val Martin et al., 2018) and in some cases the lower stratosphere (Fromm et al., 2000; Khaykin et al., 2018; Peterson et al., 2018) which may enable the efficient transport of the plume over inter-continental scales (Heilman et al., 2014).

SEAS emissions are a larger contributor to CO enhancements for Zugspitze and Jungfraujoch than for the Arctic or high-Arctic sites. However, such enhancements are not observed in the FTIR time series as the contribution from SEAS is small in comparison to Asian anthropogenic sources as illustrated in Figure 6.11. Transport of Asian biomass burning CO emissions to Europe had been identified in the springtime by Petetin et al. (2018) and attributed to uplifting of emissions into the free troposphere and efficient transport of the westerlies (Bey et al., 2001a). In all cases, Zugspitze and Jungfraujoch are most susceptible to emissions that reach the free troposphere where long-range transport is favoured (Petetin et al., 2018).

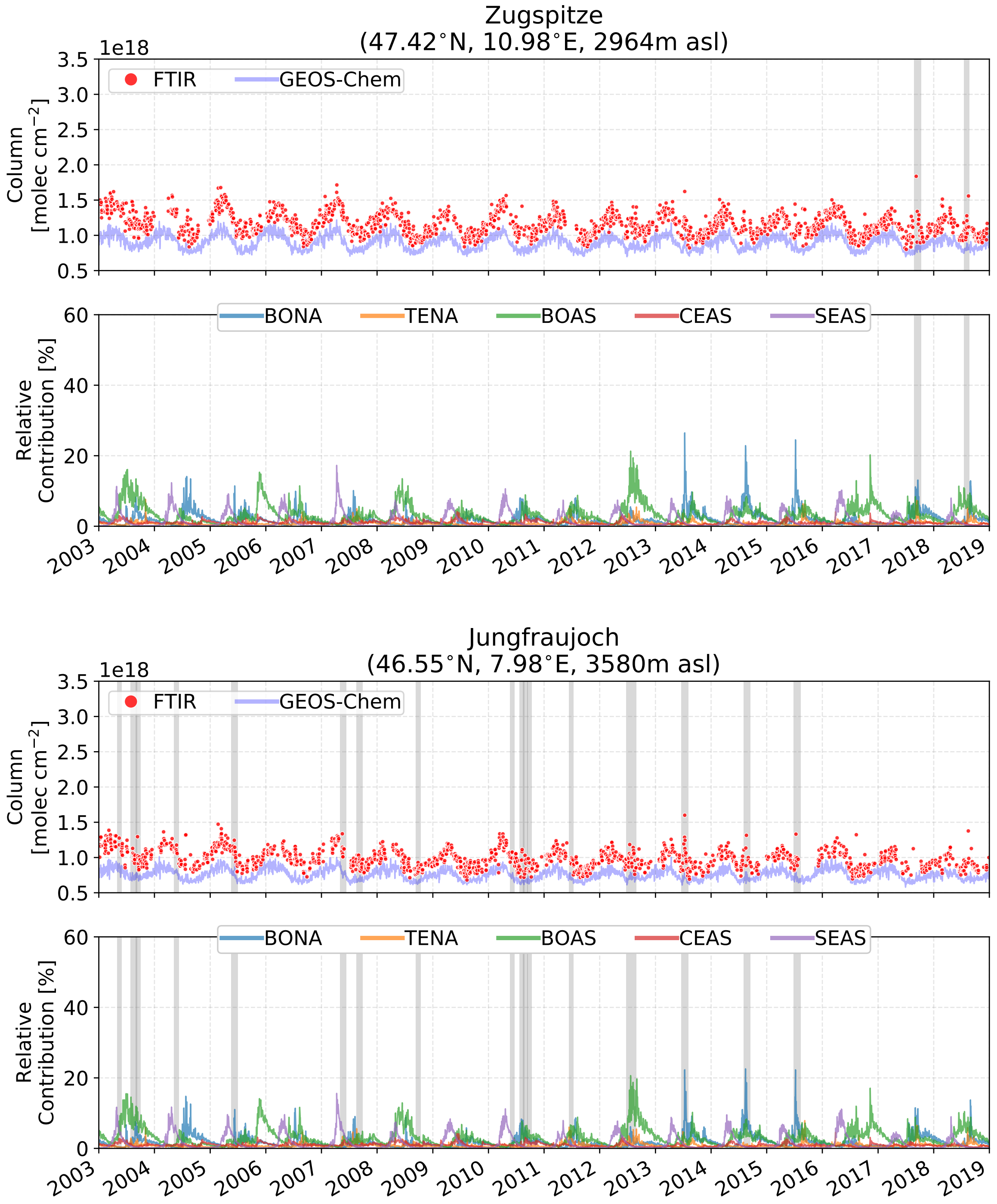

Figure 6.14: Same as Figure 6.12 but for the alpine sites: Zugspitze and Jungfraujoch.

Mid-latitude Sites

Anomalous enhancements in the Rikubetsu time series are dominated by the outflow of BOAS emissions that begin in early springtime and persist throughout the summer and autumn. Episodic BOAS enhancements are observed annually, with contributions that generally exceed 20% and are larger than 50% in many years. The greatest enhancement from BOAS was observed in 2003 as result of the exceptional emissions from Siberia wildfires (Jaffe et al., 2004; Ikeda and Tanimoto, 2015). Although the contribution from BOAS at Rikubetsu is highly variable between years, anomalous enhancements are observed annually in the GEOS-Chem time series, while detection of events in the FTIR time series is limited by the temporal sampling of the FTIR instrument. CEAS and SEAS have moderate contributions ($\sim$10%) to the CO tropospheric column at Rikubetsu in the spring and fall although the influence of these sources are often masked by the greater BOAS emissions during these periods. Other biomass burning sources have minimal contributions and Asian anthropogenic sources are dominant throughout the year as shown in Figure 6.11.

Toronto is most strongly influenced by wildfires of BONA, with detected events in the FTIR time series including 2014 from the Northwest Territories wildfires (Lutsch et al., 2016; Kochtubajda et al., 2019), 2015 from wildfires in Saskatchewan (Dreessen et al., 2016) and the 2017 British Columbia wildfires (Peterson et al., 2018). Although it is in close proximity to TENA sources, mainly from the Western and Southern United States, Toronto is minimally influenced by TENA as the magnitude of these emissions is much smaller than for BONA. Background contributions from CEAS and SEAS are also observed in the springtime although the contribution from Asian anthropogenic sources is dominant. BOAS is also a significant contribution to CO at Toronto in the summertime, but does not generally result in anomalous enhancements as a result of the longer transport times from this region. The 2018 enhancements were attributed to BOAS, while in June 2012, enhancements were present in the FTIR time series and appear to occur simultaneously with the large BOAS contribution (>30%). Minor contributions (<5%) from CEAS are observed in the springtime and autumn, while a moderate influence from SEAS of ~10% is observed in the spring.

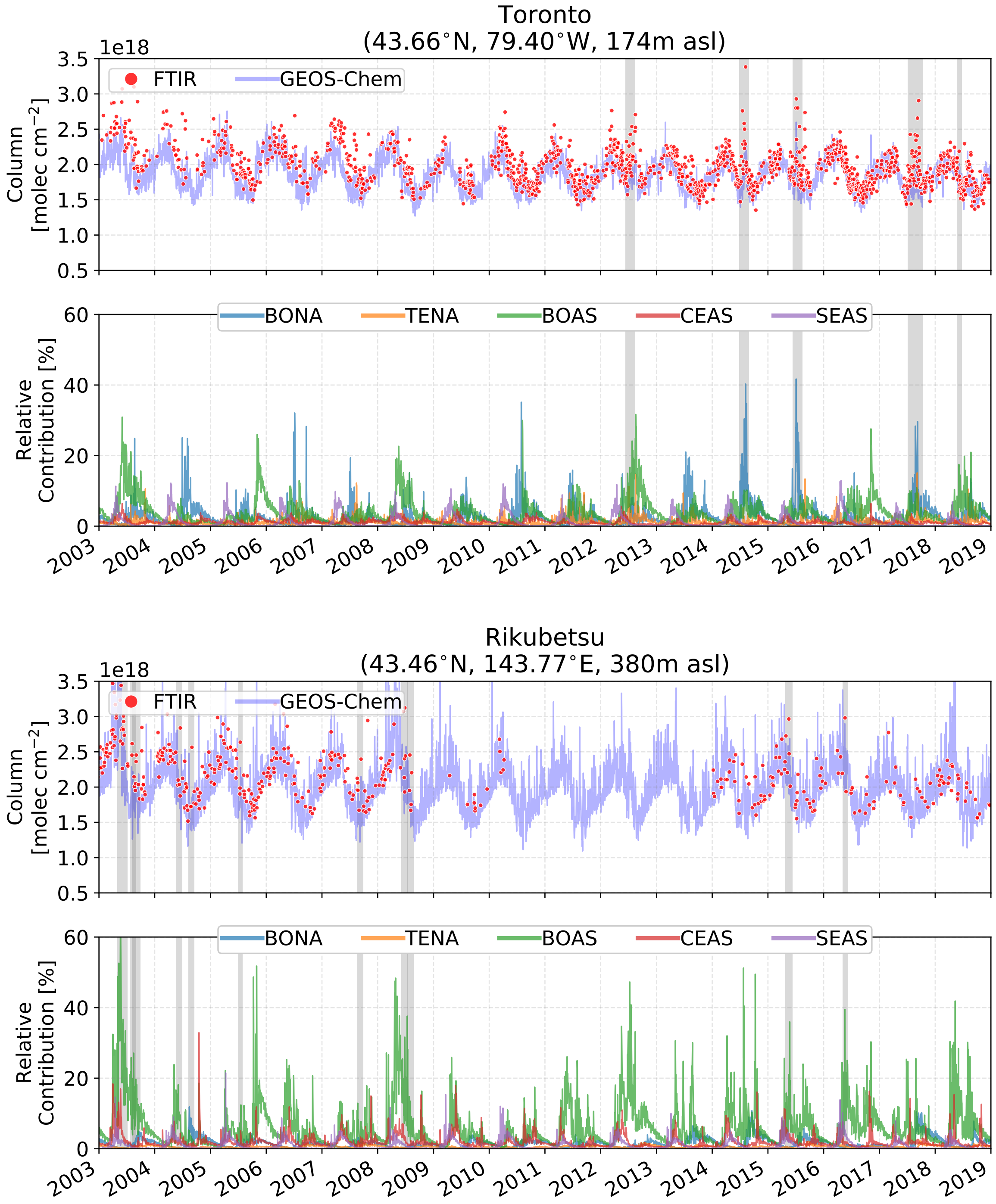

Figure 6.15: Same as Figure 6.12 but for the mid-latitude sites: Rikubetsu and Toronto.

6.3.5 GEOS-Chem to FTIR CO Comparison

The GEOS-Chem CO partial column profiles are smoothed by the normalized FTIR CO total column averaging kernel following Rodgers and Connor (2003):

$$\hat{x}_m = x_a + \mathbf{a}^T \left(\mathbf{x}_m - \mathbf{x}_a \right), \tag{5.1 revisited}$$

where $\hat{x}_m$ is the smoothed model total column, x_a is the FTIR a priori total column, $\mathbf{x}_m$ is the model partial column profile, $\mathbf{a}$ is the FTIR total column averaging kernel, and $\mathbf{x}_a$ is the FTIR a priori partial column profile. Although the smoothing has a minor influence on the smoothed partial column (~1%) it is performed here to mitigate any biases as a result of the a priori profile. The GEOS-Chem CO profiles, FTIR CO profiles and total column averaging kernels are daily averaged and the daily averaged GEOS-Chem profiles are subsequently smoothed. Correlations of the smoothed GEOS-Chem and FTIR CO tropospheric partial columns are shown in Figure 6.16.

For all sites, moderate to strong linear correlations are observed with correlation coefficients (r) ranging from a minimum of 0.66 for Toronto to a maximum of 0.89 at Thule. The slope of the linear regression is indicative of the GEOS-Chem bias relative to the FTIR measurements, with a slope greater than 1.0 representing a high-bias and a slope less than 1.0 representative of a low-bias. For all sites, GEOS-Chem has a low bias as seen in Figures 6.12-6.15. The slopes range from a minimum of 0.49 at Jungfraujoch to a maximum of 0.84 at both St. Petersburg and Rikubetsu.

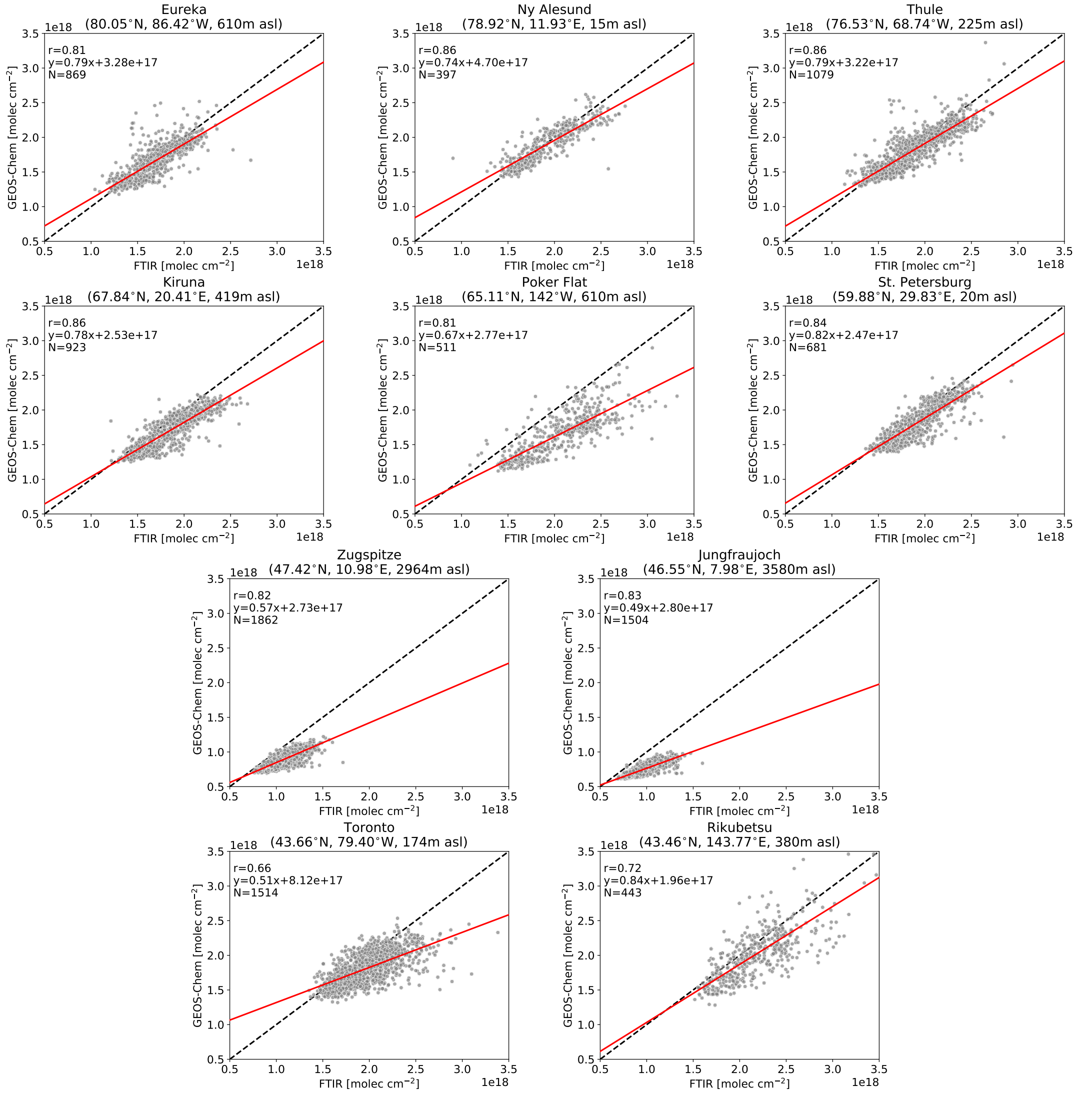

Figure 6.16: Correlation of daily-averaged GEOS-Chem and FTIR CO tropospheric partial columns for all sites from 2003-2018. The linear correlation coefficient (r), linear equation of the regression, and number of measurements (N) are also shown. The black dashed line is the one-to-one correlation and the solid red line is the fitted linear regression.

The underestimation of GEOS-Chem CO is common amongst global CTMs as a result of errors in emissions, transport, and biases in the OH concentrations (Shindell et al., 2006). It is likely that the consistent underestimation of GEOS-Chem CO at all sites is partly due to a high bias of OH (Muller et al., 2018). Seasonal variability of the GEOS-Chem bias is observed as shown in Figure 6.17. The consistent underestimation of GEOS-Chem at Zugspitze and Jungfraujoch (as shown in Figure 6.17) may be the result of excessive stratosphere-to-troposphere exchange (Fischer et al., 2000; Hoor et al., 2002; Pan et al., 2004) contributed by the coarse model resolution, resulting in a low bias of CO in the upper troposphere. A similar underestimation of GEOS-Chem CO in a full-chemistry simulation in comparison to Jungfraujoch FTIR measurements was observed by Té et al. (2016). The high altitude of Zugspitze and Jungfraujoch makes these sites more susceptible to this bias in comparison to the lower altitude sites (Ordóñez et al., 2007). The underestimation at Toronto, and the lower correlation (0.66) than all other sites is possibly the result of the temporal and spatial variability of CO being not well captured due to the coarse model resolution ($2^{\circ}\times2.5^{\circ}$).

Seasonal variability of the GEOS-Chem minus FTIR relative difference is also observed as shown in Figure 6.17 and tabulated in Table 6.6. The representation of the seasonal variability of transport at mid-latitudes and errors in the seasonality are likely to be contributing factors to the variability of the GEOS-Chem minus FTIR CO difference. However, biomass burning emissions are also seasonally dependent and underestimation of GEOS-Chem CO may be partially reflective of an underestimation of GFAS emissions. Particularly evident is the greater underestimation of GEOS-Chem at Rikubetsu in the summer months, during the boreal wildfire season. Eureka and Thule exhibit a greater underestimation of GEOS-Chem in July and August when the boreal wildfire influence is greatest as shown in Figure 6.12. A similar decrease in the GEOS-Chem minus FTIR relative difference is also observed at Kiruna, Poker Flat, St. Petersburg and Toronto. These differences could be indicative of the unresolved plume transport in the model as a result of its coarse vertical resolution (Rastigejev et al., 2010; Eastham and Jacob, 2017) as mentioned in Chapter 5. Additionally, the summertime low CO bias in GEOS-Chem may also be contributed by an underestimation of the secondary production of CO from biogenic emissions of NMVOCs.

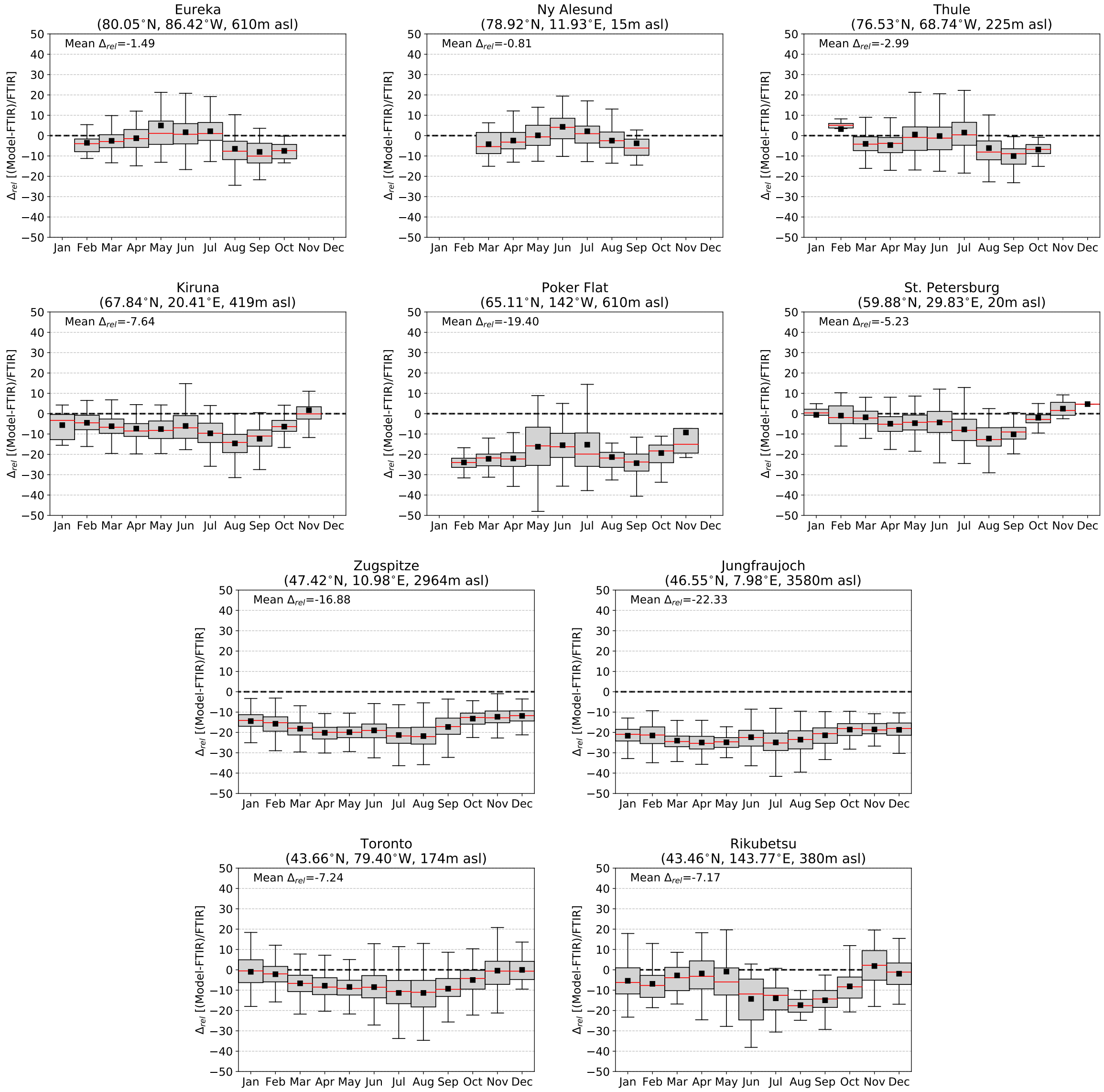

Figure 6.17: Box-and-whiskers plot of the monthly-mean relative difference (%) of GEOS-Chem and FTIR CO taken over all years from 2003-2018. The red line indicates the mean and the black square of the median. The shaded boxes represent the interquartile range of the data and the whisker represent the range. The mean relative difference of all data is listed in the top left corner.

Table 6.6: Monthly-mean relative difference of GEOS-Chem minus FTIR [(model-FTIR)/FTIR]×100% CO tropospheric partial columns over all years for measurements from 2003-2018.

Site	Jan.	Feb.	Mar.	Apr.	May	Jun.	Jul.	Aug.	Sep.	Oct.	Nov.	Dec.	**Yearly**
Eureka	–	-3.5	-2.6	-1.3	5.0	1.7	2.2	-6.5	-8.0	-7.5	–	–	-1.5
Ny-Ålesund	–	–	-4.2	-2.4	0.1	4.3	2.1	-2.5	-3.8	–	–	–	-0.8
Thule	–	3.2	-4.0	-4.6	0.5	-0.2	1.5	-6.1	-10.0	-6.8	–	–	-3.0
Kiruna	-5.6	-4.5	-6.2	-7.3	-7.6	-6.0	-9.7	-14.6	-12.3	-6.4	1.7	–	-7.6
Poker Flat	–	-23.9	-22.2	-22.0	-16.2	-15.5	-15.2	-21.3	-24.3	-19.3	-9.2	–	-19.4
Peterhof	-0.6	-0.9	-1.8	-4.9	-4.7	-4.3	-7.7	-12.2	-10.1	-2.0	2.5	4.7	-5.2
Zugspitze	-14.4	-15.7	-18.2	-20.2	-19.9	-19.0	-21.3	-21.8	-17.3	-13.2	-12.3	-11.9	-16.9
Jungfraujoch	-21.6	-21.5	-24.0	-25.0	-24.8	-22.3	-24.9	-23.6	-21.4	-18.6	-18.5	-18.7	-22.3
Toronto	-1.0	-2.2	-6.6	-7.8	-8.4	-8.5	-11.3	-11.4	-9.3	-5.0	-0.4	-0.0	-7.2
Rikubetsu	-5.4	-6.9	-2.8	-1.8	-0.9	-14.3	-14.0	-17.4	-15.0	-8.1	1.9	-1.9	-7.2

6.4 Summary

Boreal wildfires of North America (BONA) and Asia (BOAS) were found to be the greatest contributors to episodic CO enhancements at ten Northern hemisphere FTIR sites: Eureka, Ny-Ålesund, Thule, Kiruna, Poker Flat, St. Petersburg, Zugspitze, Jungfraujoch, Toronto and Rikubetsu. Wildfire pollution events were identified by detection of enhancements of CO in the FTIR time series. With the exception of Ny-Ålesund, Poker Flat and Rikubetsu, detected CO enhancements were correlated with coincident measurements of HCN and C_2H_6 to determine their enhancement ratios, providing evidence for the detection of wildfire pollution events. The GEOS-Chem tagged CO simulation allowed for source attribution of the detected events and for the source contribution to CO at each site to be evaluated.

The greatest numbers of FTIR enhancements were observed at Eureka (19) and Thule (17) due to their proximity to BONA and BOAS, with both sources contributing to greater than 40% of the CO tropospheric partial column in many cases. A similar influence of BONA and BOAS wildfires was observed at Ny-Ålesund, but the sparsity of the CO measurements limited detection of events in the FTIR time series. Furthermore, the lack of coincident measurement of HCN and C_2H_6 did not allow for enhancement ratios to be calculated for Ny-Ålesund.

Kiruna was also strongly influenced by the trans-Atlantic transport of BONA emissions and hemispheric transport of BOAS emissions, which may contribute ~5-40% of the CO tropospheric partial column during the summer months from June though September of each year. A similar contribution was observed at St. Petersburg, albeit lower in magnitude. The sparse measurements of CO, HCN and C_2H_6 at Poker Flat limited detection of events in the FTIR time series. However, the GEOS-Chem tagged CO simulation illustrated the strong influence of both BONA and BOAS sources at Poker Flat, which in several years exceeded 60% of the CO tropospheric column.

The Alpine sites, Zugspitze and Jungfraujoch, are isolated from major biomass burning sources, but on occasion are subject to the transport of both BONA and BOAS emissions which were detected in the FTIR time series at both sites. However, these emissions are generally a small contribution to the tropospheric CO partial column (~10%). Toronto was mainly influenced by North American wildfires of BONA contributing ~10-20% of the CO column. Asian anthropogenic sources strongly influence the CO background at Rikubetsu, which was also considerably influenced by BOAS wildfires.

The results of this study show the Northern Hemispheric influence of boreal wildfire emissions, which were detected using FTIR measurements of CO and the coincident measurements of HCN and C_2H_6. The inter-annual variability of boreal wildfire emissions observed in the GEOS-Chem tagged CO simulation was also observed in the detected FTIR enhancements when measurements were available. The detected FTIR enhancements from 2013-2018 were in most cases attributed to BONA, consistent with the increase in the BONA contribution to CO during this period as observed in the GEOS-Chem time series.

Chapter 7

Conclusions

The first objective of this thesis was to develop a long-term time series of biomass burning trace gas species in the Arctic using Eureka FTIR measurements. Retrievals of CO, HCN and C_2H_6 were performed as part of the NDACC IRWG harmonization initiative. As part of this thesis, I performed updated retrievals of CO for the QA4ECV and CAMS27 RD projects. The retrieval strategy for the reactive trace gas species C_2H_2, CH_3OH and HCOOH was optimized for SFIT4 following the original retrieval strategy of Viatte et al. (2014) using SFIT2. The retrievals of H_2CO were also optimized for the NIDFORVal harmonization project of Vigouroux et al. (2018) for the ongoing validation of TROPOMI. A new retrieval strategy for NH_3 was developed for the Eureka FTIR. These retrievals established a long-term time series (2006-2018) that served as the foundation for the scientific results of this thesis.

The second objective of this thesis was to quantify the emissions of boreal wildfire NH_3 and its transport to the Arctic. This objective was addressed in Chapters 4 and 5. The third objective of this thesis was to investigate the frequency and contribution of episodic wildfire sources to trace gas measurements in the Arctic and was addressed in Chapter 6. The main results and their scientific significance are discussed below.

7.1 Quantifying Boreal Wildfire NH_3 in the Arctic

7.1.1 Summary

Chapter 4 describes total columns of CO, HCN, C_2H_6 and NH_3 that were measured by ground-based FTIR instruments at Eureka and Toronto. The observed NH_3 enhancements in July-August 2014 at Eureka indicate that the 2014 NWT fires were a considerable episodic source of NH_3 to the Canadian Arctic. Simultaneous enhancements of CO, HCN and C_2H_6 at Eureka, along with FLEXPART sensitivity runs, provided confirmation that the detected NH_3 enhancements originated from the Northwest Territories fires. Detection of simultaneous enhancements of all species at Toronto further demonstrated the long-range transport of NH_3 emissions from these fires. The consistency of the emission ratios for HCN, C_2H_6 and NH_3 with respect to CO between the two sites and to literature values, particularly for NH_3 with an estimated lifetime of 48 hrs, provides further confidence in these observations.

In Chapter 5, it was shown that the 2017 BC and NWT wildfires resulted in the greatest observed enhancements of total column NH_3, CO, HCN, and C_2H_6 in the decade-long time series of FTIR measurements at Eureka (2006-2017) and Thule (1999-2017). The observed NH_3 enhancements provide evidence for the importance of wildfires as an episodic source of NH_3 in the summertime Arctic, supporting the results of Chapter 4. Enhancement ratios of NH_3, HCN, and C_2H_6 were calculated with respect to CO at both sites. Variations in these enhancement ratios were due to the influence of multiple fire plumes and variations in the burning phases of the fire events. Evidence for this was provided by FLEXPART sensitivities that showed the influence of the BC and NWT plumes, with the influence of each fire source varying between measurement days at both sites. Eureka FTIR measurements were found to be most sensitive to the NWT wildfires, and Thule FTIR measurements were most sensitive to the BC wildfires, based on the FLEXPART sensitivity analysis.

The GEOS-Chem CTM was used to simulate the transport of 2017 wildfire emissions to the Arctic. Through comparisons of GEOS-Chem NH_3 and CO to FTIR measurements at Eureka and Thule, and to observations from IASI, it was shown that the model underestimates the transport of wildfire emissions to the Arctic for the observations examined here. The underestimation of modeled NH_3 and CO in comparison to Eureka FTIR measurements suggests an underestimation of emissions from the NWT fire source. This is consistent with the model comparisons to IASI measurements, which suggested an underestimation of emissions from the NWT wildfires in the model. At Thule, GEOS-Chem showed good agreement to the FTIR measurements for CO but underestimated the wildfire NH_3 contribution. The reason for the underestimation of GEOS-Chem CO and NH_3 in comparison to FTIR and IASI measurements remains unclear and is likely the result of several factors including the underestimation of emissions, plume height, chemistry and transport errors in the model. However, simulated transport of wildfire emissions in GEOS-Chem was found to be a significant contributor to reactive nitrogen in the form of NH_3 and NH_4^+ in the high Arctic for the fire-affected period of 15-23 August 2017, indicating the episodic contribution of the 2017 BC and NWT wildfires to reactive nitrogen in the Arctic.

7.1.2 Significance

These results illustrate the advantage of column measurements of NH_3 over surface or satellite-based thermal infrared measurements. Column FTIR measurements are sensitive to the free troposphere where transported emissions are most abundant, whereas surface measurements are most sensitive to nearby sources. Solar-absorption FTIR instruments have a lower detection limit of NH_3 than satellite-based thermal infrared instruments and therefore FTIR instruments are capable of measuring low concentrations of NH_3 in the Arctic. Furthermore, the use of existing FTIR instrumentation in the

Arctic provides long-term coverage where satellite observations are scarce and surface measurements have only been made on a campaign basis.

7.2 Investigating the Contribution of Wildfire Sources to Trace Gas Measurements in the Arctic

7.2.1 Summary

The results of Chapter 6 illustrate the use of NDACC FTIR measurements for the detection of wildfire pollution events. These events were identified at ten mid- and high-latitude FTIR sites from the detection of CO enhancements and correlation with the co-emitted biomass burning tracers HCN and C_2H_6. The number of detected events was dependent on the measurement frequency and density at each site. A GEOS-Chem tagged CO simulation provided source attribution of the detected events. At all sites, the detected events were attributed mainly to boreal North America and boreal Asia wildfire sources. In recent years from 2013-2018, an increase in the number of boreal North American events was observed, which may be indicative of increased wildfire activity in boreal North America. The GEOS-Chem tagged CO simulation also allowed for the contribution of biomass burning, chemical and anthropogenic sources to the CO column measured at each site to be quantified. The contribution of these sources to CO columns varied by site as a result of the site proximity to each of the sources. However, it was found that for all sites, boreal North America and boreal Asia had the greatest contributions to episodic enhancements at all sites. Anthropogenic sources and the oxidation of CH_4 and NMVOCs were the primary contributions to background CO columns.

The GEOS-Chem simulations showed that Poker Flat was strongly influenced by boreal North American and boreal Asian wildfires, with contributions from both sources that exceeded 50% of the CO column in many years. Similarly, Rikubestsu was greatly influenced by boreal Asian emissions. However, the number of detected events was limited by the number of measurements at each of these sites. The largest numbers of detected enhancements were at Eureka and Thule, with 19 events detected at Eureka from 2006-2018 and 17 events detected at Thule from 2003-2018. The greater number of detected events at these sites is primarily due to the greater number of measurements at Eureka and Thule in comparison to Poker Flat and Rikubetsu. Aside from Poker Flat and Rikubetsu, Eureka and Thule were the sites most influenced by boreal North American and boreal Asian wildfires sources, indicating the sensitivity of these sites to boreal wildfire sources and the potential for the Canadian high Arctic and Greenland to be subject to boreal wildfire pollution events.

Kiruna was also strongly influenced by the trans-Atlantic transport of boreal North American emissions and hemispheric transport of boreal Asian emissions, which contribute ~5-40% of the CO column. A similar contribution was observed at St. Petersburg although generally lower in magnitude. The Alpine sites, Zugspitze and Jungfraujoch, are isolated from major biomass burning sources; however, on occasion are subject to the transport of both boreal North American and boreal Asian emissions, which were detected in the FTIR time series at both sites. However, these emissions are generally a small contribution to the tropospheric CO partial column (~10%). Toronto was mainly influenced by boreal North American wildfires contributing ~10-20% of the CO column.

7.2.2 Significance

Solar-absorption FTIR spectroscopy is particularly useful for measuring a multitude of trace gas species simultaneously, or within a short time frame. Although, the focus of the study was on measurements of CO, HCN and C_2H_6, this type of analysis may be applied to other biomass burning trace gas species that can be measured using an FTIR instrument such as C_2H_2, CH_3OH, H_2CO, HCOOH and NH_3. It has been shown in a previous study that boreal wildfires are a large contributor to anomalous CO enhancements in the Northern hemisphere (Petetin et al., 2018); however, Arctic observations were not considered in that study. It was shown in this work that boreal wildfires are the predominant contributor to anomalous CO enhancements in the Arctic.

7.3 Future Work

The improvement of measurement quality and quantity of the Eureka FTIR is a continuous effort. Improvements have been made in recent years, most notably the installation of the Community Solar Tracker in July 2014, which greatly improved the automation of measurement acquisition. Additionally, the reduction in the number of co-added scans from four to two for each measurement starting in March 2019, resulted in a greater number of recorded spectra. The updated measurement macro in 2014 described by Weaver (2018) enables continuous measurements until inadequate signal in all spectral filters occurs, therefore automatically ending measurements when the Sun sets. This was an improvement over the previous measurement macro, which would run for a predetermined number of measurements and required additional operator support.

For the Eureka FTIR, there are several suggestions that could further improve instrument operation in the future:

1. Sun-tracker camera: The sun-tracker camera is installed beneath the 45° mirror which directs the solar beam to the entrance window of the instrument. The 45° mirror dictates the position of the beam on the entrance aperture which could result in tracking errors as the beam may not be centred on the aperture. The sun-tracker camera should be placed in the source compartment in order to use the position of the beam on the aperture to define the position of the center of the Sun and to make solar tracking independent of the 45° mirror position.

2. Automated liquid nitrogen filling: Commercially available units exist and installation of one for the InSb and MCT detectors would reduce the requirements of

the on-site operator. This would also allow MIR measurements to be performed remotely without an operator present at the lab.

3. Precipitation sensor for the Robodome: The Robodome that houses the CST tracker is closed at the end of measurements. Currently, measurements end when the operator leaves the Ridge Lab at the end of the day or remotely later in the evening. Installation of a precipitation sensor and integration with the Robodome would allow measurements to continue running without an operator present at the lab or monitoring remotely.
4. Python automation: The OPUS software currently runs on a Windows desktop while the CST software is on a separate Linux machine. Python software for the control of the Bruker FTIR has been developed by the FTIR group at NIWA (Geddes et al., 2018) and may be used to unify the operation of the FTIR and CST, allowing for further automation.

The retrievals presented in Chapter 3 were optimized using the current SFIT4 v9.4.4 retrieval algorithm, recommended NDACC IRWG linelist of HITRAN 2008 and a priori profiles from WACCM v4 for the standard species HCN and C_2H_6. CO retrievals were updated with the atm16 linelist for the QA4ECV and CAMS27 RD projects. It is expected that these retrievals will be continually updated with further harmonization and retrieval strategy improvements set by the NDACC IRWG. In particular, this will include the release of SFIT4 v9.4.6 and a possible update to use HITRAN 2016 (Gordon et al., 2017). Additionally, the WACCM v4 a priori profiles averaged from 1980-2020, may be replaced as the year 2020 approaches. As such, the retrievals of CO, HCN and C_2H_6 will likely need to be optimized for the future NDACC IRWG guidelines. Similarly, the non-standard species, C_2H_2, CH_3OH, H_2CO and HCOOH should also be updated to maintain consistency with the retrieval strategy of the standard species. An updated retrieval strategy for NH_3 should also be the focus of future work. At the time of development of the Eureka NH_3 retrieval, there was a lack of a priori knowledge of the NH_3 vertical profile and as a result a custom a priori profile was created. It is recommended that a new NH_3 a priori profile be developed, possibly based on the full-chemistry GEOS-Chem simulation over a long period, and scaled to account for the expected model underestimation that was observed in Chapter 5.

It is recommended that full-chemistry GEOS-Chem simulations be performed for the entire Eureka measurement time series from 2006-2018 in order to examine the relative contribution of wildfire, seabird-colony and tundra sources to NH_3 in the Arctic on seasonal time scales. This would help to better understand the long-term impacts of boreal wildfire NH_3 on the Arctic, in addition to providing a means of model evaluation. Past studies of Arctic NH_3 using GEOS-Chem by Croft et al. (2016a,b) and Wentworth et al. (2016) only considered surface measurements of NH_3, and therefore may have underestimated the contribution of wildfire NH_3 which would be most abundant in the free troposphere.

The results of Chapter 6 showed that boreal wildfires are the greatest contributor to CO pollution events detected in FTIR measurements in the Arctic and mid-latitudes. However, only the long-lived species CO, HCN and C_2H_6 were considered. This study could be extended to include the short-lived reactive trace gas species C_2H_2, CH_3OH, HCOOH and H_2CO as in Viatte et al. (2015) and NH_3. This study could also examine the potential contribution of wildfire pollution to tropospheric O_3 as measured by each FTIR site. The inclusion of a variety of sites with different background conditions and wildfire contributions would provide a means of examining the physical and chemical processes of these species in a smoke plume, and quantifying the contribution of wildfires to the budget of each species at all sites.

Appendix A

Fitted Microwindows for Eureka FTIR Retrievals

The retrieval strategy for obtaining CO, HCN, C_2H_6, C_2H_2, CH_3OH, H_2CO, HCOOH and NH_3 from Eureka FTIR measurements was presented in Chapter 3. Examples of the fitted microwindows are shown here for each species. For all figures, the measured and calculated spectra are shown along with the contributions of the target and interfering species. The dates shown were selected based on the quality of the spectra that provided high SNR, low RMS and high DOFS.

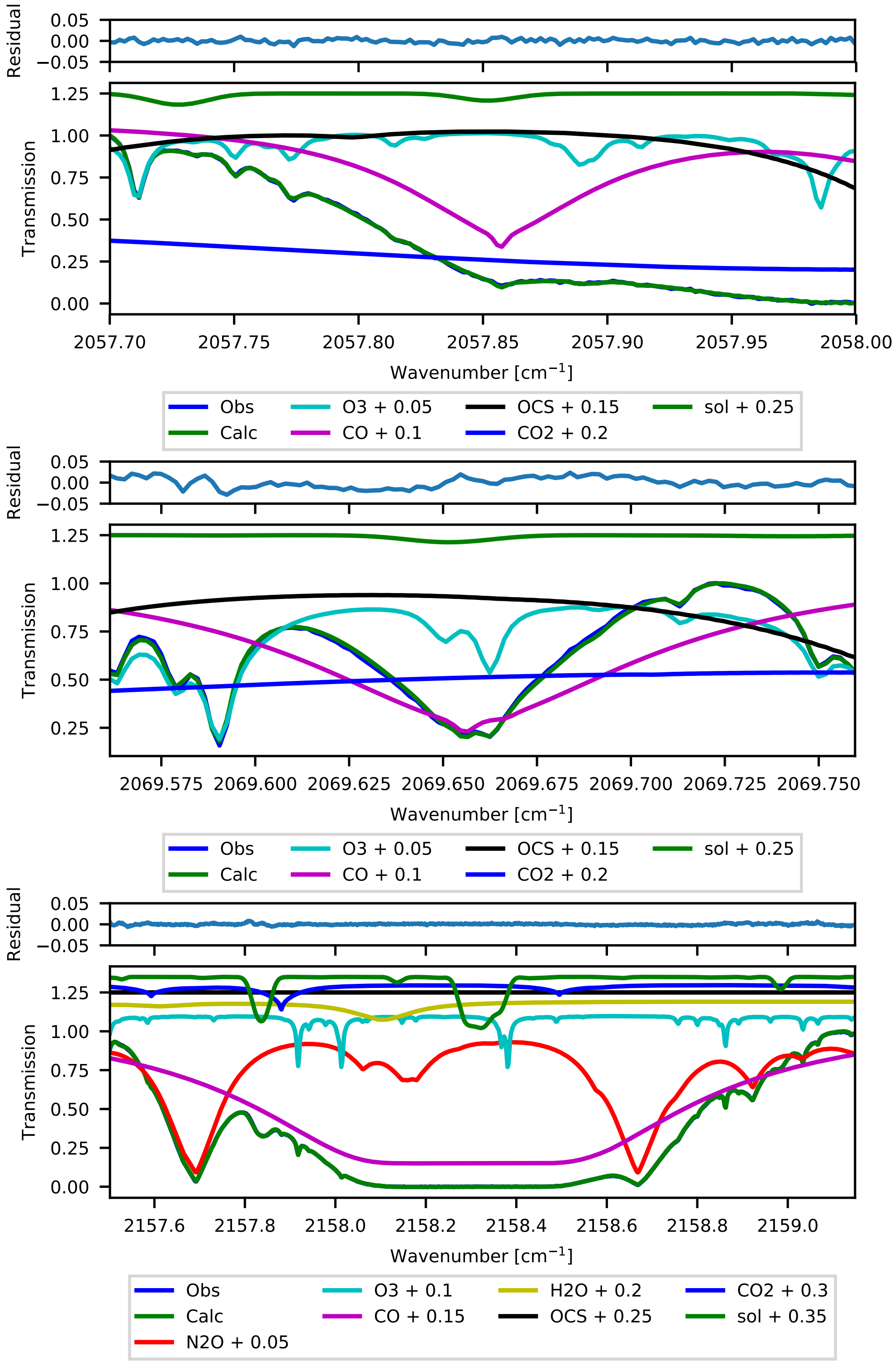

Figure A.1: Example of the spectral fit of CO for the measurement taken on 4 April 2018 at 17:45:06 UTC corresponding to an SZA of 74.18°.

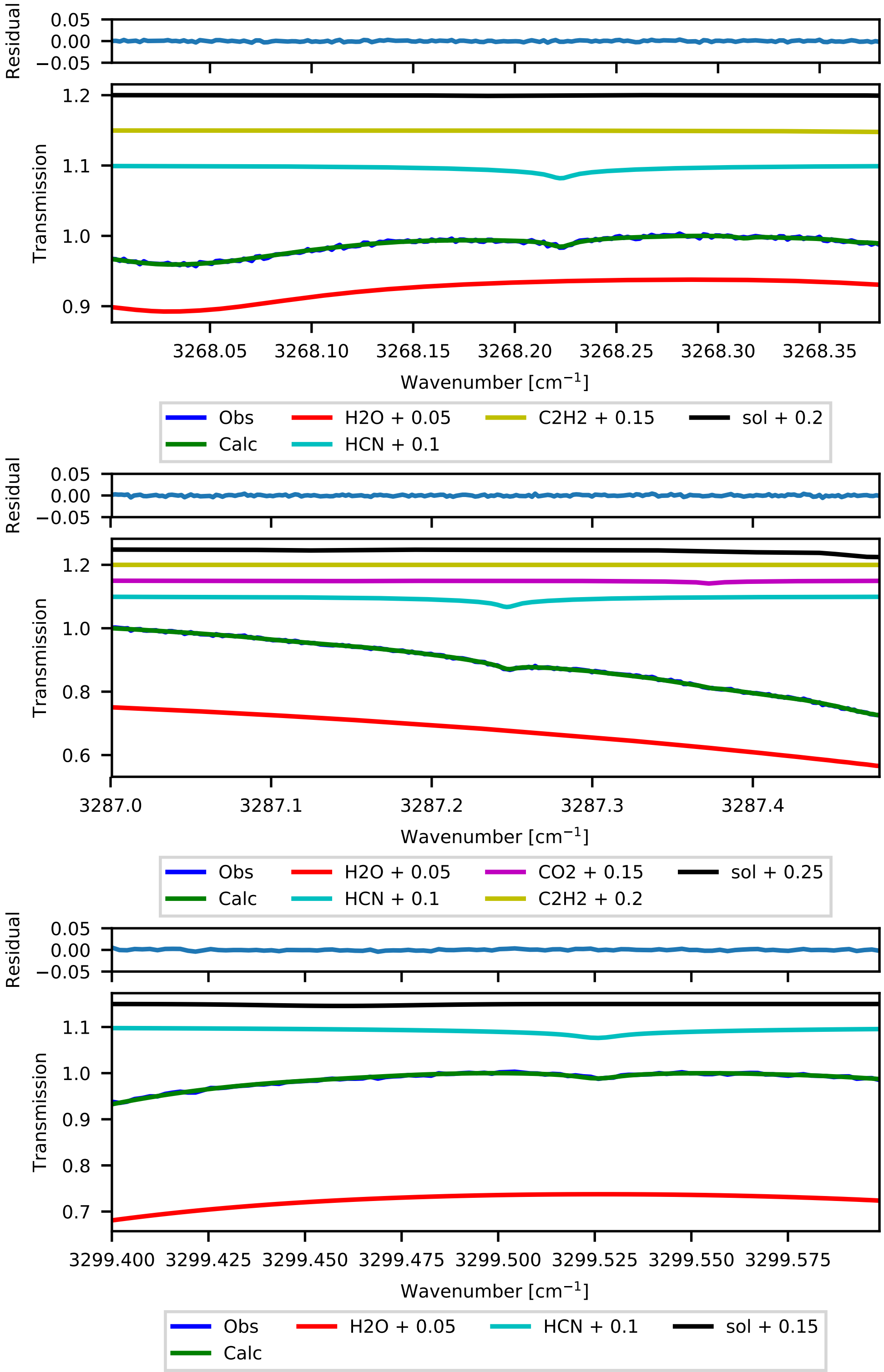

Figure A.2: Example of the spectral fit of HCN for the measurement taken on 25 July 2018 at 17:59:54 UTC corresponding to an SZA of 60.51°.

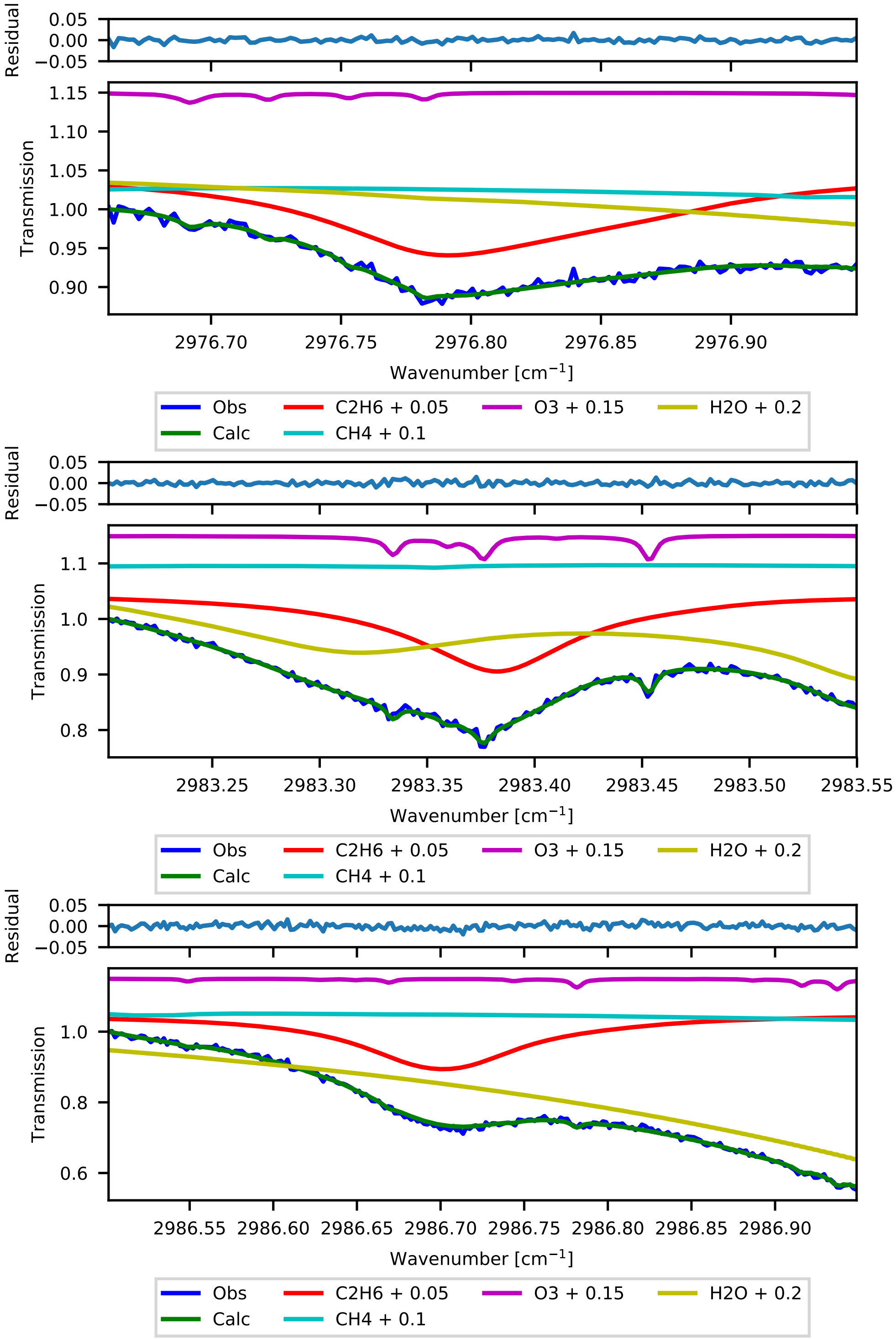

Figure A.3: Example of the spectral fit for C_2H_6 the measurement taken on 6 June 2017 at 01:10:58 UTC corresponding to an SZA of 71.34°.

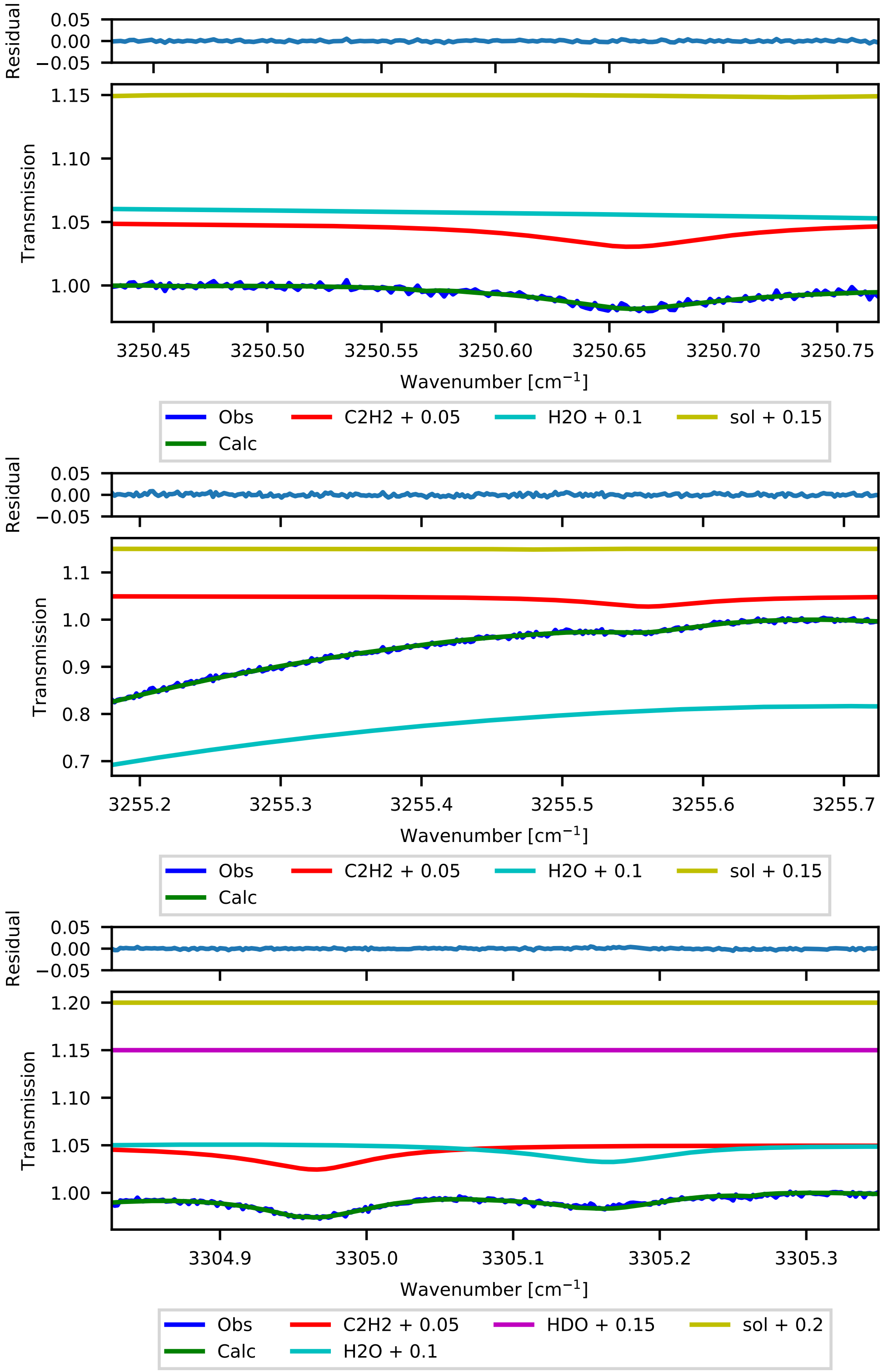

Figure A.4: Example of the spectral fit of C_2H_2 for the measurement taken on 8 April 2018 at 19:55:09 UTC corresponding to an SZA of 74.18°.

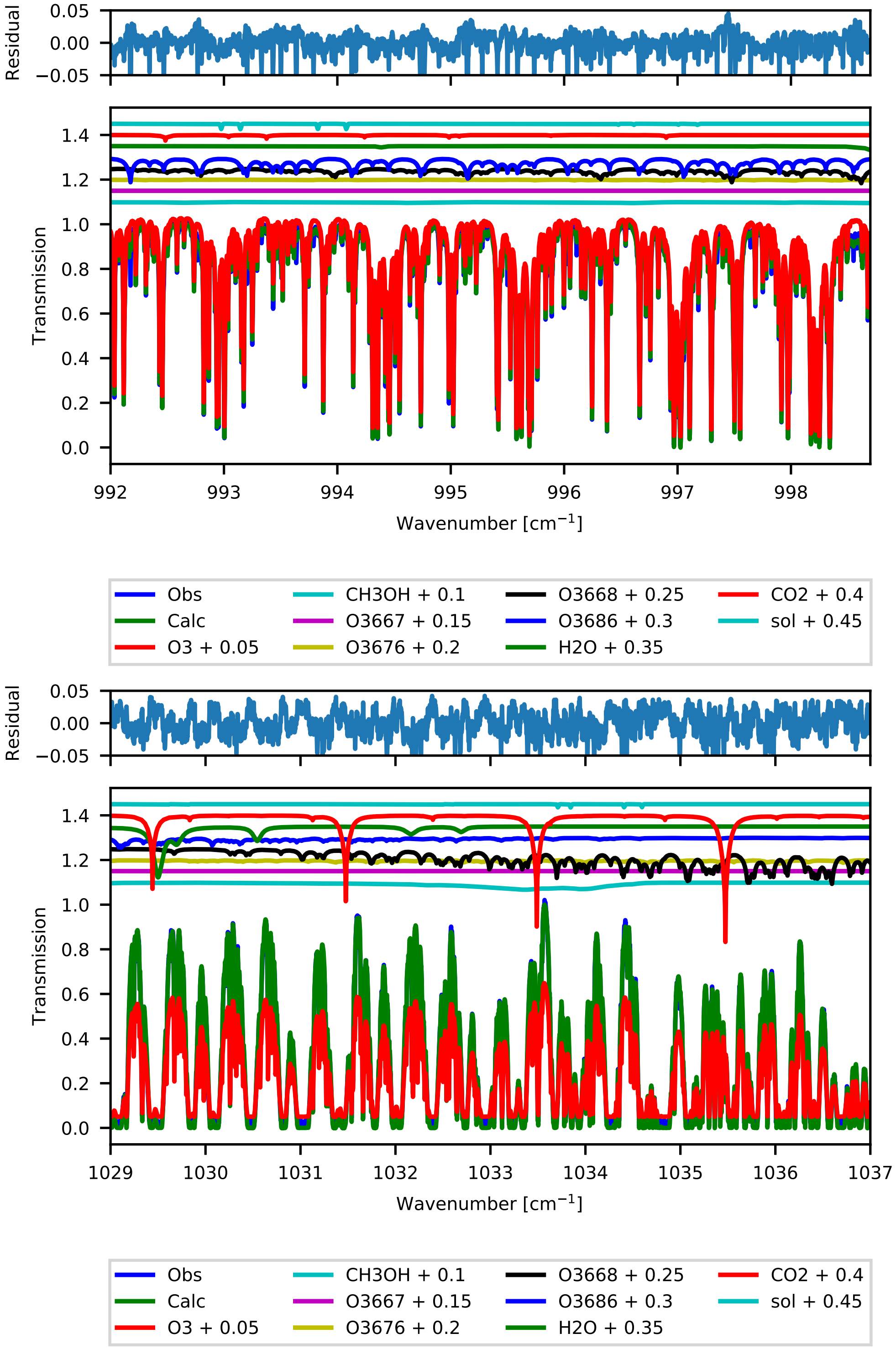

Figure A.5: Example of the spectral fit of CH_3OH for the measurement taken on 4 April 2018 at 15:56:02 UTC corresponding to an SZA of 75.14°.

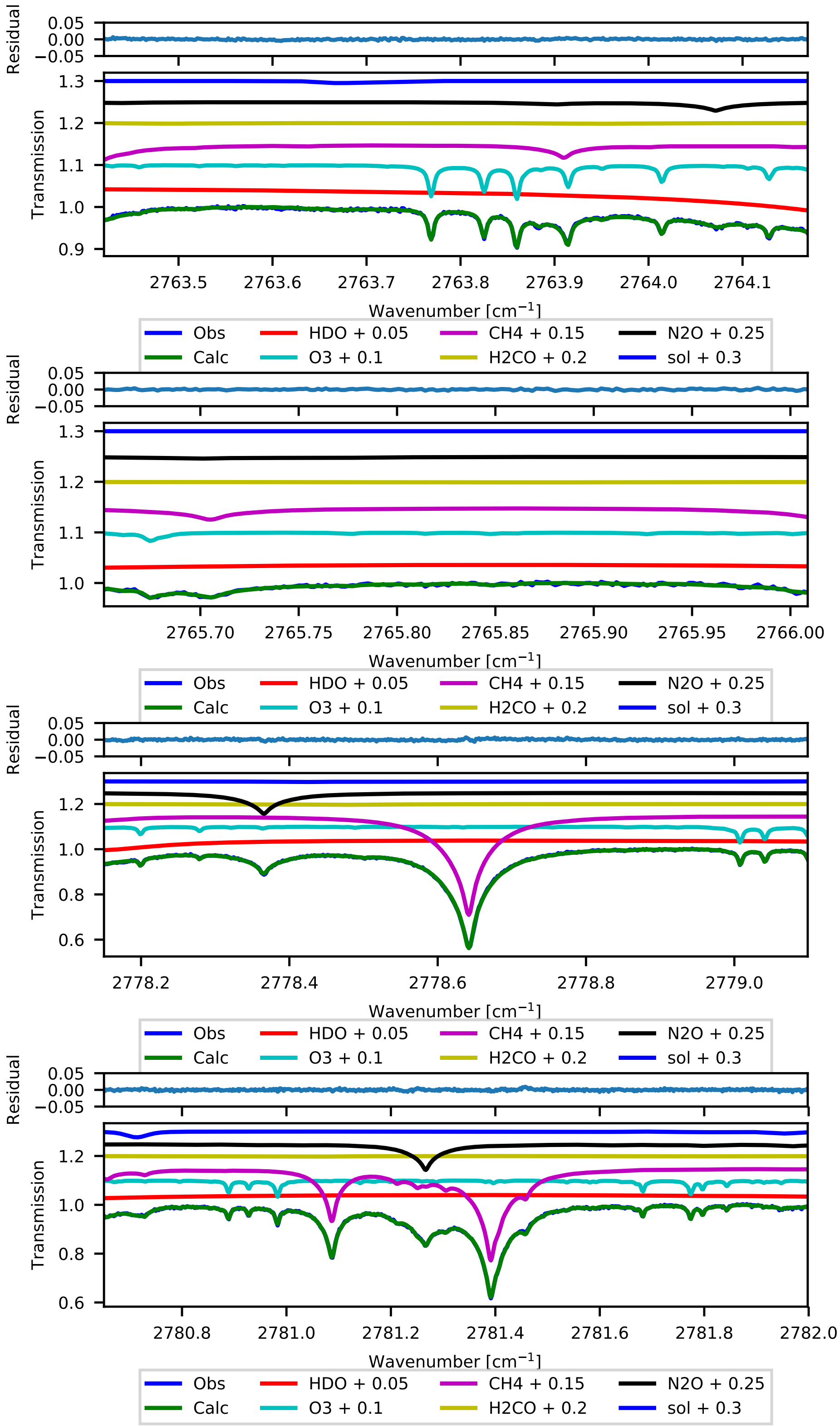

Figure A.6: Example of the spectral fit of H_2CO for the measurement taken on 25 July 2018 at 19:49:10 UTC corresponding to an SZA of 61.88°.

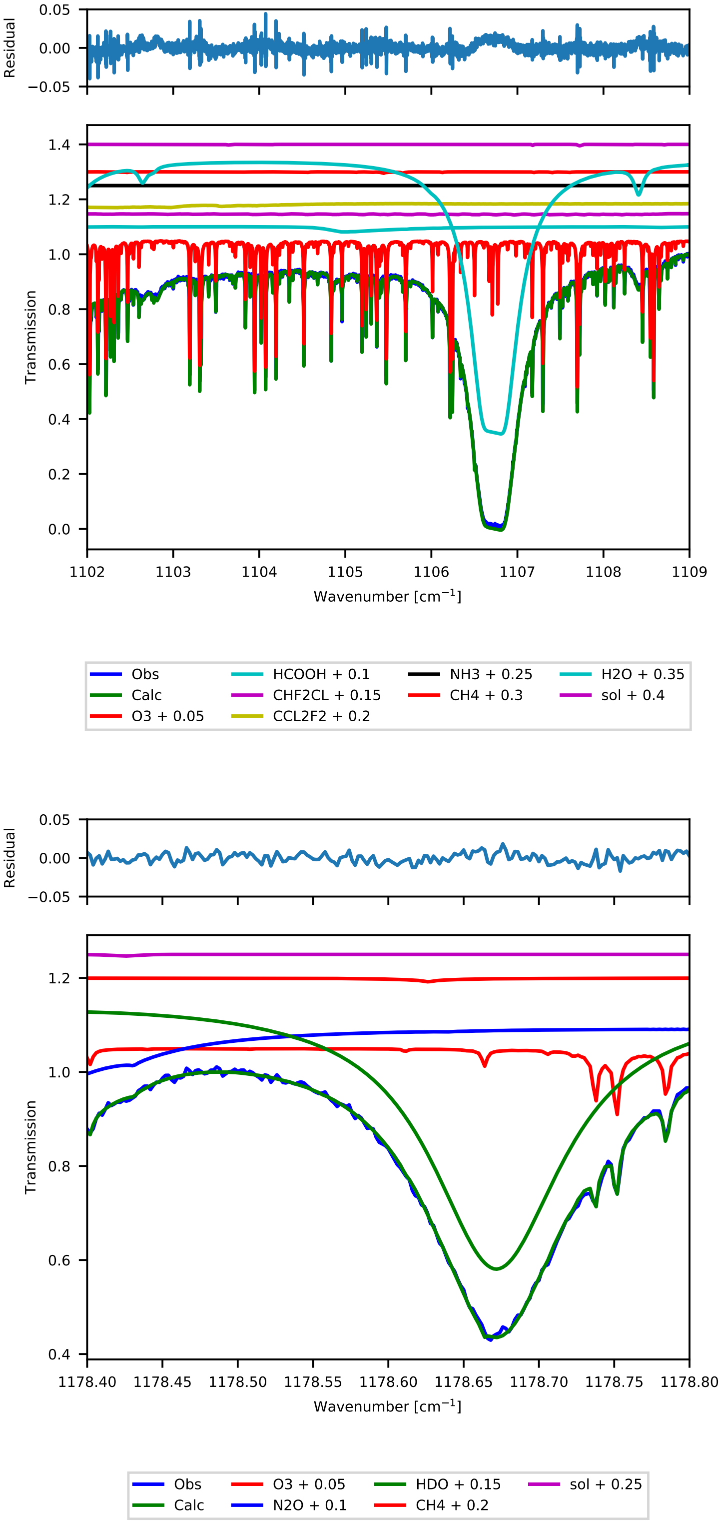

Figure A.7: Example of the spectral fit of HCOOH for the measurement taken on 14 June 2018 at 19:13:43 UTC corresponding to an SZA of 57.55°.

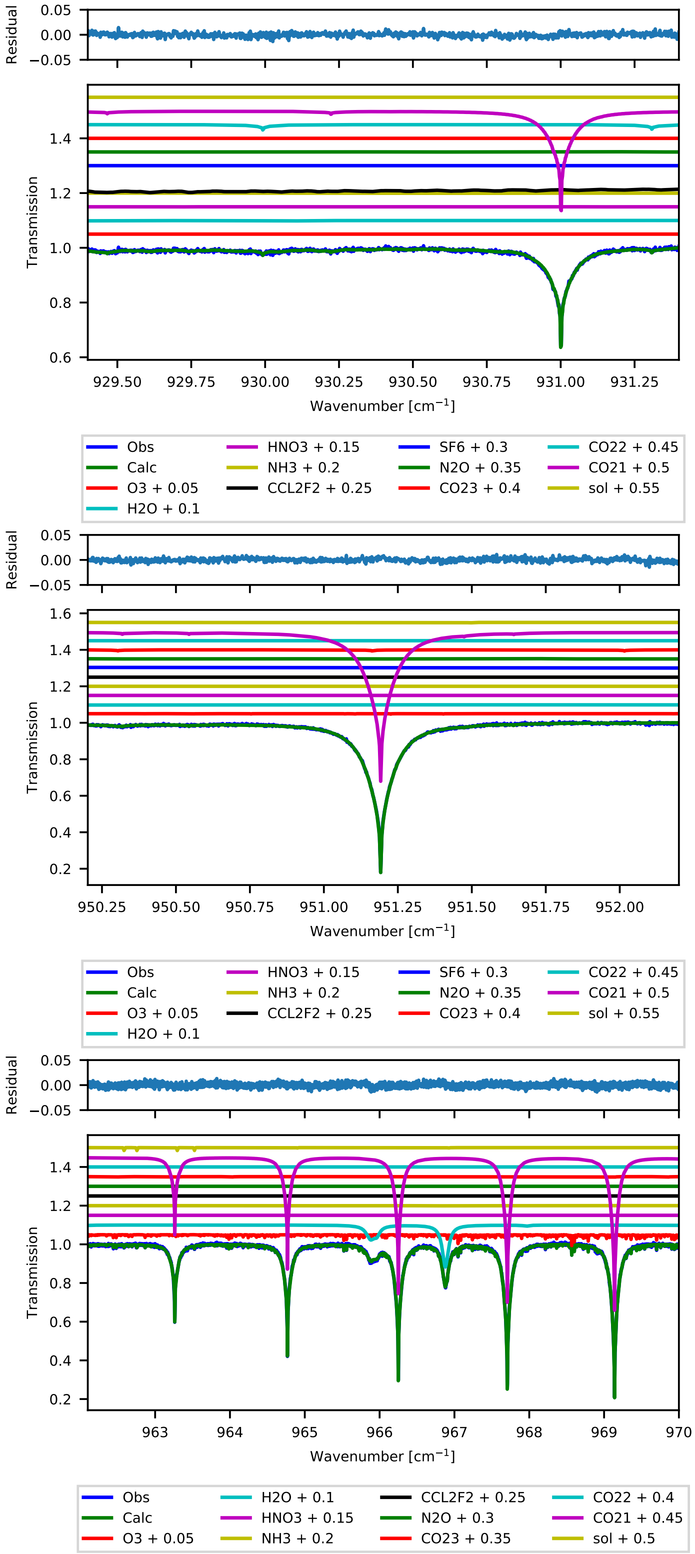

Figure A.8: Example of the spectral fit of NH_3 for the measurement taken on 25 July 2018 at 18:08:24 UTC corresponding to an SZA of 60.54°.

Bibliography

Abbatt, J. P. D., Leaitch, W. R., Aliabadi, A. A., Bertram, A. K., Blanchet, J.-P., Boivin-Rioux, A., Bozem, H., Burkart, J., Chang, R. Y. W., Charette, J., Chaubey, J. P., Christensen, R. J., Cirisan, A., Collins, D. B., Croft, B., Dionne, J., Evans, G. J., Fletcher, C. G., Galí, M., Ghahremaninezhad, R., Girard, E., Gong, W., Gosselin, M., Gourdal, M., Hanna, S. J., Hayashida, H., Herber, A. B., Hesaraki, S., Hoor, P., Huang, L., Hussherr, R., Irish, V. E., Keita, S. A., Kodros, J. K., Köllner, F., Kolonjari, F., Kunkel, D., Ladino, L. A., Law, K., Levasseur, M., Libois, Q., Liggio, J., Lizotte, M., Macdonald, K. M., Mahmood, R., Martin, R. V., Mason, R. H., Miller, L. A., Moravek, A., Mortenson, E., Mungall, E. L., Murphy, J. G., Namazi, M., Norman, A.-L., O'Neill, N. T., Pierce, J. R., Russell, L. M., Schneider, J., Schulz, H., Sharma, S., Si, M., Staebler, R. M., Steiner, N. S., Thomas, J. L., Salzen, K. v., Wentzell, J. J. B., Willis, M. D., Wentworth, G. R., Xu, J.-W., and Yakobi-Hancock, J. D. (2019). Overview paper: New insights into aerosol and climate in the Arctic. *Atmospheric Chemistry and Physics*, 19(4):2527–2560.

Adams, C., McLinden, C. A., Shephard, M. W., Dickson, N., Dammers, E., Chen, J., Makar, P., Cady-Pereira, K. E., Tam, N., Kharol, S. K., Lamsal, L. N., and Krotkov, N. A. (2019). Satellite-derived emissions of carbon monoxide, ammonia, and nitrogen dioxide from the 2016 Horse River wildfire in the Fort McMurray area. *Atmospheric Chemistry and Physics*, 19(4):2577–2599.

Akagi, S. K., Yokelson, R. J., Wiedinmyer, C., Alvarado, M. J., Reid, J. S., Karl, T., Crounse, J. D., and Wennberg, P. O. (2011). Emission factors for open and domestic biomass burning for use in atmospheric models. *Atmospheric Chemistry and Physics*, 11(9):4039–4072.

Alvarado, M. J., Cady-Pereira, K. E., Xiao, Y., Millet, D. B., and Payne, V. H. (2011). Emission ratios for ammonia and formic acid and observations of Peroxy Acetyl Nitrate (PAN) and ethylene in biomass burning smoke as seen by the Tropospheric Emission Spectrometer (TES). *Atmosphere*, 2(4):633–654.

Amiro, B. D., Cantin, A., Flannigan, and de Groot, W. J. (2009). Future emissions from canadian boreal forest fires. *Canadian Journal of Forest Research*, 39(2):383–395.

Andreae, M. O. (2019). Emission of trace gases and aerosols from biomass burning - An updated assessment. *Atmospheric Chemistry and Physics*, 19(13):8523–8546.

Andreae, M. O. and Merlet, P. (2001). Emission of trace gases and aerosols from biomass burning. *Global Biogeochemical Cycles*, 15(4):955–966.

Aneja, V. P., Bunton, B., Walker, J. T., and Malik, B. P. (2001). Measurement and analysis of atmospheric ammonia emissions from anaerobic lagoons. *Atmospheric Environment*, 35(11):1949–1958.

Arola, A., Lindfors, A., Natunen, A., and Lehtinen, K. E. J. (2007). A case study on biomass burning aerosols: effects on aerosol optical properties and surface radiation levels. *Atmospheric Chemistry and Physics*, 7(16):4257–4266.

Asman, W. A. H., Sutton, M. A., and Schjorring, J. K. (1998). Ammonia: emission, atmospheric transport and deposition. *The New Phytologist*, 139(1):27–48.

Barret, B., Mazière, M. D., and Mahieu, E. (2003). Ground-based FTIR measurements of CO from the jungfraujoch: characterisation and comparison with in situ surface and MOPITT data. *Atmospheric Chemistry and Physics*, 3(6):2217–2223.

Batchelor, R. L., Strong, K., Lindenmaier, R., Mittermeier, R. L., Fast, H., Drummond, J. R., and Fogal, P. F. (2009). A new Bruker IFS 125HR FTIR spectrometer for the Polar Environment Atmospheric Research Laboratory at Eureka, Nunavut, Canada: measurements and comparison with the existing Bomem DA8 spectrometer. *Journal of Atmospheric and Oceanic Technology*, 26(7):1328–1340.

Baum, M. M., Moss, J. A., Pastel, S. H., and Poskrebyshev, G. A. (2007). Hydrogen cyanide exhaust emissions from in-use motor vehicles. *Environmental Science & Technology*, 41(3):857–862.

BC Wildfire Service (2017). Wildfire season summary - province of british columbia. `https://www2.gov.bc.ca/gov/content/safety/wildfire-status/about-bcws/wildfire-history/wildfire-season-summary`. Accessed: 2019-1-30.

Beaudoin, A., Bernier, P., Guindon, L., Villemaire, P., Guo, X., Stinson, G., Bergeron, T., Magnussen, S., and Hall, R. (2014). Mapping attributes of Canadas forests at moderate resolution through kNN and MODIS imagery.

Bell, R. (1972). *Introductory Fourier Transform Spectroscopy*. Elsevier.

Bey, I., Jacob, D. J., Logan, J. A., and Yantosca, R. M. (2001a). Asian chemical outflow to the pacific in spring: Origins, pathways, and budgets. *Journal of Geophysical Research: Atmospheres*, 106(D19):23097–23113.

Bey, I., Jacob, D. J., Yantosca, R. M., Logan, J. A., Field, B. D., Fiore, A. M., Li, Q., Liu, H. Y., Mickley, L. J., and Schultz, M. G. (2001b). Global modeling of tropospheric chemistry with assimilated meteorology: Model description and evaluation. *Journal of Geophysical Research: Atmospheres*, 106(D19):23073–23095.

Bjorkman, A. D., Myers-Smith, I. H., Elmendorf, S. C., Normand, S., Rüger, N., Beck, P. S. A., Blach-Overgaard, A., Blok, D., Cornelissen, J. H. C., Forbes, B. C., Georges, D., Goetz, S. J., Guay, K. C., Henry, G. H. R., Hille Ris Lambers, J., Hollister, R. D., Karger, D. N., Kattge, J., Manning, P., Prevéy, J. S., Rixen, C., Schaepman-Strub, G., Thomas, H. J. D., Vellend, M., Wilmking, M., Wipf, S., Carbognani, M., Hermanutz, L., Lévesque, E., Molau, U., Petraglia, A., Soudzilovskaia, N. A., Spasojevic, M. J., Tomaselli, M., Vowles, T., Alatalo, J. M., Alexander, H. D., Anadon-Rosell, A., Angers-Blondin, S., Beest, M. T., Berner, L., Björk, R. G., Buchwal, A., Buras, A., Christie, K., Cooper, E. J., Dullinger, S., Elberling, B., Eskelinen, A., Frei, E. R., Grau, O., Grogan, P., Hallinger, M., Harper, K. A., Heijmans, M. M. P. D., Hudson, J., Hülber, K., Iturrate-Garcia, M., Iversen, C. M., Jaroszynska, F., Johnstone, J. F., Jørgensen, R. H., Kaarlejärvi, E., Klady, R., Kuleza, S., Kulonen, A., Lamarque, L. J., Lantz, T., Little, C. J., Speed, J. D. M., Michelsen, A., Milbau, A., Nabe-Nielsen, J., Nielsen, S. S., Ninot, J. M., Oberbauer, S. F., Olofsson, J., Onipchenko, V. G., Rumpf, S. B., Semenchuk, P., Shetti, R., Collier, L. S., Street, L. E., Suding, K. N., Tape, K. D., Trant, A., Treier, U. A., Tremblay, J.-P., Tremblay, M., Venn, S., Weijers, S., Zamin, T., Boulanger-Lapointe, N., Gould, W. A., Hik, D. S., Hofgaard, A., Jónsdóttir, I. S., Jorgenson, J., Klein, J., Magnusson, B., Tweedie, C., Wookey, P. A., Bahn, M., Blonder, B., van Bodegom, P. M., Bond-Lamberty, B., Campetella, G., Cerabolini, B. E. L., Chapin, 3rd, F. S., Cornwell, W. K., Craine, J., Dainese, M., de Vries, F. T., Díaz, S., Enquist, B. J., Green, W., Milla, R., Niinemets, Ü., Onoda, Y., Ordoñez, J. C., Ozinga, W. A., Penuelas, J., Poorter, H., Poschlod, P., Reich, P. B., Sandel, B., Schamp, B., Sheremetev, S., and Weiher, E. (2018). Plant functional trait change across a warming tundra biome. *Nature*, 562(7725):57–62.

Blackall, T. D., Wilson, L. J., Theobald, M. R., Milford, C., Nemitz, E., Bull, J., Bacon, P. J., Hamer, K. C., Wanless, S., and Sutton, M. A. (2007). Ammonia emissions from seabird colonies. *Geophysical Research Letters*, 34(L10801).

Blumenstock, T., Hase, F., Kramer, I., Mikuteit, S., Fischer, H., Goutail, F., and Raffalski, U. (2009). Winter to winter variability of chlorine activation and ozone loss as observed by ground-based FTIR measurements at Kiruna since winter 1993/94. *International Journal of Remote Sensing*, 30(15-16):4055–4064.

Blumenstock, T. H., Fisher, H., Friedle, A., Hase, F., and Thomas, P. (1997). Column amounts of $ClONO_2$, HCl, HNO_3, and HF from Ground-Based FTIR measurements made near Kiruna, Sweden, in late winter 1994. *Journal of Atmospheric Chemistry*, 26(3):311–321.

Bond, T. C. and Sun, H. (2005). Can reducing black carbon emissions counteract global warming? *Environmental Science & Technology*, 39(16):5921–5926.

Boulanger, Y., Gauthier, S., and Burton, P. J. (2014). A refinement of models projecting future Canadian fire regimes using homogeneous fire regime zones. *Canadian Fournal of Forest Research*, 44(4):365–376.

Bouwman, A. F., Boumans, L. J. M., and Batjes, N. H. (2002). Estimation of global NH_3 volatilization loss from synthetic fertilizers and animal manure applied to arable lands and grasslands. *Global Biogeochemical Cycles*, 16(2).

Bouwman, A. F., Lee, D. S., Asman, W. A. H., Dentener, F. J., Van Der Hoek, K. W., and Olivier, J. G. J. (1997). A global high-resolution emission inventory for ammonia. *Global Biogeochemical Cycles*, 11(4):561–587.

Bruker Optik GmbH (2006). *Bruker Optics User Manual*, 1st edition.

Burling, I. R., Yokelson, R. J., Akagi, S. K., Urbanski, S. P., Wold, C. E., Griffith, D. W. T., Johnson, T. J., Reardon, J., and Weise, D. R. (2011). Airborne and ground-based measurements of the trace gases and particles emitted by prescribed fires in the United States. *Atmospheric Chemistry and Physics*, 11(23):12197–12216.

Burling, I. R., Yokelson, R. J., Griffith, D. W. T., Johnson, T. J., Veres, P., Roberts, J. M., Warneke, C., Urbanski, S. P., Reardon, J., Weise, D. R., Hao, W. M., and de Gouw, J. (2010). Laboratory measurements of trace gas emissions from biomass burning of fuel types from the southeastern and southwestern United States. *Atmospheric Chemistry and Physics*, 10(22):11115–11130.

Choudhary, S., Blaud, A., Osborn, A. M., Press, M. C., and Phoenix, G. K. (2016). Nitrogen accumulation and partitioning in a High Arctic tundra ecosystem from extreme atmospheric N deposition events. *The Science of the Total Environment*, 554-555:303–310.

Cicerone, R. J. and Zellner, R. (1983). The atmospheric chemistry of hydrogen cyanide (HCN). *Journal of Geophysical Research: Atmospheres*, 88(C15):10689–10696.

Circumpolar Seabird Data Portal (2018). Circumpolar seabird data portal. `http://axiom.seabirds.net/maps/js/seabirds.php`. Accessed: 2018-10-30.

Clarisse, L., Shephard, M. W., Dentener, F., Hurtmans, D., Cady-Pereira, K., Karagulian, F., Van Damme, M., Clerbaux, C., and Coheur, P.-F. (2010). Satellite monitoring of ammonia: A case study of the San Joaquin Valley. *Journal of Geophysical Research: Atmospheres*, 115(D13):277.

Clerbaux, C., Boynard, A., Clarisse, L., George, M., Hadji-Lazaro, J., Herbin, H., Hurtmans, D., Pommier, M., Razavi, A., Turquety, S., Wespes, C., and Coheur, P.-F. (2009). Monitoring of atmospheric composition using the thermal infrared IASI/MetOp sounder. *Atmospheric Chemistry and Physics*, 9(16):6041–6054.

Coffey, M. T., Goldman, A., Hannigan, J. W., Mankin, W. G., Schoenfeld, W. G., Rinsland, C. P., Bernardo, C., and Griffith, D. W. T. (1998). Improved vibration-rotation (0-1) HBr line parameters for validating high resolution infrared atmospheric spectra measurements. *Journal of Quantitative Spectroscopy & Radiative Transfer*, 60:863–867.

Coheur, P.-F., Clarisse, L., Turquety, S., Hurtmans, D., and Clerbaux, C. (2009). IASI measurements of reactive trace species in biomass burning plumes. *Atmospheric Chemistry and Physics*, 9(15):5655–5667.

Conard, S. G. and Ivanova, G. A. (1997). Wildfire in Russian boreal forests - Potential impacts of fire regime characteristics on emissions and global carbon balance estimates. *Environmental Pollution*, 98(3):305–313.

Connes, J. and Connes, P. (1966). Near-Infrared planetary spectra by Fourier spectroscopy. *JOSA*, 56(7):896–910.

Crippa, M., Janssens-Maenhout, G., Dentener, F., Guizzardi, D., Sindelarova, K., Muntean, M., Van Dingenen, R., and Granier, C. (2016). Forty years of improvements in european air quality: regional policy-industry interactions with global impacts. *Atmospheric Chemistry and Physics*, 16(6):3825–3841.

Croft, B., Martin, R. V., Leaitch, W. R., Burkart, J., Chang, R. Y.-W., Collins, D. B., Hayes, P. L., Hodshire, A. L., Huang, L., Kodros, J. K., Moravek, A., Mungall, E. L., Murphy, J. G., Sharma, S., Tremblay, S., Wentworth, G. R., Willis, M. D., Abbatt, J. P. D., and Pierce, J. R. (2019). Arctic marine secondary organic aerosol contributes significantly to summertime particle size distributions in the Canadian Arctic Archipelago. *Atmospheric Chemistry and Physics*, 19(5):2787–2812.

Croft, B., Martin, R. V., Leaitch, W. R., Tunved, P., Breider, T. J., D'Andrea, S. D., and Pierce, J. R. (2016a). Processes controlling the annual cycle of Arctic aerosol number and size distributions. *Atmospheric Chemistry and Physics*, 16(6):3665–3682.

Croft, B., Wentworth, G. R., Martin, R. V., Leaitch, W. R., Murphy, J. G., Murphy, B. N., Kodros, J. K., Abbatt, J. P. D., and Pierce, J. R. (2016b). Contribution of

Arctic seabird-colony ammonia to atmospheric particles and cloud-albedo radiative effect. *Nature Communications*, 7:13444.

Dammers, E., Palm, M., Van Damme, M., Vigouroux, C., Smale, D., Conway, S., Toon, G. C., Jones, N., Nussbaumer, E., Warneke, T., Petri, C., Clarisse, L., Clerbaux, C., Hermans, C., Lutsch, E., Strong, K., Hannigan, J. W., Nakajima, H., Morino, I., Herrera, B., Stremme, W., Grutter, M., Schaap, M., Wichink Kruit, R. J., Notholt, J., Coheur, P.-F., and Erisman, J. W. (2016). An evaluation of IASI-NH_3 with ground-based fourier transform infrared spectroscopy measurements. *Atmospheric Chemistry and Physics*, 16(16):10351–10368.

Dammers, E., Shephard, M. W., Palm, M., Cady-Pereira, K., Capps, S., Lutsch, E., Strong, K., Hannigan, J. W., Ortega, I., Toon, G. C., Stremme, W., Grutter, M., Jones, N., Smale, D., Siemons, J., Hrpcek, K., Tremblay, D., Schaap, M., Notholt, J., and Erisman, J. W. (2017). Validation of the CrIS fast physical NH_3 retrieval with ground-based FTIR. *Atmospheric Measurement Techniques*, 10(7):2645–2667.

Dammers, E., Vigouroux, C., Palm, M., Mahieu, E., Warneke, T., Smale, D., Langerock, B., Franco, B., Van Damme, M., Schaap, M., Notholt, J., and Erisman, J. W. (2015). Retrieval of ammonia from ground-based FTIR solar spectra. *Atmospheric Chemistry and Physics*, 15(22):12789–12803.

Damoah, R., Spichtinger, N., Forster, C., James, P., Mattis, I., Wandinger, U., Beirle, S., Wagner, T., and Stohl, A. (2004). Around the world in 17 days - Hemispheric-scale transport of forest fire smoke from Russia in May 2003. *Atmospheric Chemistry and Physics*, 4(5):1311–1321.

Daniel, J. S. and Solomon, S. (1998). On the climate forcing of carbon monoxide. *Journal of Geophysical Research: Atmospheres*, 103(D11):13249–13260.

De Mazière, M., Thompson, A. M., Kurylo, M. J., Wild, J. D., Bernhard, G., Blumenstock, T., Braathen, G. O., Hannigan, J. W., Lambert, J.-C., Leblanc, T., McGee, T. J., Nedoluha, G., Petropavlovskikh, I., Seckmeyer, G., Simon, P. C., Steinbrecht, W., and Strahan, S. E. (2018). The Network for the Detection of Atmospheric Composition Change (NDACC): History, status and perspectives. *Atmospheric Chemistry and Physics*, 18(7):4935–4964.

Dentener, F. J. and Crutzen, P. J. (1994). A three-dimensional model of the global ammonia cycle. *Journal of Atmospheric Chemistry*, 19(4):331–369.

Dils, B., Cui, J., Henne, S., Mahieu, E., Steinbacher, M., and Mazière, M. D. (2011). 1997-2007 CO trend at the high Alpine site Jungfraujoch: A comparison between NDIR surface in situ and FTIR remote sensing observations. *Atmospheric Chemistry and Physics*, 11(13):6735–6748.

Dreessen, J., Sullivan, J., and Delgado, R. (2016). Observations and impacts of transported Canadian wildfire smoke on ozone and aerosol air quality in the Maryland region on june 9-12, 2015. *Journal of the Air & Waste Management Association*, 66(9):842–862.

Duncan, B. N., Logan, J. A., Bey, I., Megretskaia, I. A., Yantosca, R. M., Novelli, P. C., Jones, N. B., and Rinsland, C. P. (2007). Global budget of CO, 1988-1997: Source estimates and validation with a global model. *Journal of Geophysical Research: Atmospheres*, 112(D22301).

Eastham, S. D. and Jacob, D. J. (2017). Limits on the ability of global Eulerian models to resolve intercontinental transport of chemical plumes. *Atmospheric Chemistry and Physics*, 17(4):2543–2553.

Eck, T. F., Holben, B. N., Reid, J. S., Sinyuk, A., Hyer, E. J., O'Neill, N. T., Shaw, G. E., Vande Castle, J. R., Chapin, F. S., Dubovik, O., Smirnov, A., Vermote, E., Schafer,

J. S., Giles, D., Slutsker, I., Sorokine, M., and Newcomb, W. W. (2009). Optical properties of boreal region biomass burning aerosols in central Alaska and seasonal variation of aerosol optical depth at an Arctic coastal site. *Journal of Geophysical Research: Atmospheres*, 114(D11):722–4740.

Erisman, J. W., Galloway, J., Seitzinger, S., Bleeker, A., and Butterbach-Bahl, K. (2011). Reactive nitrogen in the environment and its effect on climate change. *Current Opinion in Environmental Sustainability*, 3(5):281–290.

Evangeliou, N., Balkanski, Y., Hao, W. M., Petkov, A., Silverstein, R. P., Corley, R., Nordgren, B. L., Urbanski, S. P., Eckhardt, S., Stohl, A., and Others (2016). Wildfires in northern eurasia affect the budget of black carbon in the Arctic - A 12-year retrospective synopsis (2002-2013). *Atmospheric Chemistry and Physics*, 16(12):7587–7604.

Eyring, V., Waugh, D. W., Bodeker, G. E., Cordero, E., Akiyoshi, H., Austin, J., Beagley, S. R., Boville, B. A., Braesicke, P., Brühl, C., Butchart, N., Chipperfield, M. P., Dameris, M., Deckert, R., Deushi, M., Frith, S. M., Garcia, R. R., Gettelman, A., Giorgetta, M. A., Kinnison, D. E., Mancini, E., Manzini, E., Marsh, D. R., Matthes, S., Nagashima, T., Newman, P. A., Nielsen, J. E., Pawson, S., Pitari, G., Plummer, D. A., Rozanov, E., Schraner, M., Scinocca, J. F., Semeniuk, K., Shepherd, T. G., Shibata, K., Steil, B., Stolarski, R. S., Tian, W., and Yoshiki, M. (2007). Multimodel projections of stratospheric ozone in the 21st century. *Journal of Geophysical Research: Atmospheres*, 112(D16):D03304.

Fast, H., Mittermeier, R. L., and Makino, Y. (2011). A Ten-Year record of Arctic trace gas total column measurements at Eureka, Canada, from 1997 to 2006. *Atmosphere-Ocean*, 49(2):67–94.

Fellgett, P. (1951). *The multiplex advantage.* PhD thesis, University of Cambridge.

Fischer, H., Wienhold, F. G., Hoor, P., Bujok, O., Schiller, C., Siegmund, P., Ambaum, M., Scheeren, H. A., and Lelieveld, J. (2000). Tracer correlations in the northern high latitude lowermost stratosphere: Influence of cross-tropopause mass exchange. *Geophysical Research Letters*, 27(1):97–100.

Fisher, J. A., Jacob, D. J., Purdy, M. T., Kopacz, M., Sager, P. L., Carouge, C., Holmes, C. D., Yantosca, R. M., Batchelor, R. L., Strong, K., Diskin, G. S., Fuelberg, H. E., Holloway, J. S., Hyer, E. J., McMillan, W. W., Warner, J., Streets, D. G., Zhang, Q., Wang, Y., and Wu, S. (2010). Source attribution and interannual variability of arctic pollution in spring constrained by aircraft (ARCTAS, ARCPAC) and satellite (AIRS) observations of carbon monoxide. *Atmospheric Chemistry and Physics*, 10(3):977–996.

Fisher, J. A., Murray, L., Jones, D. B. A., and Deutscher, N. M. (2017). Improved method for linear carbon monoxide simulation and source attribution in atmospheric chemistry models illustrated using GEOS-Chem v9. *Geophysical Model Development*, 10(11):4129–4144.

Flanner, M. G. (2013). Arctic climate sensitivity to local black carbon. *Journal of Geophysical Research: Atmospheres*, 118(4):1840–1851.

Flannigan, M. D., Krawchuk, M. A., de Groot, W. J., Mike Wotton, B., and Gowman, L. M. (2009). Implications of changing climate for global wildland fire. *International Journal of Wildland Fire*, 18(5):483–507.

Fountoukis, C. and Nenes, A. (2007). ISORROPIA II: a computationally efficient thermodynamic equilibrium model for K^+–Ca^{2+}–Mg^{2+}–$NH_4{}^+$–Na^+–$SO_4{}^2$–NO_3–Cl–H_2O aerosols. *Atmospheric Chemistry and Physics*, 7(17):4639–4659.

Franco, B., Bader, W., Toon, G. C., Bray, C., Perrin, A., Fischer, E. V., Sudo, K., Boone, C. D., Bovy, B., Lejeune, B., Servais, C., and Mahieu, E. (2015). Retrieval of ethane from ground-based FTIR solar spectra using improved spectroscopy: Recent burden increase above jungfraujoch. *Journal of Quantitative Spectroscopy & Radiative Transfer*, 160:36–49.

Franco, B., Mahieu, E., Emmons, L. K., Tzompa-Sosa, Z. A., Fischer, E. V., Sudo, K., Bovy, B., Conway, S., Griffin, D., Hannigan, J. W., Strong, K., and Walker, K. A. (2016). Evaluating ethane and methane emissions associated with the development of oil and natural gas extraction in North America. *Environmental Research Letters*, 11(4):044010.

Franklin, J. (2015). *Solar absorption spectroscopy at the Dalhousie Atmospheric Observatory.* PhD thesis, Dalhousie University.

Freitas, S. R., Longo, K. M., Chatfield, R., Latham, D., Silva Dias, M. A. F., Andreae, M. O., Prins, E., Santos, J. C., Gielow, R., and Carvalho, Jr, J. A. (2007). Including the sub-grid scale plume rise of vegetation fires in low resolution atmospheric transport models. *Atmospheric Chemistry and Physics*, 7(13):3385–3398.

Fromm, M., Alfred, J., Hoppel, K., Hornstein, J., Bevilacqua, R., Shettle, E., Servranckx, R., Li, Z., and Stocks, B. (2000). Observations of boreal forest fire smoke in the stratosphere by POAM III, SAGE II, and lidar in 1998. *Geophysical Research Letters*, 27(9):1407–1410.

Geddes, A., Robinson, J., and Smale, D. (2018). Python-based dynamic scheduling assistant for atmospheric measurements by Bruker instruments using OPUS. *Applied Optics*, 57(4):689–691.

Gelaro, R., McCarty, W., Suárez, M. J., Todling, R., Molod, A., Takacs, L., Randles, C. A., Darmenov, A., Bosilovich, M. G., Reichle, R., Wargan, K., Coy, L., Cullather, R., Draper, C., Akella, S., Buchard, V., Conaty, A., da Silva, A. M., Gu, W., Kim, G.-K., Koster, R., Lucchesi, R., Merkova, D., Nielsen, J. E., Partyka, G., Pawson, S., Putman, W., Rienecker, M., Schubert, S. D., Sienkiewicz, M., and Zhao, B. (2017). The

Modern-Era retrospective analysis for research and applications, version 2 (MERRA-2). *Journal of Climate*, 30(14):5419–5454.

George, M., Clerbaux, C., Hurtmans, D., Turquety, S., Coheur, P.-F., Pommier, M., Hadji-Lazaro, J., Edwards, D. P., Worden, H., Luo, M., Rinsland, C., and McMillan, W. (2009). Carbon monoxide distributions from the IASI/METOP mission: evaluation with other space-borne remote sensors. *Atmospheric Chemistry and Physics*, 9(21):8317–8330.

Giglio, L., Boschetti, L., Roy, D. P., Humber, M. L., and Justice, C. O. (2018). The Collection 6 MODIS burned area mapping algorithm and product. *Remote Sensing of the Environment*, 217:72–85.

Giglio, L., der Werf, G. R., Randerson, J. T., Collatz, G. J., and Kasibhatla, P. (2006). Global estimation of burned area using MODIS active fire observations. *Atmospheric Chemistry and Physics*, 6(4):957–974.

Giglio, L., Randerson, J. T., and van der Werf, G. R. (2013). Analysis of daily, monthly, and annual burned area using the fourth-generation global fire emissions database (GFED4). *Journal of Geophysical Research: Biogeosciences*, 118(1):317–328.

Giles, D. M., Sinyuk, A., Sorokin, M. G., Schafer, J. S., Smirnov, A., Slutsker, I., Eck, T. F., Holben, B. N., Lewis, J. R., Campbell, J. R., Welton, E. J., Korkin, S. V., and Lyapustin, A. I. (2019). Advancements in the aerosol robotic network (AERONET) version 3 database - automated near-real-time quality control algorithm with improved cloud screening for Sun photometer aerosol optical depth (AOD) measurements. *Atmospheric Measurement Techniques*, 12(1):169–209.

Giuseppe, F. D., Rémy, S., Pappenberger, F., and Wetterhall, F. (2018). Using the fire weather index (FWI) to improve the estimation of fire emissions from fire radiative power (FRP) observations. *Atmospheric Chemistry and Physics*, 18(8):5359–5370.

Goode, J. G., Yokelson, R. J., Susott, R. A., and Ward, D. E. (1999). Trace gas emissions from laboratory biomass fires measured by open-path Fourier transform infrared spectroscopy: Fires in grass and surface fuels. *Journal of Geophysical Research: Atmospheres*, 104(D17):21237–21245.

Goode, J. G., Yokelson, R. J., Ward, D. E., Susott, R. A., Babbitt, R. E., Davies, M. A., and Hao, W. M. (2000). Measurements of excess O_3, CO_2, CO, CH_4, C_2H_4, C_2H_2, HCN, NO, NH_3, HCOOH, CH_3COOH, HCHO, and CH_3OH in 1997 Alaskan biomass burning plumes by airborne Fourier transform infrared spectroscopy (AFTIR). *Journal of Geophysical Research: Atmospheres*, 105(D17):22147–22166.

Gordon, I. E., Rothman, L. S., Hill, C., Kochanov, R. V., Tan, Y., Bernath, P. F., Birk, M., Boudon, V., Campargue, A., Chance, K. V., Drouin, B. J., Flaud, J.-M., Gamache, R. R., Hodges, J. T., Jacquemart, D., Perevalov, V. I., Perrin, A., Shine, K. P., Smith, M.-A. H., Tennyson, J., Toon, G. C., Tran, H., Tyuterev, V. G., Barbe, A., Császár, A. G., Devi, V. M., Furtenbacher, T., Harrison, J. J., Hartmann, J.-M., Jolly, A., Johnson, T. J., Karman, T., Kleiner, I., Kyuberis, A. A., Loos, J., Lyulin, O. M., Massie, S. T., Mikhailenko, S. N., Moazzen-Ahmadi, N., Müller, H. S. P., Naumenko, O. V., Nikitin, A. V., Polyansky, O. L., Rey, M., Rotger, M., Sharpe, S. W., Sung, K., Starikova, E., Tashkun, S. A., Auwera, J. V., Wagner, G., Wilzewski, J., Wcisło, P., Yu, S., and Zak, E. J. (2017). The HITRAN2016 molecular spectroscopic database. *Journal of Quantitative Spectroscopy & Radiative Transfer*, 203:3–69.

Griffin, D., Walker, K. A., Franklin, J. E., Parrington, M., Whaley, C., Hopper, J., Drummond, J. R., Palmer, P. I., Strong, K., Duck, T. J., Abboud, I., Bernath, P. F., Clerbaux, C., Coheur, P.-F., Curry, K. R., Dan, L., Hyer, E., Kliever, J., Lesins, G., Maurice, M., Saha, A., Tereszchuk, K., and Weaver, D. (2013). Investigation of CO, C_2H_6 and aerosols in a boreal fire plume over eastern Canada during BORTAS 2011 using ground- and satellite-based observations and model simulations. *Atmospheric Chemistry and Physics*, 13(20):10227–10241.

Gubler, S., Gruber, S., and Purves, R. S. (2012). Uncertainties of parameterized surface downward clear-sky shortwave and all-sky longwave radiation. *Atmospheric Chemistry and Physics*, 12(11):5077–5098.

Guenther, A., Geron, C., Pierce, T., Lamb, B., Harley, P., and Fall, R. (2000). Natural emissions of non-methane volatile organic compounds, carbon monoxide, and oxides of nitrogen from North America. *Atmospheric Environment*, 34(12):2205–2230.

Guenther, A. B., Jiang, X., Heald, C. L., Sakulyanontvittaya, T., Duhl, T., Emmons, L. K., and Wang, X. (2012). The Model of Emissions of Gases and Aerosols from Nature version 2.1 (MEGAN2.1): An extended and updated framework for modeling biogenic emissions. *Geoscientific Model Development*, 5(6):1471–1492.

Hannigan, J. W., Coffey, M. T., and Goldman, A. (2009). Semiautonomous FTS observation system for remote sensing of stratospheric and tropospheric gases. *Journal of Atmospheric and Oceanic Technology*, 26(9):1814–1828.

Hase, F. (2012). Improved instrumental line shape monitoring for the ground-based, high-resolution FTIR spectrometers of the network for the detection of atmospheric composition change. *Atmospheric Measurement Techniques*, 5(3):603–610.

Hase, F., Blumenstock, T., and Paton-Walsh, C. (1999). Analysis of the instrumental line shape of high-resolution fourier transform IR spectrometers with gas cell measurements and new retrieval software. *Applied Optics*, 38(15):3417–3422.

Hase, F., Hannigan, J. W., Coffey, M. T., Goldman, A., Höpfner, M., Jones, N. B., Rinsland, C. P., and Wood, S. W. (2004). Intercomparison of retrieval codes used for the analysis of high-resolution, ground-based FTIR measurements. *Journal of Quantitative Spectroscopy & Radiative Transfer*, 87(1):25–52.

Hegg, D. A., Radke, L. F., Hobbs, P. V., and Riggan, P. J. (1988). Ammonia emissions from biomass burning. *Geophysical Research Letters*, 15(4):335–337.

Heilman, W. E., Liu, Y., Urbanski, S., Kovalev, V., and Mickler, R. (2014). Wildland fire emissions, carbon, and climate: Plume rise, atmospheric transport, and chemistry processes. *Forest Ecology and Management*, 317:70–79.

Helmig, D., Rossabi, S., Hueber, J., Tans, P., Montzka, S. A., Masarie, K., Thoning, K., Plass-Duelmer, C., Claude, A., Carpenter, L. J., Lewis, A. C., Punjabi, S., Reimann, S., Vollmer, M. K., Steinbrecher, R., Hannigan, J. W., Emmons, L. K., Mahieu, E., Franco, B., Smale, D., and Pozzer, A. (2016). Reversal of global atmospheric ethane and propane trends largely due to US oil and natural gas production. *Nature Geoscience*, 9:490–495.

Henne, S., Brunner, D., Folini, D., Solberg, S., Klausen, J., and Buchmann, B. (2010). Assessment of parameters describing representativeness of air quality in-situ measurement sites. *Atmospheric Chemistry and Physics*, 10(8):3561–3581.

Hertel, O., Skjøth, C. A., Reis, S., Bleeker, A., Harrison, R. M., Cape, J. N., Fowler, D., Skiba, U., Simpson, D., Jickells, T., Kulmala, M., Gyldenkærne, S., Sørensen, L. L., Erisman, J. W., and Sutton, M. A. (2012). Governing processes for reactive nitrogen compounds in the European atmosphere. *Biogeosciences*, 9(12):4921–4954.

Holben, B. N., Eck, T. F., Slutsker, I., Tanré, D., Buis, J. P., Setzer, A., Vermote, E., Reagan, J. A., Kaufman, Y. J., Nakajima, T., Lavenu, F., Jankowiak, I., and Smirnov, A. (1998). AERONET - A federated instrument network and data archive for aerosol characterization. *Remote Sensing of Environment*, 66(1):1–16.

Holloway, T., Levy, H., and Kasibhatla, P. (2000). Global distribution of carbon monoxide. *Journal of Geophysical Research: Atmospheres*, 105(D10):12123–12147.

Holtslag, A. A. M. and Boville, B. A. (1993). Local versus nonlocal Boundary-Layer diffusion in a global climate model. *Journal of Climate*, 6(10):1825–1842.

Honrath, R. E. (2004). Regional and hemispheric impacts of anthropogenic and biomass burning emissions on summertime CO and O_3 in the North Atlantic lower free troposphere. *Journal of Geophysical Research: Atmospheres*, 109(D24310).

Hoor, P., Fischer, H., Lange, L., Lelieveld, J., and Brunner, D. (2002). Seasonal variations of a mixing layer in the lowermost stratosphere as identified by the CO-O_3 correlation from in situ measurements. *Journal of Geophysical Research: Atmospheres*, 107(D5):ACL 1–1–ACL 1–11.

Hu, Q., Goloub, P., Veselovskii, I., Bravo-Aranda, J.-A., Popovici, I. E., Podvin, T., Haeffelin, M., Lopatin, A., Dubovik, O., Pietras, C., Huang, X., Torres, B., and Chen, C. (2019). Long-range-transported Canadian smoke plumes in the lower stratosphere over northern France. *Atmospheric Chemistry and Physics*, 19(2):1173–1193.

Hurtmans, D., Coheur, P.-F., Wespes, C., Clarisse, L., Scharf, O., Clerbaux, C., Hadji-Lazaro, J., George, M., and Turquety, S. (2012). FORLI radiative transfer and retrieval code for IASI. *Journal of Quantitative Spectroscopy & Radiative Transfer*, 113(11):1391–1408.

Ikeda, K. and Tanimoto, H. (2015). Exceedances of air quality standard level of PM2.5 in Japan caused by Siberian wildfires. *Environmental Research Letters*, 10(10):105001.

Ireland, G. and Petropoulos, G. P. (2015). Exploring the relationships between post-fire vegetation regeneration dynamics, topography and burn severity: A case study from the Montane Cordillera Ecozones of Western Canada. *Applied Geography*, 56:232–248.

Jacob, D. J., Field, B. D., Li, Q., Blake, D. R., de Gouw, J., Warneke, C., Hansel, A., Wisthaler, A., Singh, H. B., and Guenther, A. (2005). Global budget of methanol:

Constraints from atmospheric observations. *Journal of Geophysical Research: Atmospheres*, 110(D08303).

Jacquinot, P. and Dufour, C. (1948). Conditions optiques d'emploi des cellules photoélectriques dans les spectrographes et les interféromètres. *Journal Recherche CNRS*, 6(91):18.

Jaffe, D., Anderson, T., Covert, D., Kotchenruther, R., Trost, B., Danielson, J., Simpson, W., Berntsen, T., Karlsdottir, S., Blake, D., Harris, J., Carmichael, G., and Uno, I. (1999). Transport of Asian air pollution to North America. *Geophysical Research Letters*, 26(6):711–714.

Jaffe, D., Bertschi, I., Jaeglé, L., Novelli, P., Reid, J. S., Tanimoto, H., Vingarzan, R., and Westphal, D. L. (2004). Long-range transport of Siberian biomass burning emissions and impact on surface ozone in western North America. *Geophysical Research Letters*, 31(L16106).

Janssens-Maenhout, G., Pagliari, V., Guizzardi, D., and Muntean, M. (2013). Global emission inventories in the Emission Database for Global Atmospheric Research (EDGAR)-Manual (I). *Gridding: EDGAR emissions distribution on global gridmaps, Publications Office of the European Union, Luxembourg.*

Jeong, J. I., Park, R. J., and Youn, D. (2008). Effects of Siberian forest fires on air quality in East Asia during May 2003 and its climate implication. *Atmospheric Environment*, 42(39):8910–8922.

Johnson, T. J., Sams, R. L., Blake, T. A., Sharpe, S. W., and Chu, P. M. (2002). Removing aperture-induced artifacts from Fourier transform infrared intensity values. *Applied Optics*, 41(15):2831–2839.

Jones, N. B., Riedel, K., Allan, W., Wood, S., Palmer, P. I., Chance, K., and Notholt, J. (2009). Long-term tropospheric formaldehyde concentrations deduced from ground-based fourier transform solar infrared measurements. *Atmospheric Chemistry and Physics*, 9(18):7131–7142.

Kaiser, J. W., Heil, A., Andreae, M. O., Benedetti, A., Chubarova, N., Jones, L., Morcrette, J.-J., Razinger, M., Schultz, M. G., Suttie, M., and van der Werf, G. R. (2012). Biomass burning emissions estimated with a global fire assimilation system based on observed fire radiative power. *Biogeosciences*, 9(1):527–554.

Karlsson, P. E., Ferm, M., Tømmervik, H., Hole, L. R., Karlsson, G. P., Ruoho-Airola, T., Aas, W., Hellsten, S., Akselsson, C., Mikkelsen, T. N., and Nihlgård, B. (2013). Biomass burning in eastern Europe during spring 2006 caused high deposition of ammonium in northern Fennoscandia. *Environmental Pollution*, 176:71–79.

Kasai, Y. J., Kagawa, A., Jones, N., Fujiwara, A., Seki, K., Murayama, Y., and Murcray, F. (2005a). Seasonal variations of CO and HCN in the troposphere measured by solar absorption spectroscopy over Poker Flat, Alaska. *Geophysical Research Letters*, 32(19):1–4.

Kasai, Y. J., Koshiro, T., Endo, M., Jones, N. B., and Murayama, Y. (2005b). Ground-based measurement of strato–mesospheric CO by a FTIR spectrometer over Poker Flat, Alaska. *Advances in Space Research*, 35(11):2024–2030.

Keenan, T. F. and Riley, W. J. (2018). Greening of the land surface in the world's cold regions consistent with recent warming. *Nature Climate Change*, 8(9):825–828.

Kerzenmacher, T., Dils, B., Kumps, N., Blumenstock, T., Clerbaux, C., Coheur, P.-F., Demoulin, P., García, O., George, M., Griffith, D. W. T., Hase, F., Hadji-Lazaro, J., Hurtmans, D., Jones, N., Mahieu, E., Notholt, J., Paton-Walsh, C., Raffalski, U., Ridder, T., Schneider, M., Servais, C., and Mazière, M. D. (2012). Validation of IASI FORLI carbon monoxide retrievals using FTIR data from NDACC. *Atmospheric Measurement Techniques*, 5(11):2751–2761.

Kharol, S. K., Shephard, M. W., McLinden, C. A., Zhang, L., Sioris, C. E., O'Brien, J. M., Vet, R., Cady-Pereira, K. E., Hare, E., Siemons, J., and Krotkov, N. A. (2018). Dry deposition of reactive nitrogen from satellite observations of ammonia and nitrogen dioxide over North America. *Geophysical Research Letters*, 45(2):1157–1166.

Khaykin, S. M., GodinBeekmann, S., Hauchecorne, A., Pelon, J., Ravetta, F., and Keckhut, P. (2018). Stratospheric smoke with unprecedentedly high backscatter observed by lidars above southern France. *Geophysical Research Letters*, 45(3):1639–1646.

Kirchmeier-Young, M. C., Gillett, N. P., Zwiers, F. W., Cannon, A. J., and Anslow, F. S. (2019). Attribution of the influence of Human-Induced climate change on an extreme fire season. *Earth's Future*, 7(1):2–10.

Klonecki, A. (2003). Seasonal changes in the transport of pollutants into the Arctic troposphere-model study. *Journal of Geophysical Research: Atmospheres*, 108(D4):8367.

Kochtubajda, B., Stewart, R. E., Flannigan, M. D., Bonsal, B. R., Cuell, C., and Mooney, C. J. (2019). An assessment of surface and atmospheric conditions associated with the extreme 2014 wildfire season in Canada's Northwest Territories. *Atmosphere-Ocean*, 57(1):73–90.

Konovalov, I. B., Beekmann, M., Kuznetsova, I. N., Yurova, A., and Zvyagintsev, A. M. (2011). Atmospheric impacts of the 2010 Russian wildfires: Integrating modelling and measurements of an extreme air pollution episode in the Moscow region. *Atmospheric Chemistry and Physics*, 11(19):10031–10056.

Koster, R. D., Darmenov, A. S., and da Silva, A. M. (2015). *The Quick Fire Emissions Dataset (QFED): Documentation of Versions 2.1, 2.2 and 2.4. Volume 38; Technical Report Series on Global Modeling and Data Assimilation.*

Kozlov, V. S., Yausheva, E. P., Terpugova, S. A., Panchenko, M. V., Chernov, D. G., and Shmargunov, V. P. (2014). Optical–microphysical properties of smoke haze from Siberian forest fires in summer 2012. *International Journal of Remote Sensing*, 35(15):5722–5741.

Krause, A., Kloster, S., Wilkenskjeld, S., and Paeth, H. (2014). The sensitivity of global wildfires to simulated past, present, and future lightning frequency. *Journal of Geophysical Research: Biogeosciences*, 119(3):312–322.

Krupa, S. V. (2003). Effects of atmospheric ammonia (NH_3) on terrestrial vegetation: a review. *Environmental Pollution*, 124(2):179–221.

Kurylo, M. J. (1991). Network for the detection of stratospheric change.

Langerock, B. (2016). Ongoing harmonization. 2016 Joint NDACC IRWG/TCCON Meeting.

Law, K. S. and Stohl, A. (2007). Arctic air pollution: origins and impacts. *Science*, 315(5818):1537–1540.

Lefer, B. L., Talbot, R. W., Harriss, R. H., Bradshaw, J. D., Sandholm, S. T., Olson, J. O., Sachse, G. W., Collins, J., Shipham, M. A., Blake, D. R., Klemm, K. I., Klemm, O., Gorzelska, K., and Barrick, J. (1994). Enhancement of acidic gases in biomass burning impacted air masses over Canada. *Journal of Geophysical Research: Atmospheres*, 99(D1):1721–1737.

Lefer, B. L., Talbot, R. W., and Munger, J. W. (1999). Nitric acid and ammonia at a rural northeastern U.S. site. *Journal of Geophysical Research: Atmospheres*, 104(D1):1645–1661.

Levine, J. S. (2003). 4.05 - Biomass Burning: The Cycling of Gases and Particulates from the Biosphere to the Atmosphere. In Holland, H. D. and Turekian, K. K., editors, *Treatise on Geochemistry*, pages 143–158. Pergamon, Oxford.

Li, Q., Jacob, D. J., Bey, I., Yantosca, R. M., Zhao, Y., Kondo, Y., and Notholt, J. (2000). Atmospheric hydrogen cyanide (HCN): Biomass burning source, ocean sink? *Geophysical Research Letters*, 27(3):357–360.

Li, Q., Jacob, D. J., Yantosca, R. M., Heald, C. L., Singh, H. B., Koike, M., Zhao, Y., Sachse, G. W., and Streets, D. G. (2003). A global three-dimensional model analysis of the atmospheric budgets of HCN and CH_3CN: Constraints from aircraft and ground measurements. *Journal of Geophysical Research: Atmospheres*, 108(D21):8827.

Li, Q., Palmer, P. I., Pumphrey, H. C., Bernath, P., and Mahieu, E. (2009). What drives the observed variability of HCN in the troposphere and lower stratosphere? *Atmospheric Chemistry and Physics*, 9(21):8531–8543.

Lindenmaier, R. (2012). *Studies of Arctic Middle Atmosphere Chemistry using Infrared Absorption Spectroscopy*. PhD thesis, University of Toronto.

Liou, K. N. (2002). *An Introduction to Atmospheric Radiation*. Elsevier.

Liu, H., Jacob, D. J., Bey, I., and Yantosca, R. M. (2001). Constraints from 210 Pb and 7 Be on wet deposition and transport in a global three-dimensional chemical tracer model driven by assimilated meteorological fields. *Journal of Geophysical Research: Atmospheres*, 106(D11):12109–12128.

Logan, J. A., Prather, M. J., Wofsy, S. C., and McElroy, M. B. (1981). Tropospheric chemistry: A global perspective. *Journal of Geophysical Research: Oceans*, 86(C8):7210–7254.

Lutsch, E., Dammers, E., Conway, S., and Strong, K. (2016). Long-range transport of NH_3, CO, HCN, and C_2H_6 from the 2014 Canadian wildfires. *Geophysical Research Letters*, 43(15):8286–8297.

Lutsch, E., Strong, K., Jones, D. B. A., Ortega, I., Hannigan, J. W., Dammers, E., Shephard, M. W., Morris, E., Murphy, K., Evans, M. J., Parrington, M., Whitburn, S., Van Damme, M., Clarisse, L., Coheur, P., Clerbaux, C., Croft, B., Martin, R. V., Pierce, J. R., and Fisher, J. A. (2019). Unprecedented atmospheric ammonia concentrations detected in the high Arctic from the 2017 Canadian Wildfires. *Journal of Geophysical Research: Atmospheres*, 124(D14):8178–8202.

Macias Fauria, M. and Johnson, E. A. (2006). Large-scale climatic patterns control large lightning fire occurrence in Canada and Alaska forest regions. *Journal of Geophysical Research: Biogeosciences*, 111(G4).

Macias Fauria, M. and Johnson, E. A. (2008). Climate and wildfires in the North American boreal forest. *Philosophical transactions of the Royal Society of London. Series B, Biological Sciences*, 363(1501):2315–2327.

Mack, M. C., Bret-Harte, M. S., Hollingsworth, T. N., Jandt, R. R., Schuur, E. A. G., Shaver, G. R., and Verbyla, D. L. (2011). Carbon loss from an unprecedented Arctic tundra wildfire. *Nature*, 475(7357):489–492.

Mahieu, E., Zander, R., Delbouille, L., Demoulin, P., Roland, G., and Servais, C. (1997). Observed trends in total vertical column abundances of atmospheric gases from IR solar spectra recorded at the Jungfraujoch. *Journal of Atmospheric Chemistry*, 28(1-3):227–243.

Makar, P. A., Akingunola, A., Aherne, J., Cole, A. S., Aklilu, Y.-A., Zhang, J., Wong, I., Hayden, K., Li, S.-M., Kirk, J., Scott, K., Moran, M. D., Robichaud, A., Cathcart, H., Baratzedah, P., Pabla, B., Cheung, P., Zheng, Q., and Jeffries, D. S. (2018). Estimates of exceedances of critical loads for acidifying deposition in Alberta and Saskatchewan. *Atmospheric Chemistry and Physics*, 18(13):9897–9927.

Makarova, M. V., Poberovskii, A. V., and Osipov, S. I. (2011). Time variations of the total CO content in the atmosphere near St. Petersburg. *Izvestiya, Atmospheric and Oceanic Physics*, 47(6):739–746.

Marsh, D. R., Mills, M. J., Kinnison, D. E., Lamarque, J.-F., Calvo, N., and Polvani, L. M. (2013). Climate change from 1850 to 2005 simulated in CESM1 (WACCM). *Journal of Climate*, 26(19):7372–7391.

McConnell, J. R., Edwards, R., Kok, G. L., Flanner, M. G., Zender, C. S., Saltzman, E. S., Banta, J. R., Pasteris, D. R., Carter, M. M., and Kahl, J. D. W. (2007). 20th-century industrial black carbon emissions altered Arctic climate forcing. *Science*, 317(5843):1381–1384.

Meier, A., Toon, G. C., Rinsland, C. P., Goldman, A., and Hase, F. (2004). *Spectroscopic Atlas of Atmospheric Microwindows in the Middle Infra-Red*, volume 048 of *IRF Technical Report*. Swedish Institute of Space Physics.

Mendonca, J. S. (2017). *Improving the Retrievals of Greenhouse Gases from Ground-based Solar Absorption Spectra*. PhD thesis, University of Toronto.

Millet, D. B., Jacob, D. J., Custer, T. G., Gouw, J. A. d., Goldstein, A. H., Karl, T., Singh, H. B., Sive, B. C., Talbot, R. W., Warneke, C., and Williams, J. (2008). New constraints on terrestrial and oceanic sources of atmospheric methanol. *Atmospheric Chemistry and Physics*, 8(23):6887–6905.

Moussa, S. G., Leithead, A., Li, S.-M., Chan, T. W., Wentzell, J. J. B., Stroud, C., Zhang, J., Lee, P., Lu, G., Brook, J. R., Hayden, K., Narayan, J., and Liggio, J. (2016). Emissions of hydrogen cyanide from on-road gasoline and diesel vehicles. *Atmospheric Environment*, 131:185–195.

Muller, J.-F., Stavrakou, T., Bauwens, M., George, M., Hurtmans, D., Coheur, P.-F., Clerbaux, C., and Sweeney, C. (2018). Top-down CO emissions based on IASI observations and hemispheric constraints on OH levels. *Geophysical Research Letters*, 45(3):1621–1629.

Myneni, R. B., Keeling, C. D., Tucker, C. J., Asrar, G., and Nemani, R. R. (1997). Increased plant growth in the northern high latitudes from 1981 to 1991. *Nature*, 386(6626):698–702.

Nance, J. D., Hobbs, P. V., Radke, L. F., and Ward, D. E. (1993). Airborne measurements of gases and particles from an Alaskan wildfire. *Journal of Geophysical Research: Atmospheres*, 98(D8):14873–14882.

Natural Resources Canada (2013). Forest classification - Natural Resources Canada. `https://www.nrcan.gc.ca/forests/measuring-reporting/classification/13179`. Accessed: 2019-1-30.

Notholt, J., Toon, G., Stordal, F., Solberg, S., Schmidbauer, N., Becker, E., Meier, A., and Sen, B. (1997a). Seasonal variations of atmospheric trace gases in the high Arctic at 79°N. *Journal of Geophysical Research: Atmospheres*, 102(D11):12855–12861.

Notholt, J., Toon, G. C., Lehmann, R., Sen, B., and Blavier, J.-F. (1997b). Comparison of Arctic and Antarctic trace gas column abundances from ground-based Fourier transform infrared spectrometry. *Journal of Geophysical Research: Atmospheres*, 102(D11):12863–12869.

Notholt, J., Toon, G. C., Rinsland, C. P., Pougatchev, N. S., Jones, N. B., Connor, B. J., Weller, R., Gautrois, M., and Schrems, O. (2000). Latitudinal variations of trace gas concentrations in the free troposphere measured by solar absorption spectroscopy during a ship cruise. *Journal of Geophysical Research: Atmospheres*, 105(D1):1337–1349.

O'Neill, N. T., Perro, C., Saha, A., Lesins, G., Duck, T. J., Eloranta, E. W., Nott, G. J., Hoffman, A., Karumudi, M. L., Ritter, C., Bourassa, A., Abboud, I., Carn, S. A., and Savastiouk, V. (2012). Properties of Sarychev sulphate aerosols over the Arctic. *Journal of Geophysical Research: Atmospheres*, 117(D04203).

Ordóñez, C., Brunner, D., Staehelin, J., Hadjinicolaou, P., Pyle, J. A., Jonas, M., Wernli, H., and Prévôt, A. S. H. (2007). Strong influence of lowermost stratospheric ozone on lower tropospheric background ozone changes over Europe. *Geophysical Research Letters*, 34(L07805).

Palm, M. (2014). SFIT4 - a comprehensive tool to analyse spectra recorded by ground-based FTIR spectroscopy of the atmosphere. University of Toronto, Earth, Atmosphere and Planetary Physics Noble Seminar.

Pan, L. L., Randel, W. J., Gary, B. L., Mahoney, M. J., and Hintsa, E. J. (2004). Definitions and sharpness of the extratropical tropopause: A trace gas perspective. *Journal of Geophysical Research: Atmospheres*, 109(D23103).

Park, R. J., Jacob, D. J., Field, B. D., Yantosca, R. M., and Chin, M. (2004). Natural and transboundary pollution influences on sulfate-nitrate-ammonium aerosols in the United States: Implications for policy. *Journal of Geophysical Research: Atmospheres*, 109(D15204).

Park, R. J., Jacob, D. J., Kumar, N., and Yantosca, R. M. (2006). Regional visibility statistics in the United States: Natural and transboundary pollution influences, and implications for the regional haze rule. *Atmospheric Environment*, 40(28):5405–5423.

Parrington, M., Palmer, P. I., Lewis, A. C., Lee, J. D., Rickard, A. R., Carlo, P. D., Taylor, J. W., Hopkins, J. R., Punjabi, S., Oram, D. E., Forster, G., Aruffo, E., Moller, S. J., Bauguitte, S. J.-B., Allan, J. D., Coe, H., and Leigh, R. J. (2013).

Ozone photochemistry in boreal biomass burning plumes. *Atmospheric Chemistry and Physics*, 13(15):7321–7341.

Paton-Walsh, C., Deutscher, N. M., Griffith, D. W. T., Forgan, B. W., Wilson, S. R., Jones, N. B., and Edwards, D. P. (2010). Trace gas emissions from savanna fires in northern Australia. *Journal of Geophysical Research: Atmospheres*, 115(D16314).

Paton-Walsh, C., Jones, N. B., Wilson, S. R., Haverd, V., Meier, A., Griffith, D. W. T., and Rinsland, C. P. (2005). Measurements of trace gas emissions from Australian forest fires and correlations with coincident measurements of aerosol optical depth. *Journal of Geophysical Research: Atmospheres*, 110(D24305).

Patra, P. K., Houweling, S., Krol, M., Bousquet, P., Belikov, D., Bergmann, D., Bian, H., Cameron-Smith, P., Chipperfield, M. P., Corbin, K., Fortems-Cheiney, A., Fraser, A., Gloor, E., Hess, P., Ito, A., Kawa, S. R., Law, R. M., Loh, Z., Maksyutov, S., Meng, L., Palmer, P. I., Prinn, R. G., Rigby, M., Saito, R., and Wilson, C. (2011). TransCom model simulations of CH_4 and related species: Linking transport, surface flux and chemical loss with CH_4 variability in the troposphere and lower stratosphere. *Atmospheric Chemistry and Physics*, 11(24):12813–12837.

Paulot, F., Paynter, D., Ginoux, P., Naik, V., Whitburn, S., Van Damme, M., Clarisse, L., Coheur, P.-F., and Horowitz, L. W. (2017). Gas-aerosol partitioning of ammonia in biomass burning plumes: Implications for the interpretation of spaceborne observations of ammonia and the radiative forcing of ammonium nitrate. *Geophysical Research Letters*, 44(15):8084–8093.

Petersen, A. K., Warneke, T., Lawrence, M. G., Notholt, J., and Schrems, O. (2008). First ground-based FTIR observations of the seasonal variation of carbon monoxide in the tropics. *Geophysical Research Letters*, 35(L03813).

Peterson, D. A., Campbell, J. R., Hyer, E. J., Fromm, M. D., Kablick, G. P., Cossuth, J. H., and DeLand, M. T. (2018). Wildfire-driven thunderstorms cause a volcano-like stratospheric injection of smoke. *Climate and Atmospheric Science*, 1(1):30.

Petetin, H., Sauvage, B., Parrington, M., Clark, H., Fontaine, A., Athier, G., Blot, R., Boulanger, D., Cousin, J.-M., Nédélec, P., and Thouret, V. (2018). The role of biomass burning as derived from the tropospheric CO vertical profiles measured by IAGOS aircraft in 2002-2017. *Atmospheric Chemistry and Physics*, 18(23):17277–17306.

Philip, S., Martin, R. V., and Keller, C. A. (2016). Sensitivity of chemistry-transport model simulations to the duration of chemical and transport operators: a case study with GEOS-Chem v10-01. *Geoscientific Model Development*, 9(5):1683–1695.

Pougatchev, N. S., Connor, B. J., and Rinsland, C. P. (1995). Infrared measurements of the ozone vertical distribution above Kitt Peak. *Journal of Geophysical Research: Atmospheres*, 100(D8):16689–16697.

Ramanathan, V. and Carmichael, G. (2008). Global and regional climate changes due to black carbon. *Nature Geoscience*, 1:221–227.

Rastigejev, Y., Park, R., Brenner, M. P., and Jacob, D. J. (2010). Resolving intercontinental pollution plumes in global models of atmospheric transport. *Journal of Geophysical Research: Atmospheres*, 115(D02302).

Rémy, S., Veira, A., Paugam, R., Sofiev, M., Kaiser, J. W., Marenco, F., Burton, S. P., Benedetti, A., Engelen, R. J., Ferrare, R., and Hair, J. W. (2017). Two global data sets of daily fire emission injection heights since 2003. *Atmospheric Chemistry and Physics*, 17(4):2921–2942.

R'Honi, Y., Clarisse, L., Clerbaux, C., Hurtmans, D., Duflot, V., Turquety, S., Ngadi, Y., and Coheur, P.-F. (2013). Exceptional emissions of NH_3 and HCOOH in the 2010 Russian wildfires. *Atmospheric Chemistry and Physics*, 13(8):4171–4181.

Riddick, S. N., Dragosits, U., Blackall, T. D., Daunt, F., Wanless, S., and Sutton, M. A. (2012). The global distribution of ammonia emissions from seabird colonies. *Atmospheric Environment*, 55:319–327.

Rinsland, C. P., Dufour, G., Boone, C. D., Bernath, P. F., Chiou, L., Coheur, P.-F., Turquety, S., and Clerbaux, C. (2007). Satellite boreal measurements over Alaska and Canada during June-July 2004: Simultaneous measurements of upper tropospheric CO, C_2H_6, HCN, CH_3cl, CH_4, C_2H_2, CH_3OH, HCOOH, OCS, and SF_6 mixing ratios. *Global Biogeochemical Cycles*, 21(GB3008).

Rinsland, C. P., Jones, N. B., Connor, B. J., Logan, J. A., Pougatchev, N. S., Goldman, A., Murcray, F. J., Stephen, T. M., Pine, A. S., Zander, R., Mahieu, E., and Demoulin, P. (1998). Northern and Southern hemisphere ground-based infrared spectroscopic measurements of tropospheric carbon monoxide and ethane. *Journal of Geophysical Research: Atmospheres*, 103(D21):28197–28217.

Rinsland, C. P., Meier, A., Griffith, D. W. T., and Chiou, L. S. (2001). Ground-based measurements of tropospheric CO, C_2H_6, and HCN from Australia at 34°S latitude during 1997-1998. *Journal of Geophysical Research: Atmospheres*, 106(D18):20913–20924.

Rodgers, C. D. (1976). Retrieval of atmospheric temperature and composition from remote measurements of thermal radiation. *Reviews of Geophysics*, 14(4):609–624.

Rodgers, C. D. (1990). Characterization and error analysis of profiles retrieved from remote sounding measurements. *Journal of Geophysical Research: Atmospheres*, 95(D5):5587–5595.

Rodgers, C. D. (2000). *Inverse Methods for Atmospheric Sounding: Theory and Practice*. Series on Atmospheric, Oceanic and Planetary Physics. World Scientific.

Rodgers, C. D. and Connor, B. J. (2003). Intercomparison of remote sounding instruments. *Journal of Geophysical Research: Atmospheres*, 108(D3):4116.

Rodríguez, E., Toledano, C., Cachorro, V. E., Ortiz, P., Stebel, K., Berjón, A., Blindheim, S., Gausa, M., and de Frutos, A. M. (2012). Aerosol characterization at the sub-arctic site andenes (69°N, 16°E), by the analysis of columnar optical properties. *Quarterly Journal of the Royal Meteorological Society*, 138(663):471–482.

Rolph, G. D. (2016). Real-time Environmental Applications and Display sYstem (READY) Website (http://www.ready.noaa.gov). NOAA Air Resources Laboratory.

Rothman, L. S., Gordon, I. E., Babikov, Y., Barbe, A., Chris Benner, D., Bernath, P. F., Birk, M., Bizzocchi, L., Boudon, V., Brown, L. R., Campargue, A., Chance, K., Cohen, E. A., Coudert, L. H., Devi, V. M., Drouin, B. J., Fayt, A., Flaud, J.-M., Gamache, R. R., Harrison, J. J., Hartmann, J.-M., Hill, C., Hodges, J. T., Jacquemart, D., Jolly, A., Lamouroux, J., Le Roy, R. J., Li, G., Long, D. A., Lyulin, O. M., Mackie, C. J., Massie, S. T., Mikhailenko, S., Müller, H. S. P., Naumenko, O. V., Nikitin, A. V., Orphal, J., Perevalov, V., Perrin, A., Polovtseva, E. R., Richard, C., Smith, M. A. H., Starikova, E., Sung, K., Tashkun, S., Tennyson, J., Toon, G. C., Tyuterev, V. G., and Wagner, G. (2013). The HITRAN2012 molecular spectroscopic database. *Journal of Quantitative Spectroscopy & Radiative Transfer*, 130:4–50.

Rothman, L. S., Gordon, I. E., Barbe, A., Benner, D. C., Bernath, P. F., Birk, M., Boudon, V., Brown, L. R., Campargue, A., Champion, J.-P., Chance, K., Coudert, L. H., Dana, V., Devi, V. M., Fally, S., Flaud, J.-M., Gamache, R. R., Goldman, A., Jacquemart, D., Kleiner, I., Lacome, N., Lafferty, W. J., Mandin, J.-Y., Massie, S. T., Mikhailenko, S. N., Miller, C. E., Moazzen-Ahmadi, N., Naumenko, O. V., Nikitin, A. V., Orphal, J., Perevalov, V. I., Perrin, A., Predoi-Cross, A., Rinsland, C. P., Rotger, M., Šimečková, M., Smith, M. A. H., Sung, K., Tashkun, S. A., Tennyson, J., Toth, R. A., Vandaele, A. C., and Vander Auwera, J. (2009). The HITRAN 2008 molecular spectroscopic database. *Journal of Quantitative Spectroscopy & Radiative Transfer*, 110(9):533–572.

Rozwadowska, A., Zieliński, T., Petelski, T., and Sobolewski, P. (2010). Cluster analysis of the impact of air back-trajectories on aerosol optical properties at Hornsund, Spitsbergen. *Atmospheric Chemistry and Physics*, 10(3):877–893.

Rudolph, J. (1995). The tropospheric distribution and budget of ethane. *Journal of Geophysical Research: Atmospheres*, 100(D6):11369–11381.

Saha, A., O'Neill, N. T., Eloranta, E., Stone, R. S., Eck, T. F., Zidane, S., Daou, D., Lupu, A., Lesins, G., Shiobara, M., and Others (2010). Pan-Arctic sunphotometry during the ARCTAS-A campaign of April 2008. *Geophysical Research Letters*, 37(L05803).

Saha, S., Moorthi, S., Wu, X., Wang, J., Nadiga, S., Tripp, P., Behringer, D., Hou, Y.-T., Chuang, H.-Y., Iredell, M., Ek, M., Meng, J., Yang, R., Mendez, M. P., van den Dool, H., Zhang, Q., Wang, W., Chen, M., and Becker, E. (2011). NCEP Climate Forecast System Version 2 (CFSv2) 6-hourly Products.

Santín, C., Doerr, S. H., Preston, C. M., and González-Rodríguez, G. (2015). Pyrogenic organic matter production from wildfires: A missing sink in the global carbon cycle. *Global Change Biology*, 21(4):1621–1633.

Schimel, D. and Baker, D. (2002). Carbon cycle: the wildfire factor. *Nature*, 420(6911):29–30.

Schimel, J. P. and Bennett, J. (2004). Nitrogen mineralization: Challenges of a changing paradigm. *Ecology*, 85(3):591–602.

Sekimoto, K., Koss, A. R., Gilman, J. B., Selimovic, V., Coggon, M. M., Zarzana, K. J., Yuan, B., Lerner, B. M., Brown, S. S., Warneke, C., Yokelson, R. J., Roberts, J. M., and de Gouw, J. (2018). High- and low-temperature pyrolysis profiles describe volatile organic compound emissions from western US wildfire fuels. *Atmospheric Chemistry and Physics*, 18(13):9263–9281.

Sharma, S., Andrews, E., Barrie, L. A., Ogren, J. A., and Lavoué, D. (2006). Variations and sources of the equivalent black carbon in the high Arctic revealed by long-term observations at Alert and Barrow: 1989–2003. *Journal of Geophysical Research: Atmospheres*, 111(D14208).

Sharma, S., Ishizawa, M., Chan, D., Lavoué, D., Andrews, E., Eleftheriadis, K., and Maksyutov, S. (2013). 16-year simulation of arctic black carbon: Transport, source contribution, and sensitivity analysis on deposition. *Journal of Geophysical Research: Atmospheres*, 118(2):943–964.

Sharma, S., Lavoué, D., Cachier, H., Barrie, L. A., and Gong, S. L. (2004). Long-term trends of the black carbon concentrations in the Canadian Arctic. *Journal of Geophysical Research: Atmospheres*, 109(D15203).

Shaver, G. R. and Chapin, III, F. S. (1980). Response to fertilization by various plant growth forms in an Alaskan tundra: Nutrient accumulation and growth. *Ecology*, 61(3):662–675.

Shephard, M. W. and Cady-Pereira, K. E. (2015). Cross-track infrared sounder (CrIS) satellite observations of tropospheric ammonia. *Atmospheric Measurement Techniques*, 8(3):1323–1336.

Shephard, M. W., Cady-Pereira, K. E., Luo, M., Henze, D. K., Pinder, R. W., Walker, J. T., Rinsland, C. P., Bash, J. O., Zhu, L., Payne, V. H., and Clarisse, L. (2011). TES ammonia retrieval strategy and global observations of the spatial and seasonal variability of ammonia. *Atmospheric Chemistry and Physics*, 11(20):10743–10763.

Shephard, M. W., McLinden, C. A., Cady-Pereira, K. E., Luo, M., Moussa, S. G., Leithead, A., Liggio, J., Staebler, R. M., Akingunola, A., Makar, P., Lehr, P., Zhang, J., Henze, D. K., Millet, D. B., Bash, J. O., Zhu, L., Wells, K. C., Capps, S. L., Chaliyakunnel, S., Gordon, M., Hayden, K., Brook, J. R., Wolde, M., and Li, S.-M. (2015). Tropospheric Emission Spectrometer (TES) satellite observations of ammonia, methanol, formic acid, and carbon monoxide over the Canadian oil sands: Validation and model evaluation. *Atmospheric Measurement Techniques*, 8(12):5189–5211.

Shi, Y., Matsunaga, T., Saito, M., Yamaguchi, Y., and Chen, X. (2015). Comparison of global inventories of CO_2 emissions from biomass burning during 2002-2011 derived from multiple satellite products. *Environmental Pollution*, 206:479–487.

Shindell, D. T., Chin, M., Dentener, F., Doherty, R. M., Faluvegi, G., Fiore, A. M., Hess, P., Koch, D. M., MacKenzie, I. A., Sanderson, M. G., and Others (2008). A multi-model assessment of pollution transport to the Arctic. *Atmospheric Chemistry and Physics*, 8(17):5353–5372.

Shindell, D. T., Faluvegi, G., Stevenson, D. S., Krol, M. C., Emmons, L. K., Lamarque, J.-F., Pétron, G., Dentener, F. J., Ellingsen, K., Schultz, M. G., Wild, O., Amann, M., Atherton, C. S., Bergmann, D. J., Bey, I., Butler, T., Cofala, J., Collins, W. J., Derwent, R. G., Doherty, R. M., Drevet, J., Eskes, H. J., Fiore, A. M., Gauss, M., Hauglustaine, D. A., Horowitz, L. W., Isaksen, I. S. A., Lawrence, M. G., Montanaro, V., Müller, J.-F., Pitari, G., Prather, M. J., Pyle, J. A., Rast, S., Rodriguez, J. M., Sanderson, M. G., Savage, N. H., Strahan, S. E., Sudo, K., Szopa, S., Unger, N., van Noije, T. P. C., and Zeng, G. (2006). Multimodel simulations of carbon monoxide: Comparison with observations and projected near-future changes. *Journal of Geophysical Research: Atmospheres*, 111(D19):L01104.

Simpson, I. J., Akagi, S. K., Barletta, B., Blake, N. J., Choi, Y., Diskin, G. S., Fried, A., Fuelberg, H. E., Meinardi, S., Rowland, F. S., Vay, S. A., Weinheimer, A. J., Wennberg, P. O., Wiebring, P., Wisthaler, A., Yang, M., Yokelson, R. J., and Blake, D. R. (2011). Boreal forest fire emissions in fresh Canadian smoke plumes: C_1-C_{10} volatile organic compounds (VOCs), CO_2, CO, NO_2, NO, HCN and CH_3CN. *Atmospheric Chemistry and Physics*, 11(13):6445–6463.

Singh, H. B. (2003). In situ measurements of HCN and CH_3CN over the Pacific Ocean: Sources, sinks, and budgets. *Journal of Geophysical Research: Atmospheres*, 108(D20):8795.

Singh, H. B. and Zimmerman, P. (1992). Atmospheric distribution and sources of non-methane hydrocarbons. In *Gaseous Pollutants: Characterization and Cycling*, page 235. Jon Wiley and Sons, New York.

Sioris, C. E., Abboud, I., Fioletov, V. E., and McLinden, C. A. (2017). AEROCAN, the Canadian sub-network of AERONET: Aerosol monitoring and air quality applications. *Atmospheric Environment*, 167:444–457.

Sofiev, M., Ermakova, T., and Vankevich, R. (2012). Evaluation of the smoke-injection height from wild-land fires using remote-sensing data. *Atmospheric Chemistry and Physics*, 12(4):1995–2006.

Spivakovsky, C. M., Logan, J. A., Montzka, S. A., Balkanski, Y. J., Foreman-Fowler, M., Jones, D. B. A., Horowitz, L. W., Fusco, A. C., Brenninkmeijer, C. A. M., Prather, M. J., Wofsy, S. C., and McElroy, M. B. (2000). Three-dimensional climatological distribution of tropospheric OH: Update and evaluation. *Journal of Geophysical Research: Atmospheres*, 105(D7):8931–8980.

Stavrakou, T., Müller, J.-F., Peeters, J., Razavi, A., Clarisse, L., Clerbaux, C., Coheur, P.-F., Hurtmans, D., De Mazière, M., Vigouroux, C., Deutscher, N. M., Griffith, D. W. T., Jones, N., and Paton-Walsh, C. (2011). Satellite evidence for a large source of formic acid from boreal and tropical forests. *Nature Geoscience*, 5:26–30.

Stein, A. F., Draxler, R. R., Rolph, G. D., Stunder, B. J. B., Cohen, M. D., and Ngan, F. (2015). NOAA's HYSPLIT atmospheric transport and dispersion modeling system. *Bulletin of the American Meteorological Society*, 96(12):2059–2077.

Stein, O. and Rudolph, J. (2007). Modeling and interpretation of stable carbon isotope ratios of ethane in global chemical transport models. *Journal of Geophysical Research: Atmospheres*, 112(D14308).

Stohl, A. (2006). Characteristics of atmospheric transport into the Arctic troposphere. *Journal of Geophysical Research: Atmospheres*, 111(D11306).

Stohl, A., Andrews, E., Burkhart, J. F., Forster, C., Herber, A., Hoch, S. W., Kowal, D., Lunder, C., Mefford, T., Ogren, J. A., Sharma, S., Spichtinger, N., Stebel, K., Stone, R., Ström, J., Tørseth, K., Wehrli, C., and Yttri, K. E. (2006). Pan-Arctic enhancements of light absorbing aerosol concentrations due to North American boreal forest fires during summer 2004. *Journal of Geophysical Research: Atmospheres*, 111(D22214).

Stohl, A., Forster, C., Frank, A., Seibert, P., and Wotawa, G. (2005). Technical note: The Lagrangian particle dispersion model FLEXPART version 6.2. *Atmospheric Chemistry and Physics*, 5(9):2461–2474.

Streets, D. G., Yarber, K. F., Woo, J.-H., and Carmichael, G. R. (2003). Biomass burning in Asia: Annual and seasonal estimates and atmospheric emissions. *Global Biogeochemical Cycles*, 17(4):1099.

Sussmann, R. and Buchwitz, M. (2005). Initial validation of ENVISAT/SCIAMACHY columnar CO by FTIR profile retrievals at the ground-truthing station Zugspitze. *Atmospheric Chemistry and Physics*, 5(6):1497–1503.

Sussmann, R., Forster, F., Rettinger, M., and Jones, N. (2011). Strategy for high-accuracy-and-precision retrieval of atmospheric methane from the mid-infrared FTIR network. *Atmospheric Measurement Techniques*, 4(9):1943–1964.

Sussmann, R. and Schäfer, K. (1997). Infrared spectroscopy of tropospheric trace gases: combined analysis of horizontal and vertical column abundances. *Applied Optics*, 36(3):735–741.

Sutton, M. A., Nemitz, E., Erisman, J. W., Beier, C., Bahl, K. B., Cellier, P., de Vries, W., Cotrufo, F., Skiba, U., Marco, C. D., Jones, S., Laville, P., Soussana, J. F., Loubet, B., Twigg, M., Famulari, D., Whitehead, J., Gallagher, M. W., Neftel, A., Flechard, C. R., Herrmann, B., Calanca, P. L., Schjoerring, J. K., Daemmgen, U., Horvath, L., Tang, Y. S., Emmett, B. A., Tietema, A., Peñuelas, J., Kesik, M., Brueggemann, N., Pilegaard, K., Vesala, T., Campbell, C. L., Olesen, J. E., Dragosits, U., Theobald, M. R., Levy, P., Mobbs, D. C., Milne, R., Viovy, N., Vuichard, N., Smith, J. U., Smith, P., Bergamaschi, P., Fowler, D., and Reis, S. (2007). Challenges in quantifying biosphere-atmosphere exchange of nitrogen species. *Environmental Pollution*, 150(1):125–139.

Tanimoto, H., Kajii, Y., Hirokawa, J., Akimoto, H., and Minko, N. P. (2000). The atmospheric impact of boreal forest fires in far eastern Siberia on the seasonal variation of carbon monoxide: Observations at Rishiri, A northern remote island in Japan. *Geophysical Research Letters*, 27(24):4073–4076.

Té, Y., Jeseck, P., Franco, B., Mahieu, E., Jones, N., Paton-Walsh, C., Griffith, D. W. T., Buchholz, R. R., Hadji-Lazaro, J., Hurtmans, D., and Janssen, C. (2016). Seasonal variability of surface and column carbon monoxide over the megacity Paris, high-altitude Jungfraujoch and Southern Hemispheric Wollongong stations. *Atmospheric Chemistry and Physics*, 16(17):10911–10925.

Teakles, A. D., So, R., Ainslie, B., Nissen, R., Schiller, C., Vingarzan, R., McKendry, I., Macdonald, A. M., Jaffe, D. A., Bertram, A. K., Strawbridge, K. B., Leaitch, W. R., Hanna, S., Toom, D., Baik, J., and Huang, L. (2017). Impacts of the July 2012 Siberian fire plume on air quality in the Pacific Northwest. *Atmospheric Chemistry and Physics*, 17(4):2593–2611.

Tereszchuk, K. A., González Abad, G., Clerbaux, C., Hadji-Lazaro, J., Hurtmans, D., Coheur, P.-F., and Bernath, P. F. (2013). ACE-FTS observations of pyrogenic trace species in boreal biomass burning plumes during BORTAS. *Atmospheric Chemistry and Physics*, 13(9):4529–4541.

The International GEOS-Chem User Community (2018). geoschem/geos-chem: GEOS-Chem 12.1.1.

Theobald, M. R., Crittenden, P. D., Hunt, A. P., Tang, Y. S., Dragosits, U., and Sutton, M. A. (2006). Ammonia emissions from a Cape fur seal colony, Cape Cross, Namibia. *Geophysical Research Letters*, 33(L03812).

Thoning, K. W., Tans, P. P., and Komhyr, W. D. (1989). Atmospheric carbon dioxide at Mauna Loa Observatory: 2. Analysis of the NOAA GMCC data, 1974-1985. *Journal of Geophysical Research: Atmospheres*, 94(D6):8549–8565.

Tikhonov, A. N. (1963). Solution of incorrectly posed problems and the regularization method. In *Proc.(Doklady) Acad. Sci. USSR*, volume 151.

Timofeyev, Y., Virolainen, Y., Makarova, M., Poberovsky, A., Polyakov, A., Ionov, D., Osipov, S., and Imhasin, H. (2016). Ground-based spectroscopic measurements of atmospheric gas composition near Saint Petersburg (russia). *Journal of Molecular Spectroscopy*, 323:2–14.

Tomasi, C., Kokhanovsky, A. A., Lupi, A., Ritter, C., Smirnov, A., O'Neill, N. T., Stone, R. S., Holben, B. N., Nyeki, S., Wehrli, C., Stohl, A., Mazzola, M., Lanconelli, C., Vitale, V., Stebel, K., Aaltonen, V., de Leeuw, G., Rodriguez, E., Herber, A. B., Radionov, V. F., Zielinski, T., Petelski, T., Sakerin, S. M., Kabanov, D. M., Xue, Y., Mei, L., Istomina, L., Wagener, R., McArthur, B., Sobolewski, P. S., Kivi, R., Courcoux, Y., Larouche, P., Broccardo, S., and Piketh, S. J. (2015). Aerosol remote sensing in polar regions. *Earth-Science Reviews*, 140:108–157.

Toon, G. C. (2015). Atmospheric line list for the 2014 TCCON data release. `https://data.caltech.edu/records/248`.

Toon, G. C., Blavier, J.-F., Sen, B., Margitan, J. J., Webster, C. R., May, R. D., Fahey, D., Gao, R., Del Negro, L., Proffitt, M., Elkins, J., Romashkin, P. A., Hurst, D. F., Oltmans, S., Atlas, E., Schauffler, S., Flocke, F., Bui, T. P., Stimpfle, R. M., Bonne, G. P., Voss, P. B., and Cohen, R. C. (1999). Comparison of MkIV balloon and ER-2 aircraft measurements of atmospheric trace gases. *Journal of Geophysical Research: Atmospheres*, 104(D21):26779–26790.

Turquety, S., Logan, J. A., Jacob, D. J., Hudman, R. C., Leung, F. Y., Heald, C. L., Yantosca, R. M., Wu, S., Emmons, L. K., Edwards, D. P., and Sachse, G. W. (2007). Inventory of boreal fire emissions for North America in 2004: Importance of peat burning and pyroconvective injection. *Journal of Geophysical Research: Atmospheres*, 112(D12S03).

Urbanski, S. (2014). Wildland fire emissions, carbon, and climate: Emission factors. *Forest Ecology and Management*, 317:51–60.

Urbanski, S. P. (2013). Combustion efficiency and emission factors for wildfire-season fires in mixed conifer forests of the northern Rocky Mountains, US. *Atmospheric Chemistry and Physics*, 13(14):7241–7262.

Val Martin, M., Honrath, R. E., Owen, R. C., Pfister, G., Fialho, P., and Barata, F. (2006). Significant enhancements of nitrogen oxides, black carbon, and ozone in the

North Atlantic lower free troposphere resulting from North American boreal wildfires. *Journal of Geophysical Research: Atmospheres*, 111(D23S60).

Val Martin, M., Kahn, R. A., and Tosca, M. G. (2018). A global analysis of wildfire smoke injection heights derived from space-based multi-angle imaging. *Remote Sensing*, 10(10):1609.

Val Martin, M., Logan, J. A., Kahn, R. A., Leung, F.-Y., Nelson, D. L., and Diner, D. J. (2010). Smoke injection heights from fires in North America: Analysis of 5 years of satellite observations. *Atmospheric Chemistry and Physics*, 10(4):1491–1510.

Van Damme, M., Clarisse, L., Dammers, E., Liu, X., Nowak, J. B., Clerbaux, C., Flechard, C. R., Galy-Lacaux, C., Xu, W., Neuman, J. A., Tang, Y. S., Sutton, M. A., Erisman, J. W., and Coheur, P. F. (2015a). Towards validation of ammonia (NH_3) measurements from the IASI satellite. *Atmospheric Measurement Techniques*, 8(3):1575–1591.

Van Damme, M., Clarisse, L., Heald, C. L., Hurtmans, D., Ngadi, Y., Clerbaux, C., Dolman, A. J., Erisman, J. W., and Coheur, P. F. (2014). Global distributions, time series and error characterization of atmospheric ammonia (NH_3) from IASI satellite observations. *Atmospheric Chemistry and Physics*, 14(6):2905–2922.

Van Damme, M., Erisman, J. W., Clarisse, L., Dammers, E., Whitburn, S., Clerbaux, C., Dolman, A. J., and Coheur, P.-F. (2015b). Worldwide spatiotemporal atmospheric ammonia (NH_3) columns variability revealed by satellite. *Geophysical Research Letters*, 42(20):8660–8668.

Van Damme, M., Whitburn, S., Clarisse, L., Clerbaux, C., Hurtmans, D., and Coheur, P.-F. (2017). Version 2 of the IASI NH_3 neural network retrieval algorithm: Near-real-time and reanalysed datasets. *Atmospheric Measurement Techniques*, 10(12):4905–4914.

van der Werf, G. R., Randerson, J. T., Giglio, L., van Leeuwen, T. T., Chen, Y., Rogers, B. M., Mu, M., van Marle, M. J. E., Morton, D. C., Collatz, G. J., Yokelson, R. J., and Kasibhatla, P. S. (2017). Global fire emissions estimates during 1997–2016. *Earth System Science Data*, 9(2):697–720.

Veraverbeke, S., Rogers, B. M., Goulden, M. L., Jandt, R. R., Miller, C. E., Wiggins, E. B., and Randerson, J. T. (2017). Lightning as a major driver of recent large fire years in North American boreal forests. *Nature Climate Change*, 7:529–534.

Viatte, C., Strong, K., Hannigan, J., Nussbaumer, E., Emmons, L. K., Conway, S., Paton-Walsh, C., Hartley, J., Benmergui, J., and Lin, J. (2015). Identifying fire plumes in the Arctic with tropospheric FTIR measurements and transport models. *Atmospheric Chemistry and Physics*, 15(5):2227–2246.

Viatte, C., Strong, K., Paton-Walsh, C., Mendonca, J., O'Neill, N. T., and Drummond, J. R. (2013). Measurements of CO, HCN, and C_2H_6 total columns in smoke plumes transported from the 2010 Russian boreal forest fires to the Canadian high Arctic. *Atmosphere-Ocean*, 51(5):522–531.

Viatte, C., Strong, K., Walker, K. A., and Drummond, J. R. (2014). Five years of CO, HCN, C_2H_6, C_2H_2, CH_3OH, HCOOH and H_2CO total columns measured in the Canadian high Arctic. *Atmospheric Measurement Techniques*, 7(6):1547–1570.

Vigouroux, C., Bauer Aquino, C. A., Bauwens, M., Becker, C., Blumenstock, T., Mazière, M. D., García, O., Grutter, M., Guarin, C., Hannigan, J., Hase, F., Jones, N., Kivi, R., Koshelev, D., Langerock, B., Lutsch, E., Makarova, M., Metzger, J.-M., Müller, J.-F., Notholt, J., Ortega, I., Palm, M., Paton-Walsh, C., Poberovskii, A., Rettinger, M., Robinson, J., Smale, D., Stavrakou, T., Stremme, W., Strong, K., Sussmann, R., Té, Y., and Toon, G. (2018). NDACC harmonized formaldehyde time series from 21

FTIR stations covering a wide range of column abundances. *Atmospheric Measurement Techniques*, 11(9):5049–5073.

Vigouroux, C., Hendrick, F., Stavrakou, T., Dils, B., Smedt, I. D., Hermans, C., Merlaud, A., Scolas, F., Senten, C., Vanhaelewyn, G., and Others (2009). Ground-based FTIR and MAX-DOAS observations of formaldehyde at Reunion Island and comparisons with satellite and model data. *Atmospheric Chemistry and Physics*, 9(24):9523–9544.

Vigouroux, C., Stavrakou, T., Whaley, C., Dils, B., Duflot, V., Hermans, C., Kumps, N., Metzger, J.-M., Scolas, F., Vanhaelewyn, G., Müller, J.-F., Jones, D. B. A., Li, Q., and De Mazière, M. (2012). FTIR time-series of biomass burning products (HCN, C_2H_6, C_2H_2, CH_3OH, and HCOOH) at Reunion Island (21°S, 55°E) and comparisons with model data. *Atmospheric Chemistry and Physics*, 12(21):10367–10385.

von Clarmann, T. (2014). Smoothing error pitfalls. *Atmospheric Measurement Techniques*, 7(9):3023–3034.

Wang, Q., Jacob, D. J., Fisher, J. A., Mao, J., Leibensperger, E. M., Carouge, C. C., Sager, P. L., Kondo, Y., Jimenez, J. L., Cubison, M. J., and Others (2011). Sources of carbonaceous aerosols and deposited black carbon in the Arctic in winter-spring: Implications for radiative forcing. *Atmospheric Chemistry and Physics*, 11(23):12453–12473.

Ward, D. E. and Hardy, C. C. (1991). Smoke emissions from wildland fires. *Environment International*, 17(2):117–134.

Warneke, C., Bahreini, R., Brioude, J., Brock, C. A., de Gouw, J. A., Fahey, D. W., Froyd, K. D., Holloway, J. S., Middlebrook, A., Miller, L., Montzka, S., Murphy, D. M., Peischl, J., Ryerson, T. B., Schwarz, J. P., Spackman, J. R., and Veres, P. (2009). Biomass burning in Siberia and Kazakhstan as an important source for haze over the Alaskan Arctic in April 2008. *Geophysical Research Letters*, 36(2).

Warner, J. X., Wei, Z., Strow, L. L., Dickerson, R. R., and Nowak, J. B. (2016). The global tropospheric ammonia distribution as seen in the 13-year AIRS measurement record. *Atmospheric Chemistry and Physics*, 16(8):5467–5479.

Weaver, D. (2018). *Water Vapour Measurements in the Canadian High Arctic*. PhD thesis, University of Toronto.

Wentworth, G. R., Aklilu, Y.-A., Landis, M. S., and Hsu, Y.-M. (2018). Impacts of a large boreal wildfire on ground level atmospheric concentrations of PAHs, VOCs and ozone. *Atmospheric Environment*, 178:19–30.

Wentworth, G. R., Murphy, J. G., Croft, B., Martin, R. V., Pierce, J. R., Côté, J.-S., Courchesne, I., Tremblay, J.-É., Gagnon, J., Thomas, J. L., Sharma, S., Toom-Sauntry, D., Chivulescu, A., Levasseur, M., and Abbatt, J. P. D. (2016). Ammonia in the summertime arctic marine boundary layer: sources, sinks, and implications. *Atmospheric Chemistry and Physics*, 16(4):1937–1953.

Wesely, M. L. (1989). Parameterization of surface resistances to gaseous dry deposition in regional-scale numerical models. *Atmospheric Environment*, 23(6):1293–1304.

Westerling, A. L., Hidalgo, H. G., Cayan, D. R., and Swetnam, T. W. (2006). Warming and earlier spring increase western US forest wildfire activity. *Science*, 313(5789):940–943.

Whaley, C. H., Makar, P. A., Shephard, M. W., Zhang, L., Zhang, J., Zheng, Q., Akingunola, A., Wentworth, G. R., Murphy, J. G., Kharol, S. K., and Cady-Pereira, K. E. (2018). Contributions of natural and anthropogenic sources to ambient ammonia in the Athabasca Oil Sands and north-western Canada. *Atmospheric Chemistry and Physics*, 18(D3):2011–2034.

Whaley, C. H., Strong, K., Jones, D. B. A., Walker, T. W., Jiang, Z., Henze, D. K., Cooke, M. A., McLinden, C. A., Mittermeier, R. L., Pommier, M., and Fogal, P. F.

(2015). Toronto area ozone: Long-term measurements and modeled sources of poor air quality events. *Journal of Geophysical Research: Atmospheres*, 120(D21):11,368–11,390.

Whitburn, S., Van Damme, M., Clarisse, L., Bauduin, S., Heald, C. L., Hadji-Lazaro, J., Hurtmans, D., Zondlo, M. A., Clerbaux, C., and Coheur, P.-F. (2016). A flexible and robust neural network IASI-NH_3 retrieval algorithm. *Journal of Geophysical Research: Atmospheres*, 121(D11):6581–6599.

Whitburn, S., Van Damme, M., Clarisse, L., Hurtmans, D., Clerbaux, C., and Coheur, P.-F. (2017). IASI-derived NH_3 enhancement ratios relative to CO for the tropical biomass burning regions. *Atmospheric Chemistry and Physics*, 17(19):12239–12252.

Whitburn, S., Van Damme, M., Kaiser, J. W., van der Werf, G. R., Turquety, S., Hurtmans, D., Clarisse, L., Clerbaux, C., and Coheur, P.-F. (2015). Ammonia emissions in tropical biomass burning regions: Comparison between satellite-derived emissions and bottom-up fire inventories. *Atmospheric Environment*, 121:42–54.

Wiacek, A. (2006). *First Trace Gas Measurements Using Fourier Transform Infrared Solar Absorption Spectroscopy at the University of Toronto Atmospheric Observatory*. PhD thesis, University of Toronto.

Wiacek, A., Taylor, J. R., Strong, K., Saari, R., Kerzenmacher, T. E., Jones, N. B., and Griffith, D. W. T. (2007). Ground-Based solar absorption FTIR spectroscopy: Characterization of retrievals and first results from a novel optical design instrument at a new NDACC complementary station. *Journal of Atmospheric and Oceanic Technology*, 24(3):432–448.

Wiedinmyer, C., Akagi, S. K., Yokelson, R. J., Emmons, L. K., Al-Saadi, J. A., Orlando, J. J., and Soja, A. J. (2011). The Fire INventory from NCAR (FINN): A high resolution global model to estimate the emissions from open burning. *Geoscientific Model Development*, 4(3):625–641.

Winiger, P., Barrett, T. E., Sheesley, R. J., Huang, L., Sharma, S., Barrie, L. A., Yttri, K. E., Evangeliou, N., Eckhardt, S., Stohl, A., Klimont, Z., Heyes, C., Semiletov, I. P., Dudarev, O. V., Charkin, A., Shakhova, N., Holmstrand, H., Andersson, A., and Gustafsson, Ö. (2019). Source apportionment of circum-Arctic atmospheric black carbon from isotopes and modeling. *Science Advances*, 5(2):8052.

Witte, J. C., Douglass, A. R., Silva, A. d., Torres, O., Levy, R., and Duncan, B. N. (2011). NASA A-Train and Terra observations of the 2010 Russian wildfires. *Atmospheric Chemistry and Physics*, 11(17):9287–9301.

Wotton, B. M., Flannigan, M. D., and Marshall, G. A. (2017). Potential climate change impacts on fire intensity and key wildfire suppression thresholds in Canada. *Environmental Research Letters*, 12(9):095003.

Wotton, B. M., Nock, C. A., and Flannigan, M. D. (2010). Forest fire occurrence and climate change in Canada. *International Journal of Wildland Fire*, 19(3):253–271.

Wunch, D., Toon, G. C., Blavier, J.-F. L., Washenfelder, R. A., Notholt, J., Connor, B. J., Griffith, D. W. T., Sherlock, V., and Wennberg, P. O. (2011). The Total Carbon Column Observing Network. *Philosophical transactions. Series A, Mathematical, physical, and engineering sciences*, 369(1943):2087–2112.

Xiao, Y., Jacob, D. J., and Turquety, S. (2007). Atmospheric acetylene and its relationship with CO as an indicator of air mass age. *Journal of Geophysical Research: Atmospheres*, 112(D12305).

Xiao, Y., Logan, J. A., Jacob, D. J., Hudman, R. C., Yantosca, R., and Blake, D. R. (2008). Global budget of ethane and regional constraints on U.S. sources. *Journal of Geophysical Research: Atmospheres*, 113(D21306).

Yasunari, T. J., Kim, K.-M., da Silva, A. M., Hayasaki, M., Akiyama, M., and Murao, N. (2018). Extreme air pollution events in Hokkaido, Japan, traced back to early snowmelt and large-scale wildfires over East Eurasia: Case studies. *Scientific Reports*, 8(1):6413.

Yevich, R. and Logan, J. A. (2003). An assessment of biofuel use and burning of agricultural waste in the developing world. *Global Biogeochemical Cycles*, 17(4):1095.

Yokelson, R. J., Andreae, M. O., and Akagi, S. K. (2013). Pitfalls with the use of enhancement ratios or normalized excess mixing ratios measured in plumes to characterize pollution sources and aging. *Atmospheric Measurement Techniques*, 6(8):2155–2158.

Yokelson, R. J., Bertschi, I. T., Christian, T. J., Hobbs, P. V., Ward, D. E., and Hao, W. M. (2003). Trace gas measurements in nascent, aged, and cloud-processed smoke from African savanna fires by airborne Fourier transform infrared spectroscopy (AFTIR). *Journal of Geophysical Research: Atmospheres*, 108(13):8478.

Yokelson, R. J., Crounse, J. D., DeCarlo, P. F., Karl, T., Urbanski, S., Atlas, E, Campos, T., Shinozuka, Y., Kapustin, V., Clarke, A. D., Weinheimer, A., Knapp, D. J., Montzka, D. D., Holloway, J., Weibring, P., Flocke, F., Zheng, W., Toohey, D., Wennberg, P. O., Wiedinmyer, C., Mauldin, L., Fried, A., Richter, D., Walega, J., Jimenez, J. L., Adachi, K., Buseck, P. R., Hall, S. R., and Shetter, R. (2009). Emissions from biomass burning in the Yucatan. *Atmospheric Chemistry and Physics*, 9(15):5785–5812.

Yokelson, R. J., Goode, J. G., Ward, D. E., Susott, R. A., Babbitt, R. E., Wade, D. D., Bertschi, I., Griffith, D. W. T., and Hao, W. M. (1999). Emissions of formaldehyde, acetic acid, methanol, and other trace gases from biomass fires in North Carolina measured by airborne Fourier transform infrared spectroscopy. *Journal of Geophysical Research: Atmospheres*, 104(D23):30109–30125.

Yokelson, R. J., Griffith, D. W. T., and Ward, D. E. (1996). Open-path Fourier transform infrared studies of large-scale laboratory biomass fires. *Journal of Geophysical Research: Atmospheres*, 101(D15):21067–21080.

York, D., Evensen, N. M., Martınez, M. L., and De Basabe Delgado, J. (2004). Unified equations for the slope, intercept, and standard errors of the best straight line. *American Journal of Physics*, 72(3):367–375.

Yu, K., Keller, C. A., Jacob, D. J., Molod, A. M., Eastham, S. D., and Long, M. S. (2018). Errors and improvements in the use of archived meteorological data for chemical transport modeling: An analysis using GEOS-Chem v11-01 driven by GEOS-5 meteorology. *Geoscientific Model Development*, 11(1):305–319.

Yurganov, L. N., Rakitin, V., Dzhola, A., August, T., Fokeeva, E., George, M., Gorchakov, G., Grechko, E., Hannon, S., Karpov, A., Ott, L., Semutnikova, E., Shumsky, R., and Strow, L. (2011). Satellite and ground-based CO total column observations over 2010 Russian fires: accuracy of top-down estimates based on thermal IR satellite data. *Atmospheric Chemistry and Physics*, 11(15):7925–7942.

Zander, R., Mahieu, E., Demoulin, P., Duchatelet, P., Roland, G., Servais, C., De Mazière, M., Reimann, S., and Rinsland, C. P. (2008). Our changing atmosphere: evidence based on long-term infrared solar observations at the Jungfraujoch since 1950. *The Science of the Total Environment*, 391(2-3):184–195.

Zellweger, C., Hüglin, C., Klausen, J., Steinbacher, M., Vollmer, M., and Buchmann, B. (2009). Inter-comparison of four different carbon monoxide measurement techniques and evaluation of the long-term carbon monoxide time series of Jungfraujoch. *Atmospheric Chemistry and Physics*, 9(11):3491–3503.

Zhang, L., Gong, S., Padro, J., and Barrie, L. (2001). A size-segregated particle dry deposition scheme for an atmospheric aerosol module. *Atmospheric Environment*, 35(3):549–560.

Zhao, Y., Kondo, Y., Murcray, F. J., Liu, X., Koike, M., Irie, H., Strong, K., Suzuki, K., Sera, M., and Ikegami, Y. (2000). Seasonal variations of HCN over Northern Japan measured by ground-based infrared solar spectroscopy. *Geophysical Research Letters*, 27(14):2085–2088.

Zhao, Y., Kondo, Y., Murcray, F. J., Liu, X., Koike, M., Kita, K., Nakajima, H., Murata, I., and Suzuki, K. (1997). Carbon monoxide column abundances and tropospheric concentrations retrieved from high resolution ground-based infrared solar spectra at 43.5°N over Japan. *Journal of Geophysical Research: Atmospheres*, 102(D19):23403–23411.

Zhao, Y., Strong, K., Kondo, Y., Koike, M., Matsumi, Y., Irie, H., Rinsland, C. P., Jones, N. B., Suzuki, K., Nakajima, H., Nakane, H., and Murata, I. (2002). Spectroscopic measurements of tropospheric CO, C_2H_6, C_2H_2, and HCN in Northern Japan. *Journal of Geophysical Research: Atmospheres*, 107(D18):4343–4359.

Zhu, L., Henze, D., Bash, J., Jeong, G.-R., Cady-Pereira, K., Shephard, M., Luo, M., Paulot, F., and Capps, S. (2015). Global evaluation of ammonia bidirectional exchange and livestock diurnal variation schemes. *Atmospheric Chemistry and Physics*, 15(22):12823–12843.

Zhu, Z., Piao, S., Myneni, R. B., Huang, M., Zeng, Z., Canadell, J. G., Ciais, P., Sitch, S., Friedlingstein, P., Arneth, A., Cao, C., Cheng, L., Kato, E., Koven, C., Li, Y., Lian, X., Liu, Y., Liu, R., Mao, J., Pan, Y., Peng, S., Peñuelas, J., Poulter, B., Pugh, T. A. M., Stocker, B. D., Viovy, N., Wang, X., Wang, Y., Xiao, Z., Yang, H., Zaehle, S., and Zeng, N. (2016). Greening of the Earth and its drivers. *Nature Climate Change*, 6:791–795.